Synthesis of Nanoparticle Model Systems for Sustainable Catalysis by Gas Aggregation

Bodin, Anders

Publication date:
2017

Document Version
Publisher's PDF, also known as Version of record

Ph.D. Thesis

Synthesis of Nanoparticle Model Systems for Sustainable Catalysis by Gas Aggregation

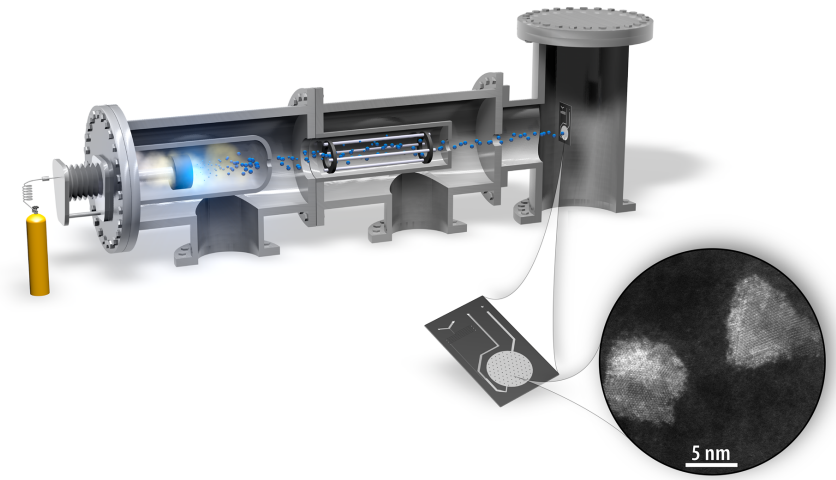

Anders Bodin

Supervisor: Professor Ib Chorkendorff
Co-supervisor: Professor Jane H. Nielsen

Technical University of Denmark
Department of Physics
Surface Physics and Catalysis (SurfCat)
Villum Center for the Science of Sustainable Fuels and Chemicals

July 2017

Abstract

The overall goal of this thesis is to develop better catalysts for chemical reactions used in sustainable energy storage and environmental protection. Specifically, the thesis presents research on well-defined catalyst model systems of nanoparticles synthesized by magnetron sputtering, gas-aggregation, and subsequent mass-filtering. The thesis opens with a presentation of the broader context of the research, particularly focusing on the societal importance of catalysis, followed by an introduction to the fundamentals of the science of catalysis. Three research projects are then described in individual chapters, summarized in the following:

Platinum Catalysts for TW-Scale H_2 Production: Platinum has the highest activity of known catalysts for the hydrogen evolution reaction (HER), but due to scarcity and price it is often assumed to by infeasible for photoelectrochemical water splitting on the terawatt-scale that is needed for significant global impact. This study investigates the relationship between catalytic activity for the HER and platinum catalyst loading using well-defined model systems with different loadings of mass-selected 5 nm Pt nanoparticles. Using the knowledge gained on these systems, a technoeconomic analysis is carried out, showing that photoelectrochemical HER at a current density of 10 $\frac{\text{mA}}{\text{cm}^2}$ and an overpotential of 50 mV could be obtained with a catalyst consumption of 54 tons of Pt per TW energy stored in H_2, corresponding to $\sim 1/4$ of the global, annual Pt production.

Synthesis of Ni−Mo−S Nanoparticles by Reactive Gas Aggregation: In this project, a method was developed for synthesizing in-flight sulfided Ni-Mo-S nanoparticles by aggregation of sputtered metal from a $Mo_{75}Ni_{25}$ target in a reactive atmosphere of Ar and H_2S. The resulting particles are undersulfided with a stoichiometry of $Mo_{0.8}Ni_{0.2}S_{1.1}$, and the particles exhibit high-surface area morphologies such as platelets, very different from the spherical morphologies observed for metal nanoparticles. The particles are mass-filtered before deposition, and it is shown that different masses results in significantly different particle morphologies. Using a microreactor platform, the catalytic activity of the nanoparticles is assesed for hydrodesulfurization (HDS) of dibenzothiophene, relevant for e.g. production of diesel with ultra-low sulfur content. It is found that in-flight sulfided Ni-Mo-S nanoparticles have more than twice as high HDS activity as Ni-Mo-S nanoparticles produced by inert gas aggregation and post-sulfidation.

This points towards the potential of engineering nanoscale catalysts for HDS by reactive gas aggregation synthesis of nanoparticles.

Dynamic Effects of Surface Oxygen in CO Electroreduction: One of the keys to developing better catalysts for energy-storage by electrolysis of CO_2 is to understand the principles behind electroreduction of the reaction intermediate CO. This study reports the discovery of a high, transient production of methane at the onset of electroreduction of CO on mass-selected copper nanoparticles produced by inert gas-aggregation, investigated with a newly developed system for electrochemical mass-spectrometry. This "dynamic methane" is only observed when the nanoparticles have been exposed to O_2 before the electrode potential is stepped to CO-reduction potentials. Based on analysis of experimental data and density functional theory, it is proposed that the dynamic methane is formed on nanoparticle kink-sites, which are activated by adsorbed oxygen; the transient nature of the dynamic methane is attributed to the fact that the adsorbed oxygen is only metastable. The results contribute to the understanding of the role of oxygen in CO-electroreduction, and could potentially be used on industrial scale if metastable active sites were cyclically regenerated.

The presented research demonstrates the insights that can be gained by studying well-defined model systems in catalysis, which can both contribute to fundamental scientific understanding and guide the development of catalysis technology.

Resumé

Det overordnede formål med denne afhandling er at udvikle bedre katalysatorer til kemiske reaktioner indenfor bæredygtig energilagring og miljøbeskyttelse. Specifikt præsenterer afhandlingen forskning omhandlende veldefinerede modelsystemer af nanopartikler, syntetiseret ved magnetron-sputtering, gas-aggregering og efterfølgende masse-filtrering. Afhandlingen starter med en præsentation af den bredere kontekst for det videnskabelige arbejde, med fokus på den samfundsmæssige vigtighed af katalyse, efterfulgt af en introduktion til grundlæggende katalysevidenskab. Dernæst beskrives tre forskningsprojekter i separate kapitler som opsummeres i det følgende:

Platin-katalysatorer til TW-skala H_2-produktion: Platin har den højeste katalytiske aktivitet af de kendte katalysatorer til hydrogen-udviklings-reaktionen (HER), men pga. dets knaphed og pris bliver det ofte antaget at det vil være umuligt at benytte Pt til at katalysere fotoelektrokemisk vandspaltning på terawatt-skala, som er nødvendigt for en signifikant global indvirkning af teknologien. Dette studie undersøger sammenhængen mellem katalytisk aktivitet til HER og loading af platin ved at bruge veldefinerede modelsystemer med forskellige masseloadings af masse-selekterede 5 nm Pt nanopartikler. Ved at bruge den viden som opnås på disse systemer laves der en teknoøkonomisk analyse som viser at fotoelektrokemisk HER ved en strømdensitet på 10 $\frac{\text{mA}}{\text{cm}^2}$ og et overpotentiale på 50 mV kan opnås ved et katalysator-forbrug på 54 tons platin per TW energi som lagres i H_2, svarende til ca. 1/4 af den globale, årlige Pt-produktion.

Syntese af Ni-Mo-S nanopartikler ved reaktiv gas-aggregering: I dette projekt blev der udviklet en metode til syntese af in-flight-sulfiderede Ni-Mo-S nanopartikler ved aggregering af sputteret metal fra et $Mo_{75}Ni_{25}$-target i en reaktiv atmosfære af Ar og H_2S. De resulterende partikler er undersulfiderede med en støkiometri på $Mo_{0.8}Ni_{0.2}S_{1.1}$, og partikerne viser morfologier med høje overfladearealer, såsom plader, hvilket er meget forskelligt fra de sfæriske morfologier som observeres for metalliske nanopartikler. Partiklerne massefiltreres før deposition, og det vises at ændringer i massen resulterer i betydeligt forskellige partikelmorfologier. Ved at bruge en mikroreaktor-platform måles nanopartiklernes katalytiske aktivitet for afsvovling (hydrodesulfurization, HDS) af dibenzothiofen, som blandt andet er relevant ved produktionen af diesel med ultra-lavt svovlind-

hold. Det observeres at in-flight-sulfiderede Ni-Mo-S nanopartikler er mere end dobbelt så aktive som Ni-Mo-S nanopartikler produceret ved gas-aggregering i ædelgas, som eftersulfideres. Dette resultat peger hen imod potentialet i at designe nanoskala-katalysatorer til HDS gennem syntese ved reaktiv gas-aggregering.

Dynamiske effekter af overflade-oxygen i CO-elektroreduktion: En af nøglerne til at udvikle bedre katalysatorer til at lagre energi ved elektrolyse af CO_2 er at forstå principperne bag elektroreduktion af CO. Dette studie beretter om opdagelsen af en høj, transient produktion af metan ved begyndelsen af elektroreduktion af CO på masse-selekterede kopper-nanopartikler produceret ved ædelgas-aggregering, ved at bruge et nyligt udviklet system til elektrokemisk masse-spektrometri. Den "dynamiske metan" observeres kun når nanopartiklerne har været eksponeret for O_2 før elektrodepotentialet bliver sat til CO-reduktionspotentialer. Baseret på analyse af de eksperimentelle resultater og densitet-funktional-teori (DFT) fremstilles det som forklaring at den dynamiske metan bliver dannet på nanopartiklernes kink-sites som bliver aktiveret af adsorberet oxygen; den dynamiske metans transiente opførsel forklares ved at den adsorberede oxygen kun er metastabil. Resultaterne bidrager til forståelsen af oxygens rolle i CO-reduktionsprocessen og kunne potentielt anvendes på industriel skala hvis de metastabile sites blev cyklisk regenereret.

De præsenterede forskningsresultater viser hvilken indsigt der kan opnås ved at studere veldefinerede katalytiske modelsystemer, som både kan bidrage til grundlæggende videnskabelig forståelse og opstille retningslinjer for udviklingen af katalyse-teknologi.

Preface

This thesis is submitted as part of the requirements for obtaining the Ph.D. degree from the Technical University of Denmark. The work presented herein was performed from February 2014 to July 2017 in the Surface physics and Catalysis (SurfCat) group at the Department of Physics under the supervision of professor Ib Chorkendorff and professor Jane H. Nielsen.

Writing a Ph.D. has involved many good experiences, but I have particularly enjoyed the research community at SurfCat which includes so many inspiring people. The synergy obtained by bringing individuals together with so diverse backgrounds and personalities have created an atmosphere of scientific curiosity and academic excellence, from which I have benefited greatly. Although we work in a competitive environment, the people of SurfCat are both warm and considerate and it has been a pleasure to meet many good friends here.

My main supervisor, Ib Chorkendorff, has had an important role in creating the environment at SurfCat, and I am happy to have written my Ph.D. with his creative, ambitious, and open-minded guidance. I have been co-supervised by Jane H. Nielsen, who is also the head of the Department of Physics. Apart from her scientific mentoring, I have also thoroughly enjoyed working with her in different committees at the department.

I would like to especially thank Béla Sebök, who did his Ph.D. along with me. His technical expertise and hard-working determination together with a great sense of humor makes him the ideal lab and office mate. Also, it has been a pleasure to share the road with Daniel Trimarco, all the way from first day on campus to now, where we finish our studies ten years later. It has been immensely important for me to have such a good friend in the group during all the ups and downs of the Ph.D.

I dedicate this thesis to my father, who introduced me to turbopumps, liquid nitrogen, and complex numbers before I could read. I am deeply grateful for the wonder and curiosity about Nature that he instilled in me.

Anders Bodin

List of Appended Papers

Paper I: Scalability and Feasibility of Photoelectrochemical H_2 Evolution: The Ultimate Limit of Pt Nanoparticles as an HER Catalyst
E. Kemppainen, **A. Bodin**, B. Sebok, T. Pedersen, B. Seger, B. Mei, D. Bae, P. C. K. Vesborg, J. Halme, O. Hansen, P. D. Lund, and I. Chorkendorff
Energy Environ. Sci., 2015, ***8****, 2991*

Paper II: Engineering Ni−Mo−S Nanoparticles for Ultra-Deep Hydrodesulfurization: Reactive Gas Aggregation Synthesis, Characterization and Catalytic Testing
A. Bodin, A. L. Christoffersen, C. F. Elkjær, J. Kibsgaard, S. Helveg, I. Chorkendorff
In preparation - abstract included

Paper III: Dynamic Effects of Surface Oxygen in CO Electroreduction
S. B. Scott*, D. B. Trimarco*, **A. Bodin***, A. Bagger, N. Mazzanti, J. E. Sørensen, T. Pedersen, O. Hansen, I. E. L. Stephens, P. C. K. Vesborg, J. Rossmeisl, I. Chorkendorff
In preparation
*These authors contributed equally

Papers not Presented in the Thesis

Paper IV: Exploring the Phase Space of Time of Flight Mass Selected Pt_xY Nanoparticles
F. Masini, P. Hernández-Fernández, D. Deiana, C. E. Strebel, D. N. McCarthy, **A. Bodin**, P. Malacrida, I. Stephens, and I. Chorkendoff
Phys. Chem. Chem. Phys., 2014, ***16****, 26506*

Paper V: Operando XAS Study of the Surface Oxidation State on a Monolayer IrO_x on RuO_x and Ru Oxide Based Nanoparticles for Oxygen Evolution in Acidic Media
A. F. Pedersen, M. Escudero-Escribano, B. Sebok, **A. Bodin**, E. Paoli, R. Frydendal, D. Friebel, I. E. L. Stephens, J. Rossmeisl, I. Chorkendorff, A. Nilsson.
Submitted to Journal of Physical Chemistry B

Paper VI: Oxygen evolution on well characterized mass-selected NiFe nanoparticles: mechanism and size-effect
C. Roy, B. Sebok, E. M. Fiordaliso, **A. Bodin**, S. B. Scott, D. B Trimarco, C. D. Damsgaard, J. Kibsgaard, I. E. L. Stephens, and I. Chorkendorff
In preparation

Paper VII: Ambient Pressure HDS of Refractory Sulfur Compounds in Highly Sensitive μ-reactor Platform Coupled to a Time-of-Flight Mass Spectrometer
A. L. Christoffersen, **A. Bodin**, C. F. Elkjær, J. E. Sørensen, J. Kibsgaard, I. Chorkendorff
In preparation

Contents

Chapter 1

Introduction

This chapter serves as an introduction to the field of catalysis and the research communicated in the thesis. I will start with a broad overview of the importance of catalysis from a societal point of view before moving on to an introduction to the fundamentals of catalysis science, and why nanoparticles can play an important role in the development of better catalysts. Finally, I will provide an overview of the thesis structure, and briefly introduce each of the research topics that I have chosen to include in the thesis.

1.1 Catalysis and Modern Society

When I chose the subject of my Ph.D. there was one thing more than anything else that drove me towards catalysis: The sheer scale of the impact that the field has on modern society. Human history was changed completely by catalysis, and it may be that catalysis will play a major role in shaping of our future.

For most people, my undergraduate self included, catalysis sounds like a relatively unimportant branch of science. The true technological revolutions, we tend to think, came with computer science, with antibiotics, airborne transportation, the internet. Yet, in 1999, at the turn of the millennium, Nature Magazine published an essay arguing that the most important scientific advance of the 20th century was the discovery of a catalytic process that could produce ammonia from hydrogen and nitrogen, the so-called Haber–Bosch process which was invented in 1909 by Fritz Haber and Carl Bosch [1].

The reason that ammonia is such a crucial chemical is that it is needed for fertilizing crops. Before the invention of the Haber–Bosch process, it was a scarce resource which severely inhibited food production in many parts of the world. In 1900, the total population of the world was 1.6 billion – today it is 7.5 billion. This enormous growth in population is closely linked to the production of artificial fertilizers from ammonia (see Figure 1.1), and today almost 50 % of global food production is based on artificial fertilizers. In fact, it has been estimated that a

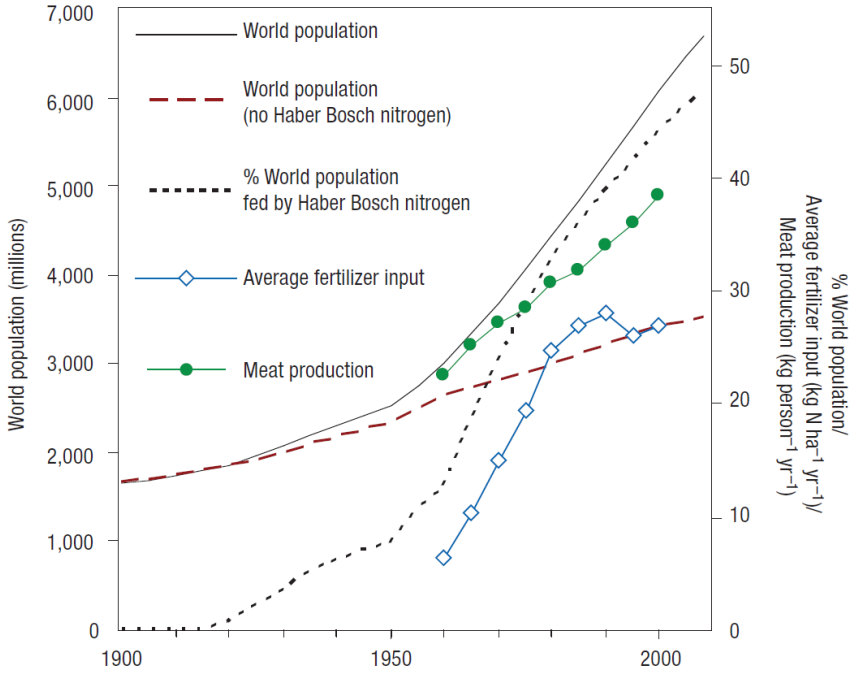

Figure 1.1: Impact of the Haber–Bosch process on the world population. Without Haber–Bosch ammonia, Earth could not sustain more than 3.5 billion people. Reproduced from [2]

world without the Haber–Bosch process could not sustain more than 3.5 billion people [2]. Thus, catalysis has truly changed the face of the Earth and the history of humanity.

1.1.1 From a Blessing to a Curse

The explosive growth in population and standards of living over the last century has led to a number of unforseen consequences – the most problematic being the enormous impact that humanity has on our natural environment and Earth's climate due to emission of greenhouse gases. I will not go into details regarding this issue, as it is discussed widely elsewhere, as e.g. in the synthesis report from the United Nation's Intergovernmental Panel on Climate Change (IPCC), which contains the most comprehensive assessment of climate change available today, made possible by the work of thousands of researchers from different fields [3]. The main point is the following, as stated in the foreword of the report:

> *The IPCC is now 95 percent certain that humans are the main cause of global warming. In addition the SYR [synthesis report] finds that the more human activities disrupt the climate, the greater risks of severe,*

> *pervasive and irreversible impacts for people and ecosystems, and long-lasting changes in all components of the climate system. ... Moreover, the longer we wait to take action, the more it will cost and the greater the technological, economic, social and institutional challenges we will face. [3]*

In 2015, every country in the world, excluding Nicaragua and Syria, signed the Paris Agreement, which agrees to "holding the increase in the global average temperature to well below 2 °C above preindustrial levels and pursuing efforts to limit the temperature increase to 1.5 °C above preindustrial levels" [4]. Although the president of the United States of America has later declared that he will withdraw from the agreement, there is still significant international momentum for combating climate change [5].

1.1.2 Strategies for Solving the Climate Crisis

Although the Paris Agreement has established global consensus on the need for immediate action to solve the climate crisis, the actual strategy for doing so is still unclear.

At the inauguration of our research center in 2016[1], the Danish minister for education and research, Ulla Tørnæs, gave a speech stating that "we will meet the climate crisis with research and not restrictions." This very well sums up the mainstream strategy for reducing humanity's emissions of greenhouse gasses: Develop better technology so that economic growth and environmental impact can be decoupled.

The view that sufficiently advanced technology can sustain continued economic growth has been harshly criticised over the years, already in 1972 in the publication "Limits to Growth", which was based on a computer model by three MIT scientists [6]. More recently, the economist Tim Jackson has written about "the myth of decoupling" in his book "Prosperity Without Growth – Economics for a Finite Planet", arguing that it is unrealistic to expect a continued exponential economic growth without severe environmental degradation [7]. A realistic scenario for a sustainable future will most likely have to depart from the previous reliance on technology to preserve the pro-growth political status quo; technology cannot save us if we continue to insist on economic growth as the cornerstone of societal progress [2]. However, technology will be an invaluable tool for creating a better future, and one of the most pressing tasks is to develop a sustainable energy system.

1.1.3 A Sustainable Energy System

One of the greatest sources of greenhouse gas emissions is the burning of fossil fuels for electricity production and transportation [3]. Therefore, any sustainable

[1] Villum Center for the Science of Sustainable Fuels and Chemicals

[2] For the interested reader, Appendix A contains some personal thoughts on this issue.

energy supply will have to be based on a different source of energy – most likely the Sun. Every hour, the solar influx contains as much energy as the ~ 17 terawatts that the entire human civilisation uses in a year [8, 9], and we thus have a magnificent source of energy at hand. Besides the direct sunlight, there are also a number of secondary ways to harvest the power of the sun with wind turbines, hydroelectric plants or wave-power.

Historically, it has not been economically feasible to utilize these renewable energy technologies, but in the recent years a dramatic decrease in price has occurred, as shown in Figure 1.2 for electricity generated with photovoltaic cells. Whereas solar energy had to be subsidized heavily in the past (as it has been done in e.g. Germany [10]), the technology and market has now matured so much that solar energy is a price-competitive energy source. It is thus realistic to imagine a future society in which sustainable electricity is cheaply accessible.

However, when moving to significant shares of power sources such as solar and wind, a big problem arises: They are only present intermittently, and not always at the time where it is needed by the electricity consumers. In Denmark, where significant amounts of wind turbines is integrated into the power grid, there are already now periods where the power surpasses the energy demand (see Figure 1.3). This energy cannot be utilized effectively, and often has to be sold cheaply or given away for free. As the amount of wind power in the grid is growing, the problem only gets worse, as exemplified by the thought experiment in Figure 1.3 where the current amount of wind power is doubled. In the periods with no wind, the energy consumption has to be covered by other means such as conventional

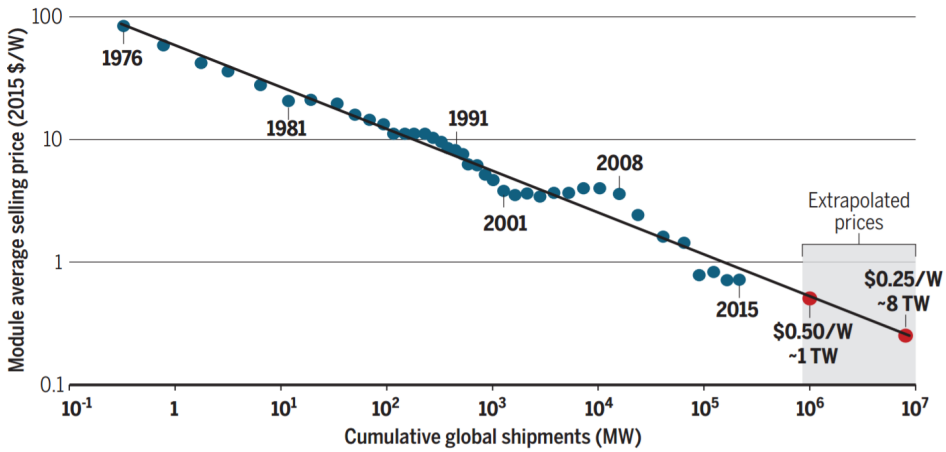

Figure 1.2: Average selling price of photovoltaic modules plotted against the cumulative global shipments of photovoltaics. The more solar cells that have been produced, the cheaper they get – underlining the importance of subsidizing early-stage technologies to allow the development of price-competitive supply chains. Note that both axes are logarithmic. Reproduced from [10].

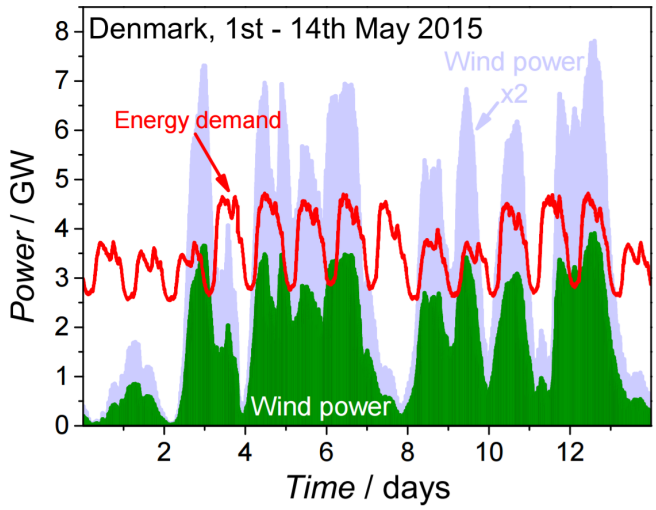

Figure 1.3: Electricity produced by wind in Denmark in a two-week period in 2015, plotted together with the energy demand at the same time. The wind power is present intermittently and does not follow the energy demand, making integration of more wind into the power grid challenging. This is exemplified with the possible scenario of doubling the wind power. Reproduced from [11], data from [12].

power plants, or imported electricity from other countries.

In light of these challenges, it would be extremely beneficial to develop efficient technologies for storing excess energy and use it at times with low energy production. A viable way to do this would be to store the energy in chemical bonds, which can then be utilized when needed [9]. This is already done in e.g. battery-driven cars, but there is a much broader range of possibilities within chemical energy storage. For instance, energy could be stored as liquid or gaseous products that could be easily integrated into existing energy and transportation infrastructure. Also, the production of chemicals and materials which are currently based on oil could move to such feedstock chemicals produced from excess electricity.

1.1.4 A Possible Framework for Chemical Energy Storage

Seh et al. very recently published a review article which contains a good overview of how chemical energy storage could be integrated into the power grid [13], as summarized in Figure 1.4. There are a number of possible chemicals that could act as energy carriers, but a common denominator is that they should be present in a reduced form so that they can release energy by reacting with oxygen from the atmosphere. Also, the chemical should be produced from an abundant feedstock, so that it is feasible to integrate large-scale production into the power grid. Another important consideration is how to drive the chemical reactions. In

short there are three main strategies:

Electrochemical route: Chemicals are produced in electrolyzers driven by electricity from, preferably, sustainable sources.

Photo-electrochemical route: Electrochemical reactions are driven directly by electron-hole pairs generated in semiconductor photo-absorber materials.

Thermochemical route: Chemicals are produced in gas-phase in large-scale high-temperature reactors.

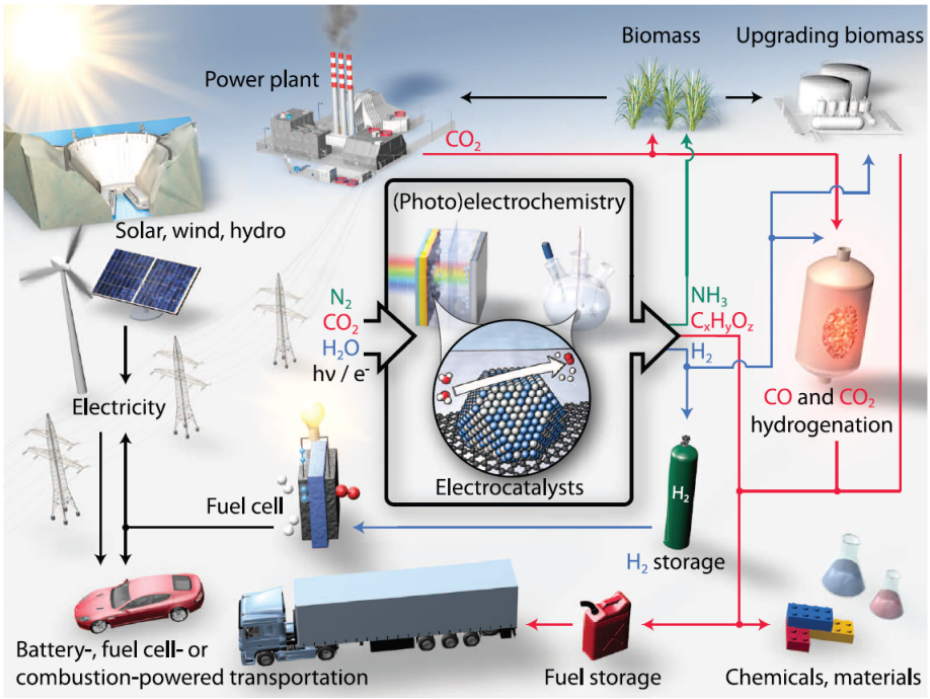

Figure 1.4: Overview of an energy system with integrated chemical energy storage. Electricity is preferably harvested from sustainable sources such as solar, wind and hydro power, which can either be used directly in the grid or stored as chemical energy in batteries or reduction of N_2, CO_2, or H_2O. Hydrogen can either be compressed and later used to generate electricity in fuel cells, or used to upgrade biomass or reduce CO or CO_2 thermochemically; NH_3 can be used as fertilizer, contributing to the production of biomass; CO_2 reduction products can be used as fuels or feedstock chemicals for the production of materials or the chemical industry. Reproduced from [13].

The most obvious energy-storage reaction would be the production of hydrogen from electrolysis of water:

$$H_2O \longrightarrow H_2 + \tfrac{1}{2}O_2, \tag{1.1}$$

which has the great benefit that it is based on an abundant feedstock: water. Unfortunately, the produced hydrogen gas has a very low volumetric energy density, which makes it inappropriate for many applications unless it is compressed. Alternatively, it can be used to upgrade biomass or to reduce CO or CO_2 in gas-phase, high-temperature reactors.

Instead of the gas-phase route, an alternative is to reduce carbon dioxide to hydrocarbons or oxygenates electrochemically. This reaction may proceed through many different intermediates, resulting in a host of different products including carbon monoxide, formate, formaldehyde, methane, methanol, as well as compounds containing multiple carbon atoms. A very generalized, and unbalanced, reaction scheme is

$$CO_2 + H_2O \longrightarrow C_xH_yO_z. \tag{1.2}$$

Carbon dioxide reduction could potentially produce liquid fuels such as methanol or ethanol, which could be integrated into the existing transportation infrastructure. Or the hydrocarbon/oxygenate compounds could be used as a sustainable feedstock in the chemical industry.

The last energy-storage reaction introduced here is the electrochemical reduction of nitrogen to ammonia

$$N_2 + 3\,H_2 \longrightarrow 2\,NH_3. \tag{1.3}$$

The N_2 reduction reaction could potentially be used to produce ammonia for fertilizers locally, thus acting as an alternative to the Haber-Bosch process which takes place in large-scale thermal catalysis plants. However, all experiments so far show extremely poor performance, and this reaction is probably far away from practical implementation.

If any such chemical energy storage is to be economically feasible, it has to be efficient, which requires a suitable catalyst to increase the chemical reaction rate. The fundamental understanding and development of such catalysts for sustainable energy conversion is the overall objective of my Ph.D. and our group as a whole. The following sections are devoted to an introduction to the fundamentals of catalysis.

1.2 Fundamentals of Catalysis

A catalyst is a material that increases the rate of a chemical reaction by participating in it, but remains unchanged at the end of the reaction. Catalysts are typically grouped into two different categories: Homogeneous catalysts, where the catalyst is present in the same phase as the reactants (e.g. liquid) and heterogeneous catalysts, where the catalyst is present in a different phase than the reactants. Enzymes are sometimes considered as a third group of "biocatalysts". In my PhD work I have worked with solid nanoparticle catalysts for reactions in the gas or liquid phase, and the further introduction is therefore focused on heterogeneous catalysis.

For illustration, consider the reaction of two reactants A and B to form the product P:

$$A + B \rightarrow P. \tag{1.4}$$

The potential energy diagram for the reaction in Figure 1.5 shows that the overall reaction is energetically favourable. However, there is a large kinetic barrier for the reaction. The reaction could still run if sufficient energy was present in the system, but the overall rate would be low. However, if a catalyst is added to the system, the reaction can proceed through a number of intermediate steps where there is only a small reaction barrier in the step between the adsorbed reactants and the adsorbed product. Even though there is now also a small positive potential energy difference in the product separation step, the overall reaction rate will be dramatically increased by the introduction of the catalyst.

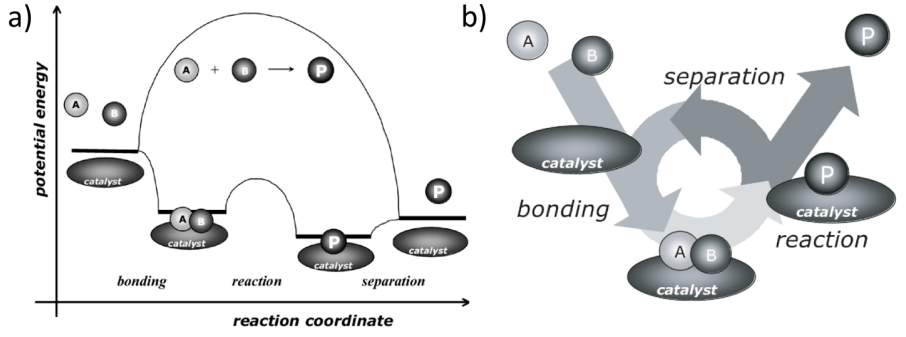

Figure 1.5: **a)** Potential energy diagram of the reaction of reactants A and B to form the product P. The energetic barrier is significantly reduced by the addition of a catalyst. **b)** Although the catalyst takes part in the reaction, it is left unchanged after product separation and can participate in a new catalytic cycle. Reproduced from [14]

1.2.1 Sabatier's Principle

One of the most basic concepts for guiding catalyst development is Sabatier's principle, which states that the optimal catalyst should bind the reacting species neither too strongly nor too weakly. I will explain the principle in more detail through an introduction to the hydrogen evolution reaction (HER), which is also the reaction of interest in chapter 3. HER is one half-cell reaction of the water splitting reaction, which was introduced earlier.

The Hydrogen Evolution Reaction

The overall electrochemical HER in acidic media can be written as

$$2\,\mathrm{H}^+ + 2\,\mathrm{e}^- \rightarrow \mathrm{H}_2, \tag{1.5}$$

where the electron is supplied by the catalyst, which acts as cathode in the electrochemical reaction. This reaction can be divided into two steps: First the adsorption of two protons to combine with two electrons:

$$2\,\mathrm{H}^+ + 2\,\mathrm{e}^- + 2* \rightarrow 2\,*\mathrm{H}, \tag{1.6}$$

where $*$ denotes a free catalytic site and $*$H denotes a hydrogen adsorbed on the surface. The reaction can now proceed through one of two different reaction steps:

$$2\,*\mathrm{H} \rightarrow \mathrm{H}_2 \qquad \text{Tafel reaction} \tag{1.7}$$

$$\mathrm{H}^+ + \mathrm{e}^- + *\mathrm{H} \rightarrow \mathrm{H}_2 \qquad \text{Heyrovsky reaction} \tag{1.8}$$

The diagram in Figure 1.6 a) shows the free energy of $*$H on four different metals, which neatly illustrates Sabatier's principle. Au interacts weakly with the H$*$ which gives low probability for the adsorption of the hydrogen. Meanwhile, Mo and Ni binds the H$*$ so strongly that the hydrogen desorption is hindered. The catalyst that gives the smallest limiting step is Pt, which only binds slightly too strongly to be a perfect catalyst.

Figure 1.6 b) shows the measured and theoretically calculated rates on different catalysts plotted as a function of the hydrogen chemisorption energy. Pt is nearest to the top of the "volcano", because it has a binding energy that is neither too weak or too strong, in accordance with Sabatier's principle.

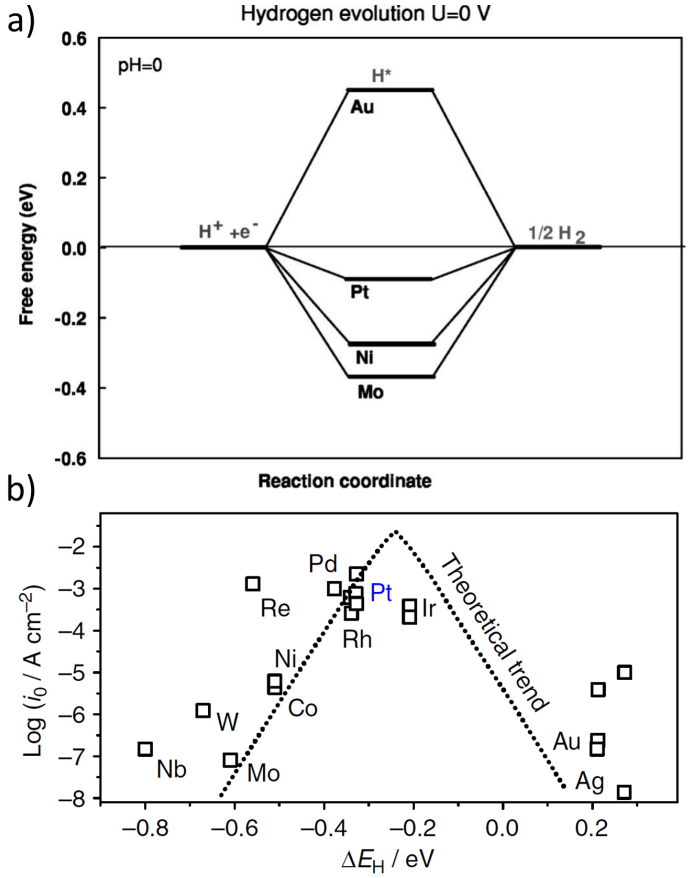

Figure 1.6: **a)** Free energy diagram for the HER on four different metal catalysts. Au binds too weakly to adsorb hydrogen effectively, while Mo and Ni bind too strongly for the hydrogen to desorb. Pt has an intermediate binding energy, and is thus closest to the ideal catalyst. The calculations are done at standard conditions, 1 bar of H_2 and pH=0 at 300 K. Reproduced from [15]. **b)** Volcano plot showing the exchange current density of different metals plotted against their hydrogen chemisorption energies at the same conditions as plotted in the free energy diagram in a). While Pt binds slightly too strongly to be at the top of the volcano, it is still the best catalyst for the HER. Reproduced from [16], original data from [15].

1.2.2 Scaling Relations

Having established Sabatier's principle it seems straightforward to design a perfect catalyst by tuning the binding energy of its surface. However, when we move to more complicated electrochemical reactions than HER, other problems arise. I will now introduce another reaction, the electrochemical reduction of carbon dioxide to methane, which is a reaction of interest in chapter 5 and can serve as an illustration of the concept of scaling relations between binding energies.

The CO_2 Reduction Reaction

According to Peterson and coworkers [17], the electrochemical reduction of CO_2 to CH_4 on a Cu catalyst proceeds through the following intermediate steps:

$$CO_2 + * + H^+ + e^- \rightarrow *COOH \tag{1.9}$$
$$*COOH + H^+ + e^- \rightarrow *CO + H_2O \tag{1.10}$$
$$*CO + H^+ + e^- \rightarrow *CHO \tag{1.11}$$
$$*CHO + H^+ + e^- \rightarrow *CH_2O \tag{1.12}$$
$$*CH_2O + H^+ + e^- \rightarrow *OCH_3 \tag{1.13}$$
$$*OCH_3 + H^+ + e^- \rightarrow *O + CH_4 \tag{1.14}$$
$$*O + H^+ + e^- \rightarrow *OH \tag{1.15}$$
$$*OH + H^+ + e^- \rightarrow H_2O + * \tag{1.16}$$

The free energy diagram for this reaction is schetched in Figure 1.7 at two different potentials: 0 V vs. the reversible hydrogen electrode (RHE) and -0.74 V vs. RHE, which is the potential at which all reactions steps are exergonic.

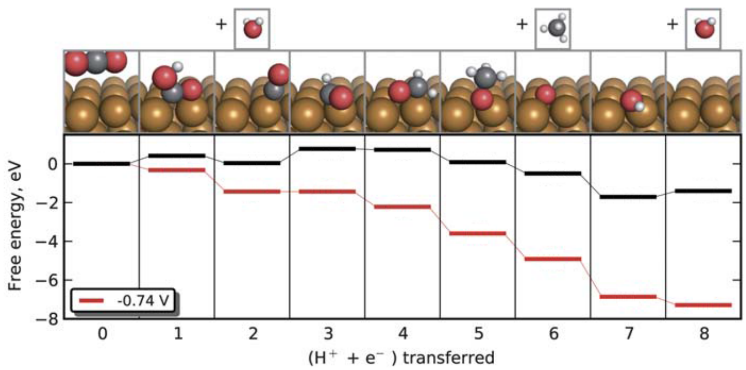

Figure 1.7: Free energy diagram of the electrochemical CO_2-reduction to methane on a Cu catalyst, where the reaction proceeds in eight intermediate steps. The black line displays the free energy at 0 V vs. RHE, whereas the red line is at -0.74 V vs. RHE, the potential at which all reaction steps are exergonic. Potentials are vs. RHE. Reproduced from [18].

At 0 V vs. RHE, the limiting step is the protonation of CO to CHO. Ideally, one would therefore want to make a catalyst that bound CO weaker and CHO stronger. This is, however, difficult as the binding energies of CO and CHO scale with each other – if you lower one, you will also lower the other. The reason for the scaling between these two intermediates is that they both bind to the surface through the carbon atom. Therefore, the binding energies of COOH and CH_2O also scale with CO, and a complete plot of scaling relations between binding energies on a group of metal surfaces can be made, such as Figure 1.8. Similar scaling relations exist between OCH_3, O and OH, which all bind through the oxygen atom.

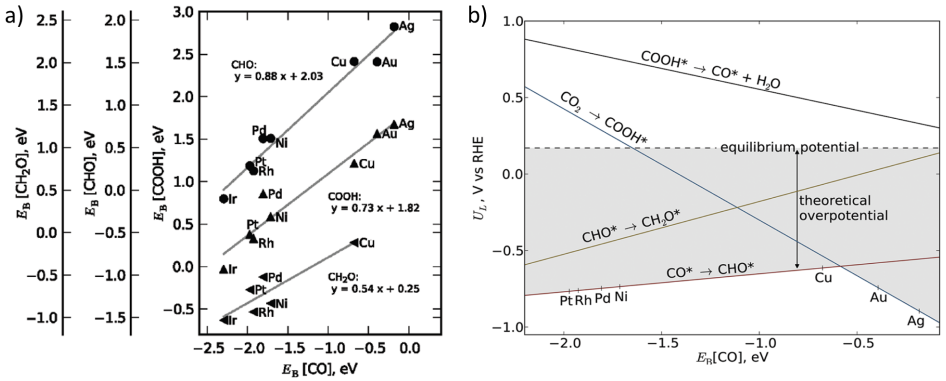

Figure 1.8: **a)** Binding energies of the intermediates in the CO_2-reduction to methane plotted vs. the CO binding energy on the (211) surface of different fcc metal surfaces. All of the displayed intermediates bind to the catalyst surface through the carbon atom, which cause their binding energies to scale with each other. **b)** The limiting potential U_L plotted as a function of CO binding energy, E_B, where the different lines correspond to different reaction steps. The dotted line indicates the thermodynamic equilibrium potential, which represent the idealized situation where there are no kinetic limitations to the reaction. The potential difference from equilibrium potential to actual potential needed to run the reaction is called the overpotential. Notice that all plotted catalysts have significant overpotentials due to the fact that the binding energies of the intermediates scale with each other. If one changes the binding energy to optimize one reaction step, another reaction will run less efficiently and thus determine the limiting potential for the overall reaction. Only the intermediates that bind through carbon are included in the plot; a similar plot can be made for the oxygen-bound species. Both plots are reproduced from [17].

Because of scaling relations, even the catalyst on top of the activity volcano for CO_2 conversion to CH_4 requires a higher applied potential to make the reaction run than what would thermodynamically be expected from the free energy difference between the reactants and products. Note that the problems with scaling relations did not arise in the case of HER, simply because there is only one adsorbed intermediate in this reaction, the atomic hydrogen $*$H. Therefore, finding

an optimal catalyst for HER is inherently much easier than for CO_2-reduction.

One of the most important research areas within catalysis today is to break the scaling relations, i.e. change the binding energies of different intermediates outside of the parameter space that is defined by the standard scaling relations. This could e.g. be achieved by using bimetallic alloys, so that different intermediates can bind to different surface atoms, or by engineering three-dimensional sites which could perturb the reaction mechanism [19].

1.3 Nanoparticles for Catalysis

Nanoparticles, typically defined as particles between 1 and 100 nm, have great importance in the field of catalysis, both in real-life applications and in fundamental research. The primary reason for this is that catalysis is a surface phenomenon, and the surface area to volume ratio of a particle goes as

$$\frac{A}{V} \propto \frac{1}{r}, \tag{1.17}$$

where r is the radius of the particle. Thus, diminishing particle size is an excellent way to get the highest amount of catalytic activity with the smallest amount of catalyst material. This is especially important for catalytic processes that utilize scarce and expensive materials such as polymer exchange membrane (PEM) fuel cells, which typically use platinum catalysts to convert chemical energy from H_2 to electric energy [20]. If a new catalytic material is to make significant global impact, it should be so abundant, accessible and cheap that it can be used for terawatt scale energy conversion [21], and be utilized so effectively as possible in e.g. nanoparticle form.

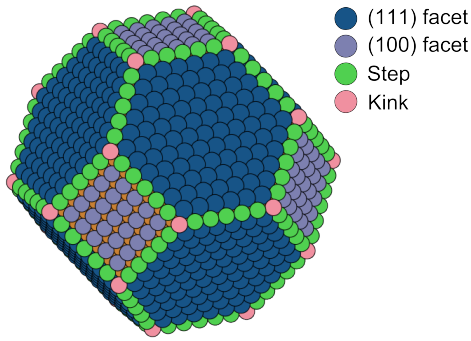

Figure 1.9: Wulff-constructed model of a Cu nanoparticle with 4000 atoms. The surface atoms are color-coded to show whether they are located in a faced, a step or a kink. The Wulff-construction model was made by Alexander Bagger.

1.3.1 Relation Between Catalysis and Nanoparticle Structure

A typical way to model the structure of a nanoparticle is by Wulff-construction, where the relative areas of the different crystalline facets are scaled with their surface energies, so that the total surface energy of the nanoparticle is minimized. Figure 1.9 shows a Wulff-constructed Cu nanoparticle with 4000 atoms as an example. It is clear that the energetically favourable close-packed (111)-surface dominates the surface together with some (100) facets present, but in the context of catalysis it is perhaps more interesting to note the step and kink-sites which can play a crucial role for reactions that are sensitive to surface structure.

One such reaction is the gas-phase conversion of CO and H_2 to methane, which has been shown to occur predominantly on undercoordinated surface atoms by Andersson and coworkers [22]. Therefore, this reaction can be used to highlight one of the interesting catalytic properties of nanoparticles: That the density of undercoordinated sites increase for decreasing particle sizes, simply because particles contain too few atoms to form structures with lower surface energies. As shown in Figure 1.10, the catalytic rate scales with particle size as $rate \propto (\frac{1}{d})^{2.63}$, which is a much stronger dependence than what would be expected if the rate merely scaled with surface area ($rate \propto (\frac{1}{d})^1$). The higher exponent is due to the fact that the density of steps and kinks increase with decreasing particle size, and thus provide more active sites for the structure-sensitive methanation reaction.

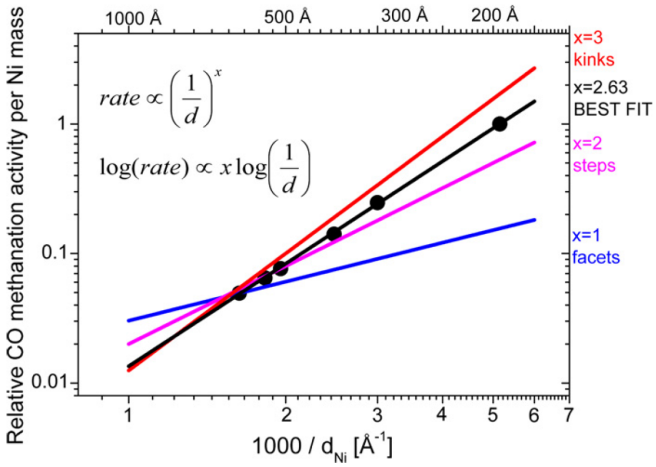

Figure 1.10: Measurements of the rate of CO methanation activity per mass of Ni catalyst, as a function of inverse average catalyst particle size, d. Note that both axes are logarithmic, in order to visualize the data as a straight line. The experiments are fitted with an exponent of $x = 2.63$ which is consistent with the view that the methanation reaction predominantly takes place on the undercoordinated step and kink sites, which are most abundant on small particles. Reproduced from [22].

Wulff-construction is a continuum model and thus cannot predict detailed particle shapes if the number of atoms is small enough for quantization to play a role. Very small particles, with a countable number of atoms, are typically referred to as "clusters", and these can have catalytic activities that are remarkably sensitive to the number of atoms. Kleis et al. find that clusters smaller than ~ 560 atoms can exhibit properties that are significantly different from those of bulk materials by a computational study. Tyo and Vajda recently published a review with a detailed account of the latest developments in the field of catalysis by clusters with precise numbers of atoms [23].

1.3.2 Studying Nanoparticle Size-Effects

In order to investigate any of the mentioned catalytic effects of nanoparticles, it is a powerful tool to be able to control the size of the particles. This can be achieved e.g. through colloidal synthesis chemistry with great precision (see e.g. [24, 25]). But in my Ph.D. work I have worked with a "physical" approach, utilizing a nanoparticle source which relies on magnetron sputtering of a metal target, gas-phase aggregation of sputtered material to form nanoparticles and subsequent mass-filtering (the technique is explained in-depth in section 2.2). This technique has a number of advantages, including narrow control of particle size, ease of use and the fact that remaining ligands and other contamination from chemical syntheses are avoided.

Nanoparticle production by gas aggregation is not presently suited for large-scale catalyst production; we typically obtain catalyst loadings on the order of $100\,\mathrm{ng/cm^2}$ with our apparatus, which is many orders of magnitudes away from industrial scales. However, the well-defined nanoparticles can serve as model systems, which allows the study of fundamental catalytic effects and explorations of new catalytic materials. If a good catalyst is found in such a model system, it could later be produced by other means, e.g. chemical synthesis, in order to be used on a larger scale.

1.4 Thesis Structure

My Ph.D. has been focused on synthesis and characterization of nanoparticle model systems, but in all of the projects, I have collaborated extensively with other researchers, especially for catalytic testing and theoretical modelling. I will convey the whole story of each research project, but there is naturally a strong focus on synthesis and characterization.

As seen in the list of papers (page 9), I have been part of more research projects than presented in this thesis, but have focused the thesis on the three topics which I have been most involved in. Before presenting my research, I will give an overview of the experimental methodologies that I have used. The thesis is thus structure in the following way:

Chapter 2 introduces the relevant experimental methods for understanding the thesis.

Chapter 3 explores the efficiency of platinum nanoparticles for catalyzing the photoelectrochemical hydrogen evolution reaction, especially focussing on the relation between mass loading of particles and the resulting catalytic performance. The fundamental knowledge gained on nanoparticle model systems is then used for a technoeconomic analysis answering the question: Is it feasible to use platinum as a catalyst for terawatt-scale photoelectrochemical hydrogen production?

Chapter 4 presents my work on synthesizing nickel-promoted molybdenum sulfide (Ni-Mo-S) nanoparticles by gas aggregation in a reactive atmosphere of H_2S and Ar. This work includes extensive characterization of the nanoparticles with X-ray photoelectron spectroscopy, scanning transmission electron microscopy, and energy-dispersive X-ray spectroscopy. The nanoparticles are tested for their catalytic performance in electrochemical hydrogen evolution and hydrodesulferization (HDS), i.e. removal of sulfur, from dibenzothiophene. This reaction is relevant for producing e.g. diesel with ultra-low levels of sulfur; it is thus falling outside the rest of my research which is focussed on renewable energy conversion, and a seperate introduction to HDS is given in the chapter.

Chapter 5 reports the finding of a high transient production of methane at the onset of electrochemical CO-reduction on mass-selected Cu nanoparticles. The transient feature disappears on the time-scale of seconds, and was therefore only observable because of a newly developed technique for in-situ product detection by electrochemistry mass-spectrometry. Based on density functional theory, we attribute the initial heightening of the methane production to oxygen adsorbed on the Cu surface, creating a new, previously inaccessible reaction pathway.

Chapter 6 summarizes the main conclusions from the thesis and provides ideas for future research.

In the study of Pt and Cu nanopartices (chapter 3 and 5, respectively), the deposition and characterization techniques were well established and routinely used in our lab. Studying Ni-Mo-S nanoparticles (chapter 4), on the other hand, involved developing a new synthesis methodology as well as extensive catalyst characterization. Therefore, chapter 4 is the longest, and include a lot of details, where chapter 3 and 5 are shorter. This does not reflect the relative scientific importance of the individual chapters.

Chapter 2

Experimental Techniques

During my Ph.D. I have used a wide range of experimental techniques, and it is beyond the scope of this thesis to describe each of them in detail. This chapter is therefore devoted to 1) experimental techniques which have a prominent place in the thesis and 2) introducing methodologies that are uncommon in our scientific community. The level of detail varies from technique to technique with the aim of providing sufficient background knowledge to understand the results presented later in the thesis.

The chapter is divided into four sections describing, respectively, the ultra-high vacuum (UHV) setups used in the thesis, the working principles of the nanoparticle sources, the characterization techniques, and finally a brief overview of methods for measuring catalyst activity.

2.1 Ultra-High Vacuum Setups

Most of my experimental work has been carried out on two ultra-high vacuum setups, known in the group by the names "Omicron" and "STM312". Each setup has a connected nanoparticle source relying on magnetron sputtering and subsequent mass-filtering, and are equipped with various spectroscopy and microscopy techniques for sample characterization.

2.1.1 Omicron Setup

The "Omicron" setup (see Figure 2.1 a) consists of a nanoparticle source (NanoBeam 2011 model from Birmingham Instruments) coupled to a UHV system (Multiscan Lab XP from Scienta Omicron GmbH) consisting of two chambers: a preparation chamber and an analysis chamber. The setup has been modified extensively for different projects by our group over the years, but only the basic functionality will be explained here. The base pressure in the preparation and analysis chambers is below the low 10^{-10} mbar regime.

The nanoparticle source is connected to the preparation chamber, where depositions on substrates take place. After deposition, the samples can be transferred without air exposure to the analysis chamber, which is equipped with a range of characterization techniques including X-ray photoelectron spectroscopy (XPS), ion scattering spectroscopy (ISS), scanning electron microscopy (SEM), auger electron spectroscopy (AES), and scanning tunnelling microscopy (STM). AES and STM have not been used in the included projects, and will therefore not be presented in the following.

X-ray radiation for XPS are supplied by a SPECS XR50 X-ray gun, and ions for ISS are supplied with an ISE100 ion gun. Both electron and ion energies are detected with an Omicron Nanosam 7-channel hemispherical analyzer. The SEM column is a Zeiss Gemini UHV equipped with an in-lens detector, which has a resolution of 3 nm.

2.1.2 STM312 Setup

The "STM312" setup consists of a costum-built main UHV chamber with a base pressure in the low 10^{-10} mbar range, coupled to a nanoparticle source (Nanogen50 model from Mantis Deposition LTD). As the name implies, the main chamber was originally designed for STM studies, but I have mostly used it for XPS. The samples can be transferred directly into the UHV chamber for XPS characterization without air exposure. The chamber is also equipped for ISS measurements.

The X-ray radiation is generated with a SPECS RQ 20/38 X-ray gun and ions are provided by a SPECS IQE 12/38 ion gun for ISS and sputtering. Photoelectrons and ions are detected with a single-channel Phoibos 100 SCD hemispherical energy analyzer.

2.2 Production of Mass-Selected Nanopartices

All of the nanoparticles samples presented in this thesis were produced by magnetron sputtering of a metal target, subsequent gas-phase aggregation of the sputtered material into nanoparticles, and mass-filtering before deposition onto a substrate.

Production of nanoparticles by sputtering and gas-phase aggregation was first reported by Yatsuya and co-workers in 1986 [26]. The efficiency of the technique was later improved by the use of magnetron sputtering [27,28]. In 2005, Pratontep et al. published a detailed description of a nanoparticle source which is coupled to a lateral time-of-flight mass-filter [29]. For more details on magnetron sputtering and gas-aggregation of nanoparticles than presented here, I refer to a recently published book-chapter by Kolipaka and Vajda [30].

As earlier noted, I have used two nanoparticle sources for producing mass-selected nanoparticles in my project, a Nano-Beam 2011 model from Birmingham Instruments, and a Nanogen50 model from Mantis Deposition LTD. Our Nano-Beam 2011 instrument is almost identical to the setup from [29] and this publica-

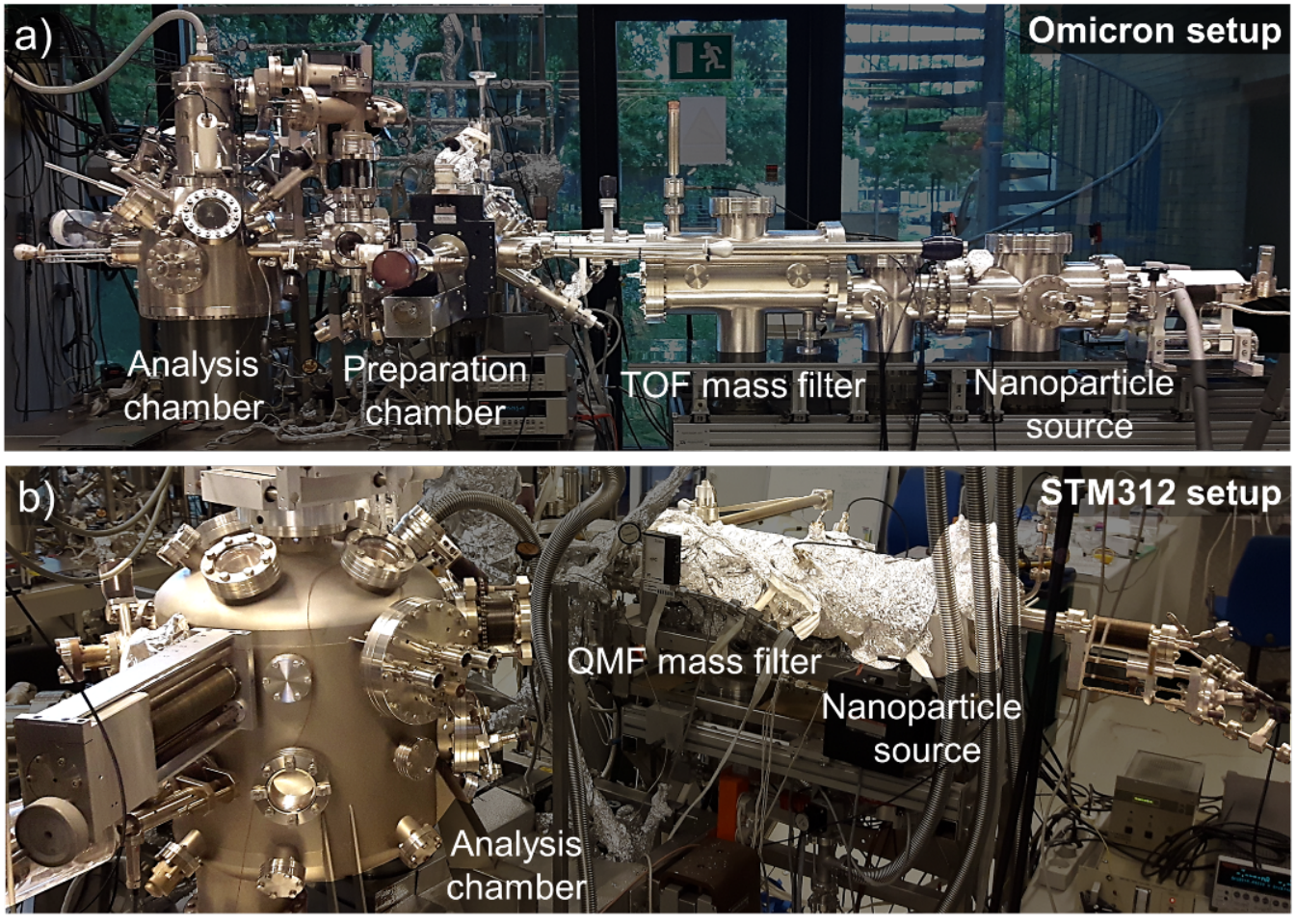

Figure 2.1: **a)** The Omicron setup consisting of a nanoparticle source and a lateral time-of-flight mass filter coupled to a preparation chamber, where the nanoparticles are deposited on a substrate, and an analysis chamber where samples can be characterized with XPS, ISS, AES, SEM or STM. **b)** The STM312 setup consisting of a nanoparticle source with a quadrupole mass filter coupled to a UHV analysis chamber equipped with ISS, XPS and an Aarhus-type STM.

tion is therefore a good reference for further reading. The Nanogen50 instrument is different in design, but most principles can be generalized. The most important difference between the two instruments is the mass-filters: the Nano-Beam 2011 uses a lateral time-of-flight mass filter, whereas the Nanogen50 uses a quadrupole mass filter.

The following subsections describes the steps in the production of nanoparticles and subsequent mass-filtering while describing the differences between the two nanoparticle sources. During my Ph.D. we have optimized and explored different aspects of the nanoparticle deposition method; I report these along the way.

2.2.1 Nanoparticle Generation: Sputtering and Aggregation

Figure 2.2 is a sketch of the nanoparticle generation method used in our instruments: A sputter target of the desired material is placed in a magnetron sputter head inside a cylindrical chamber, the so-called "aggregation zone". The aggregation zone is pumped to vacuum with a turbomolecular pump through the exit aperture furthest away from the magnetron. A flow of argon is then introduced through a flow-controller at $10-100$ SCCM, resulting in pressures in the range of $0.01-1$ mbar in the aggregation zone. The target is negatively biased (~ -200 V), causing Ar^+ ions to sputter the surface. The magnetron head is equipped with an array of permanent magnets, producing a magnetic field that confines a plasma

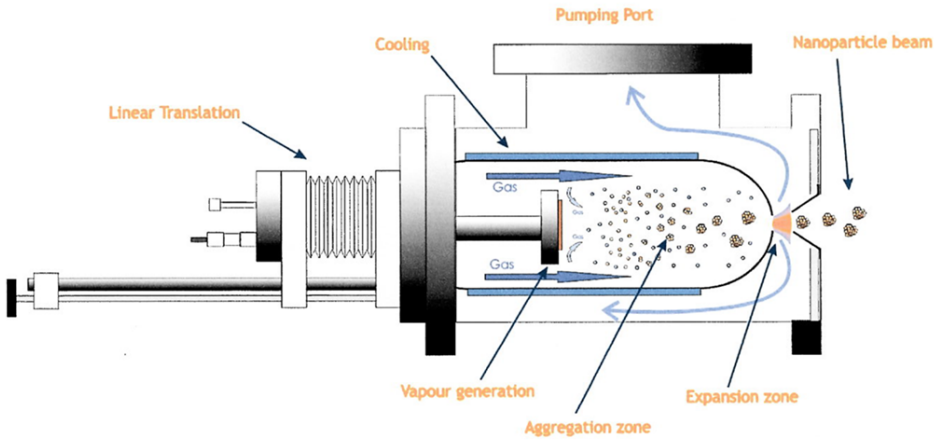

Figure 2.2: Schematic representation of a nanoparticle source in operation: A metal target is sputtered with noble gas ions, and the resulting metal "vapour" can agglomerate into nanoparticles in the cooled aggregation zone. Due to the pressure difference, the nanoparticles undergo a supersonic expansion when travelling through the exit aperture, after which the nanoparticles do not grow. Reproduced from [31].

just above the target, thus increasing the sputter rate significantly.

The sputtered target atoms can now agglomerate into clusters or nanoparticles. In order to facilitate agglomeration, the walls of the agglomeration zone are cooled with liquid nitrogen (LN_2), and helium can be introduced along with the argon. He and Ar mediates the heat transfer from walls to particles, but since He is significantly lighter it only contributes slightly to target sputtering and the He flow thus offers a way of controlling aggregation independent of sputter rate.

Apart from heat transfer, the noble gas atoms also play a more complex role in the agglomeration mechanism according to Haberland et al. [28]: The first step in particle agglomeration is the formation of a metal dimer, but due to conservation of energy and momentum a dimer cannot be formed by two colliding atoms. Therefore, dimers are typically formed by participation of a noble gas atom in a three-body collision, after which the noble gas atom leaves the dimer:

$$\mathrm{M} + \mathrm{M} + \mathrm{Ar/He} \longrightarrow \mathrm{M_2} + \mathrm{Ar/He}. \tag{2.1}$$

The dimers can now either grow through addition of metal atoms or through cluster-cluster agglomeration. Granqvist and Buhrman state that cluster-cluster aggregation dominates the growth mechanism [32], and although we have not studied the growth mechanisms in details, we have observed particle shapes that indicate such a mechanism. E.g. ruthenium nanoparticles produced in the Nano-Beam 2011 instrument have "raspberry"-like shapes when imaged with TEM, strongly indicating that they are agglomerates of smaller nanoparticles. Other materials, such as Cu do not show these shapes. It is plausible that agglomeration happens through a combination of atom-addition and cluster-cluster aggregation, depending on the material and synthesis conditions.

Outside the aggregation zone, the pressure is in the range of 10^{-4} mbar. The pressure difference creates a gas flow sweeping the particles out through the exit aperture, where they undergo supersonic expansion. After this point, the particles do not grow further.

When the particles exit the aggregation zone, a number of them will be electrically charged due to ionization or addition of electrons from the magnetron plasma. Haberland et al. observed that positively charged, negatively charged, and neutral particles occur in approximately equal amounts, i.e. $\frac{1}{3}$ of each [28]. However, our observations indicate that large particles have a stronger tendency to be negatively charged, whereas single atoms or clusters are positively charged.

Controlling the Mass-Distribution of Nanoparticles

The mass-distribution of the nanoparticles is determined by a number of parameters including flow of Ar and He, sputter power and the length of the aggregation zone, which can be altered by moving the magnetron sputter head with a linear drive. On the Nano-Beam 2011 nanoparticle source, the size of the exit aperture can be varied as well, whereas it is fixed on the Nanogen50 instrument.

Since the nanoparticle size distribution depends on so many parameters, we have not conducted a systematic study on the influence of the synthesis conditions.

In practice it has proven to be sufficiently easy to obtain the desired mass-profiles by a combination of trial and error, experience from earlier depositions and two rules of thumb:

- As a general trend, introducing He to the aggregation zone makes the average particle size smaller. This could be due to the fact that more dimers, and thus agglomeration centers, are formed, or simply that the increased He-flow sweeps the particles out faster, limiting their growth time.
- Moving the magnetron sputter head closer to the exit aperture of the aggregation zone makes the the average particle size smaller, as this gives the particles shorter time to aggregate.

When suitable synthesis conditions for a certain type of nanoparticles have been found in one experimental session, it would be fortunate if they could be reproduced in another session. However, although the synthesis conditions remain relatively stable, they can change significantly from deposition to deposition. This is mainly due to two factors:

Firstly, the temperature profile of the aggregation zone may vary from deposition to deposition. Before a deposition we typically cool the aggregation zone with liquid nitrogen for 20-60 minutes, while monitoring the temperature of the aggregation zone through a thermocouple, to ensure that the temperature is close to LN_2-temperature. But the thermocouple only measures the temperature at one point, and we have observed differences by flowing LN_2 for several hours before a deposition, indicating that it takes longer for the system to thermally equilibrate. Thus, the pre-deposition cooling time is a compromise between waiting time and homogeneous temperature distributions in the cluster source. During a deposition, the heat from sputtering may also change the temperature distribution which would change synthesis conditions between two consecutive depositions.

Another factor which changes synthesis conditions over time is that the sputter target is deformed as material is removed. Since the plasma formed in the magnetron sputter head is "doughnut-shaped", the targets develop a circular trench, similar to a racetrack, as they are sputtered. As this trench grows deeper and deeper, the sputter conditions change and the particle size distribution is altered.

Due to the above complications, we fine-tune the synthesis conditions before each deposition.

2.2.2 Mass-Filtering the Nanoparticles

Since a large fraction of the nanoparticles are charged when they exit the aggregation zone, they can be manipulated with electric fields. If a particle with charge q and mass m experiences an electric field E, it will result in the acceleration

$$a = \frac{qE}{m}, \tag{2.2}$$

Thus, particles with the same $\frac{q}{m}$ ratio will experience the same acceleration, and particles can therefore be filtered with an electric field. Most nanoparticles will

carry a single elementary charge; however, a significant portion of the nanoparticles can carry two charges, and it is unfortunately impossible to distinguish between particles with the same $\frac{q}{m}$-ratios ($\frac{q}{m}$ vs. $\frac{2q}{2m}$). When mass-filtering, we have therefore been aware of double mass/double charge particles which might be deposited along with the single mass/single charge particles.

The following subsections describe lateral time-of-flight mass filtering and quadrupole mass filtering, which are used on the Nano-Beam 2011 and Nanogen50 nanoparticle sources, respectively.

Lateral Time-of-Flight Mass Filter

The lateral time-of-flight (TOF) mass filter was invented by Issendorff and Palmer and first described in 1999 [33]. The basic working principle of a lateral TOF can be described using the sketch in Figure 2.3.

A narrow, accelerated beam of charged nanoparticles enters the mass-filter through an aperture, after which a short high-voltage pulse is applied to plate 1, accelerating the particles upwards. Shortly after, an identical pulse is applied to plate 2, redirecting the trajectory of the particles so that they now travel in the same direction as the original beam, but now laterally displaced. The displacement of a particle will depend on $\frac{m}{q}$, and thus the particles will be dispersed laterally according to their mass-to-charge ratio. Now an exit aperture can be used to select a narrow range of the particles, completing mass-filtering.

The high-voltage pulses are applied consecutively at a high frequency. This frequency determines which mass is selected, and thereby a mass-scan can be obtained by sweeping the frequency. The mass filter at the Nano-Beam 2011 can select masses from 30 amu − 20 million amu.

The mass-resolution of our lateral TOF can be varied in the range of $\frac{m}{\Delta m} = 20-100$ by changing the size of the entrance and exit apertures. We have typically

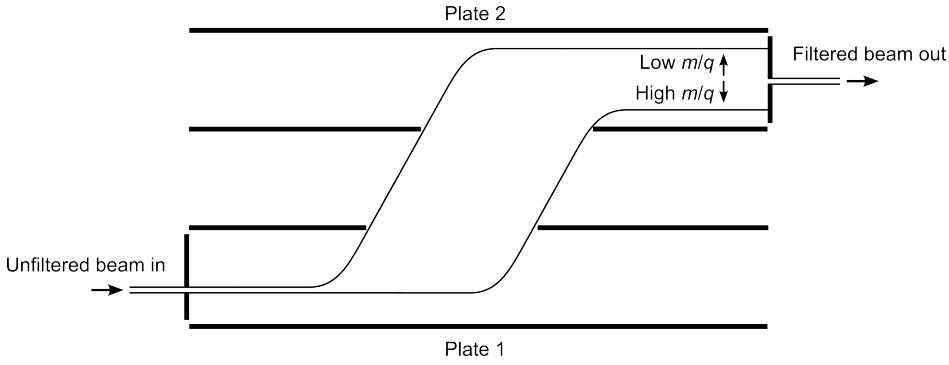

Figure 2.3: Sketch of a lateral time-of-flight mass filter. An unfiltered nanoparticle beam enters the mass filter, and is displaced laterally by a short pulse on plate 1, followed by a pulse on plate 2. This causes the particles to be displaced according to $\frac{m}{q}$ ratio, which allows for filtering the particles with an exit aperture.

run the setup at the lowest resolution of $\frac{m}{\Delta m} = 20$ in order to maximize the flux of nanoparticles.

Before entering the mass filter in the Nano-Beam 2011 system, the nanoparticles are accelerated to 500 eV and focussed by a series of ion optic lenses, so that they are condensed into a narrow beam. The entire system of lenses and mass-filter can be run with both negative and positive bias, which allows us to select either positive or negatively charged particles.

Quadrupole Mass Filter

Quadropole mass filtering (QMF) was first described by Wolfgang and Steinwedel in 1953 [34]. Figure 2.4 shows a simplified sketch of the working principles of the mass filter.

Four electrically conducting rods are connected in pairs, and a constant voltage difference U is applied between the pairs. Superimposed on this DC voltage is an AC component with amplitude V. The resulting electrical field will force charged particles entering the mass filter into helical motion. At a certain AC frequency, only particles within a narrow mass/charge ratio will be able to pass through the filter. Other particles will be attracted to one of the quadrupoles and neutralized.

The QMF on the Nanogen50 nanoparticle source is a MesoQ model from Mantis Deposition LTD, which can filter particles in the range 350 amu $- 10^6$ amu with a maximum mass-resolution of $\frac{m}{\Delta m} = 50$. The resolution is determined by

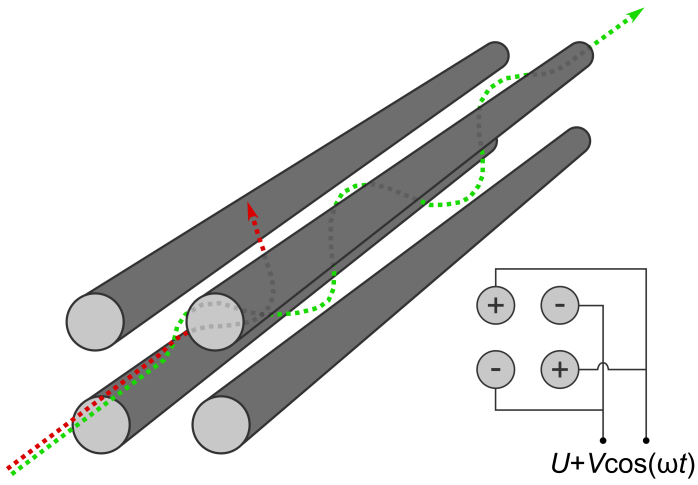

Figure 2.4: Sketch of the working principle of quadrupole mass filtering. The four rods are connected in pairs and electrically biased with both a DC and an AC component. The green trajectory symbolizes a particle which has a suitable mass/charge ratio and passes through the filter in a stable helical path, whereas the red trajectory ends on a quadrupole rod.

the U/V-ratio, which I have set to $U/V = 0.14$ in all depositions, giving a mass resolution of $\frac{m}{\Delta m} = 20$. Thus, the mass resolution of the two nanoparticle sources has been the same in all depositions.

2.2.3 Depositing Nanoparticles on a Substrate

Current Measurement and Sample Bias

After exiting the mass-filter, the nanoparticles are ready to be deposited on a sample. Since the particles are charged, the number of deposited nanoparticles can be determined by measuring the deposition current on the sample. In order to attract nanoparticles to the sample, it can be electrically biased. On the NanoBeam 2011 setup, a bias of 48 V was obtained by a stack of 9 V batteries, since batteries give a stable and noise-free potential. On the Nanogen50 setup, the potential is set with a source-meter unit, which can provide a potential while measuring the deposition current. Typically, depositions on the Nanogen50 were, however, done with a grounded sample as the velocity of the particles exiting the aggregation zone proved sufficient to deposit particles on the sample.

The kinetic energy of a nanoparticle has an important influence on the landing on the substrate. High-energy particles may be shattered or even implanted, but by staying within the so-called "soft-landing" regime, the particles retain their shape to some degree. As a rule of thumb, the kinetic energy of a particle should be less than 1 eV per atom, as this is on the order of magnitude of the energy of a chemical bond. Since small clusters have fewer atoms, the landing energy is especially important in this size-regime (see e.g. [35] for a detailed treatment of cluster-surface interactions). I have mostly deposited much larger nanoparticles, and thus the kinetic energies on the order of 50 eV are well inside the soft-landing regime. We have never observed shattered or deformed particles due to hard landing in any microscopy investigations.

Deposition Procedure

Before depositing on an actual sample, it is necessary to find the right synthesis conditions. This is done by placing a metal plate in front of the sample and detecting the nanoparticle current as a function of the mass, thus obtaining a mass spectrum of the particles that are produced in the aggregation zone. The plate is set to the same potential as the sample. Using this mass spectrum, it is possible to optimize the synthesis parameters towards the desired mass without depositing on the sample. The criteria for a good mass profile is 1) that there is sufficient current to deposit the desired loading in a reasonable time (typically below 2 hours) and 2) that the amount of double-mass particles is low, to avoid deposition of double-mass/double-charged particles (we aim for an order of magnitude less double mass than single mass). We became aware of the problem with double-mass depositions in the beginning of my Ph.D., and published a paper discussing the issue in 2014, which I refer to for a deeper discussion [36].

When the nanoparticle mass distribution in the aggregation zone has been optimized, the actual deposition can begin. The mass filter is now set to filter a single mass instead of scanning for mass spectra. The deposition is done through an aperture which has approximately the same size as the sample. On the Nano-Beam 2011 setup apertures of two sizes ($\varnothing = 4.5\,\mathrm{mm}$ and $\varnothing = 9\,\mathrm{mm}$) are drilled into the metal plate which is also used for measuring mass spectra; the plate can be moved with a linear drive to expose the sample through an aperture. On the Nanogen50 setup, a metal plate with an aperture is mounted directly on the sample stage, and the mass spectra are recorded on a different metal plate.

During deposition it is not possible to monitor the mass distribution in the aggregation zone. Therefore a mass spectrum is recorded again directly after deposition to ensure that the mass-profile has not changed dramatically. Especially, if the mass profile has shifted towards higher amounts of double masses, the sample has to be discarded. Figure 2.5 a) shows two mass spectra obtained before and after a deposition of Pt nanoparticles in the Nano-Beam 2011 nanoparticle source. We aimed for a mass of 850.000 amu, corresponding to a diameter of 5 nm, and the mass-profile only changed slightly during deposition.

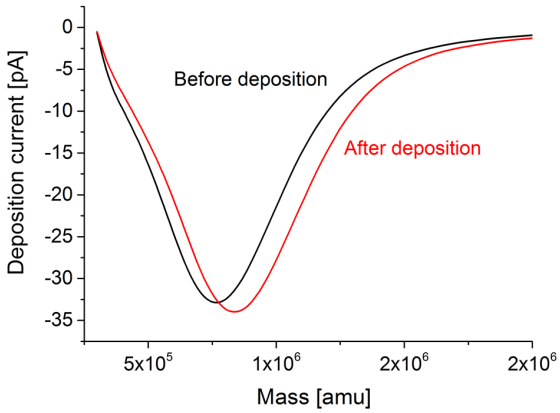

Figure 2.5: Mass distribution of nanoparticles exiting the aggregation zone before and after a deposition. The shift to higher masses can be problematic if it results in large quantities of particles with double mass.

Nanoparticle Coverage

Assuming that each nanoparticle carries one elementary charge, the number of nanoparticles deposited on a sample can be determined by integrating the deposition current. The mass of each particle is known, and thus the total mass loading can be calculated. Since catalysis takes place on the surface of the particles, it is often more relevant to calculate the projected area coverage of the sample surface than the mass loading. In the calculation of area coverage, we often estimate the particle diameter by assuming that the density of the particle is the same as

the bulk density of the target material. TEM investigations of particle diameters have shown that this is a reasonable assumption.

Typically, we have deposited loadings in the range from 5 % to 15 % projected area coverage. For catalytic measurements, higher loadings would be ideal but that would result in a large fraction of particles landing on top of each other, and thus 5-15 % is a good compromise, resulting in $18 - 45\,\%$ overlapping particles, according to Monte-Carlo simulations by my co-worker Bela Sebok. For TEM studies, lower loadings in the range from 1 % to 5 % are advantageous to have the individual nanoparticles well separated.

Besides the number of particles on a surface, it is also important that they are homogeneously distributed on the sample, which can be challenging since the beam of nanoparticles exiting the mass filter is not necessarily completely homogeneous. The Nanogen50 has been customized with a set of x- and y-translation lenses so that the focused nanoparticle beam can be rastered during the deposition, thus ensuring a homogeneous coverage of nanoparticles. On the Nano-Beam 2011 setup we do not have such an option. With the small deposition aperture ($\varnothing = 4.5\,\mathrm{mm}$), the deposition seems to be relatively homogeneous, but when depositing through the 9 mm aperture, we have seen large variations in coverage over the sample area. We observed the inhomogeneity when depositing on microreactors (see section 2.4), where the nanoparticle depositions can be seen in the reflected light. For future work with the 9 mm, it would be advantageous to mount a raster lens system.

2.3 Nanoparticle Characterization

In order to characterize the nanoparticles after deposition, we have employed a range of spectroscopy and microscopy techniques, most prominently X-ray photoelectron spectroscopy (XPS), ion scattering spectroscopy (ISS), scanning electron microscopy (SEM), transmission electron microscopy (TEM), and energy-dispersive x-ray spectroscopy (EDX). These techniques are presented in the following subsections.

2.3.1 X-ray Photoelectron Spectroscopy

X-ray photoelectron spectroscopy (XPS) relies on the photoelectric effect to provide quantitative information on the elemental composition and chemical state of the outermost few nanometers of a surface. The surface sensitivity makes it an ideal spectroscopic technique for catalysis research, where the reactions take place on the surface.

Physical principles of XPS

XPS relies on the measurement of the kinetic energies of photoelectrons that are ejected from the analyzed material by monochromatic X-rays. The energy of such

a photoelectron can be expressed as

$$E_{kin} = h\nu - E_{binding} - \phi_{detector}, \tag{2.3}$$

where $h\nu$ is the energy of the X-ray photon and $\phi_{detector}$ is the work-function of the detector used to measure the kinetic energy. The photoelectrons ejected from core levels have discrete binding energies which are distinct for each element, and thus provide a way to identify the sample composition.

X-rays penetrate several microns into a surface, but the generated photoelectons have energies in the range of 0-1500 eV which result in much shorter mean-free paths, typically on the order of tens of Ångstrøms as seen in Figure 2.6. This means that only photoelectrons very close to the surface can be detected, which is the origin of the surface-sensitivity of XPS.

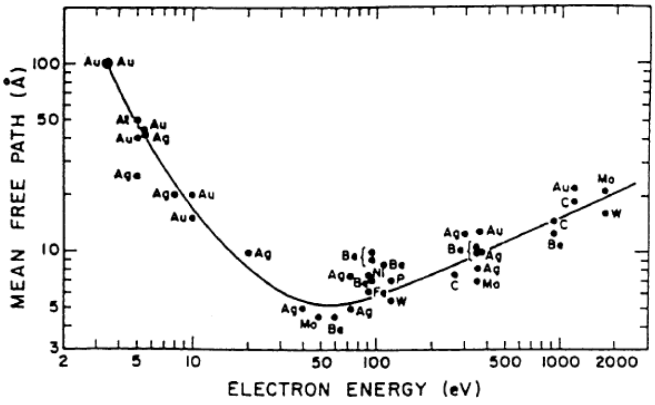

Figure 2.6: Electron mean free path as a function of kinetic energy over a wide range of materials. The data points fall on a so-called "universal curve" with a minimum around 50 eV. Reproduced from [37], data originally from [38].

Apart from elemental identification, XPS is also sensitive to the chemical state of an element. Binding energies of an element can shift several electron volts, typically increasing for oxidized elements relative to the same element in a reduced state.

Instead of emitting photoelectrons, excited atoms can also relax by emitting Auger-electrons created in a three-electron process where 1) a core-electron is emitted as a photo-electron, 2) another electron relaxes to fill the empty core-hole, and 3) a higher-lying electron is emitted as an Auger electron. The energy of Auger electrons is independent on incident X-ray energy, and Auger peaks can thus easily be identified in an XPS spectrum by varying the X-ray energy.

Quantitative XPS interpretation

The intensity of an XPS peak is proportional to the number of atoms in the surface of the sample that are emitting those photoelectrons. Therefore, the

composition of a surface can be quantified by means of relative peak areas of the analyzed elements. However, since the yield of photoelectrons from different orbitals varies, it is necessary to scale the peak areas with a relative sensitivity factor (RSF). These sensitivity factors are obtained from standards and can be found in various databases or handbooks, such as [39]. The ratio of concentration of two elements in a sample can thus be calculated as

$$\frac{c_1}{c_2} = \frac{A_1/RSF_1}{A_2/RSF_2}, \tag{2.4}$$

where c_i is the concentration of an element, A_i is the integrated intensity of a peak from that element, and RSF_i is the relative sensitivity factor.

Fitting XPS spectra can be advantageous for quantification, especially when peaks are overlapping either from different elements or from the same element present in multiple oxidation states. I have fitted most peaks with a convolution of Gaussian and a Lorenzian functions, since this line shape captures both the inherent life-time broadening of the photoelectron emission process (which gives a Lorenzian shape) and the broadening from the electron detection and X-ray line shape (which is Gaussian).

Due to inelastic scattering of the photoelectrons when they exit the material, each peak will have a "tail" at lower kinetic energies which contributes to a background in the XPS spectrum. When determining the area of a peak, it is necessary to subtract this background. Various functions can be used to fit the background, but the most commonly used is the Shirley background which has empirically been shown to yield robust results, although it is not derived from physical principles. All fits in this thesis are done with Shirley backgrounds.

X-ray generation and photoelectron detection

The X-rays used in XPS can come from various sources, but in normal laboratory settings the radiation is generated in an X-ray gun that relies on bombarding a Mg or Al anode with electrons from a heated filament at $10-15\,\mathrm{keV}$. The electron bombardment ionizes the anode material, and when the excited atoms relax, they may release X-ray photons. The most intense X-ray line is the $K\alpha$ line which comes from a relaxation of a 2p electrons into 1s holes. $\mathrm{Mg}_{K\alpha}$ has an energy of 1253.6 eV with a FWHM of 0.70 eV, whereas $\mathrm{Al}_{K\alpha}$ has an energy of 1486.6 eV with a FWHM of 0.85 eV.

Unfortunately, apart from the desired X-ray lines, other electron transitions can also occur, giving rise to a number of other X-ray energies which cause so-called "satellite" peaks to arise in the XPS spectra. The positions and relative intensities of these peaks are, however, known and can thus be accounted for in the spectrum interpretation. If more detailed spectra are required, one can use a monochromator to filter the X-rays, or obtain the radiation from a synchrotron which gives extremely intense and monochromatic X-rays.

The photoelectrons escaping the sample can be detected in a so-called hemispherical analyzer which consists of two concentric hemispherical elecrode plates

which are held at appropriate voltages such that electrons with a specific energy, the pass energy, can pass between the two plates and hit an electron multiplier to be detected. The electrons are guided into the analyzer with a lens system which retards the electrons with a varying voltage, thereby making it possible to map out the energy-distribution of the electrons exiting the sample. The choice of pass-energy is a compromise: Low pass-energies give high energy resolution, but lower signal. For broad overview scans, it is therefore advantageous to use high pass energies, whereas detailed scans for e.g. chemical shifts require low pass-energies.

2.3.2 Ion Scattering Spectroscopy

Ion scattering spectroscopy (ISS), also known as low-energy ion scattering spectroscopy (LEIS), relies on ion scattering to provide information about the elemental composition of the outermost atomic layer of a sample surface. The following provides a short introduction to the technique – for more detailed knowledge, see e.g. [40].

An ion gun is used to ionize noble gas atoms and accelerate them towards a sample with a fixed kinetic energy, typically 1-10 keV. Some ions will backscatter and these can be detected with e.g. a hemispherical analyzer, so that the kinetic energy distribution of the scattered ions can be measured.

The collision of a kV-range noble gas ion with a surface atom can be described as an elastic collision with conservation of momentum and kinetic energy [41]. Based on this simple assumption, the following relation between initial ion energy, E_0, and scattered ion energy, E_1, can be found:

$$E_1 = E_0 \left[\frac{\sqrt{M_s^2 - M_i^2 \sin^2(\theta)} + M_i \cos(\theta)}{M_s + M_i} \right]^2 , \tag{2.5}$$

where θ is the angle between ion gun and analyzer, M_s is the mass of the surface atom, and M_i is the mass of the noble gas ion. The only unknown term in this equation is M_s which makes it possible to identify the mass of the different atoms present in the surface of a sample. Although elastic scattering is a good assumption, a scattering event can also cause some energy-losses, causing the peaks in an ISS spectrum to be slightly shifted towards lower kinetic energies than would be expected.

The ion scattering spectrum is only based on signals from the very top layer of a surface, since ions penetrating deeper into the sample will be neutralized, and thus not detected. This makes ISS a uniquely surface sensitive technique.

Although the ideal ion scattering event would leave the surface unchanged, in reality ISS is a destructive technique which sputters away surface atoms. All ISS spectra in this thesis have been obtained with He^+ in order to minimize such sputtering. It is possible to do ISS with heavier noble gasses such as neon, argon, or krypton which yields higher mass-resolution at higher masses, but are more destructive.

2.3.3 Electron Microscopy

Electron microscopy relies on accelerated electrons to produce magnified images of samples. Since high-energy electrons have a shorter de Broglie wavelength than visible light, it is possible to obtain far higher magnifications with electron microscopes than light microscopes.

Figure 2.7 shows the variety of signals that are generated when a beam of high-energy electrons interacts with a thin specimen. Scanning Electron Microscopy (SEM) relies on measuring the secondary or backscattered electrons whereas Transmission Electron Microscopy (TEM) is based on detection of transmitted electrons. It is possible to utilize the emitted X-rays for elemental quantification with Energy Dispersive X-ray spectroscopy (EDX). The following subsections explain the different techniques in more detail. For a thorough treatment of electron microscopy, to e.g. [42, 43].

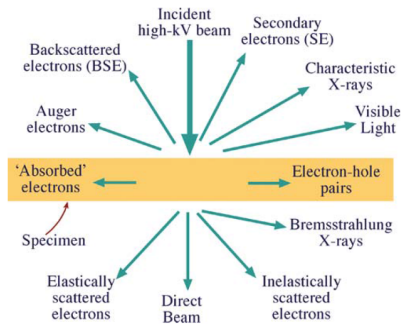

Figure 2.7: Schematic representation of the different signals that are produced when a beam of high-energy electrons interact with a thin specimen. Reproduced from [43].

Scanning Electron Microscopy (SEM)

Scanning electron microscopy works by rastering a focussed electron beam accelerated to 0.5-30 kV over a sample while detecting the resulting secondary or backscattered electrons as a function of position on the sample. Modern high-resolution scanning electron microscopes have resolutions 0.5-1 nm, and SEM is thus well suited for imaging nanoparticles on a surface. Unlike TEM, which require thin samples to allow electron transmission, SEM can measure on most samples as long as they are conductive and compatible with vacuum. Depending on the choice of detector, image formation in SEM can either be based on backscattered electrons (BSE) or secondary electrons (SE).

Backscattered electrons (BSE) originate from the primary beam but are scattered back from the sample. They can therefore have energies ranging from $0-E_0$, where the highest energy is defined by the primary beam energy. The contrast of a BSE-based image will be dominated by atomic number variations, so-called

Z-contrast, since the backscattering cross-section is dependent on the mass of the backscattering atom.

The penetration depth of the primary electrons depend on the sample and acceleration voltage and can vary from a few nanometers to several microns. If the primary electrons are inelastically scattered, they can ionize sample atoms to create secondary electrons. Since both the scattered primary electrons and the secondary electrons can excite more atoms, it is useful to define a so-called interaction volume, which is the volume of the sample in which secondary electrons are generated. The secondary electrons by definition have energies in the range of 0-50 eV (to distinguish from BSE), and thereby a short mean free path, so that only SE's generated near the surface of the sample can be detected. Sample features which expose high surface area, such as edges, protrusions, holes, etc., will appear bright in a SE image, since more SE's from the interaction volume can escape from the sample. Thus, the contrast in images based on secondary electrons is dominated by topography of the sample surface.

The Zeiss Gemini UHV SEM column on the Omicron setup uses an in-lens electron detector which almost exclusively detects secondary electrons. The microscope has a resolution of 3 nm, which is not sufficient to image the structure of nanoparticles, but is suitable for overviews of nanoparticle depositions to verify e.g. the catalyst loading of a sample.

Transmission Electron Microscopy (TEM)

Transmission electron microscopy (TEM) works by sending a parallel beam of electrons accelerated to 100-300 kV into thin samples (<100 nm) and detecting the transmitted electrons. Modern high-resolution TEM can obtain resolutions below 1 Å, and atomic columns can thus routinely be imaged.

The contrast in a TEM image is formed by a combination of sample thickness/density and interference phenomena due to the wave-nature of the electrons. Often, a distinction is made between actual diffraction, resulting in spots reflecting the reciprocal space, and phase contrast, which is especially prominent in high-resolution TEM images, where the phase difference of transmitted electrons near e.g. edges or periodic structures, contributes to image contrast. However, both diffraction and phase contrast arise from the same phenomenon: interference of electron waves.

TEM can be run in different modes, detecting either the directly transmitted beam (bright field) or the scattered electrons (dark field). In bright field, samples features will appear dark, whereas they will appear bright in dark field-imaging.

Scanning Transmission Electron Microscopy (STEM)

Scanning transmission electron microscopy (STEM) also relies on transmitted electrons, but uses a focussed beam of electrons instead of a parallel beam. As in SEM, the image is formed by rastering the beam over the region of interest, but here the transmitted electrons are detected. In this thesis, we have used STEM

in high angle annular dark field (HAADF) mode, where the electrons scattered at an angle higher than 50 mrad are detected. One key advantage of this imaging mode is that the image contrast is only due to thickness and density variations, which makes it simpler to analyze than TEM where phase constrast also plays a role.

Elemental Mapping with Energy-Dispersive X-ray Spectroscopy

As shown in Figure 2.7, the excitation of sample atoms by the incoming electrons can result in emission of X-rays with quantized energies. These X-rays can be used to quantify the elemental composition of the specimen with so-called energy-dispersive X-ray spectroscopy (EDX).

All electron microscopies can in principle be combined with EDX, but especially SEM and STEM are interesting, since these techniques probe one point of the sample at a time, which makes it possible to obtain local EDX data. By combining such EDX spectra it is possible to form an elemental map of a sample, where e.g. the spatial distribution of a certain element can be displayed.

2.4 Measuring Catalytic Activity and Stability

When measuring catalytic activity and stability, it has to be taken into account that the catalyst loadings deposited in our nanoparticle sources are very low, typically on the order of 100 $\frac{\text{ng}}{\text{cm}^2}$.

Electrochemical reactions are fairly straightforward to characterize despite the low loadings since the reactions involve transfer of electrons, which can be measured very accurately as current. Gas-phase reactions are more challenging since typical reactors have large volumes where the reaction products from small catalyst loadings would be difficult to detect. To circumvent this problem, a micro-reactor measurement platform has been developed in our group over the last 10 years, allowing us to measure catalytic reactions on minute amounts of catalyst.

I have not performed any electrochemical or micro-reactor experiments, but I have collaborated extensively with colleagues who did, and therefore briefly present the different methods for measuring catalytic performance in the following.

2.4.1 Electrochemical Measurements

Electrochemistry deals with redox reactions that involve transfer of electrical charge, typically between a liquid electrolyte to a solid electrode. A redox reaction can be divided into two half-cell reactions, where one involves oxidation (and takes place on the anode), and the other involves reduction (and takes place on the cathode). If a potential difference is applied between the two electrodes, the equilibrium of the reaction can be shifted.

When testing a catalyst for an electrochemical half-cell reaction, it is necessary to measure its performance independently of the other half-cell reaction. This can be done by the use of a three-electrode setup as shown in Figure 2.8.

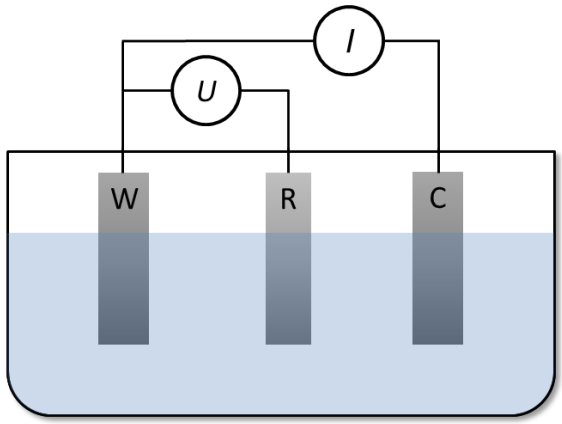

Figure 2.8: Schematic representation of a three-electrode setup with a working electrode (W), a reference electrode (R), and a counter electrode (C). A potentiostat is used to control/measure the current between W and C and the potential on W relative to R.

In a three-electrode setup, the half-cell reaction of interest takes place on the "working electrode"; the other half-cell reaction takes place on the "counter electrode". In order to measure the potential of the working electrode, a third electrode is introduced, the so-called "reference electrode" which has a known potential and thereby acts as a reference for the potential measurements. The current running between working and counter electrode is also measured, thereby allowing a correlation between potential on the working electrode and electrochemical current.

The current and potential is controlled by the use of a potentiostat, which allows for different electrochemical experiments, e.g. "cyclic voltammetry" where the potential of the working electrode is cycled, while the resulting current between working and counter electrode is measured.

2.4.2 Electrochemical Mass-Spectrometry

In an electrochemical experiment, the current going to oxidation/reduction is measured, but there may be multiple competing reactions taking place on the electrode. For reactions where this is the case, such as CO_2 electroreduction, it can be advantageous to measure the product distribution. This is often done with gas chromatography (as in e.g. [44]), but in our group a different methodology has been developed recently, where a mass spectrometer is used for product detection – so-called electrochemical mass-spectrometry (EC-MS).

Using a mass-spectrometer for electrochemistry is inherently difficult since

mass spectrometry is a vacuum technique while the products are formed in a liquid. The key component in our EC-MS setup is a microfabricated silicon chip, which can form a liquid/vacuum interface as seen in Figure 2.9. This so-called "sniffer chip" has been in continuous development since it was first presented in 2014 by Trimarco and coworkers [45]. The main feature of the sniffer chip is a perforated and hydrophobic membrane, which allows for evaporation of volatile species from the liquid without letting liquid-phase products through. An inert carrier gas then carries the gas-phase species to the mass spectrometer through a capillary which bridges the pressure gap from ambient pressure in the chip to vacuum in the mass spectrometer.

Since the sniffer-chip relies on evaporation of products, the EC-MS system only effectively detects volatile species.

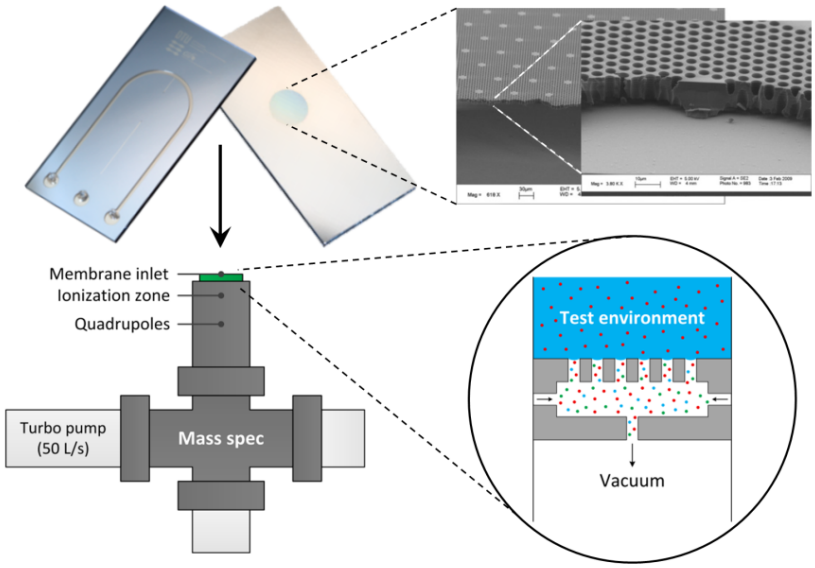

Figure 2.9: Sketch of the EC-MS setup: a sniffer chip with a perforated, hydrophobic membrane is used to connect a mass spectrometer to a liquid phase test environment. Volatile species evaporate through the membrane and are swept to the mass spectrometer high vacuum with an inert carrier gas through a capillary inlet.

2.4.3 Micro-Reactor Measurements

For gas-phase reactions, our group has developed a micro-reactor platform that can be used to test minute amounts of catalyst by use of a microfabricated silicon chip. The micro-reactors were first presented by Henriksen et al. in 2009 [46] after which there has been an ongoing effort to improve and optimize the system [47,48]

Figure 2.10 a) shows a schematic overview of a micro-reactor. The reactant gases are dosed through flow-controllers to the two inlets together with an inert carrier gas and mixed in the meander channel system. Before entering the reactor, a bypass channel leads to outlet 1, which is connected to a pressure controller that controls the reactor pressure. The gas not going to outlet 1 enter the reactor volume, where the catalytic reaction takes place, after which the resulting gas mixture is led to outlet 2, which is connected to a mass-spectrometer through a capillary, thus reducing the pressure from reactor pressure (typically 0.1-2 bar) to vacuum. The reactor volume is 236 nL, which is the reason for the high sensitivity since even small loadings of catalysts can produce a significant partial pressure of product gases. An important feature of the micro-reactor system is that all product molecules produced in the reactor volume are detected in the mass spectrometer (neglecting a tiny loss from back-diffusion through outlet 1).

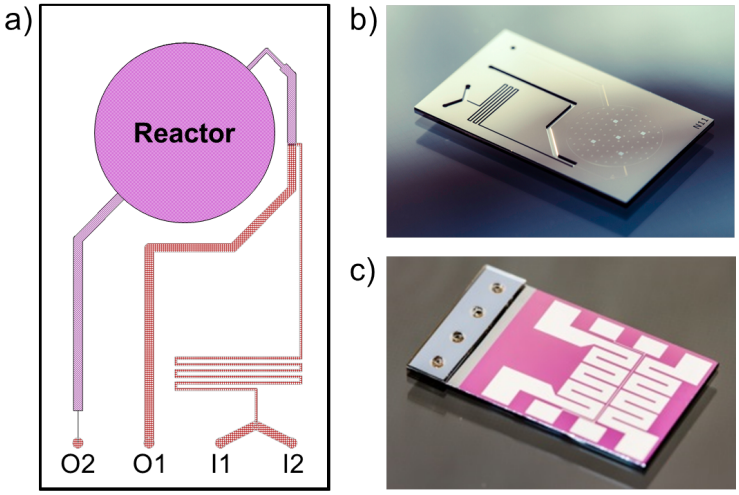

Figure 2.10: **a)** Schematic drawing of our micro-reactor chip, showing the gas inlets (I1 and I2), the reactor chamber, the bypass outlet, O1, going to a pressure controller, and outlet O2, connected to a mass spectrometer through a capillary. **b)** Photograph of the top of a micro-reactor. The bright spots in the reactor volume are support pillars that keep the lid from collapsing to the reactor bottom. **c)** The backside of a micro-reactor showing the resistive heaters and contacts for the resistance temperature detector (RTD). The four channel inlets holes are going through an insulating pyrex spacer.

As seen in Figure 2.10 c) an array of metal films are deposited on the backside of the reactors. These are 1) two sets of heating elements which are used to define the reactor temperature and 2) a resistance temperature detector (RTD) which can be contacted for a four-point measurement. Thus, the reactor temperature can be controlled, allowing for a correlation of reaction temperature and mass-spectrometer signal.

The micro-reactors are loaded with catalyst material by depositing nanopar-

ticles on the reactor area in vacuum with one of our nanoparticle sources. Subsequently, they are taken out in air and a pyrex lid is used to seal the reactor by an anodic bonding process [49], after which they can be mounted in a dedicated mass-spectrometry setup through an interface-block designed to fit the in- and outlets and electrical contacts on the chip.

Chapter 3

Platinum Catalysts for TW-Scale H_2 Production

Platinum is the most active catalyst for the hydrogen evolution reaction (HER) known today, but due to its scarcity and price it is often assumed to be infeasible for (photo)electrochemical hydrogen production on the terawatt scale. In this study we investigated the photoelectrochemical HER catalyzed by ultra-low loadings of mass-selected Pt nanoparticles in order to map out their catalytic efficiency as a function of mass loading. Using the knowledge gained from these well-defined model systems, we conducted a technoeconomic analysis in order to answer the question: Is platinum a feasible catalyst for terawatt scale photoelectrochemical hydrogen production?

The project was conducted in collaboration with Erno Kemppainenen who was a visiting PhD student from Aalto University, Finland. He developed a computational model which predicted the photoelectrochemical performance of Pt nanoparticles catalyzing HER. Together with Béla Sebök, I produced and characterized model systems of Pt nanoparticles using the Nano-Beam 2011 nanoparticle source for inert gas aggregation synthesis. The photoelectrochemical performance of the nanoparticle model systems was then assessed by Brian Seger and Dowon Bae.

The results in this chapter were published in Energy and Environmental Science in 2015 [50]; the paper is appended at the end of the thesis. My contributions to the study was mainly in synthesizing and characterizing the Pt nanopartice model systems, as well as taking part in the paper writing. Therefore I do not present the computational modelling and photoelectrochemical measurements in detail, but go though the most important conclusions. I refer to the paper and its supplementary information for more details.

Before presenting our results, I will provide a brief introduction to photoelectrochemical water splitting and the field of HER catalysis.

3.1 Introduction

Electrochemical water splitting has two half-cell reactions which, in an acidic electrolyte, are:

$$H_2O \rightarrow \tfrac{1}{2}O_2 + 2\,H^+ + 2\,e^- \qquad \text{Oxygen Evolution} \qquad (3.1)$$

$$2\,H^+ + 2\,e^- \rightarrow H_2 \qquad \text{Hydrogen Evolution} \qquad (3.2)$$

The oxygen evolution reaction (OER) takes place on the anode and the hydrogen evolution reaction (HER) takes place on the cathode. Thermodynamically, the water splitting reaction requires 1.23 eV to run, which is supplied by an electrical potential difference in conventional electrolysis. However, it is also possible to run the reaction by photon-generated electron-hole pairs by photoelectrochemical (PEC) water splitting.

3.1.1 Photoelectrochemical Water Splitting

Photoelectrochemical (PEC) water splitting is a complex topic, but the basic principle can be explained simply: If a semiconductor material is irradiated with photons, electron-hole pairs can be generated which can then be used to drive electrochemical reactions on the semiconductor surface. In the water-splitting reaction the holes will drive the OER and the electrons will drive the HER. There are different possible ways to design PEC devices, summarized in e.g. [51].

One could imagine that a semiconductor with a band-gap of 1.23 eV or greater would be able to run the reaction, since this is the thermodynamic energy difference in the water splitting reaction. However, in practice there are significant energy-losses primarily due to overpotentials for both the OER and HER, and the fact that the actual potential difference produced in the semiconductor is lower than the band-gap. Therefore, it has been shown that the band-gap needs to be at least 2.3 eV to run the water splitting reaction [52].

Only a small fraction of the solar photons have enough energy to create electron-hole pairs in semiconductors with such band-gaps. Therefore, it has been proposed to use so-called 2-photon tandem devices, which utilize a sandwich-structure of two semiconductors with a small and a large band-gap, respectively, as shown in Figure 3.1 (see e.g. [53]). In such a design, the blue part of the solar spectrum would be captured by the semiconductor with a large band-gap whereas the red part would be captured by the semiconductor with a small band-gap. This way, the energy of the blue photons is used effectively, instead of loosing the difference between photon energy and band-gap as heat, while the red photons can still be captured.

In this study, we investigated Pt as a catalyst for the HER on a Si-based photocathode exposed to light simulating the red part of the solar spectrum. The results thus provide knowledge that could be used for a 2-electron tandem device, but we study the photocathode separately from the photoanode.

In a conventional electrolyzer, typical current densities are in the range of $\sim$ A/cm^2, but in a photoelectrochemical device, the current is limited by the

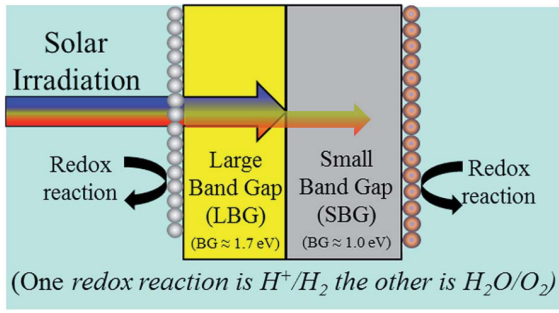

Figure 3.1: Sketch of a two-electron tandem photoelectrochemical water splitting device. Reproduced from [53]

solar flux of photons. Therefore, it would typically run at current densities in the range of $\sim 5 - 20\,\mathrm{mA/cm^2}$. Our study is focussed on this current regime, and is therefore not directly applicable to conventional electrolyzer systems.

3.1.2 Non-Noble HER Catalysts

Since the total energy consumption of humanity is $\sim 17\,\mathrm{TW}$ [8], water splitting with PEC has to be scalable to the terawatt level to have significant impact. The supply of catalyst material is limited [21], and it is therefore of critical importance to asses the scalability of the HER and OER catalysts. I will not go into detail with OER catalysts, since HER is the focus on this chapter. It should, however, be noted that the OER is currently the limiting factor in water splitting since no known catalysts can catalyze it with a sufficiently low overpotential (see e.g. [13]).

Platinum is the most active catalyst for HER known today, but since it is so scarce and expensive, there has been a large effort to find non-precious catalyst alternatives. One of the most studied non-precious HER catalysts is MoS_2 [54–57], which will be introduced thoroughly in Chapter 4. In the recent years, other catalysts have also been tested, prominently sulfides and phosphides of transition metals such as Mo, Co, Fe, or Ni [58–63]. One of the most active non-precious catalysts known today is FeP [64], which requires an overpotential of 50 mV to run a current density of $10\,\mathrm{mA/cm^2}$.

3.1.3 Platinum Versus Non-Noble Catalysts

Although the current non-noble HER catalysts are promising, they are problematic in a number of ways. Firstly, the catalyst loadings needed to obtain a reasonable overpotential is often very high compared to Pt; although the materials are more abundant, the higher loadings required thus make them less attractive than one might think. The higher loadings can also cause problems since the catalyst can block the incoming photons, if the HER catalyst is on the light-exposed side of the PEC device. This problem is less significant with Pt where smaller

loadings could be used. Lastly, the stability of the non-noble catalysts has not been proven, and many of them, such as FeP [64], are already known to degrade too fast to be used in practical applications.

It is therefore relevant to consider whether Pt may still be the best HER catalyst, despite its price and scarcity, if it is used with extremely small loadings. Dasgupta et al. have investigated thin films of Pt [65] and Chen et al. have investigated nanostructured patterns of Pt with different coverages [66]. Both studies get very high catalytic activity with small amounts of Pt, but it is difficult to precisely quantify the Pt mass due to the used synthesis methods.

Our aim with this study was to provide further knowledge to this field by accurately determining the catalytic activity of Pt as a function of mass loading for photoelectrochemical water splitting. Having introduced the necessary background knowledge, I will now proceed to our experimental work, starting with a description of the preparation of photocathodes with well-defined loadings of platinum nanoparticles.

3.2 Photocathode Preparation and Characterization

We used a photocathode substrate consisting of TiO_2-coated pn^+ silicon. The doped silicon acted as a photoabsorber, while the TiO_2 is a transparent protection layer that prevents surface passivation of the silicon, which would hinder electron transfer. The detailed photocathode preparation procedure is described in [67,68].

3.2.1 Nanoparticle Deposition

Platinum nanoparticles were deposited in the Nano-Beam 2011 nanoparticle source with inert gas aggregation in He and Ar with LN_2 cooling of the aggregation zone. The particles were deposited at a mass of 850 kamu, which corresponds to 5 nm spherical particles assuming bulk density of Pt. There is no particular reason that we chose this mass, other than the fact that it was easy to get high, stable deposition currents at 850 kamu. In principle, by going to smaller sizes, we could gain even more mass activity due to the higher surface-to-mass ratio, but we would probably also experience greater problems with sintering and corrosion at these sizes [69]. While depositing, the deposition current was measured, thus enabling us to control the Pt loading. We deposited four different loadings of Pt: $10\frac{\text{ng}}{\text{cm}^2}$, $50\frac{\text{ng}}{\text{cm}^2}$, $100\frac{\text{ng}}{\text{cm}^2}$, and $1000\frac{\text{ng}}{\text{cm}^2}$, thus varying the Pt mass loading with two orders of magnitude.

3.2.2 Characterization

After deposition, the substrates were characterized with XPS and ISS, as shown in Figure 3.2. Only Ti, O, and Pt was observed in XPS, along with some carbon contamination. The differences in loading is clearly observable in the XPS spectra,

Table 3.1: Typical deposition conditions for Pt nanoparticles with a mass of 850 kamu. Before each deposition, the parameters were optimized, leading to some variations in conditions.

Ar flow	He flow	Agg. zone pressure	Sputter power
52 SCCM	9 SCCM	7E-2 mbar	40 W

especially in Figure 3.2 b), which shows a close-up of the Pt4f peaks. The Pt signal for the $10\frac{\text{ng}}{\text{cm}^2}$ is so low that it is not detectable in XPS, but using the higher sensitivity of ISS, it is clearly visible. As later described, we observed significant catalytic activity even for the lowest Pt loading, which underlines the importance of Pt-free electrodes when testing less active HER catalysts, and the need for surface characterization methods more sensitive than XPS to reveal these Pt contaminants.

In order to verify the narrow size-distribution of the nanoparticles, we deposited them on a Cu/lacey carbon TEM grid and imaged them with a FEI Tecnai T20 G2 transmission electron microscope in bright-field TEM mode. The particle shapes were generally close to spherical, although some faceting was observed, as seen in Figure 3.3 a). The particle size distribution was found using the "analyze particles" function in the software ImageJ to determine the projected particle areas, which were then converted into an average diameter for each particle. In order to exclude particles that had landed on top of each other, only particles with a circularity in the range 0.8-1.0 were included in the analysis. The result for 533 analyzed particles is displayed in Figure 3.3 b), where a Gaussian has been fitted to the distribution, resulting in a average size of 5.0 nm with a standard deviation of 0.3 nm.

Besides TEM investigations of the nanoparticle size distributions, we also used SEM to image the nanoparticles on actual photocathode samples as seen in Figure 3.4. The images were acquired without air exposure between deposition and microscopy in the Gemini SEM on the Omicron UHV system at 7 kV acceleration voltage and a beam current of 400 pA. The electrons were detected with an in-lens detector, giving almost exclusively secondary electron contrast, which highlights the sample topography. The platinum nanoparticles are visible as bright dots in the images on the rough TiO_2 surface, and the difference between loadings is clearly visible.

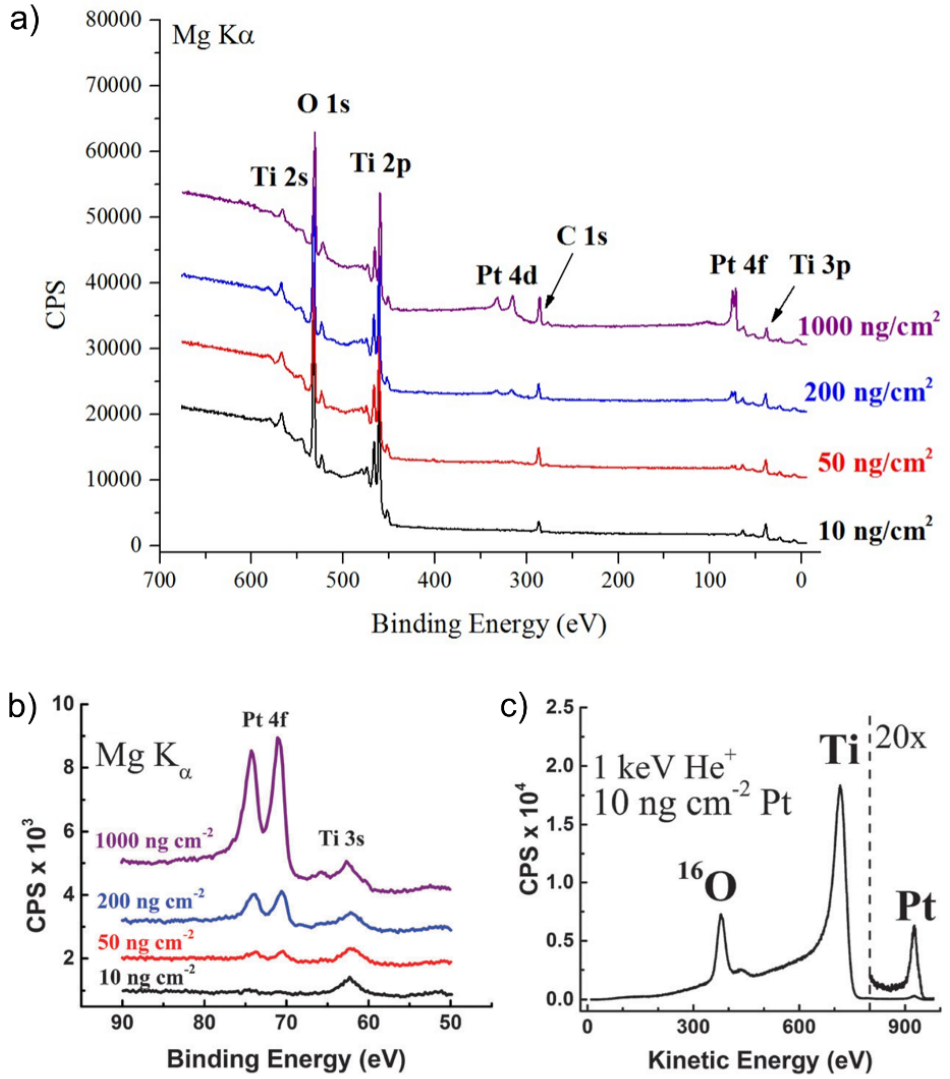

Figure 3.2: Spectroscopy of photocathodes with different loadings of platinum nanoparticles. **a)** shows XPS overview spectra revealing Ti, O and Pt, as well as some carbon contamination. As the Pt loading is decreased, the XPS signal gets weaker, as evidenced in the close-up scan in **b)**, where the $10\frac{\text{ng}}{\text{cm}^2}$ of Pt is below the detection limit with XPS. **c)** shows an ISS spectrum where Pt is clearly visible on the $10\frac{\text{ng}}{\text{cm}^2}$ sample, due to the higher sensitivity of this technique. Reproduced from [50].

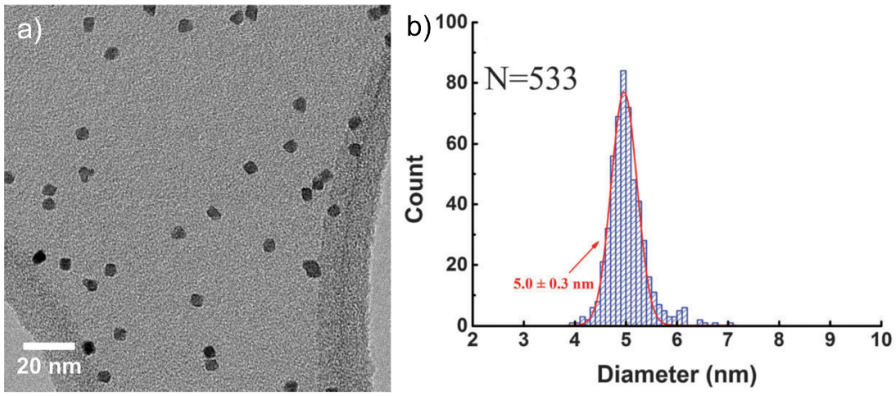

Figure 3.3: **a)** TEM image of platinum nanoparticles deposited at a mass of 850 kamu on Cu/lacey carbon TEM grids. **b)** Histogram showing the distribution of particle diameters observed for 533 nanoparticles. Adapted from [50].

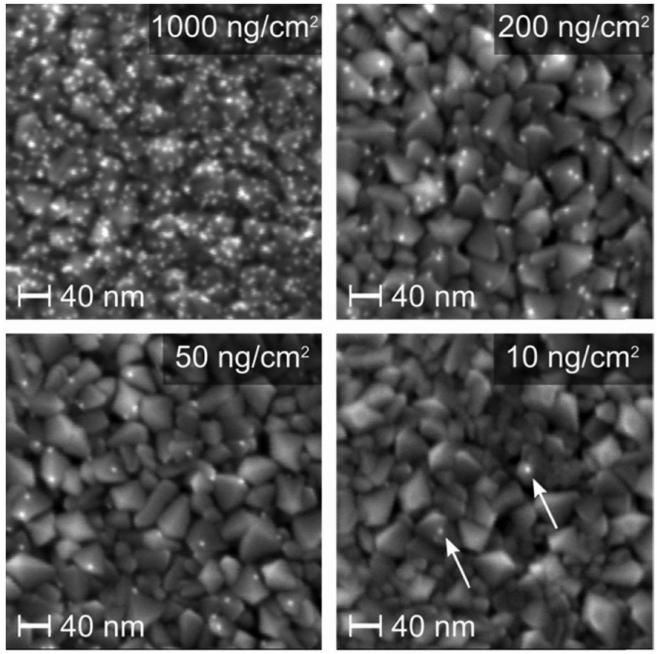

Figure 3.4: SEM images on photocathodes with four different loadings of Pt nanoparticles, visible as bright dots on the rough TiO_2 substrate. The particle density is clearly varying as a function of loading. In the image of the $10\frac{\text{ng}}{\text{cm}^2}$ sample, the particles are indicated with arrows. Reproduced from [50].

3.3 HER Experiments and Modelling

3.3.1 Photoelectrochemical Measurement Methodology

The TiO_2/pn^+Si photocathodes deposited with 5 nm Pt nanoparticles at different loadings were tested for their performance in photoelectrochemical HER in a three-electrode setup with illumination that simulated the red part of the solar spectrum.

The three-electrode setup had an H-cell design with a glass frit between working and counter electrodes. The electrolyte was aqueous 1 M $HClO_4$ (Aldrich 99.99 %). The electrolyte was cleaned by performing chronoamperometry with Pt meshes as counter and working electrodes overnight. The photoelectrochemical experiments were run with a Pt counter electrode and a $Hg/HgSO_4$ reference electrode. Before each experiment, the electrolyte was saturated with gaseous H_2, which was kept running during the entire experiment.

The illumination was provided with a xenon lamp equipped with a 635 nm cut-off filter and an AM1.5 filter, in order to simulate the red part of the solar spectrum ($\lambda > 635$ nm, 38.6 $\frac{\mathrm{mW}}{\mathrm{cm}^2}$). The cyclic voltammograms were acquired at 50 $\frac{\mathrm{mV}}{\mathrm{s}}$.

The photocathodes were prepared for photoelectrochemical testing by encapsulating them in epoxy resin, ensuring that only the areas protected by TiO_2 were exposed to electrolyte. After the photoelectrochemical measurements, the Pt loading on each sample was verified using inductively coupled plasma mass spectrometry (ICP-MS, iCAPQC ICP-MS, Thermo Fischer Scientific) after dissolving the Pt in an aqua regia solution. The ICP-MS measurements clearly reproduced the nanoparticle loadings expected from the deposition current measurements in the nanoparticle source.

3.3.2 Computational Modelling Methodology

A computational model was created by Erno Kemppainen to describe the current-overpotential relationship of the photocathodes, especially focussing on the relative importance of HER kinetics vs. mass transport effects. The model is described in great detail in [50], but I will give a short overview of the most important assumptions in the model.

The photocathode surface is modelled as an array of cylindrical unit cells with a Pt nanoparticle in the centre. Since the unit cell is symmetric around the z-axis, it can be simplified to the 2D-model shown in Figure 3.5 a). The unit cell extends 100 nm into the TiO_2 substrate and 100 μm into the electrolyte; the radial size of the unit cell is determined as half the average particle-particle distance, which varies as a function of loading as seen in Figure 3.5 b). The nanoparticle was assumed to be embedded 0.25 nm into the TiO_2-substrate, thus exposing 95 % of the Pt surface area to electrolyte. A zero-flux boundary condition was set for the unit cell.

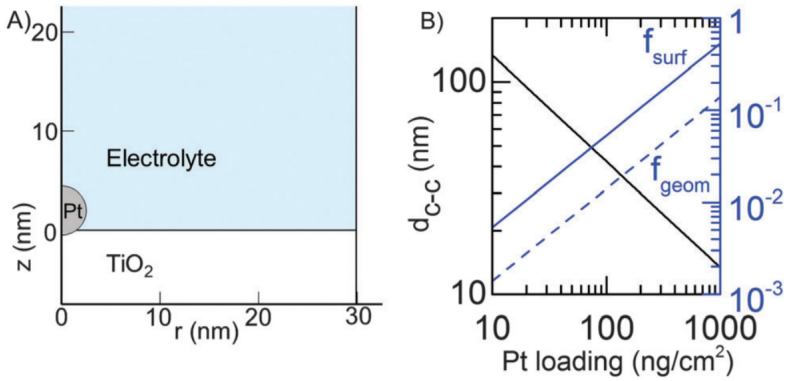

Figure 3.5: **a)** The photocathode surface is modelled as an array of cylindrical unit cells, which are symmetric around the z-axis; they can therefore be simplified to the 2D system shown in the figure. The boundary of the cell is at 30 nm for this $50\,\frac{\text{ng}}{\text{cm}^2}$ sample, which is half the average distance between two particles. **b)** The black line shows the average center-to-center distance between Pt particles as a function of mass loading. f_{surf} shows the fraction of the surface covered by Pt, whereas f_{geom} shows the ratio between Pt surface area and geometrical electrode area. Reproduced from [50].

The steady state of the catalyst system was calculated with a transient simulation, starting from equilibrium at 0 V vs. RHE, and then allowing the concentration profiles to converge. The presented IV-curves use the last calculated point in the simulation. The IV-curve of an ideal silicon PV cell, without kinetic or mass-transport limitations from the catalytic process, was simulated for later comparison with experimental data.

3.3.3 Results of Photoelectrochemical Experiments

Figure 3.6 shows an anodic sweep from the cyclic voltammograms of four different samples with different Pt loading. As seen from the curves, the current saturates at $-22\,\frac{\text{mA}}{\text{cm}^2}$, the light-limited photocurrent. For all samples, the open-circuit photovoltage (V_{OC}) was 495 ± 4 mV vs. RHE. Both the light-limited photocurrent and V_{OC} matches earlier experiments from our group with Pt nanoparticles deposited by conventional drop-casting of a Pt salt solution [67, 70].

The activity of the electrodes fell during HER testing, which we attribute to blocking of catalytic sites by impurities from the epoxy resin. Due to these problems with instability, we did not investigate catalyst stability further. However, at least the first 5 cycles in the cyclic voltammograms were stable, and the data in Figure 3.6 is therefore the third anodic sweep of each sample.

In order to compare the samples, Table 3.2 lists the overpotentials at $10\,\frac{\text{mA}}{\text{cm}^2}$ of HER (defined as $\eta = V_{\text{OC}} - V_{10\,\text{mA}\,\text{cm}^{-2}}$). We choose $10\,\frac{\text{mA}}{\text{cm}^2}$ for comparison, since this is a realistic current for a photoelectrochemical water splitting device. Just as visually represented in Figure 3.6, the overpotential drops with increasing

loadings, but it should be noted that the relative drop is much higher by increasing from e.g. $10\frac{\text{ng}}{\text{cm}^2}$ to $50\frac{\text{ng}}{\text{cm}^2}$ than when going from $200\frac{\text{ng}}{\text{cm}^2}$ to $1000\frac{\text{ng}}{\text{cm}^2}$. This is partly due to mass-transport limitations, which I discuss later.

Table 3.2: Experimentally observed overpotentials needed to drive $10\,\frac{\text{mA}}{\text{cm}^2}$ of HER at different loadings of platinum nanoparticles.

Pt loading	$10\frac{\text{ng}}{\text{cm}^2}$	$50\frac{\text{ng}}{\text{cm}^2}$	$200\frac{\text{ng}}{\text{cm}^2}$	$1000\frac{\text{ng}}{\text{cm}^2}$
Overpotential, η	231 mV	142 mV	46 mV	32 mV

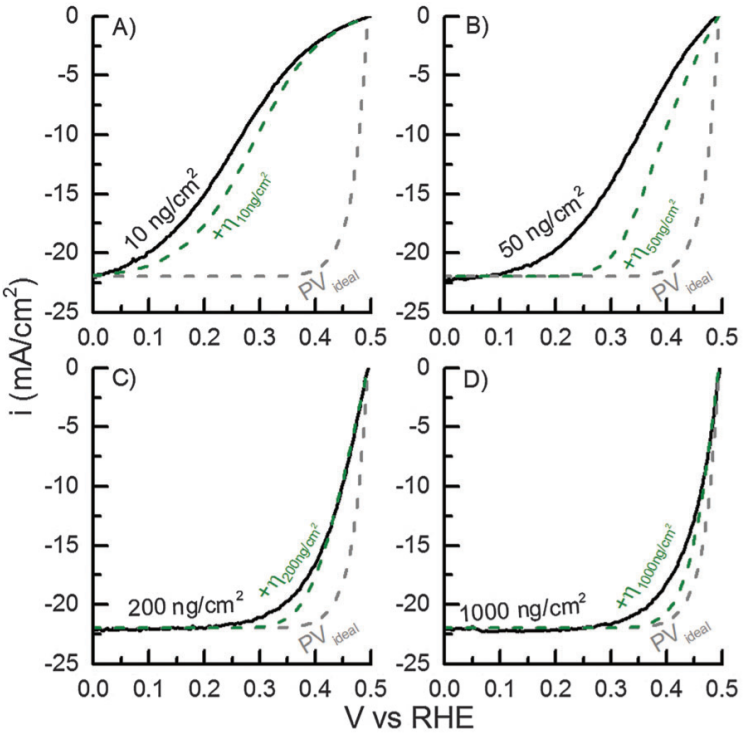

Figure 3.6: IV-curves for four different loadings of Pt nanoparticles, clearly showing that the HER overpotential decreases as a function of loading. The black lines represent experimentally measured data, whereas the dashed, green line represents the modelling, which shows the same trend as the experimental data. The dashed gray line shows the IV-curve for an ideal photovoltaic device. Reproduced from [50].

3.3.4 Results of Computational Modelling

Co-plotted with the experimental data in Figure 3.6 are the results from computational modelling. The dashed green lines represent the modelled IV-curves, which follow the same general trend as the experimental curves. The model systematically underestimates the overpotentials, especially in the high-current range. This may be due to overestimation of the fill-factor for the modelled photovoltaic compared to the actual PV used in the experiment. The gray dashed line shows the modelled IV-curve for an ideal photovoltaic, which represents the case where the PV is not limited by the catalytic reaction.

3.3.5 Effect of Mass Transport Limitations

In order to analyze the relative importance of catalytic kinetics and mass transport, the total overpotential can be divided into two parts:

$$\eta_{\text{total}} = \eta_{\text{kinetic}} + \eta_{\text{MT}}, \tag{3.3}$$

where η_{MT} is the overpotential due to mass transport. It is not conventional to think of mass transport in terms of overpotentials; furthermore, the formula is a Taylor expansion of the total expression for the overpotential, and therefore only valid in the low-current regime. However, the simple mathematical representation provides a good approximative understanding of the mechanisms behind the total overpotential.

Figure 3.7 a) shows the current densities as a function of η_{total} and η_{MT} as calculated with the computational model for the four different Pt loadings. A flat Pt

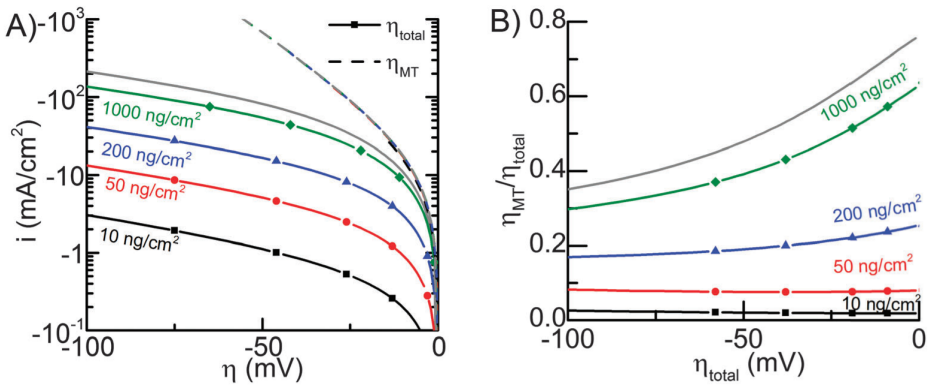

Figure 3.7: **a)** Current density as a function of total overpotential, η_{total}, and mass-transport-induced overpotential, η_{MT}. The mass-transport-limited current, plotted as dashed lines, are identical for all samples, but the total current is increasing with Pt loading. The gray lines represent a flat Pt film. **b)** The $\eta_{\text{MT}}/\eta_{\text{total}}$ ratio plotted as a function of total overpotential. The low loadings are not limited by mass transport, but for the higher loadings it plays a significant role. Reproduced from [50].

film, i.e. full surface coverage of Pt, is also plotted as a reference (gray lines). The mass-transport-induced overpotential is constant for all samples, which can be understood by the fact that diffusion in the z-direction (out through the electrolyte) is dominating the mass transport since it happens on a much larger length scale than the inter-particle distance. In Figure 3.7, the $\eta_{\mathrm{MT}}/\eta_{\mathrm{total}}$ ratio is plotted, illustrating the greater relative importance of mass-transport in the high-loading samples, where kinetics are less limiting. Thus, increasing the Pt loading will boost the catalytic activity less and less the higher the Pt loading is.

3.4 Technoeconomic Implications

The photocathodes that we have investigated are highly active in terms of catalytic activity per platinum mass. Therefore, they can provide a good estimate of the lower bound for the Pt consumption needed to produce a given amount of hydrogen. Since the total energy-consumption of the human civilization is $\sim 17\,\mathrm{TW}$ [8], photoelectrochemical water splitting would have to convert energy in the TW-range. Therefore, we asked the question: How much platinum does it take to store an average of 1 TW electricity in the chemical bonds of H_2?

3.4.1 Calculating Pt Consumption per Terawatt H_2

To provide an answer to the question, a simple technoeconomic analysis can be performed. First, the average power density (power per area) of a photoelectrochemical water splitting device is calculated as

$$P_{\mathrm{avg}} = 0.15 \times i \times 1.23\,\mathrm{V} = 0.1854\,\mathrm{V} \times i, \tag{3.4}$$

where i is the current density, 1.23 V is the voltage difference needed to split water, and 0.15 is the "capacity factor" which accounts for the fact that a PEC device cannot operate at full efficiency all the time, due to fluctuations in the incoming sunlight. A capacity factor of 0.15 is a conservative estimate [71]. If a PEC device was run at $10\,\frac{\mathrm{mA}}{\mathrm{cm}^2}$, Equation 3.4 would predict an average power density (H_2 generation rate) of $18.54\,\frac{\mathrm{W}}{\mathrm{m}^2}$. It should be noted that a real PEC device would also have overpotential losses on the anode side, which are far greater than the cathode overpotentials, thus increasing the effective voltage difference needed to split water. However, in this analysis we are only focusing on the HER side, and therefore use the thermodynamic water-splitting potential of 1.23 V.

Having assessed the average power density of a PEC device, the area needed to produce 1 TW can be calculated as

$$A_{\mathrm{TW}} = 1\,\frac{\mathrm{TW}}{P_{\mathrm{avg}}} = \frac{542\,000\,\mathrm{km}^2}{i[\mathrm{mA\ cm}^{-2}]}. \tag{3.5}$$

At a current density of $10\,\frac{\mathrm{mA}}{\mathrm{cm}^2}$, it would thus require $54\,000\,\mathrm{km}^2$ of PEC water splitting devices to produce 1 TW. Now, by multiplying Eq. 3.5 with the platinum

loading (in weight per area), we arrive at the needed amount of platinum catalyst to store 1 TW of electricity in H_2 through HER as a function of current density.

3.4.2 How Much Pt is Needed per Terawatt H_2?

Now, an assumption has to be made regarding what current density, i, and overpotential, η, the PECs should run at. Figure 3.8 shows the overpotential as a function of Pt loading at four realistic current densities, as calculated with the computational model. The first thing that should be noticed is that a loading of $1000\frac{\text{ng}}{\text{cm}^2}$ performs almost as good as the flat Pt film (overpotentials of 12 mV vs. 9 mV, respectively). At higher loadings the mass transport will dominate, making it infeasible to increase the loading further.

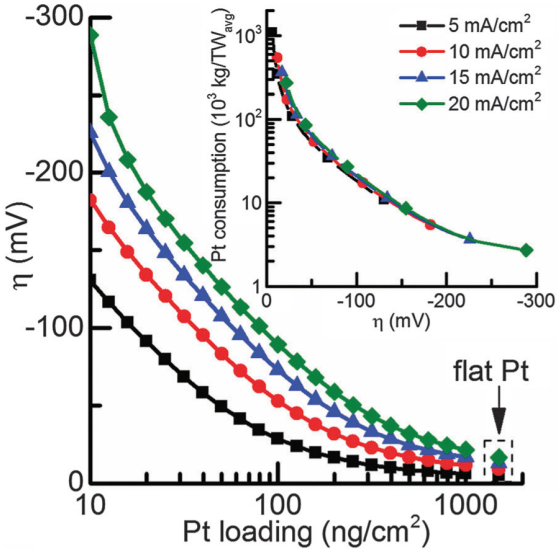

Figure 3.8: The main graph shows the HER overpotential as a function of platinum loading on the photocathode at four relevant current densities. The highest loading of Pt nanoparticles performs almost as well as flat Pt. The inset shows the Pt consumption per TW of hydrogen produced with photoelectrochemical HER as a function of overpotential. Reproduced from [50].

The inset in Figure 3.8 shows the Pt consumption per TW as a function of overpotential at different current densities. If the PECs were run at $10\frac{\text{mA}}{\text{cm}^2}$ with a loading of $1000\frac{\text{ng}}{\text{cm}^2}$ the total platinum consumption would be 542 tons per TW. If, on the other hand, an overpotential of 50 mV was accepted, similar to good non-noble catalysts [59–62, 64], the Pt loading could be decreased to 54 tons per TW. The lines for different current densities in the inset lie on top of each other, showing that the Pt consumption per TW H_2 does not depend on the current density at which the PECs are run. It should, however, be noted that the area

of PEC devices would have to be increased if operated at a lower current density, thus increasing the total system cost.

The current Pt production is $\sim$ 180 tons per year, where the consumption is divided into $\sim$ 70 tons for jewellery and $\sim$ 65 tons for automotive catalytic converters [21, 72, 73]. Therefore, a Pt consumption of 54 tons per TW H_2 might be feasible for incorporating several TWs into the energy system, especially since the PEC hydrogen capacity would be built over years.

Research in non-noble HER catalysts is often motivated by the fact that they would be more scalable, since the catalyst materials are more abundant. However, it should be noted that they require order-of-magnitude higher catalyst loadings for obtaining similar HER overpotentials as Pt. In Table 3.3 we compare the scalability of state-of-the-art non-noble catalysts with that of Pt by reporting the percentage of the annual world production of the catalytic material needed for producing 1 TW of H_2. For most of the catalysts, the metal (Mo, Co, or Ni) is the limiting material, but for FeP, P is the limiting factor and therefore the percentage is reported for P instead. The numbers are reported for an overpotential of $\eta = 75$ mV since data was available for all materials at this potential.

Table 3.3: Comparison of non-noble HER catalysts and the Pt nanoparticle system from this study. The current density at overpotential $\eta = 75$ mV is listed along with the percentage of the world production of the catalyst material needed to produce one TW of H_2.

Catalyst	Reference	i [mA mg^{-1}] at $\eta = 75$ mV	% of annual production/TW
MoS_2	[74]	0.6	2200 (of Mo)
CoP	[61]	6.5	670 (of Co)
Ni_2P	[60]	1.5	220 (of Ni)
FeP	[64]	48	0.13 (of P)
Pt	This study	171 600	16

The most promising catalyst in Table 3.3 appears to be FeP. However, this catalyst has severe durability issues, and degrade so that the overpotential is doubled in $\sim$ 16 hours [64]. The conclusion of the technoeconomic analysis is therefore: Pt may be more scalable than the state-of-the-art non-noble catalysts, despite its scarcity, because of its unprecedented activity.

3.4.3 Limitations to our Study

It is important to bear in mind that we only studied the cathodic half-cell reaction of water splitting, which is much less problematic from a catalytic point of view than the anodic oxygen evolution reaction (OER). Unless better catalysts for OER in acidic media are discovered, the problems regarding HER catalysis are insignificant.

In this study, we chose to investigate nanoparticles of 5 nm in diameter. It may be that even higher mass activities could be achieved by lowering the particle sizes, but as previously mentioned, it would likely come at a price of greater problems with sintering and corrosion [69].

We did not investigate the durability of our photocathodes thoroughly, but they are seemingly unstable, especially at low loadings. It might be possible to stabilize the catalytic system by suitable photocathode engineering, e.g. by ensuring better nanoparticle anchoring on the substrate or higher system purity, but it might also be practically impossible to ensure sufficient stability on ultra-low loading Pt samples.

3.5 Conclusion and Outlook

In this study, we investigated the possibilities in using ultra-low loadings of platinum nanoparticles for catalyzing the photoelectrochemical hydrogen evolution reaction (HER). Our main focus was to understand the correlation between platinum mass loading and HER overpotential, and to use this fundamental understanding to estimate the Pt consumption for storing terawatts of solar power in hydrogen.

Using TiO_2-protected pn^+ silicon photocathode substrates, we synthesized model systems of mass-selcted 5 nm platinum nanoparticle catalysts with well-defined loadings ranging from $10\,\frac{\mathrm{ng}}{\mathrm{cm}^2}$ to $1000\,\frac{\mathrm{ng}}{\mathrm{cm}^2}$ using a nanoparticle source relying on gas aggregation of sputtered Pt. Under photo-illumination conditions simulating the red part of the solar spectrum, the overpotentials needed to obtain a current density of $10\,\frac{\mathrm{mA}}{\mathrm{cm}^2}$ ranged from 231 mV at $10\,\frac{\mathrm{ng}}{\mathrm{cm}^2}$ to 32 mV at $1000\,\frac{\mathrm{ng}}{\mathrm{cm}^2}$. No light-blocking due to the Pt nanoparticles was observed.

The experimental results were complemented with a computational model of the current-overpotential relationship of the photocathodes, especially focussing on the relative importance of HER kinetics vs. mass transport effects. It was shown that the photocathodes with high loadings of Pt were significantly mass-transport-limited.

Finally, a simple technoeconomic analysis was conducted to estimate the Pt consumption per terawatt of H_2. In order to obtain a current density of $10\,\frac{\mathrm{mA}}{\mathrm{cm}^2}$ and an overpotential of 50 mV, it would take a Pt loading of $100\,\frac{\mathrm{ng}}{\mathrm{cm}^2}$ which would translate into a Pt consumption of 54 tons per TW H_2. Although this represents a significant percentage of the annual platinum production (180 tons/year), it is still more scalable than most state-of-the-art non-noble HER catalysts, due to the much higher mass loadings needed for these catalysts. Thus, despite its scarcity, the extremely high HER activity of Pt may enable its use as a catalyst for terawatt-scale photoelectrochemical hydrogen production.

For further studies, it would be interesting to focus on the durability of different HER catalysts. If a catalyst is to have industrial-scale impacts, it will have to be stable or regeneratable on the order of years, which is a significant challenge, both for noble and non-noble catalysts.

Chapter 4

Synthesis of Ni-Mo-S Nanoparticles by Reactive Gas Aggregation

A substantial part of my Ph.D. has been devoted to the study of mass-selected molybdenum-nickel sulfide nanoparticles produced by reactive gas aggregation, i.e. where the particles are sulfided "in flight" by co-feeding H_2S gas together with the Ar into the aggregation zone of the nanoparticle source. Besides the fundamental interest in such nanoparticles, we were also interested in their catalytic activity for two reactions: the hydrodesulfurization reaction (HDS), which is the removal of sulfur from crude oil compounds, and the hydrogen evolution reaction (HER). Our main focus was on HDS, and HER was only investigated shortly in a side-project. Figure 4.1 summarizes the research project in a schematic form, where the nanoparticles are deposited in a micro-reactor for HDS testing.

A number of people have been involved in the project besides me, most prominently Ann-Louise Christoffersen, who developed a setup for testing catalytic activity for HDS in microreactors in her Ph.D. in our group, and Christian Elkjær, who currently has a post-doctoral position at Haldor Topsøe A/S, and is an expert microscopist who operated the microscope when we imaged nanoparticles with STEM and provided important inputs and discussion along the way. Both Ann-Louise and Christian are part of the HYDECAT project (Enabling Ultra Deep Hydrodesulphurization by Nanoscale Engineering of New Catalysts), which is financed by Innovation Fund Denmark as collaboration between DTU, University of Copenhagen, Aarhus University and Haldor Topsøe A/S. The HER measurements were done by Jakob Kibsgaard together with Jonas Bertelsen, a master student who did a small experimental project with us. All other experimental work, analysis, etc. presented in this chapter was done by myself unless otherwise indicated.

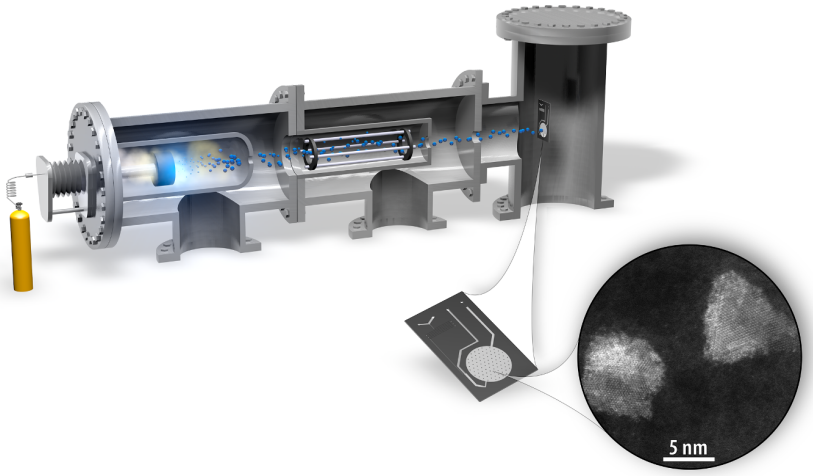

Figure 4.1: Schematic overview of the research strategy in this project. Ni-Mo-S nanoparticles are produced in the Nanogen50 nanoparticle source by sputtering a $Mo_{75}Ni_{25}$ metal target in a reactive atmosphere of Ar and H_2S. They are then mass-filtered and deposited on a micro-reactor for investigations of their catalytic activity for HDS. Figure by Jakob Kibsgaard.

4.1 Introduction

4.1.1 Why Study Molybdenum Sulfide Nanoparticles?

The list of applications for molybdenum disulfide is long and constantly growing. Besides catalysis, it has long been used as a lubricant [75], and there is currently a broad interest in its semi-conducting properties for applications in e.g. nanofabricated electronics [76].

In the field of catalysis, molybdenum sulfides have been used for hydrodesulfurization (HDS) for decades, resulting in thousands of research papers and patents [77]. There are, however, still remaining challenges in optimizing this catalytic reaction, which is the main motivation for my work on molybdenum sulfide nanoparticles.

In 2005, it was found that molybdenum sulfides could also catalyze the electrochemical hydrogen evolution reaction (HER) [78]. This discovery has led to a booming field of research [54–57], and the possible application of molybdenum sulfides for HER was another motivation for my research.

In the following subsections I will give a short introduction to the HDS and HER, and the aim of my research in those fields. The introduction then proceeds to a description of the MoS_2 crystal structure and properties, which is crucial for understanding the structural characterization presented later in the chapter. Finally, I will provide an introduction to nanoparticle synthesis by reactive gas aggregation.

4.1.2 Hydrodesulfurization (HDS)

Crude oil is a complex mixture of chemicals which, apart from hydrocarbons, contain e.g. sulfur compounds, nitrogen compounds and oxygenates. The sulfur content can be up to 6 wt%, and an important step in the refining process to produce e.g. diesel and gasoline, is therefore to remove the sulfur-containing compounds in the so-called hydrodesulfurization (HDS) process [77, 79]. The sulfur is removed by letting hydrogen react with the crude oil compound, typically at temperatures of $300 - 400\,^{\circ}\mathrm{C}$ and a pressure of 150 bar over MoS_2 catalysts promoted with either Co or Ni [77].

Increased environmental concerns due to e.g. acid rain has led to introduction of increasingly strict regulations on sulfur content in fuels, so that today, no more than 10 ppm is allowed in European diesel [80]. As the environmental regulations have tightened, the last bit of sulfur left is becoming increasingly difficult to remove. The reason for this is that the remaining sulfur is "hidden" inside molecules where it is hard to access, as illustrated by Figure 4.2, thus sterically hindering the HDS process. The aim of the HYDECAT project has been to design nanoscale catalysts which could circumvent the steric hinderance and thus remove this last stronghold of sulfur.

One of the outcomes of HYDECAT has been a combined scanning tunneling microscopy (STM) and density functional theory (DFT) study of the sterical hinderance effect in the adsorption of 4,6-dimethyldibenzothiophene (4,6-DMDBT) by Grønborg et al. [81]. This study found that the only option for direct chemisorption of 4,6-DMDBT on a Co-promoted MoS_2 nanoparticle was through a vacancy in the corner position of an S-edge. Since DFT shows that this type of site only occurs infrequently under HDS conditions, it is clear why the HDS has a low rate. This specific study is one example of a more general idea: The ideal catalyst will have to expose "pointed" features which can access the hidden sulfur.

Normally, the Ni/Co-doped MoS_2 catalysts for this reaction would be produced by heating a metal oxide precursor in H_2S, leading to nanoparticle structures close to equilibrium. In-flight-sulfided particles, on the other hand, are formed at room-temperature by gas-phase aggregation in H_2S, which may result in particles with non-equilibrium structures, exposing many corner-sites.

In our project, the focus was on HDS of dibenzothiophene (DBT), which according to Houalla et al. [82] has two HDS reaction pathways as seen in Figure 4.3, the hydrogenation pathway (HYD) and the direct desulfurization pathway. Houalla et al. report that the HYD pathway is very slow, especially at low pressures; this matches our own experiences, as we have only observed Biphenyl as a product from HDS of DBT.

Since we study catalytic activity in microreactors, we operate at pressures around 1 bar, far from the reaction conditions in industrial reactors. However, we anticipate that the model system investigations will lead to insights that are applicable to real-life systems.

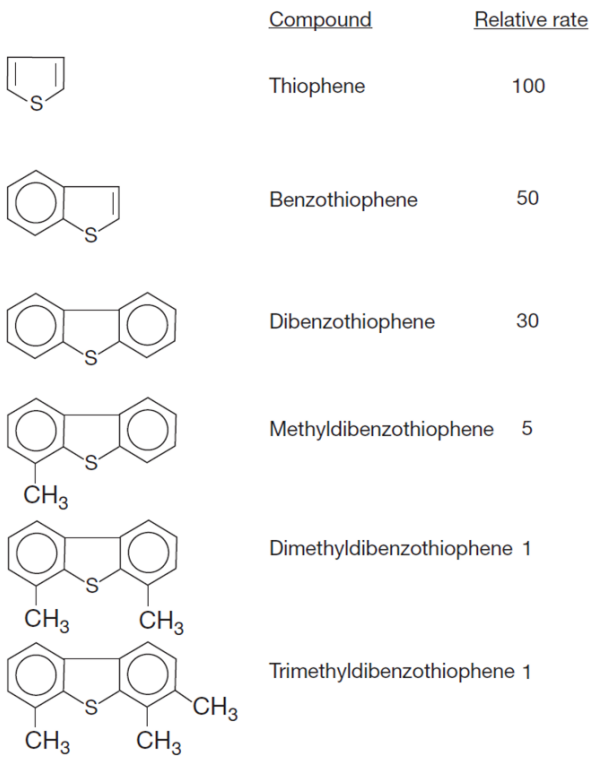

Figure 4.2: HDS rates of different sulfur-containing compounds from crude oil, given relative to the rate of thiophene. In this project, we have focused on dibenzothiophene (DBT). Figure from [77].

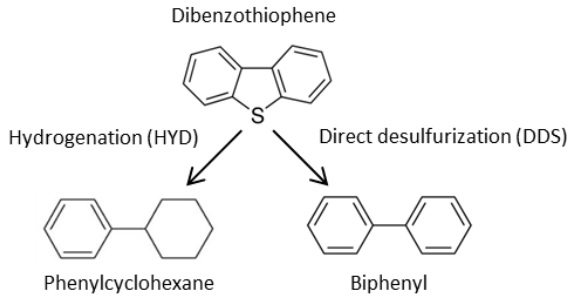

Figure 4.3: The two reaction pathways for HDS of dibenzothiophene (DBT), hydrogenation (HYD) and direct desulfurization (DDS). In our project, we have only observed Biphenyl as a product, implying the dominance of the DDS pathway.

4.1.3 Hydrogen Evolution Reaction (HER)

As mentioned in Chapter 3, one of the most studied non-noble HER catalysts is molybdenum disulfide. Since it was identified as an HER catalyst in 2005 [78], it has been the subject of intense research as documented in several review papers in the recent years [54–57].

MoS_2 is catalytically inert on basal planes [79], and thus catalytic reactions typically take place on edges [78, 83]. It has therefore been attempted to optimize the activity of MoS_2 by engineering structures that expose as many edge-like sites as possible [54]. Since the in-flight sulfided Ni-Mo-S nanoparticles are expected to form many edge-like sites, it was obvious to test them for HER, which we did in a small sub-project.

4.1.4 MoS_2 Crystal Structure and Properties

The crystal structure of molybdenum disulfide was first reported in 1923 [84]. It has a layered structure, similar to e.g. graphite, where the individual MoS_2 slabs are held together by weak Van der Waals forces. As seen in Figure 4.4, each slab has a hexagonal structure and consist of a Mo layer sandwiched between two S layers. For bulk materials the lattice parameter is 3.15 Å for the Mo-Mo/S-S distance in-plane, and 6.15 Å between the layers [84, 85].

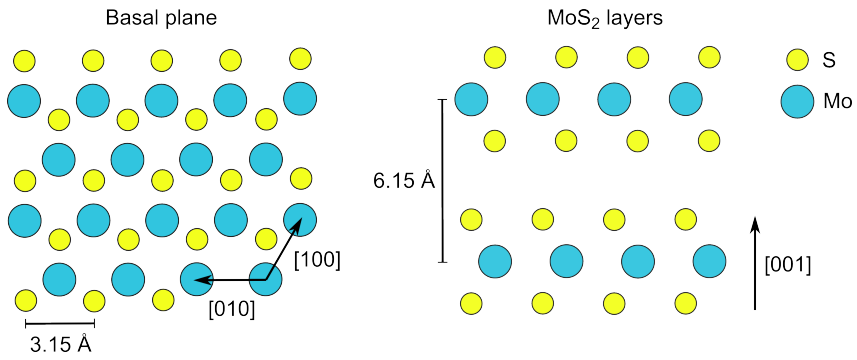

Figure 4.4: Crystal structure of MoS_2 showing the hexagonal lattice of the basal plane and the layered structure of the MoS_2 slabs held together by weak Van der Waals forces. The stacking shown here is the most common so-called "2H" stacking where the layers are alternately rotated 60° around the [001] axis, resulting in S atoms in one layer being above the Mo atom in the next layer. The reported lattice parameters are from [84].

In literature, at least three different lattice vector conventions are used, which can cause some confusion. In Figure 4.4, a three-vector notation is used which makes it easy to grasp the crystal unit cell. In e.g. [86], four-vector notation is used instead, and e.g. [87] used a three-vector notation different from the one in Figure 4.4, which results in low-index names for the crystalline planes observed in STEM. In the following, all references to lattice vectors use the latter notation, since this is most suitable for STEM image analysis.

Due to the layered structure, the electrical conductivity of MoS_2 depends strongly on direction relative to the crystal lattice. Evans and Young report almost a factor of 200 difference between conductivity along the basal planes and perpendicular to them at room temperature [88].

Molybdenum Disulfide Nanoparticles

The structure of molybdenum disulfide nanoparticles has been investigated thoroughly in the recent years. Some of the key groups have been Besenbacher et al. who have performed scanning tunneling microscopy (STM) (e.g. [86, 89]) and Helveg et al. who have focused on transmission electron microscopy (e.g. [90,91]).

Figure 4.5 shows a STEM image from the Helveg group of a molybdenum disulfide platelet nanoparticle, which has the slightly truncated triangular shape often observed for these nanoparticles. The Fourier transform of the nanoparticle image reveals distinct periodicities from the MoS_2 (100) and (110) planes of 2.7 Å and 1.6 Å, respectively, besides a periodicity from the C substrate.

It is also possible to image the inter-plane periodicity, as e.g. Lu et al. [92], who observe interplanar distances between 6.3 Å and 7.0 Å when imaging MoS_2 "nanoflowers" with HRTEM. The spread in inter-plane distances could be due to the fact that the Van der Waals binding between the layers are weak, and thus allow the structures to be easily strained.

Industrial-style MoS_2 catalysts are, as earlier noted, often promoted with Co or Ni. Instead of noting precise stoichiometry, the catalysts are often named "M-

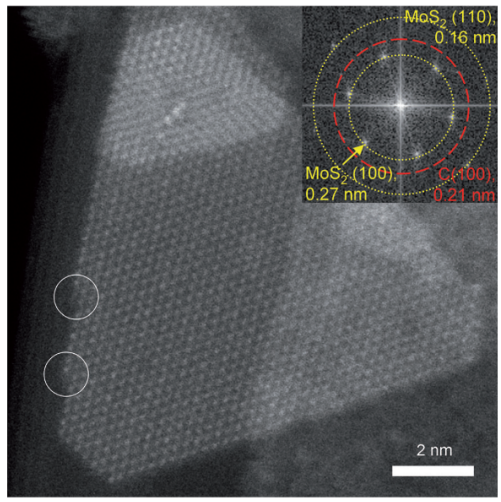

Figure 4.5: Molybdenum disulfide platelet nanoparticle imaged with STEM to show the slightly truncated triangular shape characteristic of MoS_2. The inset shows the Fourier transform of the image, revealing the spatial periodicities characteristic for MoS_2 and the carbon substrate. The white circles indicate kink sites. Image from [90].

Mo-S", where M is the promoter, which is also done in this study on Ni-Mo-S nanoparticles. The promoters have been shown to be preferentially located on the edges of the basal planes both by STM and STEM [86, 91]. Also, it has been observed that doped particles have a tendency to form hexagonal shapes, contrary to the triangles observed for pure MoS_2 [86].

4.1.5 Nanoparticle Synthesis by Reactive Gas Aggregation

During this project, we have developed techniques to synthesize nanoparticles with H_2S in the aggregation zone, as our group has previously only worked with inert gas aggregation. The subject of reactive sputtering has been investigated in several publications, e.g. [93–99], where the earliest that I could find was from 2001 by Hihara and coworkers [93]. Most of the studies use oxygen as reactive gas, but also nitrogen is quite common as in e.g. [98]. Reports of H_2S as reactive gas are seemingly scarce, but Majeski et al. produced $Cu_{2-x}S$ nanoparticles by magnetron sputtering in a nanoparticle source identical to our Nanogen50 model from Mantis Deposition Ltd. [100]. Kolipka and Vajda very recently published a book chapter dealing with the subject which I refer to for detailed information [30].

The reactive gas can lead to a more complex synthesis procedure, and can introduce a number of problems. E.g. the reactive gas can passivate the sputter target surface, making it insulating. As a consequence of the insulating surfaces, charge can build up and result in discharge arcs. Therefore, radiofrequency sputtering or pulsed DC sputtering is sometimes used for reactive conditions. Also, the particle production rate can be highly dependent on the concentration of the reactive gas, where either too little or too much can extinguish the nanoparticle production. Therefore, it can take some optimization work to find suitable synthesis conditions, which I also experienced in my work.

Morphology Changes Induced by Reactive Gas Synthesis

The available microscopy data suggests that the morphologies of nanoparticles produced by reactive gas synthesis are very different from the typically spherical shapes observed for metallic nanoparticles. E.g. Chen et al. mixed oxygen into their argon sputtering gas and thereby produced chromium oxide nanoparticles as seen in Figure 4.6, which have flat, platelet-like shapes very different from what we usually observe with metallic particles [101]. Another example is by Hihara et al. who observe seemingly porous structures of chromium oxides [93]. The common denominator is that the reactive gas aggregation form high-surface area structures, which can be explained by the fact that the reactive gas bind to the undercoordinated metal atoms, thus passivating them and preventing the formation of low-surface area structures such as spheres.

Sputtering of Pre-Sulfided Targets

Besides reactive gas aggregation, it is also possible to produce sulfided nanoparticles by sputtering an already sulfided target. The disadvantage of this synthesis

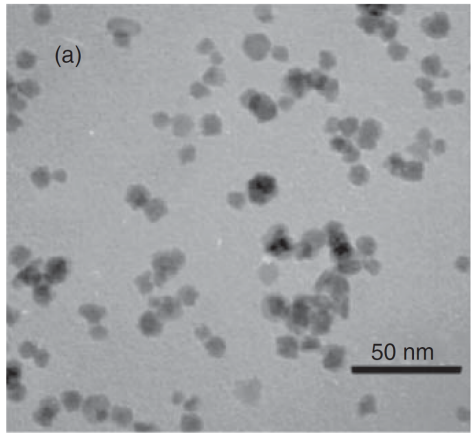

Figure 4.6: Chromium oxide nanoparticles produced by Chen et al. with a gas aggregation nanoparticle source, using reactive sputtering with a 2 % O_2/Ar ratio and deposition without mass filtering. The morphologies of the particles are quite varied, and far from the spherical shapes typically seen for metallic nanoparticles. Reproduced from [101].

technique is that it is not possible to vary the sulfur content by the H_2S gas as done in e.g. [100]. On the other hand, it is significantly less complicated to produce molybdenum sulfides in this manner. This approach was taken by the group of Richard Palmer by Cuddy et al. [102]. In a subsequent publication nanoparticles produced in this fashion are tested for the hydrogen evolution reaction and it is observed that doping the nanoparticles with Ni enhances their HER activity three-fold compared to non-doped particles [103], but they do not report any comparison with turn-over frequencies obtained on other MoS_2-systems. Nonetheless, this alternative strategy for producing Ni-Mo-S nanoparticles serves as an interesting comparison to my work.

The Need for Testing Catalytic Activity

Although some of the above reports on reactive gas aggregation investigate e.g. the magnetic properties of the produced nanoparticles, most of the studies are fundamentally focused on the synthesis procedure in itself, and only Escalera-Lopez et al. investigate catalytic properties [103]. Thus, there seem to be a knowledge gap in the utilization of nanoparticles produced by reactive gas aggregation for catalysis, which was the key motivation for my project.

4.2 Synthesis of Ni-Mo-S Nanoparticles

Having introduced the background for this research project, I now move into our own experimental results. This section presents our synthesis procedure for producing in-flight sulfided Ni-Mo-S nanoparticles by reactive gas aggregation. Appendix B contains a detailed account of the development of the synthesis procedure for interested readers.

4.2.1 Synthesis Procedure for Ni-Mo-S Nanoparticles

The synthesis was carried out in the Nanogen50 nanoparticle source from Mantis Deposition Ltd. Pure H_2S and Ar were dosed through two individual flow-controllers and mixed before introduction in front of the $Mo_{75}Ni_{25}$ sputter target. The aggregation zone was not cooled, as we experienced problems with H_2S condensing on the chamber walls at LN_2 temperatures (see Appendix B). Before each deposition, H_2S was dosed first, to asses the pressure in the aggregation zone with a pirani gauge, after which Ar was dosed and the total deposition pressure was measured. The sputter power was supplied by a DC power supply set to current-limitation.

Before an actual deposition, the mass distribution of particles in the aggregation zone was optimized. Typical parameters used for a deposition of particles with a mass of 200 kamu are listed in Table 4.1, along with parameters for metallic particles with a mass of 134 kamu. The metallic particle mass corresponds to a spherical particle diameter of 3.5 nm (assuming a density of $9.9\frac{g}{cm^3}$ – a weighted average of Mo and Ni densities), and the particles have approximately the same metal content as the in-flight sulfided Ni-Mo-S nanoparticles of 200 kamu. In general, we were interested in small particle sizes and therefore chose to have the magnetron head as close to the exit aperture as possible. A typical pre-deposition mass profile and deposition current for 200 kamu $MoNiS_x$ nanoparticles is plotted in Figure 4.7.

Table 4.1: Typical deposition conditions for Ni-Mo-S nanoparticles with a mass of 200 kamu and metallic particles with approximately the same metal content, but without sulfur (mass 134 kamu). The conditions were optimized before each deposition, and the parameters thus varied slightly between depositions

	Ar flow	H_2S flow	p_{H_2S}	p_{total}	$I_{sput.}$	$U_{sput.}$	$P_{sput.}$	LN_2 cool.
Sulfided	16 SCCM	0.2 SCCM	5.7E-3 mbar	0.109 mbar	0.04 A	267 V	11 W	No
Metallic	92 SCCM	NA	NA	0.718 mbar	0.26 A	170 V	44 W	Yes

A significant positive background current is observed in Figure 4.7, which is likely due to Ar^+ ions passing through the QMF. These ions should optimally be filtered away, but the mass filter is not designed to filter particles lighter

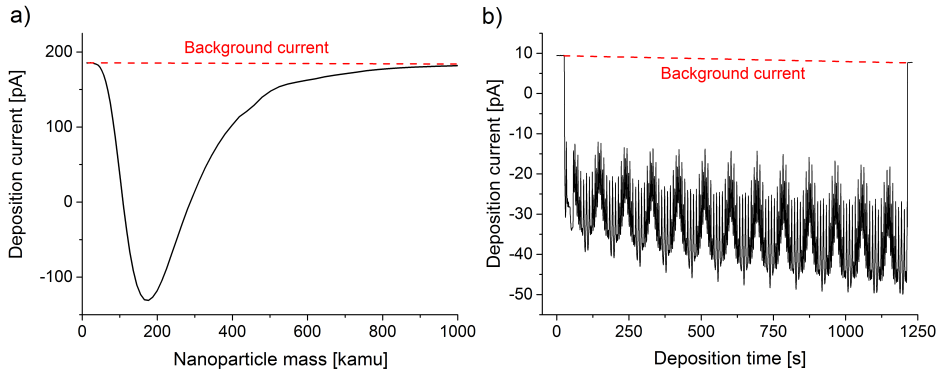

Figure 4.7: **a)** Pre-deposition mass spectrum of the particles coming out of the aggregation zone at conditions optimized for deposition of 200 kamu nanoparticles. **b)** Current measured during a deposition of nanoparticles on a sample. The oscillations are due to rastering of the nanoparticle beam to disperse the particles equally. Note that the current is reduced as compared to a), as the deposition is done through an aperture. Both spectra show a significant positive background current likely due to co-deposition of Ar^+ ions.

than 350 amu, and thus it could be a possibility that Ar^+ ions are co-deposited along with the nanoparticles. One could fear that metal/sulfur ions would also be deposited, but our electron microscopy and EDS mapping show that Mo, Ni and S is only present in nanoparticles and not dispersed on the substrate (explained more fully in section 4.3). Note that such co-deposition of species that are not captured with the mass filter would not be possible in the Nano-Beam2011 nanoparticle source, as the lateral displacement in the TOF-filter ensures that the sample is not in line-of-sight of the primary beam of nanoparticles coming out of the aggregation zone.

4.2.2 Attempts at Varying the Nanoparticle Sulfur Content

The minimum flow that could be delivered with the H_2S flow-controller was 0.1 SCCM. I found that it was only possible to run a deposition plasma by keeping the flow below 0.2 SCCM, and there was thus a very narrow range of flows accessible, consistent with the reports from [30]. Curiously, variations in the flow from 0.1 SCCM − 0.2 SCCM produces no changes in sample composition as evidenced with XPS measurements. This could be due to a saturation mechanism in the nanoparticle formation. All samples presented in the following were synthesized at a flow of 0.2 SCCM H_2S.

Earlier experiments where H_2S were dosed through a leak valve (see Appendix B) indicated that it was possible to tune the sulfur content by going to lower pressures, but these studies were not entirely systematic due to the problems of keeping a constant H_2S pressure during deposition. It is, however, an interesting

aspect of the in-flight sulfidation synthesis that the degree of sulfidation might be changed with great precision (as is done in [100]), which may not be easy in chemical synthesis procedures. For future studies it would be interesting to investigate the deposition dependence on H_2S partial pressure by e.g. dosing H_2S gas diluted in Ar through the flow-controller, and thus effectively operate at lower H_2S flows.

4.2.3 Varying Nanoparticle Mass

My primary focus in this project has been the in-flight sulfidation process in itself, and it has been beyond the scope of this work to conduct a full investigation of the effects of varying nanoparticle mass. However, I did conduct a limited set of experiments.

My general experience was that the size distributions obtainable with in-flight sulfidation were rather limited. Figure 4.8 shows two deposition spectra, the first optimized for particles at 200 kamu. The second spectrum was obtained after significant effort to move the profile towards higher masses, but still the current maximum has not moved more than ~ 100 kamu. I did some experiments depositing particles with a mass of 440 kamu, which were among the highest mass that I could deposit without extreme amounts of double mass current. The reason that I deposited 200 kamu particles with a relatively small deposition current was also to avoid double mass particles.

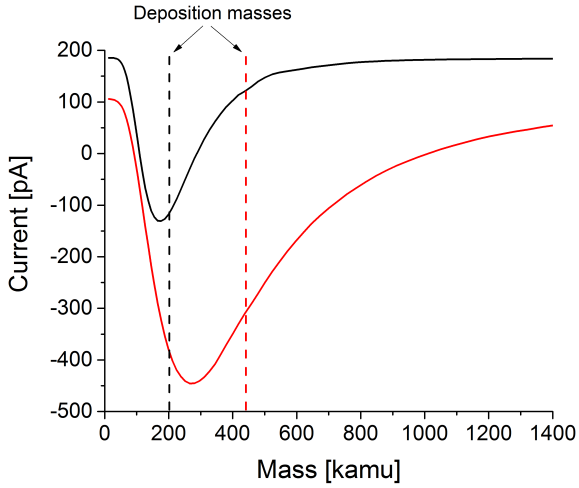

Figure 4.8: Two different nanoparticle mass profiles, where the red spectrum is shifted as much to the higher masses as possible with the current setup. The dotted lines indicate masses that I have deposited on substrates for further characterization. Note the difference in background current, which I speculate is due to different co-deposition rates of Ar^+ ions.

For further studies, it would be interesting to introduce He to the aggregation zone along with Ar to get another parameter for tuning particle sizes. It should be noted that the aggregation zone exit aperture is fixed on the Nanogen50 nanoparticle source, which also limits the parameter space for choosing different masses. For the present setup, it seems as though there is a preference for forming particles with masses in the range of $150 - 400$ kamu.

Section 4.3.2 presents characterization and further discussion of the effects of varying nanoparticle mass in the in-flight sulfidation synthesis. The 440 kamu particles were tested for HDS catalysis as presented in section 4.4.

4.2.4 Substrates and Cleaning Procedure

I used two different types of substrates for deposition of nanoparticles in this project: Microreactors for HDS catalysis tests and glassy carbon cylinders for rotating disk electrode measurements for HER testing.

The microreactors are covered with a protective plastic film when we receive them from the clean-room. This was removed before a reactor was mounted in a sample-holder and loaded into the UHV system. Here, the microreactors were sputtered for 30 min with 1 kV Ar^+ ions before deposition of nanoparticles in order to remove contaminants from the reactor area.

The glassy carbon disks were cleaned using a procedure which was established for studying Cu nanoparticles (see chapter 5, section 5.2.3 for detailed description). The method removes all metals detectable with XPS. Trace amounts of 3d and 5d metal impurities are still left, as evidenced with ISS, but since ISS is an extremely surface-sensitive technique this is almost unavoidable. Before depositing nanoparticles on the substrates, they were sputtered for 30 min with 1 kV Ar^+ ions just as the microreactors.

4.3 Characterization of Ni-Mo-S Nanoparticles

I have mainly used two techniques for nanoparticle characterization in this project: X-ray photoelectron spectroscopy (XPS) and Scanning Transmission Electron Microscopy (STEM). The following two sections describe the characterization in detail, along with analysis and discussion of the results.

4.3.1 X-ray Photoelectron Spectroscopy (XPS)

After deposition in the Nanogen50 nanoparticle source, I transferred each of the nanoparticle samples directly into the STM312 vacuum chamber for XPS analysis. Thus, every deposition was "quality checked". For a detailed XPS study, I deposited in-flight sulfided Ni-Mo-S nanoparticles on a microreactor at a target mass of 200 kamu at 50 % area coverage (assuming spherical particles and bulk MoS_2 density), or 850 $\frac{\text{ng}}{\text{cm}^2}$. This loading is higher than what we usually aim

for and results in a high fraction of overlapping particles, but it was chosen to maximize the XPS signal, especially for the small Ni signal.

Figure 4.9 shows an overview XPS spectrum obtained on this sample at a pass energy of 100 eV. The spectrum is dominated by Si and O from the substrate, but Mo and S is also clearly present. Ni is only visible through a small Ni2p feature, illustrating the importance of the high loading of nanoparticles. In some other microreactor depositions, small carbon contaminations were observed, but no other elements have been detected with XPS.

For more detailed investigations I acquired close-up scans of peaks from Mo, Ni and S with a lower pass energy of 20 eV. The Mo3d and S2s peaks overlap, so I also scanned the S2p region. In Figure 4.10 I have plotted close-up scans of three different samples: metallic Ni-Mo nanoparticles (134 kamu - same metal content as in-flight sulfided), in-flight sulfided Ni-Mo-S (200 kamu), and a single-crystalline MoS_2 sample from SPI supplies as a reference. Figure 4.10 contains a lot of information which I will break down into subsections, starting with the details of how the spectra are fitted and the underlying assumptions, and then moving on to interpretation of the data.

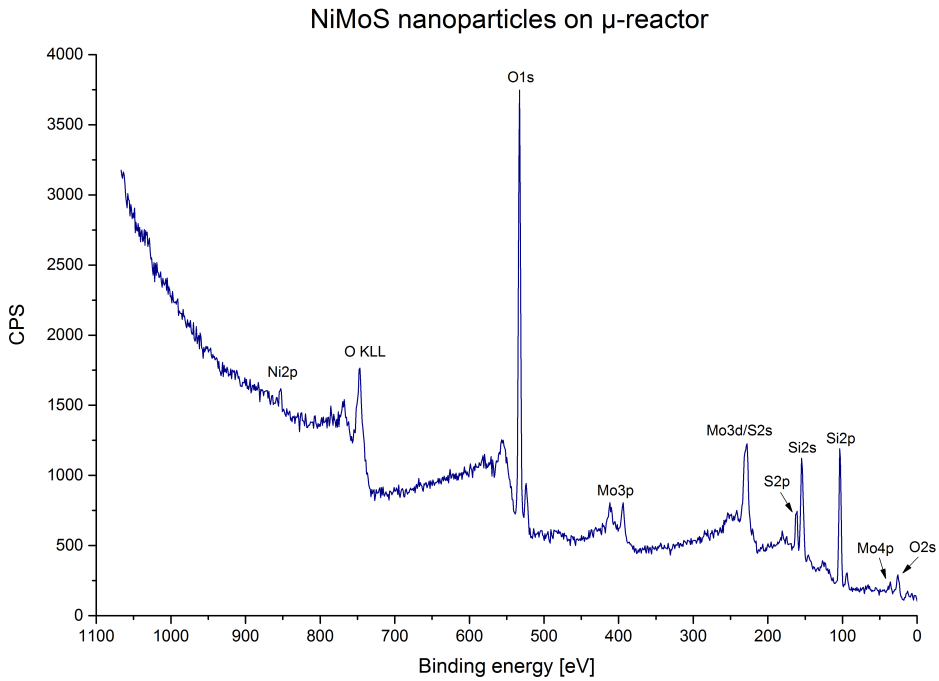

Figure 4.9: Overview X-ray photoelectron spectrum showing in-flight sulfided Ni-Mo-S nanoparticles deposited on a sputter-cleaned microreactor at a target mass of 200 kamu.

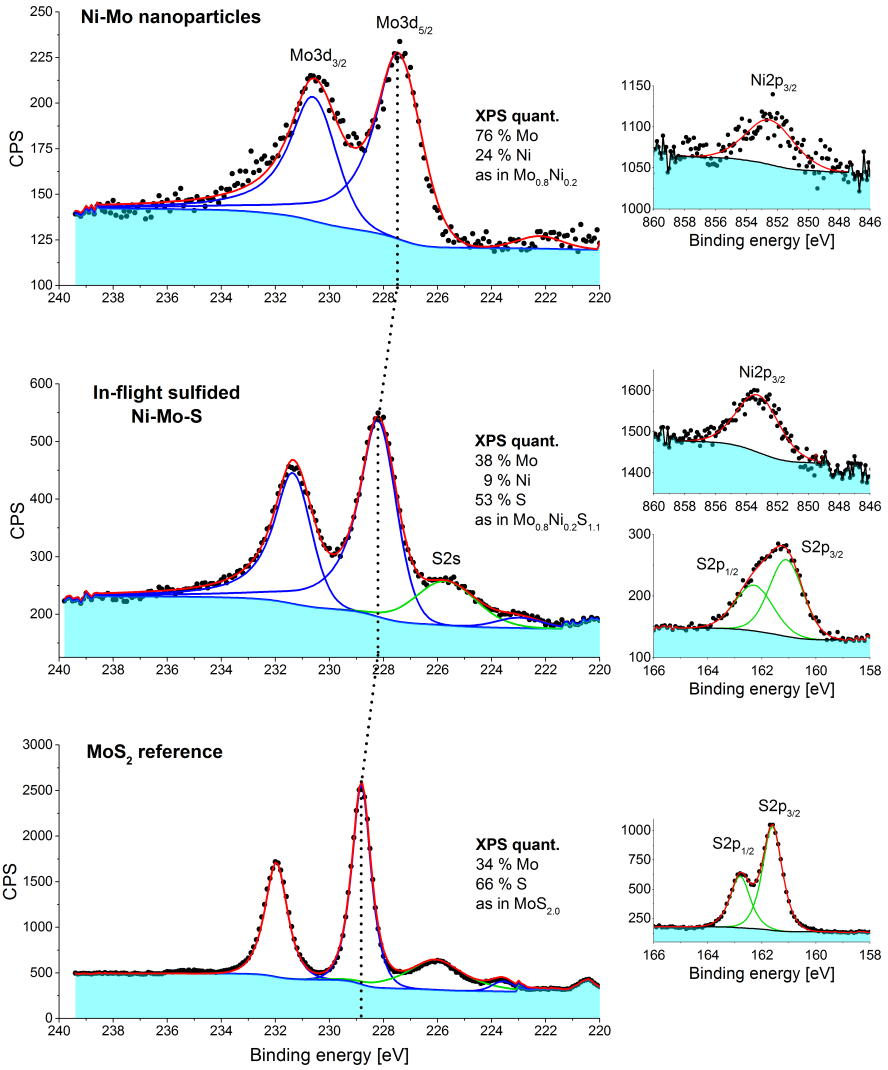

Figure 4.10: XPS spectra of metallic Ni-Mo nanoparticles, in-flight sulfided nanoparticles and a MoS_2 single crystal as a reference, showing the Mo3d region, overlapping with S2s, the Ni2p, and the S2p regions. The Mo3d peaks shift towards higher binding energies when sulfided, from $Mo3d_{5/2}$ at 227.5 eV in metallic Ni-Mo to 228.2 eV in Ni-Mo-S and 228.8 eV in MoS_2; The intermediate binding energy of Ni-Mo-S shows that it is not fully sulfided, which is also indicated by the low sulfur content seen in the quantification. The $Ni2p_{3/2}$ peak also shifts to higher binding energies in Ni-Mo-S (853.2 eV) as compared to Ni-Mo (852.5 eV). The peaks in the MoS_2 reference are more narrow due to the ordered crystal structure.

Fitting the Spectra

The raw data in Figure 4.10 is plotted as dots, whereas fits, performed in the software CasaXPS, are plotted as lines. The background is estimated with a Shirley function, where the boundaries were determined as an average of 5 data points. The area ratios between spin-orbit coupling-induced doublet peaks were fixed so that $Mo3d_{5/2}/Mo3d_{3/2}$=3/2 and $S2p_{3/2}/S2p_{1/2}$=1/2, and the distance between the two Mo3d doublets was fixed to 3.15 eV (as reported in e.g. [39,104]).

The S2s peak is difficult to fit as it is overlapping with the Mo3d peaks, which also has satellite peaks located just below S2s, contributing to a higher background that will diminish the S2s area. In order to circumvent this problem, I acquired an extended scan on the MoS_2 crystal which enabled me to fit all of the satellites (included in Appendix C), and estimate how much of the background that should be subtracted to remove the satellite contributions. In the shown fits, 5 % of the background is subtracted at the low-energy boundary, and the $Mo3d_{3/2}$ satellite arising from from $K_{\alpha 3}$ radiation from the Mg anode is included, fixed to 8% of the area and at a position 8.4 eV negative of the $Mo3d_{3/2}$ peak [39].

Whereas the MoS_2 reference has symmetric peak shapes that can be fitted with a product of a Gaussian and a Lorentzian function (80 % Lorentzian, GL(80) in CasaXPS), the metallic and in-flight sulfided particles are asymmetric. Such asymmetry is often observed in metals due to shake-up effects by excitation of the conduction electrons, and in order to capture the asymmetry in the fits, a Gaussian-Lorentzian line-shape was modified with a Doniach-Sunjic function [105] (DS(0,0)GL(30) in CasaXPS). The peaks of the metallic nanoparticles seem more asymmetric than the Ni-Mo-S as evidenced in the high-binding shoulder that is not captured by the fit.

Since SiO_2 has a low conductivity, some charging was observed in the XPS spectra on microreactors (<0.5 eV). In order to compensate for this, all spectra were shifted to a Si2p position of 103.4 eV as expected for SiO_2 [39]. In the case of the MoS_2 reference crystal, I did not have a stable reference, and I suspected charging of the sample due to the semi-conducting nature of MoS_2. Therefore, I shifted the $Mo3d_{5/2}$ to 228.8 eV which is a typically reported value for MoS_2 (see table 4.2). The measured peak position before energy correction was 229.4 eV which may be correct since monocrystalline MoS_2 has been reported to have higher binding energies than the polycrystalline phase [106]. However, since the polycrystalline phase is more relevant as a reference for the nanoparticles, I chose the shift to 228.8 eV.

Spectrum Interpretation – Peak Position and Shape

The first thing that should be noticed in Figure 4.10 is that the Mo3d peaks shift as a function of sulfidation, from Mo $3d_{5/2}$ at 227.5 eV in metallic Ni-Mo to 228.2 eV in Ni-Mo-S and 228.8 eV in MoS_2. In order to interpret these shifts, I have compiled a list of binding energies from literature for different oxidation states of Mo in Table 4.2. The in-flight sulfided particles have a $Mo3d_{5/2}$ binding

energy between metallic Mo and MoS_2. The 3d peaks also show some asymmetry, whereas the MoS_2 reference is symmetric. These facts indicate that the in-flight sulfided particles are sulfided to some degree, but still retain some metallic character. Nielsen et al. observe a similar asymmetric line shape for partially sulfided molybdenum produced in UHV by evaporation of Mo onto a Au(111) crystal in an atmosphere of H_2S at room temperature [107]. In their study, the molybdenum is subsequently fully sulfided by annealing in H_2S, which results in more symmetric peak shapes, although they still retain some asymmetry due to conduction electrons from the substrate. Since the particles are partially sulfided, it is possible that a range of different oxidation states are present, from metallic Mo(0) to sulfided Mo(IV), especially since there will be a large variation in chemical/structural environment in the non-equilibrium-shaped particles. Bruix et al. observe that Mo in edges of MoS_2 have lower binding energies than Mo in basal planes, and this could also contribute to both the low binding energies and width of the peaks relative to the reference MoS_2, since the particles are expected to expose many undercoordinated atoms.

Table 4.2: Binding energies for the Mo $3d_{5/2}$ peak for different oxidation states of Mo. Since there is some disagreement in literature, the table shows the range of values reported in [39, 104, 108–111].

Mo(0) as Mo	Mo(IV) as MoS_2	Mo(V) as MoO_xS_y	Mo(VI) as MoO_3
227.4 eV – 228.0 eV	228.7 eV – 228.9 eV	229.8 eV – 231.2 eV	232.1 eV – 233.0 eV

The Ni$2p_{3/2}$ peak also shifts to higher binding energies in Ni-Mo-S (853.2 eV) as compared to Ni-Mo (852.5 eV). Marchand et al. also observe a similar Ni$2p_{3/2}$ binding energy of 853.1 eV after sulfidizing a Ni catalyst, and they attribute this to a rather undefined NiS_x, since it is difficult to determine the exact stoichiometry [109]. For the Ni-Mo-S phase, they report a binding energy of 854.0 eV, and thus our results could indicate that the Mo and Ni sulfides in the deposited particles are segregated.

Spectrum Interpretation – Elemental Quantification

The peak areas determined by fitting were used for quantification after normalization with the relevant sensitivity factors from the element library in CasaXPS. I used the Mo$3d_{5/2}$, Ni$2p_{3/2}$, and S2p peak areas for quantification (the S2s overlap with Mo3d makes this peaks less suitable for quantification).

The results of the quantification can be seen in Figure 4.10. Firstly, it is worth noting that the ratio of Mo and Ni in the metallic particles is very close to the sputter target composition ($Mo_{75}Ni_{25}$). This is not always the case, as we have observed in e.g. sputtering of platinum-yttrium alloys, where the nanoparticle composition was significantly different than the sputter target [36]. Secondly, the

MoS_2 quantification matches the expected composition perfectly, indicating that the used sensitivity factors are adequate.

In case of the in-flight sulfided Ni-Mo-S nanoparticles the quantification indicates a stoichiometry of $Mo_{0.8}Ni_{0.2}S_{1.1}$, showing clearly that the particles are not fully sulfided. This is in agreement with the binding energies and peak shapes, as discussed earlier.

Effect of Air Exposure

The previous characterization took place in UHV, but for catalytic testing the particles are exposed to air during transfer. In order to investigate the effect of ambient conditions, I exposed the particles to air for one hour in the load-lock before pumping the system down to UHV again for another XPS measurement. The results can be seen in Figure 4.11 (the as-deposited particle spectrum is identical to the one in Figure 4.10).

The air-exposure affects the spectrum in two ways: Firstly, a shoulder arises on the high-binding side of the $Mo3d_{3/2}$ peak; secondly, the $Mo3d_{5/2}$ moves 0.4 eV towards higher binding energies. I accounted for the peak shoulder in the fit by introducing a second pair of Mo3d peaks (locked at an area ratio of 3:2 and an inter-peak distance of 3.15 eV). The binding energy of the new Mo $3d_{5/2}$ peak is 231.8 eV.

A plausible explanation for the observed changes is that the air-exposure oxidizes the unsaturated bonds of Mo atoms. Thus, the semi-sulfided as-deposited Ni-Mo-S nanoparticles, which contained an intermediate between metallic and sulfided Mo (oxidation states IV or below), are oxidized leading to a mixture between sulfided and oxidized Mo (oxidation states IV, V, and VI). This also explains the shift in the primary Mo $3d_{5/2}$ towards higher binding energies: as the undersulfided "metal-like" Mo atoms are oxidized, the remaining atoms are in the Mo(IV) state. Therefore, I chose to fit the Mo(IV) peak with the same, symmetric line shape as used for the reference MoS_2 crystal (GL(80) in CasaXPS). After air-exposure, 73 % of the Mo is in the Mo(IV) state, and 27 % in Mo(V+VI), showing that the majority of the particle remains sulfided.

The peak positions of the new set of Mo3d peaks indicates a mixture between MoO_xS_y and MoO_3, which also seems intuitively reasonable. It would be possible to fit the V and VI states seperately, but I chose to stay with one set of peaks as this explains the qualitative trends sufficiently without introducing too many degrees of freedom to the fit.

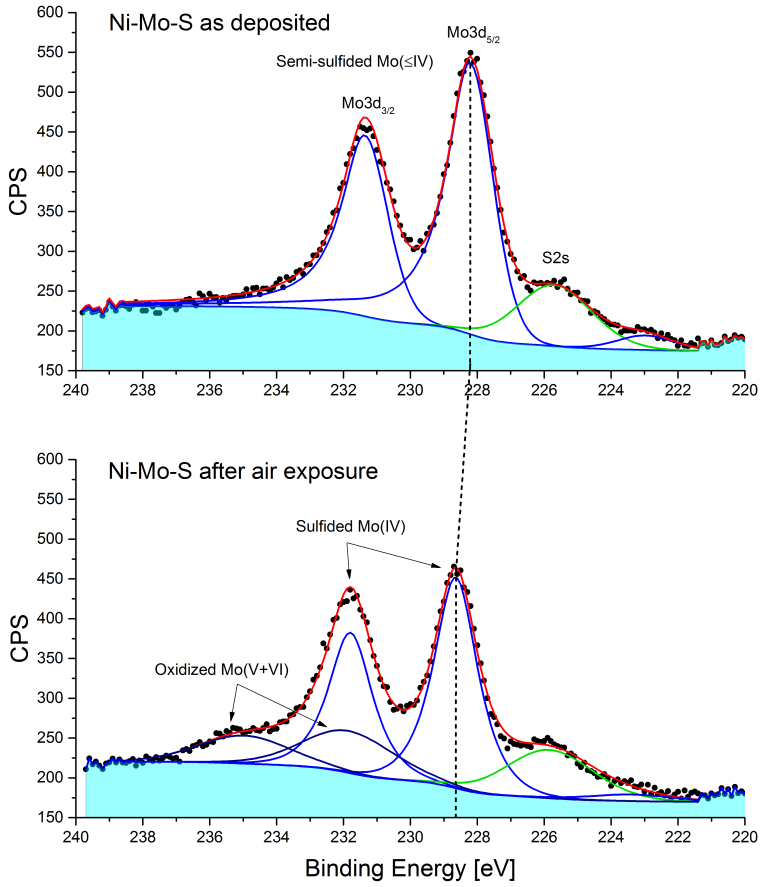

Figure 4.11: X-ray photoelectron spectra of the Mo3d/S 2s region, showing the effect of exposing the as-deposited Ni-Mo-S nanoparticles to air. While the position of the $Mo3d_{5/2}$ peak in the as-deposited nanoparticles has a binding energy of 228.2 eV, slightly too low for Mo(IV) as in MoS_2, the air-exposed particles form two distinct sets of Mo3d peaks corresponding to Mo(IV) at 228.6 eV and Mo(V+VI) at 231.8 eV.

4.3.2 Scanning Transmission Electron Microscopy (STEM)

In order to investigate the structure of the particles, we imaged them with STEM using a probe-corrected FEI Titan Analytical 80-300ST TEM located at DTU's Center for Electron Nanoscopy (CEN). The images were acquired in collaboration with Christian Elkjær from Haldor Topsøe A/S, who operated the microscope. All images were obtained at 300 kV acceleration voltage in high-angle annular dark-field (HAADF) mode which means that particles will appear light on a dark background.

I prepared samples for STEM by depositing particles on TEM grids of two types. For imaging on a substrate similar to the micro-reactors, we used SiO_2 TEM-grids of 20 nm in thickness. For high-resolution imaging it is advantageous with a very low background from the substrate, especially since molybdenum sulfides form flat, layered structures. Therefore, we modified standard lacey carbon/Cu grids by dropcasting graphene agglomerates onto them, before depositing nanoparticles in the nanoparticle source. In some places, there will be single/few graphene layers protruding, which can then be used for low-background high-resolution imaging. Figure 4.12 a) shows a graphene agglomerate on the lacey carbon, and b) shows a higher magnification of metallic Ni-Mo nanoparticles on an area where discrete graphene layers can be seen in the background, with the characteristic terminations of a hexagonal lattice. Note that the particles were exposed to air in the transfer between deposition and microscope; the exposure time was typically on the order of an hour, thus resembling the exposure between deposition and catalytic tests.

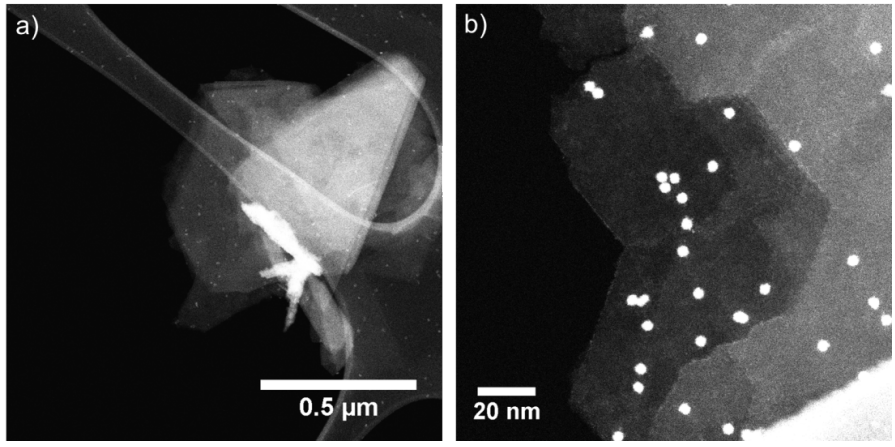

Figure 4.12: **a)** Low-magnification image of a lacey-carbon TEM grid on which a deposited rolled-up graphene ball can be seen. Some areas expose thin graphene layers which can be used for high-resolution imaging. **b)** Higher magnification image of metallic Ni-Mo nanoparticles on an area of thin graphene which forms discrete layers and have characteristic hexagonal terminations.

Structure of In-Flight Sulfided Ni-Mo-S Nanoparticle

Figure 4.13 a) shows a deposition of Ni-Mo-S nanoparticles, deposited at a target mass of 200 kamu. Whereas e.g. metallic particles are typically uniformly spherical (see e.g. Figure 4.12 b), the shape of the in-flight sulfided particles vary greatly, although there seems to be a preference towards platelet-like structures. This is consistent with other observations on reactive gas aggregation of nanoparticles, reported by e.g. [100, 101].

Figure 4.13 b) shows a high-magnification image of two nanoparticles where the individual atomic columns are clearly visible. There are large monocrystalline areas in each particle, and a Fourier transform of the image (inset) reveals a clear hexagonal lattice with a periodicity of 2.7 Å, corresponding to the $MoS_2(100)$ periodicity [91]. Since the lattices in the two particles are oriented differently, there are 12 spots in the Fourier transform of which 6 originate from each particle. Curiously, one of the particles is triangular, as also observed in e.g. [83], but it should be noted that this was not characteristic of the other particles. All of the above structural information indicate that the particles contain a MoS_2-like phase. The particles are, however, not perfectly crystalline and e.g. the particle edges seem to be rather disordered. It should be noted that the particles were not completely stable under the electron beam.

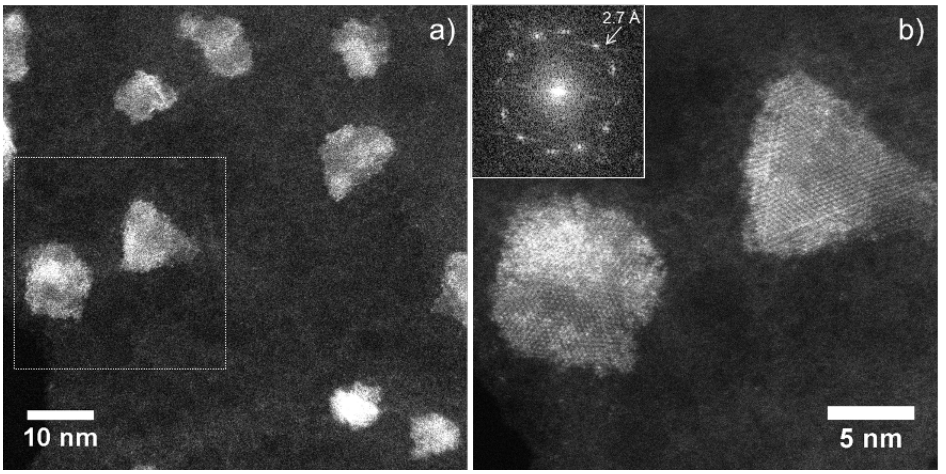

Figure 4.13: **a)** Ni-Mo-S nanoparticles on a graphene substrate deposited with a target mass of 200 kamu. **b)** High-magnification image of the two nanoparticles marked in **a)**, revealing the hexagonal structure expected from the basal planes in molybdenum disulfide. The inset shows the Fourier transform of the image, revealing a periodicity of 2.7 Å, corresponding to $MoS_2(100)$.

Although most of the nanoparticles are lying flat on the substrate, we also observed layers of Ni-Mo-S standing perpendicular on the substrate as seen in Figure 4.14 a) which shows a particle that seems to have grown in two direc-

tions simultaneously or consist of two agglomerated platelet nanoparticles. The distance between the two layers is 6.8 Å, which is consistent with the inter-plane distance (001) in MoS_2 (see e.g. [92]). The interplane periodicity from the upright-standing layers are visible in the Fourier transform in Figure 4.14 b), along with the features from the in-plane MoS_2(100) periodicities. A feature at a 1.7 Å period occurs as well, corresponding to MoS_2 (110) planes [91].

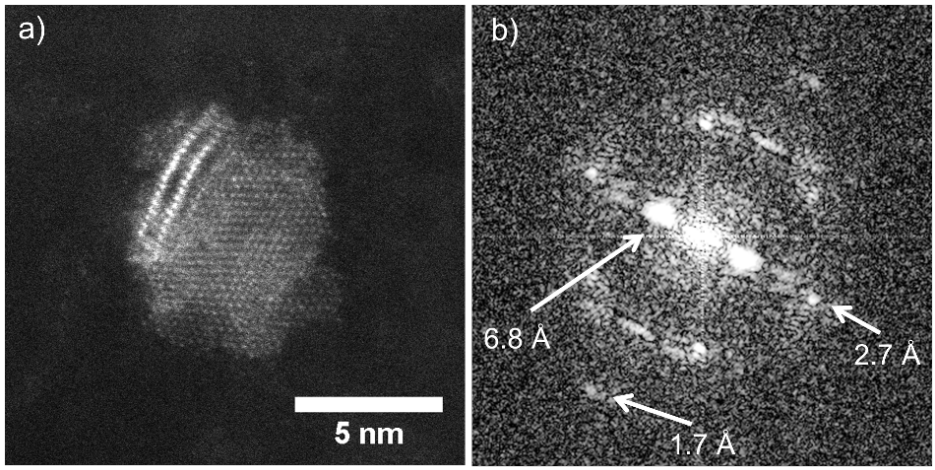

Figure 4.14: **a)** Ni-Mo-S nanoparticle deposited with a target mass of 200 kamu, showing both the basal-plane molybdenum-sulfide structure as well as two up-right standing layers, showing the inter-plane distance. **b)** Fourier transform of a), revealing two distinct periodicities corresponding to in-plane (100) and (110) as well as inter-plane (001) MoS_2 crystal distances.

Size Distributions from STEM

When depositing mass-selected nanoparticles we have established a practice of always using TEM to verify the size-distribution of the particles. TEM projects 3-D structures to a 2-D image, but since most metallic nanoparticles have spherical shapes, the projected area of a particle is a good measure of its volume, and, assuming a constant density, thereby its mass. Typically, we calculate the average diameter of the nanoparticle instead of reporting its projected area, as this is a more intuitive quantity.

In the case of the in-flight sulfided Ni-Mo-S nanoparticles, however, the complicated morphologies introduced several problems: First of all, the particles are thin, and thus give low contrast, which necessitates the use of more drastic image processing for particle detection. Secondly, the particles are not spherical, and thus their projected area is not a good measure of their volume.

Using the software ImageJ, the particle circumferences were detected by applying a band-pass filter to the images by Fourier transforming it, masking out

features with sizes between 1.5 nm and 30 nm, and then performing a reverse Fourier transform. I then used an algorithm developed by Li and co-workers [112] to detect the particles and ImageJ's "analyze particles" feature to measure particle sizes. Some noise was detected as particles with diameters from $0 - 2$ nm; these were filtered out.

For comparison, I deposited metallic Ni-Mo particles at a mass of 134 kamu, having similar metal content as the in-flight sulfided nanoparticles. Due to problems in getting sulfur-free depositions in the Nanogen50 nanoparticle source at the time, we used the Nano-Beam 2011 source for producing these particles, which could result in a slightly different size distribution due to the different mass fil-

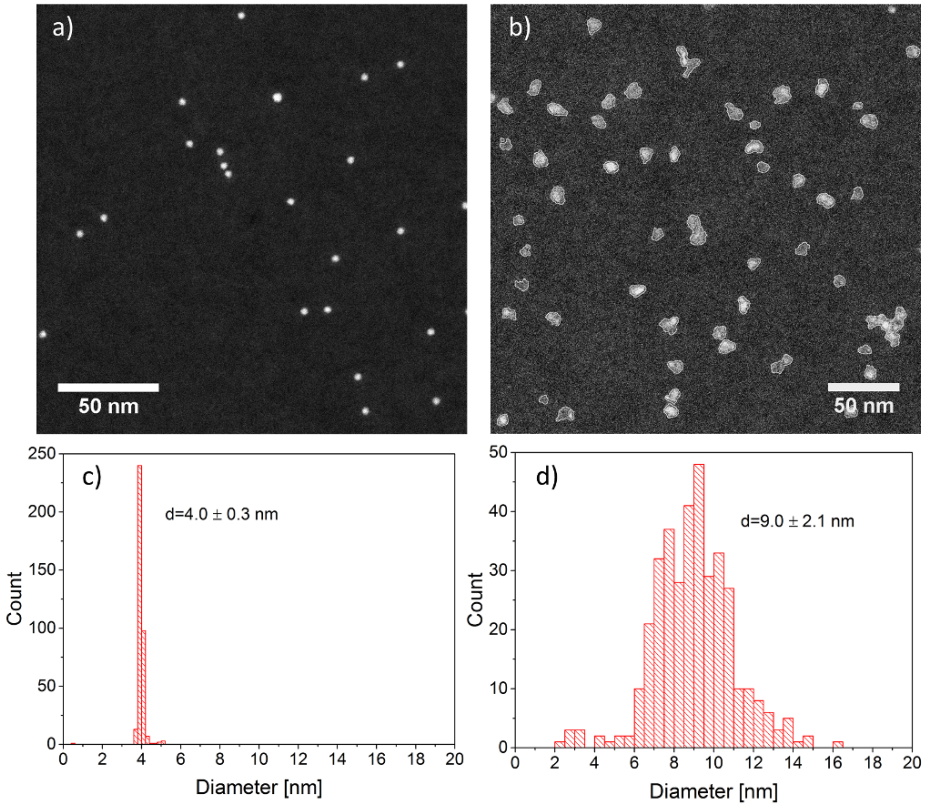

Figure 4.15: **a)** STEM image of metallic Ni-Mo nanoparticles with a mass of 134 kamu (same amount of metal as in 200 kamu in-flight sulfided particles) deposited with the Nano-Beam 2011 nanoparticle source on a SiO_2 TEM grid. **b)** In-flight sulfided Ni-Mo-S nanoparticles, deposited at a target mass of 200 kamu on a SiO_2 TEM grid. The nanoparticle circumferences used in the size-distribution are marked in white. **c)** Size-distribution of the metallic particles. **d)** Size-distribution of the in-flight sulfided Ni-Mo-S nanoparticles. A Gaussian was fitted to both distributions resulting in the reported average diameters and standard deviations.

ters. However, this difference should be small compared to the difference betwen metallic and in-flight sulfided particles. For particle size detection in ImageJ, I used the same methodology as for the in-flight sulfided particles, but due to the much higher contrast, the band-pass filter could be replaced with a simple mean filter with a radius of 0.4 nm.

Figure 4.15 shows representative STEM images of a) metallic Ni-Mo nanoparticles with a mass of 134 kamu and b) In-flight sulfided Ni-Mo-S nanoparticles, with a target mass of 200 kamu, both on SiO_2 TEM grids. The corresponding size-distributions are plotted in c) and d), where the projected area is converted to an average diameter. There is a vast difference between the two distributions, both in average size and spread of the distribution. When fitted with a gaussian, the metallic nanoparticles have a narrow distribution around 4.0 nm with a standard deviation of 0.3 nm, whereas the in-flight sulfided particles are distributed at 9.0 ± 2.1 nm. Some of this spread in sizes can be explained by the large variations in morphologies, and the fact that the diameter of a "2D" platelet structure is proportional to the square-root of its volume, whereas the diameter of a sphere is proportional to the third root of its volume. This means that an identical spread in mass (and thereby volume) would be translated into a larger variation in diameter for a platelet than a sphere. But in order to conduct a more accurate analysis, I conducted a mass-thickness-weighted particle size distribution.

Mass-Thickness-Weighted Particle Size Distribution

The contrast in an STEM image is formed by mass-thickness differences in the sample. Therefore, it is possible to asses the volume of the nanoparticles by making a size-distribution that is weighted with the integrated pixel density inside the particles. The SiO_2 TEM grids are well suited for this purpose, as they give a very homogeneous background contrast. I created an algorithm for making a mass-thickness-weighted particle size distribution in the following steps:

- Particle circumferences were obtained by the method described in the previous section (Bandpass-filter, thresholding with Li algorithm).
- The mean pixel intensity in each particle was detected in the original images, using ImageJ's "analyze particles" function.
- The background contrast from the substrate was subtracted from the mean pixel intensity of each particle.
- The mean pixel intensity was normalized by the intensity of a single-layer Ni-Mo-S nanoparticle, which was assumed to be 6.8 nm thick (the periodicity found by high-resolution STEM to be the interlayer distance).
- The normalized mean particle thickness was multiplied with the particle area to find the particle volume.

The resulting volume distribution is presented in Figure 4.16. It is clear that the histogram is divided into several distinct peaks, and that the peak volumes are integer multiples of the first peak. If the first peak around 53 nm^3 is assumed to correspond to 200 kamu, it would give a particle density of 6.27 $\frac{g}{cm^3}$, which is not far away from the bulk density of MoS_2, which is 5.06 $\frac{g}{cm^3}$. Considering the uncertainties that are undoubtedly introduced in the assessment of the particle volumes, it seems reasonable to assume that the first peak is thus single mass/single charge particles with a mass of 200 kamu. A plausible explanation for the other peaks is that particles with $\frac{2m}{2q}$, $\frac{3m}{3q}$, and $\frac{4m}{4q}$ have been codeposited along with the single charge/single mass particles. Integration of each peaks show that the particles are distributed so that 40 % is $\frac{1m}{1q}$, 35 % is $\frac{2m}{2q}$, 16 % is $\frac{3m}{3q}$, and 10 % is $\frac{\geq 4m}{\geq 4q}$.

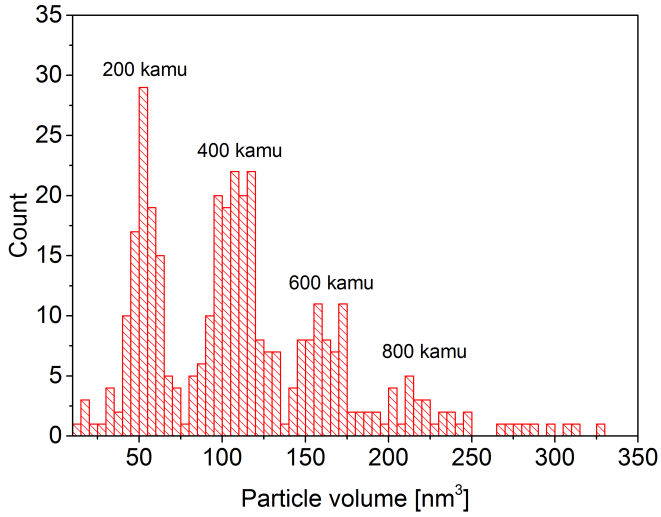

Figure 4.16: Volume distribution of in-flight sulfided Ni-Mo-S nanoparticles, deposited at a target mass of 200 kamu on a SiO_2 TEM grid. The histogram is divided into distinct peaks corresponding to particles with $\frac{2m}{2q}$, $\frac{3m}{3q}$, and $\frac{4m}{4q}$.

In our group, have never observed so large quantities of multiply charged particles before in any nanoparticle system. I speculate that the reason that the sulfide nanoparticles can carry more charge is because they are much more conducting in-plane than out of plane [88]. If the particles consist of agglomerates of platelet nanoparticles of the primary mass, and that the agglomerates are insulated from each other due to the poor out-of-plane conductivity, it would perhaps be possible to carry multiple charge. It should also be noted that the aggregation zone mass-distributions (as e.g. Figure 4.7) are broader than usually observed for metallic particles, so that the currents of particles with double, triple and quadruple mass are relatively large.

Effect of Sulfidation (STEM)

In some of the catalytic testing for HDS, we re-sulfided the in-flight sulfided Ni-Mo-S nanoparticles in a microreactor at 1000 mbar of 10 % H_2S/90 % H_2 at 350 °C for an hour. The idea behind this treatment was to resulfide the oxide formed after air-exposure, but that the particles should retain their high-surface-area shapes obtained by in-flight sulfidation. In order to verify this, we deposited 200 kamu Ni-Mo-S nanoparticles on SiO_2 TEM grids. We simulated the microreactor-sulfidation in a tube furnace and imaged particles with STEM both before and after sulfidation. The results are presented in Figure 4.17.

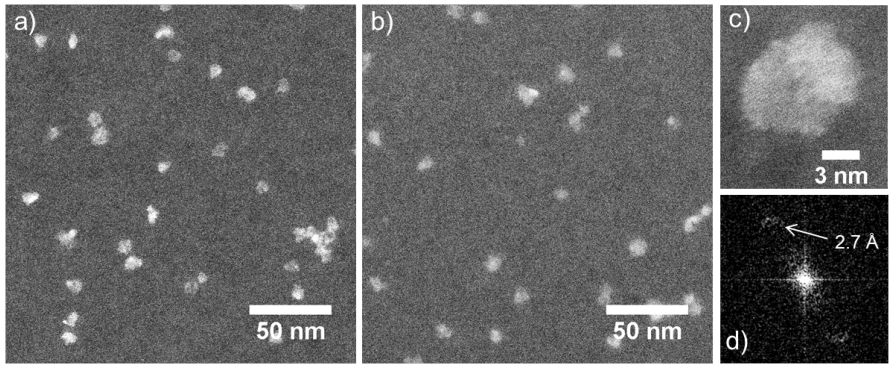

Figure 4.17: Effect of re-sulfidizing in-flight sulfided Ni-Mo-S nanoparticles. **a)** in-flight sulfided Ni-Mo-S deposited on a SiO_2 TEM grid, **b)** particles from the same deposition after re-sulfidation in a tube furnace; the particle morphology is retained through the sulfidation. **c)** a high-resolution image of one of the particles from b), displaying a MoS_2 (100) periodicity as evidenced in the Fourier transform in **d)**.

The STEM overview images in Figure 4.17 suggest that the particles retain their shapes during sulfidation. High-resolution microscopy was difficult due to the thick SiO_2 which create a significant background, but as shown in 4.17 c) and d) the characteristic MoS_2 (100) periodicity of 2.7 Å can be observed, confirming that the MoS_2 phase is still present, as would also be expected after sulfidation. We thus conclude that the re-sulfidation treatment does not alter the structure of the in-flight sulfided Ni-Mo-S nanoparticles significantly.

Elemental Mapping with Energy-Dispersive X-Ray Spectroscopy (EDX)

Microscopy with STEM has the distinct advantage that it is possible to correlate EDX signal and sample position, thus creating an elemental map of a sample. In this project, it was interesting to acquire such maps in order to image the location of Mo, Ni and S in the nanoparticles. The presence of MoS_2-phase particles had already been indicated by the previous structural investigations, so especially the location of the Ni promoter was interesting. As mentioned in the introduction, the promoter atoms are located on the edges of Ni-Mo-S nanoparticles [86, 91].

The EDX spectra were acquired at the FEI Talos microscope at Aarhus University operated at 200 kV in STEM mode by Christian Elkjær. The microscope is equipped with the chemiSTEM EDX detector system which allows for fast acquisition of elemental maps. Typical acquisition times were 5-10 minutes for the maps shown in this work. Maps are plotted as peak intensity after an average filtering in order to smooth the signal. No other postprocessing was performed. The sample presented here is Ni-Mo-S nanoparticles on a Cu/lacey carbon/graphene TEM grid, deposited at a target mass of 200 kamu.

Before creating an elemental map, we summed an EDX spectrum over a $\sim$ 100 nm $\times$ 100 nm area of the sample as seen in Figure 4.18. The most intense Mo and S lines ($Mo_{L\alpha}$ and $S_{K\alpha}$) overlap, which complicates EDX mapping. If a peak deconvolution is performed, a rough quantification indicates a S/(Mo+Ni) ratio of 1.7. This is 50 % higher than observed with XPS measurements, but also measured on a small area with high uncertainty.

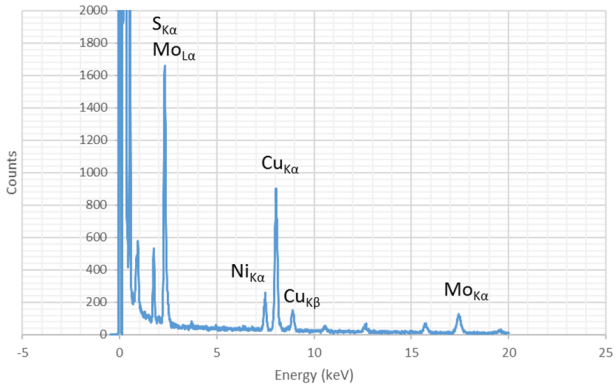

Figure 4.18: EDX spectrum summed over a $\sim$ 100 nm $\times$ 100 nm area of Ni-Mo-S nanoparticles on a Cu/lacey carbon/graphene TEM grid. The $Mo_{L\alpha}$ and $S_{K\alpha}$ peaks overlap, making individual EDX mapping of these elements difficult. The $Cu_{K\alpha}$ signal comes from the TEM grid.

After acquiring an average spectrum, a map of the chemical composition was recorded as shown in Figure 4.19. Since the Mo and S peaks overlap, the map of these elements are very similar, and the S+Ni map in the bottom of the figure is thus similar to a Mo+Ni map. Two main points can be drawn from the figure: 1) The Ni is present only in the particles together with Mo, and there is no indication of deposition of seperate NiS_x nanoparticles 2) The Ni seems to be relatively homogeneously distributed in the particles. There are, however, variations in the Ni content across the particles and no clear indications of Ni being predominantly on the edges of molybdenum sulfide platelets. XPS indicated the formation of a NiS_x phase and the EDX measurements cannot reject this. It may thus be that the particles consist of MoS_2 decorated with small NiS_x, rather than a Ni-Mo-S structure with Ni-promoters at the particle edges.

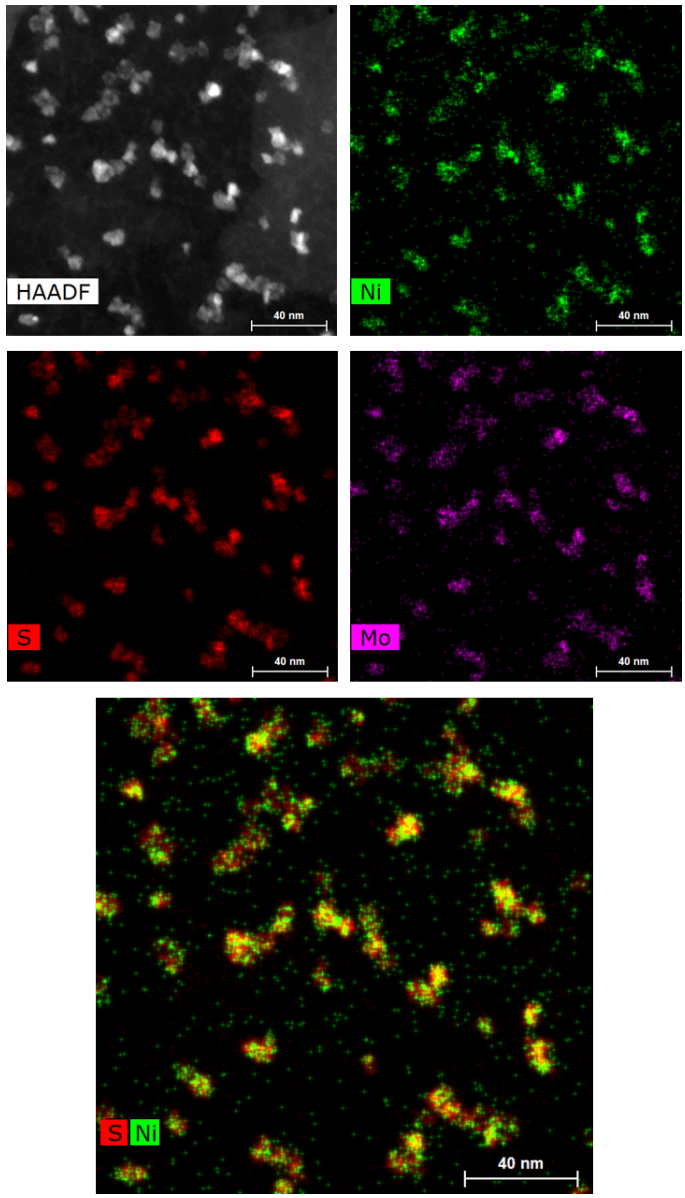

Figure 4.19: Elemental maps of Ni, S, and Mo obtained on Ni-Mo-S nanoparticles, deposited at a target mass of 200 kamu, as shown in the HAADF image. The Mo and S EDX peaks overlap, making the S and Mo maps very similar. In the S+Ni map, it can be seen that Ni is present in the particles along with the Mo and S (the Ni signal on the substrate is noise).

Structure Dependence on Nanoparticle Mass

Whereas up-right sulfide layers were relatively rare on the 200 kamu samples, electron microscopy on 440 kamu revealed a completely different morphology with most particles exposing up-right sulfide layers. One example can be seen in Figure 4.20, where a Fourier transform of a high-resolution image reveals both in-plane (100) and inter-plane lattice (001) distances in a representative particle.

The difference in particle structure could be due to the fact that the mass-profile obtained before deposition had its minimum at $\sim$ 280 kamu, whereas the deposition was done at 440 kamu. It may be that platelets are formed at $\sim$ 280 kamu, and that the higher masses are agglomerates of these platelets, but there could also be other factors changing the morphology by depositing 440 kamu instead of 200 kamu.

Regardless of the reason to the changed morphology, the upright-standing layers are highly interesting, as these might protrude and thereby provide reactive sites that could access the sulfur which is difficult to access in the HDS of DBT, thus circumventing the steric hinderance effects.

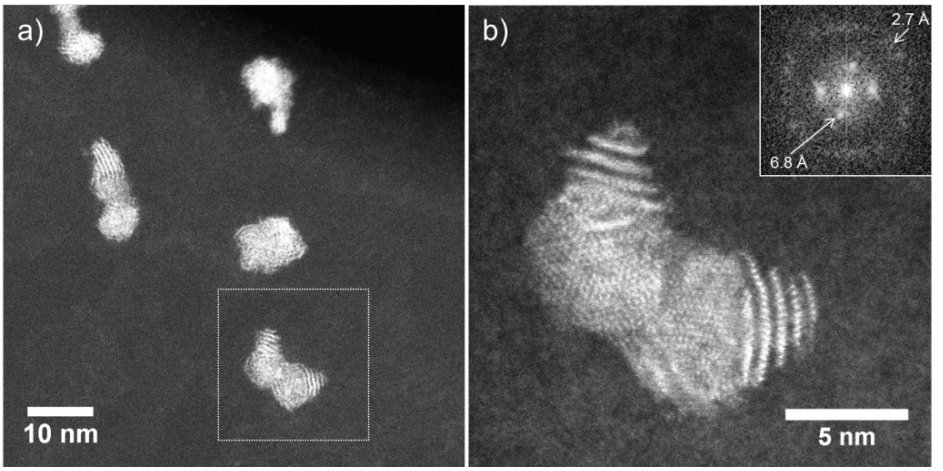

Figure 4.20: **a)** Ni-Mo-S nanoparticles on a graphene substrate deposited with a target mass of 440 kamu. **b)** High-magnification image of a nanoparticle marked in **a)**, exposing both basal planes lying flat on the substrate and perpendicular to it. The Fourier transform in the inset confirms the in-plane (100) and inter-plane (001) lattice distances expected for MoS_2.

4.3.3 Summary of XPS and STEM Characterization

After the detailed presentation of XPS and STEM data, a brief summary of the knowledge gained from characterization will be presented.

The most important conclusion is that the in-flight sulfided Ni-Mo-S nanoparticles consist of a MoS_2-like phase, but that they retain some of their metallic character due to insufficient sulfidation. This is based on XPS data, showing a particle stoichiometry of $Mo_{0.8}Ni_{0.2}S_{1.1}$ as well as a chemical shift in the Mo3d peaks that supports a partial sulfidation.

After exposure to air, XPS showed that the Mo in the Ni-Mo-S nanoparticles was present in two different chemical states: 73 % in the Mo(IV) state (as in MoS_2), and 27 % in Mo(V+VI) state (as in MoO_xS_y or MoO_3), showing that the majority of the particle remains sulfided. High-resolution STEM images after air-exposure also showed the presence of a MoS_2 phase with the expected lattice periodicities, but also revealed highly disordered areas on the particles which may be due to the insufficient sulfidation.

Whereas metallic Ni-Mo nanoparticles have uniformly spherical shapes, the in-flight sulfided Ni-Mo-S nanoparticles deposited with a target mass of 200 kamu form platelet structures. The platelets average projected diameters of a 9.0 nm with a standard deviation of 2.1 nm. This is a large spread in size, both due to the growth mechanism of the Ni-Mo-S particles, but also to the fact that multiple mass/charge ratios, which cannot be distinguished in the quadropole mass filter are co-deposited. A mass-thickness-weighted size-distributions revealed at least four deposited mass/charge ratios distributed so that 40 % is $\frac{1m}{1q}$, 35 % is $\frac{2m}{2q}$, 16 % is $\frac{3m}{3q}$, and 10 % is $\frac{\geq 4m}{\geq 4q}$.

Maps of the elemental composition of a sample were obtained with spatially resolved EDX during STEM, showing that Mo, Ni and S was relatively homogeneously distributed in the deposited nanoparticles. However, XPS indicate that the Ni may not be incorporated in a MoNiS structure, but rather be present as a seperate NiS_x phase.

Post-sulfidizing in-flight sulfided Ni-Mo-S nanoparticles at 1000 mbar of 10 % H_2S/90 % H_2 at 350 °C did not induce significant structural changes to the particles, indicating that they can retain their shapes during activation for HDS in microreactors.

Finally, varying the nanoparticle mass to 440 kamu show that it is possible to obtain particle structures consisting of agglomerated, up-right layers of Ni-Mo-S, instead of the predominantly flat platelets at 200 kamu.

4.4 Catalytic Tests for HDS and HER

Having presented the synthesis technique and characterization of the in-flight sulfided Ni-Mo-S nanoparticles, I will now present the results of the catalytic tests for HDS and HER.

The HDS measurements were done by Ann-Louise Christoffersen, who has developed a setup that can measure catalytic HDS activity in microreactors. The catalytic measurements take place in gas-phase, but since DBT is solid at room temperature it has been very challenging to develop a microreactor system without technical problems such as clogging of capillaries, condensation of reactants/products etc. Therefore I cannot report all experimental details, but refer to Ann-Louise Christoffersen's Ph.D.-thesis, which will be published shortly after mine, for more detailed discussion. I will present a short summary here, focussing on the results.

After the HDS results, a brief overview is given of the HER testing which was performed by Jakob Kibsgaard and Jonas Bertelsen.

4.4.1 Hydrodesulfurization (HDS)

The HDS test setup has not been calibrated for the reactant/product gasses, and we can thus not measure absolute reactivity of the reactors in e.g. turn-over frequency. Instead, we focus on comparisons between different samples, to asses their relative activities.

Due to the technical difficulties, we have only reliably measured three samples at the time of writing, one 440 kamu Ni-Mo-S reactor and two metallic Ni-Mo 134 kamu reactors. This is, however, enough to give a clear indication of an increased activity of in-flight sulfided nanoparticles.

Ideally, we would have liked to compare the activity of in-flight sulfided Ni-Mo-S particles with masses 200 kamu and 440 kamu to metallic MoiNi particles of 134 kamu, post-sulfided in the microreactors to provide a benchmark for Mo-NiS particles produced without in-flight sulfidation. Also, it is necessary with additional measurements before any firm conclusions can be made.

Microreactor Deposition

The Ni-Mo-S nanoparticles with a target mass of 440 kamu were deposited in a sputter-cleaned microreactor at a total mass loading of 107 ng; Metallic Ni-Mo nanoparticles of 134 kamu were deposited at a mass loading of 72 ng. As earlier reported, XPS quantification indicated a stoichiometry of $Mo_{0.8}Ni_{0.2}S_{1.1}$ for the in-flight sulfided particles, which would lead to a total metal loading of ~ 75 ng in these samples; thus the total metal loading is very similar for in-flight sulfided and metallic particle depositions. The microreactors were characterized with XPS to ensure the quality of deposition.

Catalytic Test Procedure

After deposition and characterization, the microreactor samples were taken out of vacuum and directly to bonding, typically with ~ 1 hour of air exposure before bonding. When a reactor is bonded, it is only exposed to the 236 nL of air that is trapped in the reactor volume, and thus the majority of air-induced changes to the catalyst are expected to happen between deposition and bonding.

After bonding, the microreactors were mounted in the test setup which allowed us to dose reactant gases, vary the temperature of the microreactor, and measure the products in a time-of-flight mass spectrometer (TOF-MS). Since DBT is solid at room temperature, it was dosed by heating DBT pellets to 110 °C in a "DBT source" while dosing He gas at a flow of 2 $\frac{\text{mL}}{\text{min}}$ through the DBT source and into the microreactor as shown in Figure 4.21. At this temperature, the resulting DBT vapour pressure in the reactor volume is ~ 0.4 mbar. Through the other microreator inlet, hydrogen was dosed at a flow of 1 $\frac{\text{mL}}{\text{min}}$. As explained in Section 2.4.3, the gases from the two inlets are mixed in the meander structure on the microreactor, and the pressure in the reactor is set by the pressure-controller at the bypass channel, in this case to 800 mbar. The products from the reactor volume then enter the TOF mass spectrometer through a capillary.

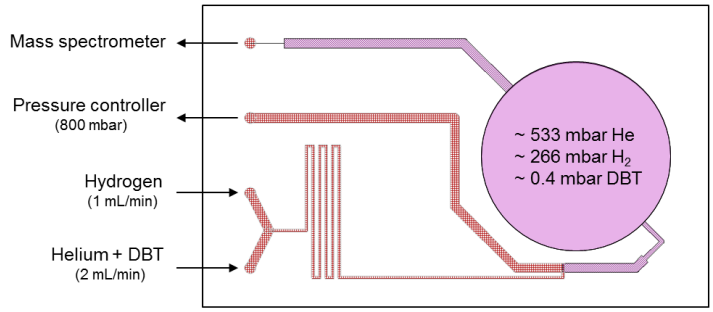

Figure 4.21: Schematic overview of the catalytic tests for HDS perfomed in a microreactor.

Each of the compounds entering the TOF-MS will result in a number of peaks in the mass spectrum (the cracking pattern). The area of these peaks is proportional to the concentration of the respective gas in the reactor volume, and thus the reaction products could be detected in real-time by the integrated area of a peak from each compound as a function of time.

In a catalytic activity measurement, the reactor temperature was increased in steps of 15 °C every half hour, ramping from 170 °C to 380 °C and down again. Normally, the temperature of the reactor would be measured by the resistance temperature detector (RTD) evaporated on the backside of the microreactor, but we experienced problems due to fabrication errors of the evaporated Pt that constitute the RTDs. Therefore, we measured temperatures with a K-type thermocouple mounted directly on top of the reactor volume.

Result of Catalytic Tests

Figure 4.22 a) shows the raw integrated peak areas measured over time as the temperature is varied on the 440 kamu Ni-Mo-S nanoparticle deposition.

Although some conversion takes place in the high-temperature range of the ramp, as evidenced by the small signal of biphenyl, the overall activity of this reactor was not impressive. This indicated that the oxidation induced by air exposure between deposition and bonding had deactivated the particles, and they were therefore re-sulfided in the microreactor at 350 °C in 10 % H_2S/90 % H_2 at 1000 mbar for an hour before a second temperature ramp. As evidenced in Figure 4.22 b), the reactivity of the particles was significantly increased by this treatment.

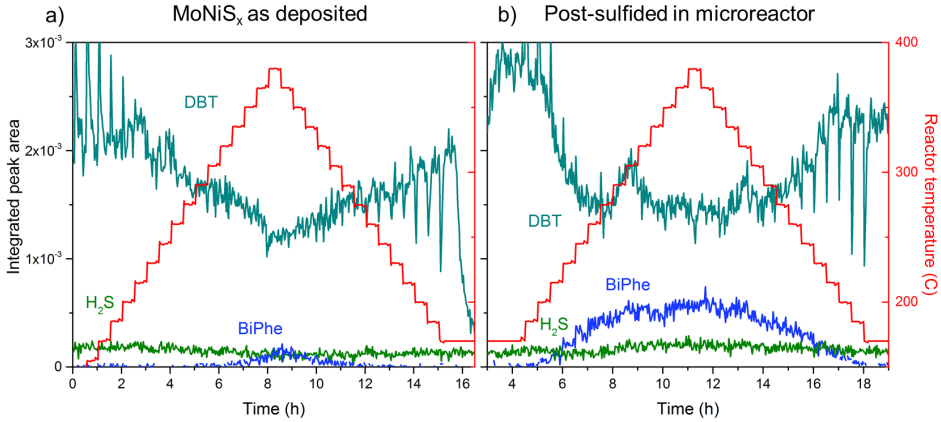

Figure 4.22: The amount of dibenzothiophene (DBT), biphenyl (BiPhe) and H_2S, plotted as a function of time during temperature ramps. **a)** shows the signals obtained on a Ni-Mo-S sample which had been exposed to air between deposition and bonding, where **b)** had been resulfided in the microreactor after bonding, resulting in a much higher HDS activity as seen in the BiPhe signal.

Comparison With Ni-Mo Nanoparticles Sulfided in Microreactor

As seen in Figure 4.22, the DBT signal fluctuates somewhat, which was due to difficulties in keeping a constant temperature in the DBT source – since the vapour pressure of DBT depends exponentially on the temperature of the DBT source, fluctuations of a few degrees resulted in the observed variations. In order to report a meaningful activity metric, we therefore plot the conversion ratio instead of the raw signals, defined as

$$\text{Conversion} = \frac{S \times A_{\text{BiPhe}}}{S \times A_{\text{BiPhe}} + A_{\text{DBT}}}, \tag{4.1}$$

where A is a raw integrated peak area and S is a relative sensitivity factor that accounts for the different ionization cross-sections of BiPhe and DBT in the mass spectrometer. S was found to be 1.3 on the TOF setup by going to full conversion of DBT to BiPhe by loading a reactor with highly active Pt nanoparticles (see Ann-Louise Christoffersen's thesis).

Figure 4.23 shows the conversion as a function of temperature in the reactor. Each conversion datapoint in this plot is an average of the entire half-hour temperature step, and the error bars represent the standard deviation. For comparison, two microreactors with deposited Ni-Mo, which had also been sulfided in the reactor, are included in the plot. It is clear that the in-flight sulfided particles have at least twice as high activity. As shown in section 4.3, the in-flight sulfided particles retain their shapes during this resulfidation treatment, and the difference between metallic and in-flight sulfided depositions could thus be attributed to the morphology induced by reactive gas aggregation synthesis procedure.

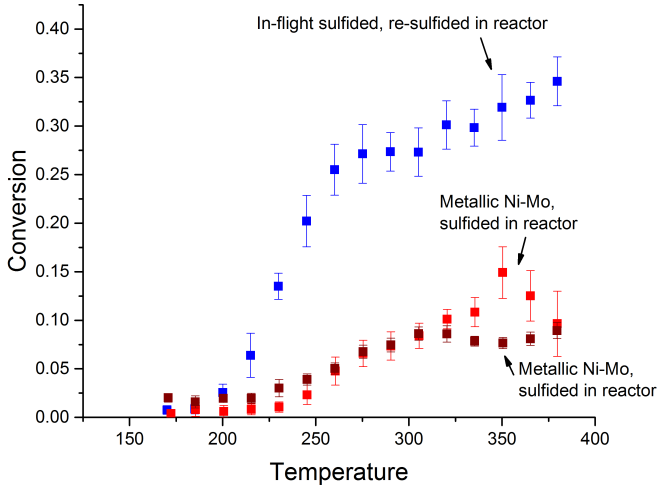

Figure 4.23: Conversion of DBT to BiPhe for one microreactor with 440 kamu in-flight sulfided Ni-Mo-S nanoparticles, and two microreactors with metallic Ni-Mo nanoparticles of 134 kamu. All three reactors had been sulfided in the microreactor after bonding.

It should be noted that the mass of the metallic Ni-Mo nanoparticles was chosen as a reference for the 200 kamu Ni-Mo-S particles, and thus only contain approximately half as much metal as the 440 kamu particles. However, the fact that the metallic particles were smaller should only increase their mass activity, since they will expose more surface per mass. Although additional measurements would be beneficial for more stable conclusions, our experiments thus point toward a significant enhancement in catalytic activity for HDS of DBT by using in-flight sulfided Ni-Mo-S nanoparticle catalysts compared to post-deposition-sulfided Ni-Mo metallic particles. It is especially interesting that the morphology with up-right layers of Ni-Mo-S achieved by depositing 440 kamu show this activity increase.

4.4.2 Hydrogen Evolution Reaction (HER)

For HER measurements, we deposited in-flight sulfided Ni-Mo-S nanoparticles at a mass of 200 kamu on a glassy carbon stub, with a total mass loading of 315 ng. The HER measurements were carried out in 0.5 M H_2SO_4 bubbled with H_2 in a three-electrode setup with a graphite rod as counter electrode and a $Hg/HgSO_4$ reference electrode. The glassy carbon substrate was mounted for rotating disk electrode (RDE) measurements, which were conducted at 1600 RPM. We ran cyclic voltammetry (CV) experiments which were IR-corrected after measurements.

Figure 4.24 shows two CVs obtained on the sample, the 2nd and 26th cycle, respectively. For comparison, a blank glassy carbon stub was also tested, and the higher HER activity of the Ni-Mo-S-sample is clearly visible. As seen in the difference between cycle 2 and cycle 26, the sample was not stable during the experiment.

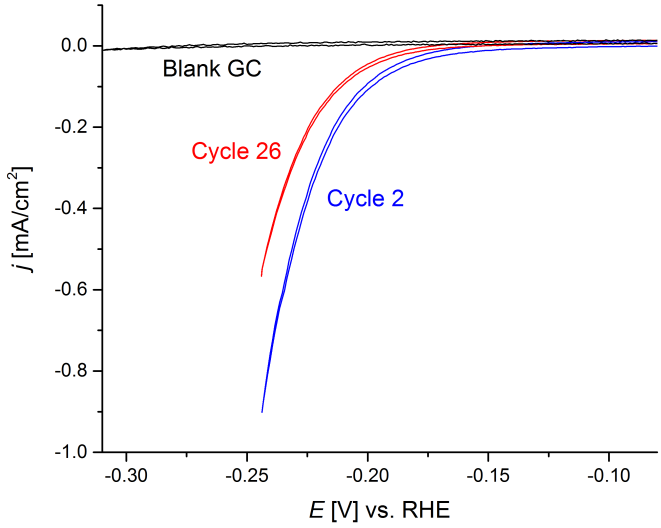

Figure 4.24: Cyclic voltammetry HER measurements of 200 kamu in-flight sulfided Ni-Mo-S nanoparticles plotted together with the CV of a blank glassy carbon (GC) stub. As shown in the difference between cycle 2 and 26, the catalyst was not stable during the experiment.

In order to compare the catalytic activity of the nanoparticles with literature, the turn-over frequency (TOF) per metal atom (Ni and Mo) in the sample was calculated. The amount of catalyst is known from the deposition current, and using the stoichiometry obtained from XPS analysis the accurate number of metal atoms in the sample could be determined. Using the current density from cycle 2 in the cyclic voltammetry, the TOF was calculated. The result is plotted in Figure 4.25 together with other Mo-S catalysts from literature, unfortunately revealing that the in-flight sulfided Ni-Mo-S nanoparticles have a quite poor performance.

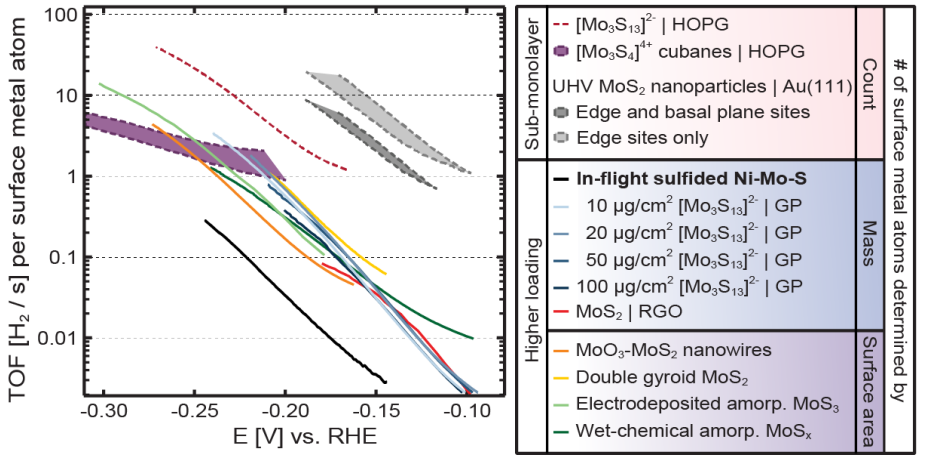

Figure 4.25: HER turn-over frequencies plotted as a function of potential. The TOF of the in-flight sulfided Ni-Mo-S nanoparticles is shown as a black line, which reveals the poor performance of this catalyst. The figure is an altered version of a plot shown in [113].

The other catalysts in the figure are not promoted with Ni, and one could speculate that this was the reason for the low activity. However, Merki et al. report that Ni-promotion should increase the catalytic performance of molybdenum sulfides [114], which makes this hypothesis implausible. A more likely reason for the poor activity is the fact that the Ni-Mo-S nanoparticles are insufficiently sulfided. Hinnemann et al. report that hydrogen is bound to sulfur atoms in the MoS_2 edges; therefore, an undersulfided catalyst would have a lower amount of active sites, leading to a lower TOF per metal atom. A post-sulfidation treatment might increase the HER activity of the Ni-Mo-S nanoparticles, but was beyond the scope of this small sub-project.

4.5 Conclusion and Outlook

In this project I developed a synthesis procedure for depositing in-flight sulfided Ni-Mo-S nanoparticles by aggregation of sputtered metal from a $Mo_{75}Ni_{25}$ target in a reactive atmosphere of Ar and H_2S. The resulting particles were undersulfided with a stoichiometry of $Mo_{0.8}Ni_{0.2}S_{1.1}$, and the particles exhibited high-surface area morphologies such as platelets, very different from the spherical morphologies observed for metal nanoparticles. The particles were mass-filtered before deposition, which allowed for changing the particle morphologies significantly, from platelet structures at 200 kamu to agglomerates of up-right platelets at 440 kamu.

By testing the catalytic activity of the nanoparticles for the sterically hindered hydrodesulferization (HDS) of dibenzothiophene (DBT) in microreactors, it was found that in-flight sulfided Ni-Mo-S nanoparticles of 440 kamu had more than twice as high mass activity as metal Ni-Mo nanoparticles deposited by inert gas aggregation at 134 kamu and post-sulfided in the reactor. This points towards the potential of engineering nanoscale catalysts for HDS by reactive gas aggregation synthesis of nanoparticles.

The hydrogen evolution activity of in-flight sulfided Ni-Mo-S nanoparticles with a mass of 200 kamu was assessed, showing that the catalytic turn-over frequency per metal atom was significantly below Mo-S catalysts reported in literature.

For further studies, it would be interesting to map out the capabilities of the synthesis procedure further, especially focusing on varying the deposition mass of nanoparticles and the effect of different partial pressures of H_2S in the aggregation process. The combination of model system synthesis and test of catalytic activity in microreactors is also a promising strategy, and it would be beneficial to conduct more measurements to establish a more firm understanding of the relation between synthesis parameters and catalytic activity.

Chapter 5

Dynamic Effects of Surface Oxygen in CO Electroreduction

In this chapter I report the discovery of a new phenomenon in the electroreduction of carbon monoxide. We show that adsorbing oxygen onto a model system of copper nanoparticles significantly alters the catalytic mechanism for CO-electroreduction, making the surface highly selective towards methane production. The phenomenon is short-lived and has previously not been observed due to the lack of time-resolution in previous investigations of CO-reduction.

The study was a collaborative effort involving synthesis and characterization of mass-selected nanoparticles, catalytic measurements with electrochemical mass spectrometry (EC-MS), and density functional calculations (DFT). The synthesis and characterization was done by myself and Jakob E. Sørensen, the EC-MS measurements were done by Søren B. Scott, Daniel B. Trimarco, and Nicola Mazzanti, and the DFT modelling was done by Alexander Bagger, who is a Ph.D. student at the University of Copenhagen. Besides my experimental work I have also been involved in discussion and analysis of results, design of experiments and writing the paper draft that is attached at the end of the thesis.

Before presenting our own results, I will present an introduction to the field of CO_2-electroreduction. Also, a description of the time-line of the project is included, along with an important note about a systematic error in our study which was discovered shortly before the writing of this thesis. The error results in some reservations in the later data treatment, but the overall conclusions are most likely unchanged.

5.1 Introduction

5.1.1 Electroreduction of CO_2

Already in the 1980'es Hori et al. did pioneering work in investigating the electrochemical reduction of CO_2, and found that copper surfaces could catalyze the formation of a range of products including carbon monoxide, methane, ethylene, ethanol, and propanol besides hydrogen from the competing HER [115,116]. Later, the reaction products from CO_2 reduction on polycrystalline copper have been thoroughly mapped out by Kuhl et al. [44], as seen in Figure 5.1.

One of the major challenges in CO_2 electrocatalysis is the poor selectivity of the Cu catalyst. Preferably, the catalyst would selectively produce a product with high energy density, such as methanol or ethanol, at a low overpotential, but as seen in Figure 5.1, only a small fraction of the current goes to such products. There have, however, been significant progress in finding catalysts that can convert CO_2 to CO, which is the first step in carbon dioxide reduction [117,118]. Thus, many studies, including our own, focus on the further reduction of CO to hydrocarbons and oxygenates.

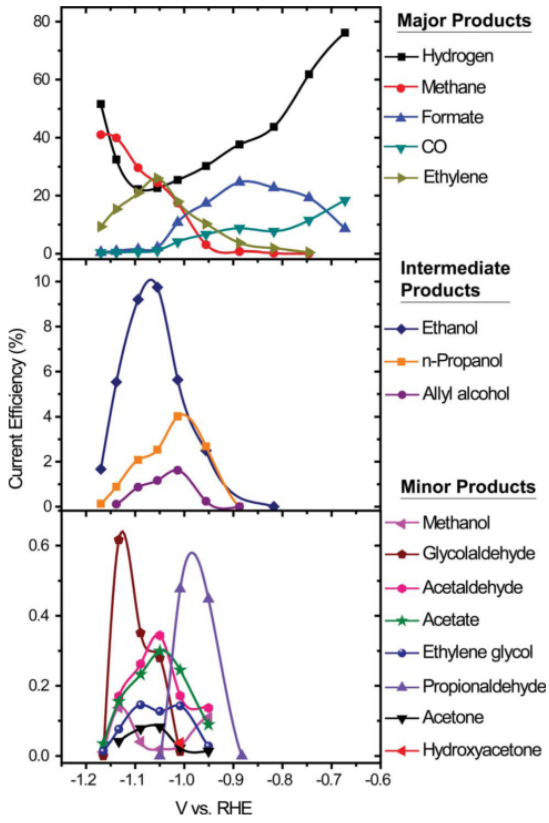

Figure 5.1: Current efficiencies of CO_2 electroreduction on polycrystalline copper to different products as a function of reduction potential. Reproduced from [44].

Recently, it has been shown that the activity of Cu electrodes for CO-reduction to multi-carbon products could be greatly enhanced by preparing the catalyst from an oxidized precursor producing "oxide-derived Cu". One important example is from the group of M. Kanan who showed that CO could be converted to ethanol, acetate and propanol with up to 57 % Faradaic efficiency at modest potentials of -0.25 to -0.5 V vs. RHE [119].

However, the reason for the heightened CO-reduction activity is still debated. Feng et al. have shown a direct correlation between CO reduction activity and boundaries between crystalline grains in Cu nanoparticles produced from oxidized precursors [120] and Verdaguer-Casadevall et al. have shown that oxide-derived copper has sites which bind CO strongly by temperature programmed desorption which they attribute to strucures around grain boundaries [121]. On the other hand, Mistry et al. have recently suggested that oxidized copper species remain at the catalyst surface at reductive potentials, playing a key role in increasing the CO-reduction activity [122]. Along the same lines, Eilert et al. have suggested that sub-surface oxygen is present in the catalyst under reaction conditions, changing the activity of the catalyst [123]. One of the important knowledge gaps is thus to understand the role of oxygen in copper catalysts for CO-electroreduction. In this study we isolate the effect of adsorbed oxygen on Cu nanoparticles, and thus contribute to the further understanding of this subject.

5.1.2 Timeline of the Project

As many scientific discoveries, this study was initiated by an experimental accident. In a computational study, Chan et al. had reported that Ni-doped molybdenum disulfides might catalyze the reduction of CO to hydrocarbons and/or alcohols [124], and since I had synthesized the Ni-Mo-S nanoparticles described in Chapter 4 we decided to test them for CO electroreduction while monitoring the product distribution with electrochemical mass-spectrometry. Unfortunately, the only significant product was hydrogen from the competing HER, but on one sample we saw a curious phenomenon: A high, transient production of methane at the onset of CO-electroreduction, which disappeared within seconds. Subsequent XPS characterization of the sample showed that it was contaminated with copper which later turned out to be the origin of the methane production. In order to investigate the phenomenon, we decided to create samples with "controlled Cu impurities" in the form of small loadings of nanoparticles and investigate these with electrochemical mass-spectrometry.

5.1.3 Important Note: Systematic Error in Experiments

Appended to this thesis is a completed draft of a paper on the transient methane phenomenon which we had planned to submit for publication. However, shortly before submission we discovered a systematic error in our experiments: When the nanoparticles are introduced to electrolyte for electrochemical measurements, a significant amount of Cu corrodes due to lack of potential control at the introduction of electrolyte. This diminishes the value of our nanoparticle model systems, since they have been in an undefined state during measurements, and the quantitative conclusions are weakened. Therefore, we are currently redoing the experiments before submission of the study.

The data presented in this chapter was obtained on four samples which showed similar CO-reduction activity. We speculate that the electrolyte introduction will

have deactivated the samples in the same manner, and this originally led us to believe that the samples were intact during measurements.

Although the sample deactivation leads to some reservations regarding the presented conclusions, the transient CO-reduction phenomenon is still highly interesting, and the general conclusions should still hold. During the chapter I will make the reader aware of the limited validity of our data when necessary.

After this short introduction, I will now present our experimental work, beginning with the production and characterization of the mass-selected copper nanoparticle model system.

5.2 Sample Preparation and Characterization

5.2.1 Nanoparticle Deposition

Cu nanoparticles were deposited with the Nano-Beam 2011 nanoparticle source by sputtering of a Cu target and aggregation in an inert atmosphere of Ar and He. As a substrate we used glassy carbon cylinders with $\varnothing = 5\,\text{mm}$. A nanoparticle mass of 350 kamu was chosen, corresponding to a particle diameter of 5 nm if the bulk density of Cu is assumed. This particle size was not chosen for any particular reason, other than it enabled a high and stable deposition current. At high electrochemical currents, bubble formation can occur in the EC-MS cell; therefore we chose a relatively small nanoparticle loading of 5 % projected area coverage, corresponding to 24 ng of catalyst on each sample. This also minimize particle-particle interaction and mass-transport effects.

Table 5.1: Typical deposition conditions for Cu nanoparticles with a mass of 350 kamu. In each deposition, the parameters were optimized, leading to some variations in deposition conditions.

Ar flow	He flow	Agg. zone pressure	Sputter power
50 SCCM	55 SCCM	4E-1 mbar	18 W

5.2.2 Sample Characterization

After deposition, the samples were transferred to the Omicron analysis chamber for XPS and ISS analysis. Figure 5.2 shows the XPS spectrum of a Cu sample, where no other materials than Cu, C and some oxygen from the substrate is visible. Before the catalytic measurements, the sample would be exposed to air; a spectrum of a sample after 15 hours of air exposure was therefore obtained, shown as the red spectrum in Figure 5.2. Closeup scans of the $Cu2p_{3/2}$ and LMM Auger regions reveal a spectral shape corresponding to Cu^+ as in Cu_2O after air exposure (see Figure C.2 in Appendix C for spectra of Cu nanoparticles in different oxidation states).

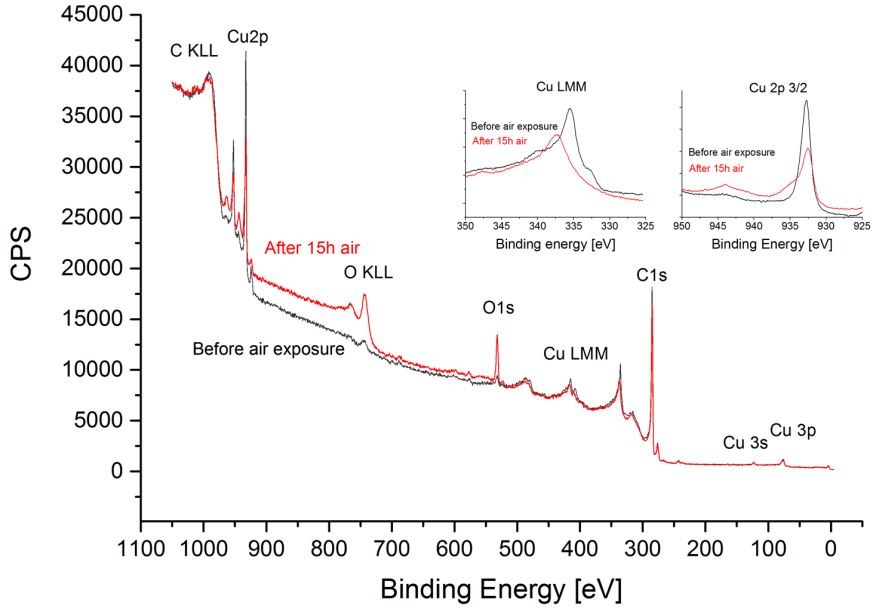

Figure 5.2: XPS spectra on Cu nanoparticles before and after air exposure. The spectral shape of the $Cu2p_{3/2}$ and LMM Auger features indicate Cu^{+} as in Cu_2O after air exposure.

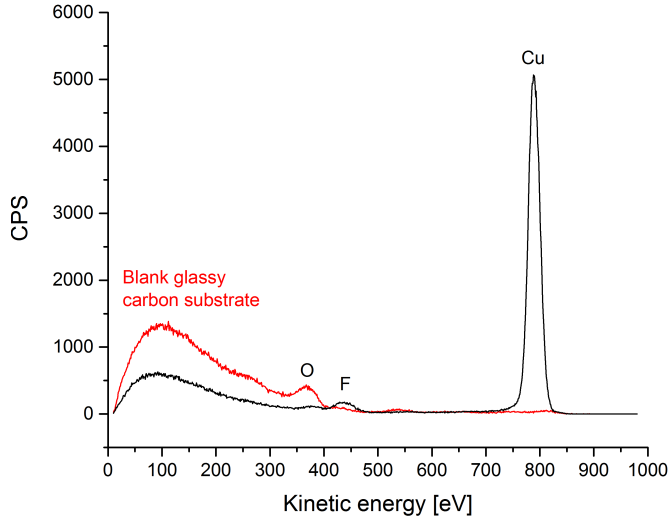

Figure 5.3: ISS spectra before and after deposition on a glassy carbon substrate. The background below 300 eV is due to sputtered ions contributing to signals at low energies.

ISS spectra were obtained both on a deposited sample and a blank glassy carbon substrate, to assert its the cleanliness, as shown in Figure 5.3. Apart from oxygen, which was also observed in XPS, a small amount of fluorine is also on the surface, most likely due to a teflon holder used during polishing of the substrates. Apart from that, no major impurities are present, and Cu is clearly visible after deposition.

To verify the narrow size distribution, Cu nanoparticles were deposited on Cu/lacey carbon TEM grids and imaged in a a FEI Tecnai T20 G2 transmission electron microscope in bright-field TEM mode. A representative image is presented in Figure 5.4 a). The particle size distribution was found using the "analyze particles" function in the software ImageJ, where only particles with a circularity of 0.7-1 were included to avoid nanoparticles that had landed on top of each other. The resulting histogram of average diameters is presented in Figure 5.4 b), where a Gaussian has been fitted to the main peak, resulting in an average size of 4.8 nm with a standard deviation of 0.2 nm, very close to the expected 5 nm. A small peak is visible at higher masses, probably due to particles that were deposited with double mass/double charge or have sintered on the substrate.

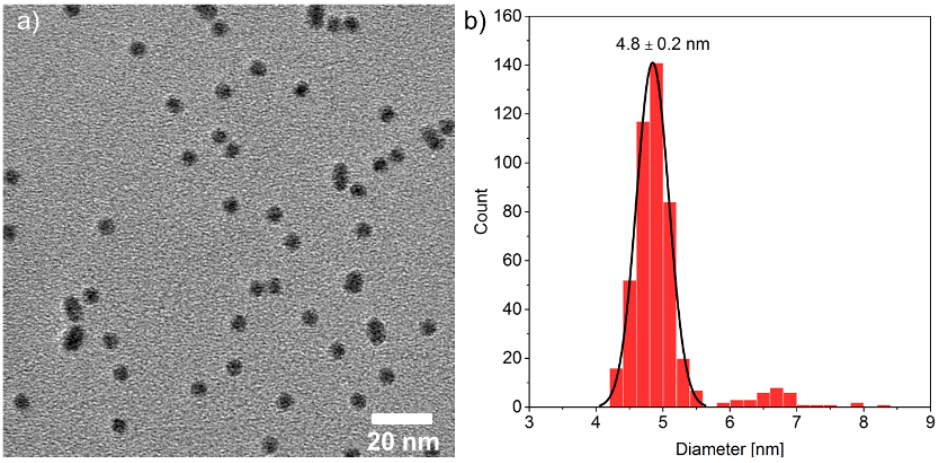

Figure 5.4: **a)** TEM image of Cu nanoparticles deposited at a mass of 350 kamu on a lacey carbon TEM grid. **b)** Histogram of average particle diameters revealing a major peak at 4.8 ± 0.2 nm.

5.2.3 Substrate Cleaning

The glassy carbon substrates were cleaned before nanoparticle deposition in the following steps: 1) Rinsing in ultrapure water 2) Cleaning in 65 % suprapure nitric acid for one hour, then rinsing in ultrapure water 3) Polishing with $\frac{1}{4}\,\mu$m diamond paste 4) Sonicating two times for 10 minutes, first in ethanol and then in ultrapure water 5) Repeating the acid treatment (step 2) and 6) Sonicating two

times in ultrapure water for 10 minutes. We found that this method removes all metals detectable with XPS as seen in Figure 5.2. Trace amounts of 3d and 5d metal impurities are still left, as evidenced with ISS (barely visible at $\sim 820\,\text{eV}$ in Figure 5.3), but since ISS is an extremely surface-sensitive technique this is almost unavoidable.

5.3 CO-Electroreduction Experiments

The CO-electroreduction experiments presented below were performed by Søren B. Scott, Daniel B. Trimarco, and Nicola Mazzanti. Before presenting the results, I will briefly introduce the experimental methodologies.

5.3.1 The Electrochemical Mass-Spectrometry Cell

The electrochemical mass spectrometry (EC-MS) measurements were carried out in a specially designed electrochemical cell shown schematically in Figure 5.5. The main function of the cell is to perform electrochemical measurements with the working electrode very close to a sniffer chip (which was presented in Section 2.4.2), in order to perform EC-MS where the diffusion time from sample to membrane is minimized. The cell is thoroughly described in D. Trimarco's Ph.D. thesis, but a short description will be given here:

The glassy carbon substrate is mounted in a U-cup holder, similar to those used in rotating ring electrode measurements, which provides electrical contact so that it can be used as a working electrode (WE). It is then placed so that the substrate surface faces the membrane of the sniffer chip, with a distance of $100\,\mu\text{m}$

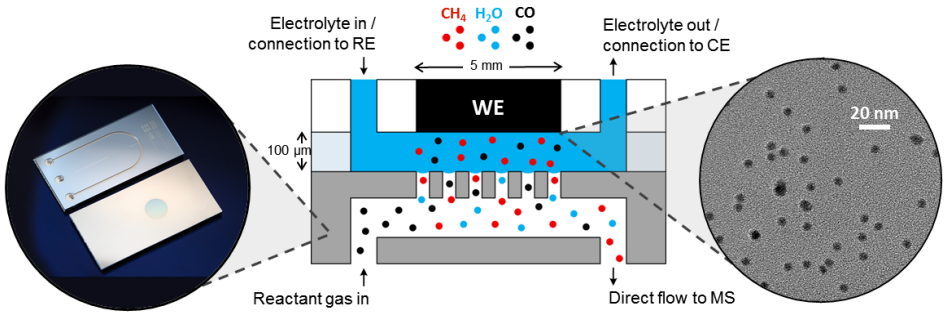

Figure 5.5: Schematic presentation of the EC-MS cell during operation. The glassy carbon working electrode with deposited Cu nanoparticles (right inset), is mounted $100\,\mu\text{m}$ away from the membrane of the sniffer chip (left inset). CO reactant gas is dosed through the membrane, and the volatile electrochemical products evaporate though the membrane and are detected in a mass spectrometer. The EC-MS cell has connections for reference and counter electrodes, and thus enable three-electrode electrochemical experiments.

defined by a teflon spacer. The EC-MS cell has connections to both a counter and a reference electrode, allowing three-electrode electrochemical experiments.

When electrolyte is introduced into the "working volume" between WE and sniffer chip, the hydrophobic membrane forms a liquid/gas interface through which volatile species can evaporate and be led directly into a quadrupole mass spectrometer through a capillary channel. A main advantage of the sniffer chip is that it is possible to dose gases to the WE through the membrane; in our experiments, CO was dosed this way to avoid depletion of reactant gas.

5.3.2 Experimental Details

All experiments were carried out in a 0.5 M potassium carbonate buffer titrated to pH = 12 with KOH. During the experiments, the electrolyte was kept stagnant, i.e. without any electrolyte flow, but was purged between experiments as later described. Before each experiment, all components of the EC-MS cell which were exposed to electrolyte were cleaned by leaving them overnight in a Piranha solution in order to remove organic impurities and non-precious metals. Finally, they were then thoroughly rinsed with water five times.

In this study, we run the CO-reduction at constant potential while detecting the current (chronoamperometry). At the same time, we measure the mass-spectrometer signals for the reaction products; since the sniffer chip only effectively detects volatile species, we only detect CH_4 and C_2H_4 as CO-reduction products.

5.3.3 The Dynamic Methane Phenomenon

Figure 5.6 shows the mass spectrometer signals from a CO-reduction experiment plotted together with the working electrode potential and current; we refer to this type of plot as an "EC-MS plot". The potential is stepped from a "resting potential" of 0 V to a "working potential" of −0.8 V vs. RHE.

The MS-signal shows the key phenomenon in this study: A high transient production of methane at the onset of CO-reduction. This dynamic behaviour is not observed for hydrogen (not plotted in the figure) or ethylene, which indicates that the phenomenon does not affect 2-carbon CO reduction products. Before the electroreduction process, fresh oxygen-containing electrolyte was flushed for 5 seconds, exchanging the working volume more than 10 times; this gave rise to an oxygen signal in the MS, as well as a brief oxygen reduction current. We found that the oxygen exposure was necessary for activating the high, transient methane production as shown later.

5.3.4 Effect of Working Potential on Dynamic Methane

In order to quantify the observed phenomenon, we separated the total methane production into a "steady-state" component and a "dynamic methane" component, as seen in the inset in Figure 5.7. The integrated mass-spectrometer signals of

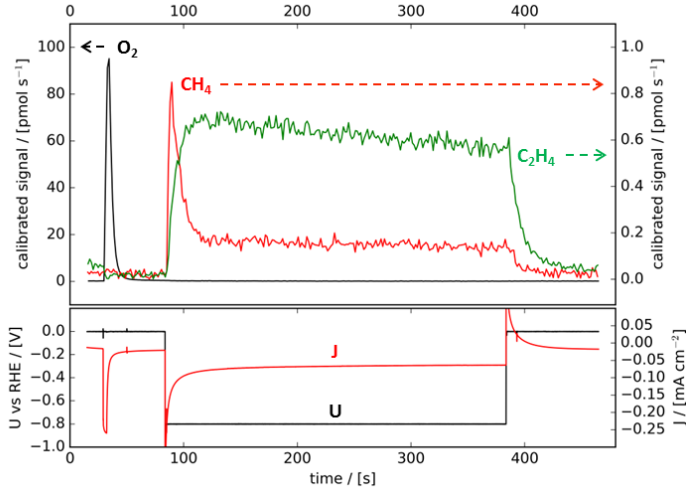

Figure 5.6: EC-MS plot showing the calibrated mass-spectrometry signals during CO-electroreduction in the top graph, and the current and potential on the WE in the lower graph, both as a function of time.

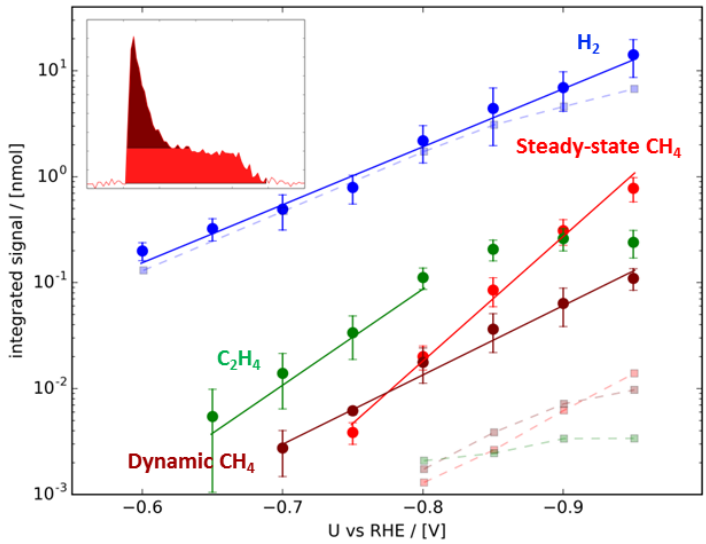

Figure 5.7: Integrated mass-spectrometer signals of reaction products as a function of working potential during the one-minute CO-reduction pulse. The methane signal is divided into a steady-state and a dynamic component as shown in the inset. The transparent datapoints are from a blank glassy carbon sample.

the two methane-components as well as hydrogen and ethylene are plotted as a function of working potential as shown in Figure 5.7. The integrated signals were obtained from one-minute chronoamperometic CO-reduction pulses; between the pulses, the working volume was flushed with aerated electrolyte at a resting potential of 0 V, just as in Figure 5.6. The shown data points are mean values between four different samples, where the error bars represent the standard deviation. As mentioned in the introduction, the samples were deactivated during electrolyte introduction, but as evidenced in the small error bars, the samples must have deactivated to a similar extent.

In this representation, it is clear that the potential dependencies of steady-state and dynamic methane are different, with tafel slopes of 91 mV/decade and 151 mV/decade, respectively, indicating a different reaction mechanism. The general trend that the ethylene/methane ratio decreases at high overpotentials is in agreement with the observations of Kuhl et al. [44], as seen in Figure 5.1, and Hori et al. [116]. The transparent datapoints in Figure 5.7 were obtained on a blank glassy carbon sample, and show similar hydrogen production as the Cu-samples, indicating that the majority of hydrogen evolution is coming from the substrates. We attribute the small amount of CO-reduction products on the blank sample to trace-level Cu impurities in the sample [125].

5.3.5 Effect of Oxygen on the Dynamic Methane

As previously mentioned, it is necessary to expose the Cu nanoparticles to oxygen to obtain the dynamic methane phenomenon. In Figure 5.6 we flushed aerated electrolyte to the working volume to obtain the dynamic methane activation. However, the electrolyte flushing may induce other effects than just the oxygen exposure, and therefore we performed a different, more well-defined experiment by dosing gaseous oxygen through the sniffer chip membrane while keeping a stagnant electrolyte.

Figure 5.8 a) shows this experiment where gaseous oxygen is dosed at a resting potential of 0 V vs. RHE. At the onset of CO-electroreduction at −0.9 V vs. RHE, the dynamic methane phenomenon is observed. As a control experiment, we dosed Ar instead, resulting in Figure 5.8 b), where the dynamic feature is absent. Note that the CO-reduction product signals are significantly smaller than in Figure 5.6; this is due to sample deactivation during the electrochemical measurements before we obtained a successful measurement.

5.3.6 Effect of Resting Potential on Dynamic Methane

To investigate the mechanism in which the catalyst is activated for dynamic methane production, we did a series of experiments with a constant working potential, but varying the resting potential during which oxygen was introduced by flushing aerated electrolyte for five seconds. The results are plotted in Figure 5.9, where each point is the integrated MS-signal during a one-minute CO-reduction pulse at −0.85 V vs. RHE.

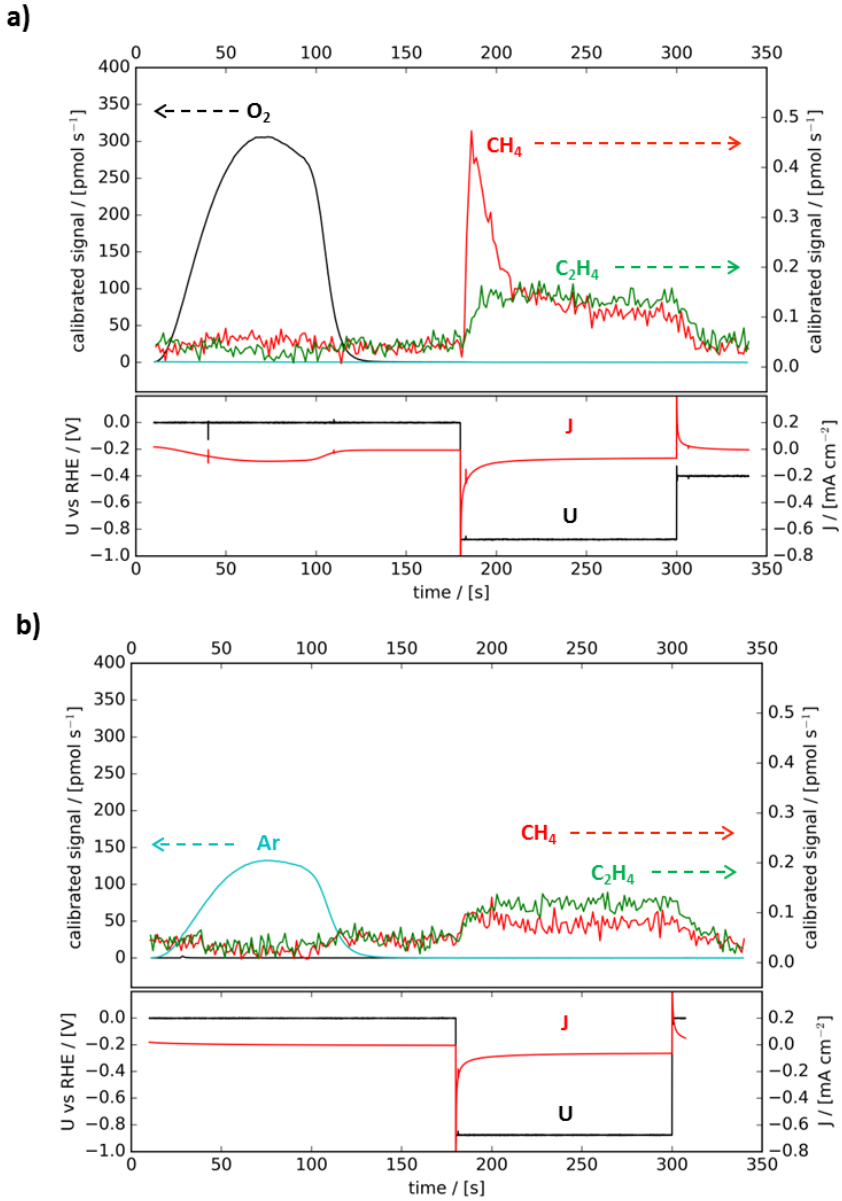

Figure 5.8: **a)** CO reduction pulse after exposing the Cu nanoparticles to oxygen dosed through the sniffer membrane. The dynamic methane phenomenon is clearly observable. **b)** Control experiment where the nanoparticles are exposed to Ar before a CO-reduction pulse. No dynamic methane is observed.

Interestingly, the figure shows that the dynamic methane is only activated if the oxygen is introduced at a resting potential above $\sim -0.2\,\mathrm{V}$ vs. RHE. Also, the dynamic methane signal increases until a certain point ($\sim 0.2\,\mathrm{V}$ vs. RHE), after which a further increase in resting potential does not affect the dynamic methane production. It is also observed that the steady-state ethylene and methane signals start to grow at resting potentials above $\sim 0\,\mathrm{V}$ vs. RHE. A similar increase in steady-state CO-reduction products can be seen by going to potentials anodic of $+0.5\,\mathrm{V}$ vs. RHE without any O_2 in the electrolyte. This does, however, not activate the dynamic methane.

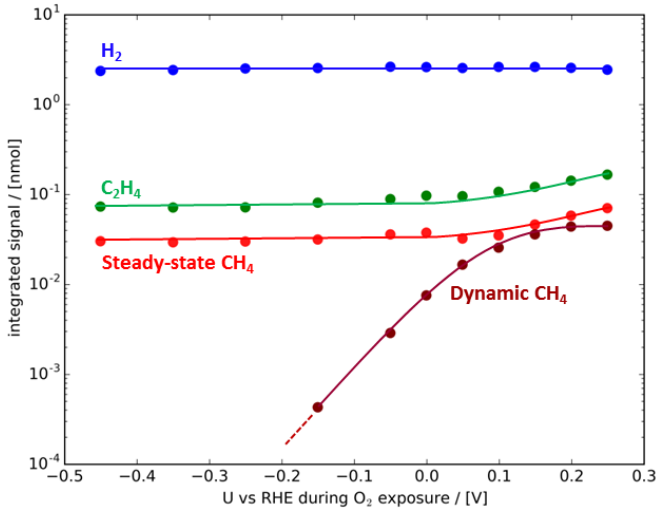

Figure 5.9: Integrated MS-signals of products from 1-minute pulses of CO-reduction as a function of the resting potential during which the Cu nanoparticles are exposed to O_2 by flushing the working volume with aerated electrolyte. The dynamic methane is only observed if the resting potential is above $\sim -0.2\,\mathrm{V}$.

We propose that the dynamic methane is activated by adsorption of oxygen on specific surface sites, which is only (meta)stable at resting potentials above $\sim -0.2\,\mathrm{V}$ vs. RHE. After the active sites for dynamic CH_4 production are saturated, further oxidation leads to increases in steady-state CO reduction activity, consistent with observations on oxide-derived CU surfaces [119, 126, 127].

5.3.7 Why Dynamic Methane was not Observed Before

Time-resolved CO-reduction on Cu surfaces has previously been studied with online electrochemical mass-spectrometry (OLEMS) by e.g. Roberts et al. [127] and Schouten et al. [128], and one might wonder why the dynamic methane phenomenon has not been observed before. There are two answers to this question: Firstly, we have dosed oxygen before each observation of dynamic methane. Secondly, even if the Cu surfaces had been oxidized in the previous studies, they

were run with a continuous variation of working electrode potential (i.e. cyclic voltammetry), whereas we initiate the CO-reduction with a step to the working potential. If we monitor the reaction products during a potential sweep with a rate of 5 $\frac{\text{mV}}{\text{s}}$, as seen in Figure 5.10, we do not observe any dynamic methane either. This is likely due to the fact that the surface oxygen is reduced before the dynamic methane can be produced.

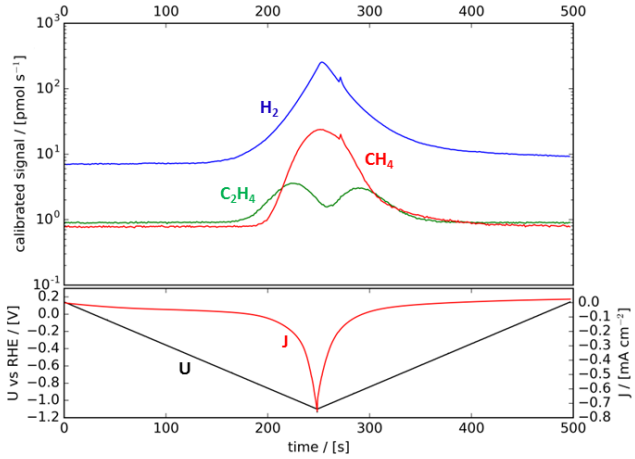

Figure 5.10: EC-MS plot showing the mass spectrometer signals of the products from electrochemical CO-reduction during a sweep of the working electrode potential at a rate of 5 $\frac{\text{mV}}{\text{s}}$. No dynamic methane is observed, since the surface oxygen is not stable during the potential sweep.

5.4 Computational Modelling

The computational modelling was done by Alexander Bagger, who is a Ph.D. student in the group of Rossmeisl at the University of Copenhagen. I will not present the details of the DFT model here, but only present the results. More information can be found in the "Methods Summary" of the appended paper draft.

5.4.1 Density Functional Theory: What is the Active Site?

Figure 5.11 a) shows a Wulff-constructed model of a Cu nanoparticle with a mass of 350 kamu, where the surface atoms are color-coded according to their coordination number (CN). Previous DFT studies by Shi et al. have been conducted on reduced copper surfaces [129], showing that the terrace sites (CN = 8 or 9) have very small CO binding energies (< 0.1 eV), making CO-adsorption rate-limiting. We do therefore not expect these sites to contribute significantly

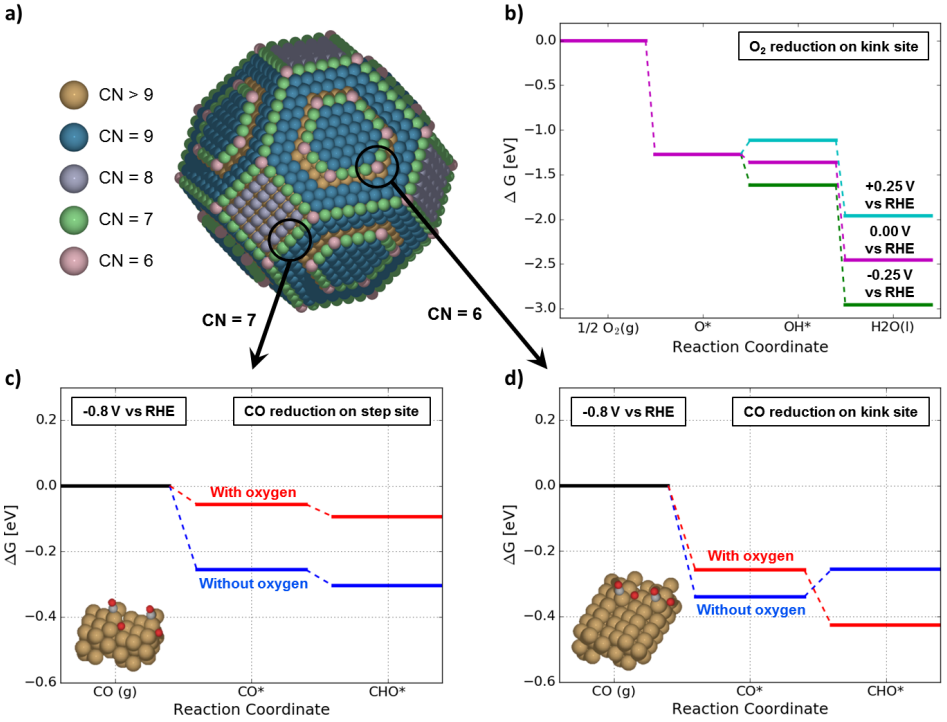

Figure 5.11: **a)** Wulff-construction of a Cu nanoparticle with a mass of 350 kamu, where the surface atoms are color-coded to show their coordination number. **b)** Free-energy diagram of the reduction of O_2 to water, at three different potentials. The ∗O intermediate is metastable at 0.25 V, but may also be present at lower potentials due to kinetic barriers. **c)** and **d)** Free-energy diagrams of the CO-reduction on a step and kink sites, respectively, with and without adsorbed surface oxygen. The kink site is activated for CO-reduction by the adsorbed oxygen due to stabilization of the ∗COH intermediate with respect to ∗CO.

to the overall CO-reduction rate. On undercoordinated sites, the rate-limiting step for CO-reduction to methane is $*CO \rightarrow *CHO$, and all subsequent steps to methane are down-hill in energy. Kink-sites (CN=6) have higher reactivity than step sites (CN=7), which makes their limiting potential higher because ∗CO is double-bonded to the surface, increasing its binding energy relatively more than ∗CHO, which is single-bonded. The results in [129] thus imply that the majority of methane production should take place on step-sites during CO-electroreduction on the reduced Cu-nanoparticles. This trend is reproduced in our own DFT-modelling, shown as blue lines in the free-energy diagrams in Figure 5.11 c) and d), clearly demonstrating that the steps have the most favorable free-energy landscape for protonation of ∗CO, and thereby methane production, on reduced Cu surfaces.

Using the DFT model, we now investigate the effect of adsorbing oxygen (∗O

surface oxygen) on a site adjacent to the ∗CO. As seen from the red lines in Figure 5.11 c) and d), the ∗O generally weakens the binding energies of the CO-reduction intermediates, but for ∗CHO on kink sites, the binding energy is increased, which cause the ∗CO → ∗CHO to be exergonic. Thereby, the kink sites are activated for methane production by the adsorbed oxygen.

The fact that CHO is stabilized by ∗O on kink sites, but destabilized on step sites, is due to a geometrical effect where the ∗CHO intermediate can tilt to orient itself favourably with respect to the ∗O. Adsorbed CO is double-bonded to the surface and therefore cannot tilt in the same way on either site. The general trend is observed irrespective of the precise position of the ∗O.

We attribute the transient nature of the dynamic methane to the fact that surface oxygen is quickly reduced to water at CO-reduction potentials. However, at resting potentials, the ∗O may be stable, as shown in the free-energy diagram in Figure 5.11 b). At +0.25 V vs. RHE, the ∗O intermediate is stable, whereas it is reduced to ∗OH at more negative potentials. However, the free-energy diagram does not include kinetic barriers. If such a kinetic barrier is present between ∗O and ∗OH, it may be that the surface oxygen could be present in a metastable state, even at CO reduction potentials. The duration of the dynamic methane phenomenon would then correspond to the life-time of the adsorbed surface oxygen. Fitting the experimentally observed methane signal with a model of diffusion and evaporation in the EC-MS system indicates that the life-time of the active site is on the order of 1 s.

5.4.2 Number of Catalytic Turn-Overs per Active Site

Another metric for the lifetime of the active site is the turn-over-number (TON), which describes how many catalytic cycles that take place on the active site before it disappears. To determine the TON, it is necessary to estimate the number of active sites on the sample. The number of nanoparticles on the sample surface is known from the integrated deposition current. We assume that each particle is Wulff-constructed, leading to ∼ 1300 surface atoms in each particle. Of these, only 72 are kink sites, as seen in Table 5.2.

Table 5.2: Average number of surface atoms from 8 Wulff-constructed Cu nanoparticles with a mass around 350 kamu.

All surface atoms, N_{surface}	1302±318
Number of step sites, N_{step}	185±15
Number of kink sites, N_{kink}	72±8

We can now estimate a maximum TON, assuming only kink sites are active, and a minimum TON, assuming all surface atoms are active. In the latter situation, the number of surface sites has to be divided with 2, as there has to be one adsorption site for oxygen for each adsorbed CO. For the calculations, we use the amount of dynamic methane produced at -0.95 V vs. RHE, $n_{\text{methane}} = 0.1$ nmol,

and the total number of deposited particles, $N_{\text{particles}} = 4.11 \times 10^{10}$:

$$\text{TON}_{\text{max}} = \frac{n_{\text{methane}} \cdot N_{\text{Avogadro}}}{N_{\text{kink}} \cdot N_{\text{particles}}} = \frac{0.1 \times 10^{-9}\,\text{mol} \cdot 6 \times 10^{23}\,\text{mol}^{-1}}{72 \cdot 4.11 \times 10^{10}} = 20.4 \quad (5.1)$$

$$\text{TON}_{\text{min}} = \frac{n_{\text{methane}} \cdot N_{\text{Avogadro}}}{\frac{N_{\text{surface}}}{2} \cdot N_{\text{particles}}} = \frac{0.1 \times 10^{-9}\,\text{mol} \cdot 6 \times 10^{23}\,\text{mol}^{-1}}{1302 \cdot 4.11 \times 10^{10}} = 2.2 \quad (5.2)$$

The estimates thus indicate that between 2 and 20 catalytic turnovers take place on each active site before it disappears. It should be noted that these calculations only hold if the number of particles is the same as when they were deposited in the nanoparticle source. This is not the case due to sample deactivation at the introduction of electrolyte. However, the TONs should only increase if the amount of Cu on the sample surface has decreased, which still make the calculations relevant as conservative estimates.

5.5 Discussion

Previous studies have reported that oxidative treatments of Cu-surfaces increase their production of CO-reduction products with two C-atoms (C2-products) [66, 122]. This stands in contrast to our studies, where oxygen exposure results in an increase in the C1-product CH_4, while the C2 ethylene remains unaffected. The difference is that we investigate the effect of adsorbed oxygen, which has previously been unexplored due to lack of time-resolution or the use of cyclic voltammetry experiments instead of stepped, constant potential measurements. However, our study does confirm the understanding that C1 and C2 products are formed in different mechanisms with distinct limiting potentials [130, 131]. It should be noted that our studies were conducted on nanoparticles, which have a higher density of undercoordinated sites than e.g. polycrystalline copper.

As mentioned in the introduction, all of the data reported in this chapter was obtained on samples where Cu was lost during introduction of electrolyte, due to lack of potential control. The value of the well-defined model system of mass-selected nanoparticles is thus diminished, since it was in an undefined state during the EC-MS experiments. Although the quantitative conclusions in this study are thus less firm than we would have hoped, the discovery of the dynamic methane phenomenon in itself is still significant. It should also be noted that samples without Cu-loss may have even higher catalytic activities, which could reinforce our conclusions. However, it is necessary with more well-defined experiments before a final conclusion can be made.

Methane is not a high-value product due to its abundance as natural gas, and thus the broader relevance of our findings could be questioned. To the best of our knowledge, it is, however, the first time that EC-MS has been used to study intrinsically transient catalytic phenomena, and the ideas in this study may thus open a new area of catalyst investigations. One could e.g. imagine studying

transition metals for catalyzing oxygen evolution in their metallic state, before they are oxidized, or study the intrinsic activity of catalysts that become poisoned by intermediates. If highly efficient catalysts were found this way, they could potentially be utilized on industrial scale by cyclically regenerating metastable catalytic sites.

5.6 Conclusion and Outlook

Using a newly developed system for electrochemical mass-spectrometry, we have discovered a high, transient production of methane at the onset of electroreduction of CO on mass-selected copper nanoparticles produced by inert gas-aggregation. This "dynamic methane" is only observed when the nanoparticles have been exposed to O_2 before the electrode potential is stepped to CO-reduction potentials.

The dynamic methane is shown to have a different dependence on electroreduction potential than steady-state methane production, indicating that the two methane components are formed by two distinct mechanisms. By varying the potential at which the oxygen is introduced, the "resting potential", it was found that dynamic methane only appears at resting potentials higher than $-0.2\,\mathrm{V}$ vs. RHE, and that the amount of dynamic methane increases with the resting potential until $\sim 0.2\,\mathrm{V}$. This saturation mechanism is attributed to the fact that the surface of the Cu nanoparticles is covered with adsorbed oxygen.

Based on density functional theory, we propose that the dynamic methane is formed on nanoparticle kink-sites, which are activated by adsorbed oxygen on a neighbouring site, due to stabilisation of the $*$CHO intermediate relative to $*$CO. The transient nature of the dynamic methane is attributed to the fact that the adsorbed oxygen is reduced to water within $\sim 1\,\mathrm{s}$ after the onset of CO-electroreduction. In this time, we estimate that $2 - 20$ catalytic turnovers take place on each catalytic site.

Unfortunately, the data in this study was acquired on samples which were significantly deactivated due to lack of potential control during introduction of electrolyte. Therefore, the amount of Cu on the samples was undefined during measurements, which diminishes the value of the well-defined model systems. However, the discovery of the dynamic methane phenomenon is still significant, and we anticipate that the general conclusions from this study still hold.

Before publication, it is necessary to obtain new data where the samples are introduced to electrolyte under potential control. At the time of writing, we have just established a procedure with this purpose, and should soon be able to establish more firm conclusions. After these measurements, it would be interesting to study the effect of particle size, since the number of undercoordinated surface atoms could thus be varied in an elegant way. It would also be exciting to explore the possibilities in regenerating the metastable sites at a high frequency, and thus utilize the dynamic methane to increase the average CO-reduction efficiency. Besides these further studies on CO-electroreduction, transient phenomena could be studied on other systems such as OER catalysts, as mentioned in the discussion.

Chapter 6

Conclusion and Outlook

The overall goal of this thesis has been to develop better catalysts for sustainable energy conversion and environmental protection by investigating well-defined nanoparticle model systems. Here, at the end of the thesis, I will try to summarize the presented research projects and provide an outlook towards future research.

In chapter 3, the relationship between between catalytic activity for the photoelectrochemical HER and platinum catalyst loading was investigated using different loadings of 5 nm Pt nanoparticles. Using the knowledge gained on these systems, a technoeconomic analysis was carried out, showing that photoelectrochemical HER at a current density of 10 $\frac{\text{mA}}{\text{cm}^2}$ and an overpotential of 50 mV could be obtained with a catalyst consumption of 54 tons of Pt per TW energy stored in H_2. Since the global annual production of Pt is $\sim$ 180 ton, it was thereby demonstrated that it may be feasible to use Pt HER catalysts on the TW-scale.

The topic of chapter 4 was in-flight sulfided Ni-Mo-S nanoparticles synthesized by reactive gas aggregation. The resulting nanoparticles exhibited high-surface area morphologies such as platelets, and were unsaturated with sulfur. The catalytic activity of the nanoparticles for HDS of dibenzothiophene was assesed in microreactors, and it was found that in-flight sulfided Ni-Mo-S nanoparticles were more than twice as active as Ni-Mo-S nanoparticles produced by inert gas aggregation and post-sulfidation. Thereby, we have shown the potential of engineering HDS catalysts by reactive gas aggregation.

Chapter 5 reported the discovery of a high, transient production of methane at the onset of electroreduction of CO on mass-selected copper nanoparticles produced by inert gas-aggregation. The "dynamic methane" was shown to be due to metastable adsorbed oxygen, activating specific surface-sites for methane production. The phenomenon is highly interesting in itself, but may also open new possibilities within the study of transient electrochemical phenomena.

The three research topics presented in the thesis all relied on nanoparticle synthesis by sputtering, gas-aggregation, and mass-filtering, but the focus was very different in the studies. Thus, the thesis has covered a broad range of subjects within the study of nanoparticles for catalysis.

It is a daunting task to write a Ph.D. thesis, but after three years of intense research it has been a great experience to collect the results into a single publication; hopefully, this thesis communicates that experience, and has assured the reader of the benefits of studying well-defined nanoparticles in the science of catalysis. I hope that the results can play a small role in the development of the technologies that we so urgently need for building a sustainable future.

Outlook

Although this Ph.D. is now concluded, there are naturally several topics that would be interesting to pursue further. Besides the obvious tasks, such as continuing the projects presented in chapter 4 and 5, there are especially two things that I would have liked to explore, and which I already started to investigate in the final stages of my Ph.D.

The first of these projects is a continuation of our studies on Cu nanoparticles for CO-electroreduction. One of the inherent difficulties in this project was to relate the UHV-characterization to catalytic activity. A tool that could bridge this gap is temperature programmed desorption (TPD), where binding energies can be studied in the UHV-chamber by adsorbing CO-molecules onto the sample and measure their desorption as a function of temperature with a mass-spectrometer. CO binding energy can act as a descriptor for catalytic activity, and if we could measure e.g. CO-binding energies vs. Cu nanoparticle size, or as a function of oxidation treatment, it could potentially provide crucial information for understanding the CO-reduction. Jakob Ejler Sørensen and I have designed a stage for performing such TPDs, which will hopefully produce interesting results. The stage is briefly presented in Appendix D.

The second future project would be to study catalysis on smaller clusters. Although we have made some attempts in this direction (see Appendix D), it has been problematic to achieve sufficient cluster deposition rates to study their catalytic properties. At the time of writing, our group is therefore procuring a new cluster source with the aim of investigating the smaller size-regime in the project "Discovering new Catalysts in the Cluster-Nanoparticle Transition Regime" (CLUNATRA). We anticipate that this path of research can lead to more radical developments, e.g. within breaking catalytic scaling relations, which are unobtainable in materials where bulk-like properties still dominate.

Bibliography

[1] Vaclav Smil. Detonator of the population explosion. *Nature*, 400(July):415–415, 1999.

[2] Jan Willem Erisman, Mark A. Sutton, James Galloway, Zbigniew Klimont, and Wilfried Winiwarter. How a century of ammonia synthesis changed the world. *Nature Geoscience*, 1(October 2008):636–639, 2008.

[3] Intergovernmental Panel on Climate Change (IPCC). *Climate Change 2014 Synthesis Report*. 2014.

[4] Adoption of the Paris Agreement, 2015.

[5] Barack Obama. The irreversible momentum of clean energy. *Science*, 355(6321):126–129, 2017.

[6] Donella Meadows, Dennis Meadows, Jorgen Randers, and William III Behrens. *Limits to Growth: the 30 year update*. Universe Books, 1972.

[7] Tim Jackson. *Prosperity without growth. Economics for a finite planet*. Earthscan, 2009.

[8] U.S. Energy Information Agency. International Energy Outlook 2013. *Outlook 2013*, page 312, 2013.

[9] Nathan S. Lewis and Daniel G. Nocera. Powering the planet: Chemical challenges in solar energy utilization. *Proceedings of the National Academy of Sciences*, 103(43):15729–15735, 2006.

[10] Nancy M. Haegel, Robert Margolis, Tonio Buonassisi, David Feldman, Armin Froitzheim, Raffi Garabedian, Martin Green, Stefan Glunz, Hansmartin Henning, Burkhard Holder, Izumi Kaizuka, Benjamin Kroposki, Koji Matsubara, Shigeru Niki, Keiichiro Sakurai, Roland A Schindler, William Tumas, Eicke R Weber, Gregory Wilson, Michael Woodhouse, and Sarah Kurtz. Terawatt-scale photovoltaics: Trajectories and challenges. *Science*, 356(6334):141–143, 2017.

[11] Rasmus Frydendal. Improving performance of catalysts for water electrolysis: The MnOx case, 2015.

[12] EMD International A/S. Elforbrug og vindmølleproduktion, 2015.

[13] Zhi Wei Seh, Jakob Kibsgaard, Colin F. Dickens, Ib Chorkendorff, Jens K. Nørskov, and Thomas F. Jaramillo. Combining theory and experiment in electrocatalysis: Insights into materials design. *Science*, 355(6321):eaad4998, 2017.

[14] Ib Chorkendorff and J. W. Niemantsverdriet. *Concepts of Modern Catalysis and Kinetics*. Wiley-VCH, 2. edition edition, 2007.

[15] J. K. Nørskov, T. Bligaard, A. Logadottir, J. R. Kitchin, J. G. Chen, S. Pandelov, and U. Stimming. Trends in the Exchange Current for Hydrogen Evolution. *Journal of The Electrochemical Society*, 152(3):J23, 2005.

[16] Jakub Tymoczko, Federico Calle-Vallejo, Wolfgang Schuhmann, and Aliaksandr S. Bandarenka. Making the hydrogen evolution reaction in polymer electrolyte membrane electrolysers even faster. *Nature Communications*, 7:10990, 2016.

[17] Andrew Peterson and Jens Nørskov. Activity Descriptors for CO2 Electroreduction to Methane on Transition-Metal Catalysts. *The Journal of Physical Chemistry Letters*, 3:251–258, 2012.

[18] Andrew A. Peterson, Frank Abild-Pedersen, Felix Studt, Jan Rossmeisl, and Jens K. Nørskov. How copper catalyzes the electroreduction of carbon dioxide into hydrocarbon fuels. *Energy & Environmental Science*, 3(9):1311, 2010.

[19] Joseph H. Montoya, Linsey C. Seitz, Pongkarn Chakthranont, Aleksandra Vojvodic, Thomas F. Jaramillo, and Jens K. Nørskov. Materials for solar fuels and chemicals. *Nature Materials*, 16(1):70–81, 2016.

[20] Hubert A. Gasteiger, Shyam S. Kocha, Bhaskar Sompalli, and Frederick T. Wagner. Activity benchmarks and requirements for Pt, Pt-alloy, and non-Pt oxygen reduction catalysts for PEMFCs. *Applied Catalysis B: Environmental*, 56(1-2 SPEC. ISS.):9–35, 2005.

[21] Peter C. K. Vesborg and Thomas F. Jaramillo. Addressing the terawatt challenge: scalability in the supply of chemical elements for renewable energy. *RSC Advances*, 2(21):7933, 2012.

[22] M.P. Andersson, F. Abild-Pedersen, I.N. Remediakis, T. Bligaard, G. Jones, J. Engbæk, O. Lytken, S. Horch, J.H. Nielsen, J. Sehested, J. R. Rostrup-Nielsen, J. K. Nørskov, and I. Chorkendorff. Structure sensitivity of the methanation reaction: H2-induced CO dissociation on nickel surfaces. *Journal of Catalysis*, 255:6–19, apr 2008.

[23] Eric C. Tyo and Stefan Vajda. Catalysis by clusters with precise numbers of atoms. *Nat. Nanotechnol.*, 10(7):577–588, 2015.

[24] Kwangjin An and Gabor A. Somorjai. Size and Shape Control of Metal Nanoparticles for Reaction Selectivity in Catalysis. *ChemCatChem*, 4(10):1512–1524, 2012.

[25] Lakshminarayana Polavarapu, Stefanos Mourdikoudis, Isabel Pastoriza-Santos, and Jorge Pérez-Juste. Nanocrystal engineering of noble metals and metal chalcogenides: controlling the morphology, composition and crystallinity. *CrystEngComm*, 17(20):3727–3762, 2015.

[26] Shigeki Yatsuya, Takanobu Kamakura, Kenji Yamauchi, and Kazuhiro Mihama. A new technique for the formation of ultrafine particles by sputtering. *Japanese Journal of Applied Physics*, 25(1):L42–L44, 1986.

[27] H. Hahn and R. S. Averback. The production of nanocrystalline powders by magnetron sputtering. *Journal of Applied Physics*, 67(2):1113–1115, 1990.

[28] Hellmut Haberland, Martin Karrais, Martin Mall, and Yonca Thurner. Thin films from energetic cluster impact: A feasibility study. *Journal of Vacuum Science & Technology A: Vacuum, Surfaces, and Films*, 10(5):3266, sep 1992.

[29] S. Pratontep, S. J. Carroll, C. Xirouchaki, M. Streun, and R. E. Palmer. Size-selected cluster beam source based on radio frequency magnetron plasma sputtering and gas condensation. *Review of Scientific Instruments*, 76(4), 2005.

[30] Lakshmi Kolipaka and Stefan Vajda. High-Pressure and Reactive Gas Magnetron Sputtering. In Yves Huttel, editor, *Gas-Phase Synthesis of Nanoparticles*, pages 243–268. Wiley-VCH Verlag GmbH, 2017.

[31] Nanogen50 Operations Manual.

[32] C. G. Granqvist and R. A. Buhrman. Ultrafine metal particles. *Journal of Applied Physics*, 47(5):2200–2219, 1976.

[33] B. von Issendorff and R. E. Palmer. A new high transmission infinite range mass selector for cluster and nanoparticle beams. *Review of Scientific Instruments*, 70(12):4497–4501, 1999.

[34] Paul Wolfgang and Helmut Steinwedel. Ein neues Massenspektrometer ohne Magnetfeld. *Z. Naturforschg.*, 8a:448–450, 1953.

[35] Vladimir N. Popok, Ingo Barke, Eleanor E B Campbell, and Karl Heinz Meiwes-Broer. Clustersurface interaction: From soft landing to implantation. *Surface Science Reports*, 66(10):347–377, 2011.

[36] Federico Masini, Patricia Hernández-Fernández, Davide Deiana, Christian Ejersbo Strebel, David Norman McCarthy, Anders Bodin, Paolo Malacrida, Ifan Stephens, and Ib Chorkendorff. Exploring the phase space

of time of flight mass selected PtxY nanoparticles. *Phys. Chem. Chem. Phys.*, 16(48):26506–26513, 2014.

[37] G. A. Somorjai. *Chemistry in Two Dimensions.* Cornell University Press, 1981.

[38] M.P. Seah and W.A. Dench. Quantitative electron spectroscopy of surfaces. *Surface and Interface Analysis*, 1(1):46–55, 1979.

[39] C. D. Wagner, W. M. Riggs, L. E. Davis, J. F. Moulder, and G. E. Muilenberg. Handbook of X-ray photoelectron spectroscopy, 1979.

[40] Cody V. Cushman, Philipp Brüner, Julia Zakel, George H. Major, Barry M. Lunt, Nicholas J. Smith, Thomas Grehl, and Matthew R. Linford. Low energy ion scattering (LEIS). A practical introduction to its theory, instrumentation, and applications. *Anal. Methods*, 8(17):3419–3439, 2016.

[41] David P. Smith. Scattering of low-energy noble gas ions from metal surfaces. *Journal of Applied Physics*, 38(1):340–347, 1967.

[42] P. W. Hawkes and J. C. H. Spence. *Science of Microscopy.* Springer, 2007.

[43] David B Williams and C Barry Carter. *Transmission Electron Microscopy.* Springer Science + Business Media, 2009.

[44] Kendra P. Kuhl, Etosha R. Cave, David N. Abram, and Thomas F. Jaramillo. New insights into the electrochemical reduction of carbon dioxide on metallic copper surfaces. *Energy & Environmental Science*, 5(5):7050, 2012.

[45] Daniel B. Trimarco, Thomas Pedersen, Ole Hansen, Ib Chorkendorff, and Peter C K Vesborg. Fast and sensitive method for detecting volatile species in liquids. *Review of Scientific Instruments*, 86(7), 2015.

[46] Toke R. Henriksen, Jakob L. Olsen, Peter Vesborg, Ib Chorkendorff, and Ole Hansen. Highly sensitive silicon microreactor for catalyst testing. *Review of Scientific Instruments*, 80(12), 2009.

[47] Peter C K Vesborg, Jakob L. Olsen, Toke R. Henriksen, Ib Chorkendorff, and Ole Hansen. Gas-phase photocatalysis in micro-reactors. *Chemical Engineering Journal*, 160(2):738–741, 2010.

[48] T. Andersen, R. Jensen, M. K. Christensen, T. Pedersen, O. Hansen, and I. Chorkendorff. High mass resolution time of flight mass spectrometer for measuring products in heterogeneous catalysis in highly sensitive microreactors. *Review of Scientific Instruments*, 83(7), 2012.

[49] Peter C K Vesborg, Jakob L. Olsen, Toke R. Henriksen, I. B. Chorkendorff, and Ole Hansen. Note: Anodic bonding with cooling of heat-sensitive areas. *Review of Scientific Instruments*, 81(1), 2010.

[50] E. Kemppainen, A. Bodin, B. Sebok, T. Pedersen, B. Seger, B. Mei, D. Bae, P. C. K. Vesborg, J. Halme, O. Hansen, P. D. Lund, and I. Chorkendorff. Scalability and feasibility of photoelectrochemical H2 evolution: the ultimate limit of Pt nanoparticle as an HER catalyst. *Energy Environ. Sci.*, 8(10):2991–2999, 2015.

[51] Blaise A. Pinaud, Jesse D. Benck, Linsey C. Seitz, Arnold J. Forman, Zhebo Chen, Todd G. Deutsch, Brian D. James, Kevin N. Baum, George N. Baum, Shane Ardo, Heli Wang, Eric Miller, and Thomas F. Jaramillo. Technical and economic feasibility of centralized facilities for solar hydrogen production via photocatalysis and photoelectrochemistry. *Energy & Environmental Science*, 6(7):1983, 2013.

[52] M. F. Weber and M. J. Dignam. Splitting water with semiconducting photoelectrodes-Efficiency considerations. *International Journal of Hydrogen Energy*, 11(4):225–232, 1986.

[53] Brian Seger, Ivano E. Castelli, Peter C. K. Vesborg, Karsten W. Jacobsen, Ole Hansen, and Ib Chorkendorff. 2-Photon tandem device for water splitting: comparing photocathode first versus photoanode first designs. *Energy Environ. Sci.*, 7(8):2397–2413, 2014.

[54] Jesse D Benck, Thomas R Hellstern, Jakob Kibsgaard, Pongkarn Chakthranont, and Thomas F Jaramillo. Catalyzing the Hydrogen Evolution Reaction (HER) with Molybdenum Sulfide Nanomaterials. *ACS Catalysis*, 4(11):3957–3971, 2014.

[55] Jieun Yang and Hyeon Suk Shin. Recent advances in layered transition metal dichalcogenides for hydrogen evolution reaction. *J. Mater. Chem. A*, 2(17):5979–5985, 2014.

[56] Ya Yan, Baoyu Xia, Zhichuan Xu, and Xin Wang. Recent Development of Molybdenum Sul fi des as Advanced Electrocatalysts for Hydrogen Evolution Reaction. *ACS Catalysis*, 4:1693–1705, 2014.

[57] Anders B. Laursen, Søren Kegnæs, Søren Dahl, and Ib Chorkendorff. Molybdenum sulfides—efficient and viable materials for electro - and photoelectrocatalytic hydrogen evolution. *Energy & Environmental Science*, 5(2):5577, 2012.

[58] Peter C K Vesborg, Brian Seger, and Ib Chorkendorff. Recent development in hydrogen evolution reaction catalysts and their practical implementation. *Journal of Physical Chemistry Letters*, 6(6):951–957, 2015.

[59] James R Mckone, Bryce F Sadtler, Caroline a Werlang, Nathan S Lewis, and Harry B Gray. Ni-Mo Nanopowders for Efficient Electrochemical Hydrogen Evolution. *ACS Catalysis*, 3(2):166–169, 2013.

[60] Eric J. Popczun, James R. Mckone, Carlos G. Read, Adam J. Biacchi, Alex M. Wiltrout, Nathan S. Lewis, and Raymond E. Schaak. Nanostructured Nickel Phosphide as an Electrocatalyst for the Hydrogen Evolution Reaction. *Journal of the American Chemical Society*, 135:9267–9270, 2013.

[61] Eric J. Popczun, Carlos G. Read, Christopher W. Roske, Nathan S. Lewis, and Raymond E. Schaak. Highly active electrocatalysis of the hydrogen evolution reaction by cobalt phosphide nanoparticles. *Angewandte Chemie - International Edition*, 53(21):5427–5430, 2014.

[62] Jakob Kibsgaard and Thomas F. Jaramillo. Molybdenum phosphosulfide: An active, acid-stable, earth- Abundant catalyst for the hydrogen evolution reaction. *Angewandte Chemie - International Edition*, 53(52):14433–14437, 2014.

[63] Yidong Hou, Billie L Abrams, Peter C K Vesborg, Mårten E Björketun, Konrad Herbst, Lone Bech, Alessandro M Setti, Christian D Damsgaard, Thomas Pedersen, Ole Hansen, Jan Rossmeisl, Søren Dahl, Jens K Nørskov, and Ib Chorkendorff. Bioinspired molecular co-catalysts bonded to a silicon photocathode for solar hydrogen evolution. *Nature materials*, 10(6):434–8, jun 2011.

[64] Juan F. Callejas, Joshua M. McEnaney, Carlos G. Read, J. Chance Crompton, Adam J. Biacchi, Eric J. Popczun, Thomas R. Gordon, Nathan S. Lewis, and Raymond E. Schaak. Electrocatalytic and photocatalytic hydrogen production from acidic and neutral-pH aqueous solutions using iron phosphide nanoparticles. *ACS Nano*, 8(11):11101–11107, 2014.

[65] N P Dasgupta, C Liu, S Andrews, F B Prinz, and P Yang. Atomic layer deposition of platinum catalysts on nanowire surfaces for photoelectrochemical water reduction. *J Am Chem Soc*, 135(35):12932–12935, 2013.

[66] Yikai Chen, Ke Sun, Heather Audesirk, Chengxiang Xiang, and Nathan S. Lewis. A quantitative analysis of the efficiency of solar-driven water-splitting device designs based on tandem photoabsorbers patterned with islands of metallic electrocatalysts. *Energy Environ. Sci.*, 8(6):1736–1747, 2015.

[67] Brian Seger, Thomas Pedersen, Anders B Laursen, Peter C K Vesborg, Ole Hansen, and Ib Chorkendorff. Using TiO 2 as a Conductive Protective Layer for Photocathodic H 2 Evolution. 2013.

[68] Dowon Bae, Thomas Pedersen, Brian Seger, Mauro Malizia, Andrej Kuznetsov, Ole Hansen, Ib Chorkendorff, and Peter C. K. Vesborg. Back-illuminated Si photocathode: a combined experimental and theoretical study for photocatalytic hydrogen evolution. *Energy Environ. Sci.*, 8(2):650–660, 2015.

[69] Josef C. Meier, Ioannis Katsounaros, Carolina Galeano, Hans J. Bongard, Angel A. Topalov, Aleksander Kostka, Arndt Karschin, Ferdi Schüth, and Karl J. J. Mayrhofer. Stability investigations of electrocatalysts on the nanoscale. *Energy & Environmental Science*, 5(11):9319, 2012.

[70] Brian Seger, David S. Tilley, Thomas Pedersen, Peter C. K. Vesborg, Ole Hansen, Michael Grätzel, and Ib Chorkendorff. Silicon protected with atomic layer deposited TiO2: durability studies of photocathodic H2 evolution. *RSC Advances*, 3(48):25902, 2013.

[71] NREL. http://www.nrel.gov/analysis/tech_cap_factor.html.

[72] P. J. Loferski. Platinum-Group Metals. *2012 Minerals Yearbook*, 2013.

[73] World Platinum Investment Council. WPIC Platinum Quarterly Q1 2015. 2015.

[74] H. Wang, Z. Lu, J. Sun, T.M. Hymel, and Y. Cui. Electrochemical Tuning of MoS 2 Nanoparticles on Three-Dimensional Substrate for Efficient Hydrogen Evolution. *ACS nano*, 8(5):4940–4947, 2014.

[75] W. O. Winer. Molybdenum disulfide as a lubricant: A review of the fundamental knowledge. *Wear*, 10(6):422–452, 1967.

[76] B. Radisavljevic, A. Radenovic, J. Brivio, V. Giacometti, and A. Kis. Single-layer MoS2 transistors. *Nature Nanotechnology*, 6(3):147–150, 2011.

[77] W. Bensch. *Hydrotreating: Removal of Sulfur from Crude Oil Fractions with Sulfide Catalysts*, volume 7. Elsevier Ltd., 2nd editio edition, 2013.

[78] Berit Hinnemann, Poul Georg Moses, Jacob Bonde, Kristina P. Jørgensen, Jane H Nielsen, Sebastian Horch, Ib Chorkendorff, and Jens K Nørskov. Biomimetic Hydrogen Evolution: MoS 2 Nanoparticles as Catalyst for Hydrogen Evolution. *Journal of the American Chemical Society*, 127(15):5308–5309, 2005.

[79] H. Topsøe, B. S. Clausen, and F. E. Massoth. *Hydrotreating Catalysis Science and Technology*. Springer Verlag, 1996.

[80] www.dieselnet.com/standards/eu/fuel.php.

[81] Signe S. Gronborg, Manuel Saric, Poul G. Moses, Jan Rossmeisl, and Jeppe V. Lauritsen. Atomic scale analysis of sterical effects in the adsorption of 4,6-dimethyldibenzothiophene on a CoMoS hydrotreating catalyst. *Journal of Catalysis*, 344:121–128, 2016.

[82] Marwan Houalla, N. K. Nag, A. V. Sapre, D. H. Broderick, and B. C. Gates. Hydrodesulfurization of dibenzothiophene catalyzed by sulfided CoO-MoO3-Al2O3: The reaction network. *AIChE Journal*, 24(6):1015–1021, 1978.

[83] T. F. Jaramillo, K. P. Jorgensen, J. Bonde, J. H. Nielsen, S. Horch, and I. Chorkendorff. Identification of Active Edge Sites for Electrochemical H2 Evolution from MoS2 Nanocatalysts. *Science*, 317(5834):100–102, 2007.

[84] Roscoe G. Dickinson, Pauling, and Linus. The Crystal Structure of Molybdenite. *J. Am. Chem. Soc.*, 45(27):1466–1471, 1923.

[85] K. D. Bronsema, J. L. De Boer, and F. Jellinek. On the structure of molybdenum diselenide and disulfide. *Journal of Inorganic and General Chemistry*, 540(9-10):15–17, 1986.

[86] Jeppe V. Lauritsen, Jakob Kibsgaard, Georg H. Olesen, Poul G. Moses, Berit Hinnemann, Stig Helveg, Jens K. Nørskov, Bjerne S. Clausen, Henrik Topsøe, Erik Lægsgaard, and Flemming Besenbacher. Location and coordination of promoter atoms in Co- and Ni-promoted MoS2-based hydrotreating catalysts. *Journal of Catalysis*, 249(2):220–233, 2007.

[87] Yuanyuan Zhu, Quentin M. Ramasse, Michael Brorson, Poul G. Moses, Lars P. Hansen, Christian F. Kisielowski, and Stig Helveg. Visualizing the stoichiometry of industrial-style Co-Mo-S catalysts with single-atom sensitivity. *Angewandte Chemie - International Edition*, 53(40):10723–10727, 2014.

[88] B. L. Evans and P. A. Young. Optical Absorption and Dispersion in Molybdenum Disulphide. *Proceedings of the Royal Society A*, 284(1398):402–422, 1965.

[89] Jeppe V. Lauritsen, Jakob Kibsgaard, Stig Helveg, Henrik Topsøe, Bjerne S. Clausen, Erik Lægsgaard, and Flemming Besenbacher. Size-dependent structure of MoS2 nanocrystals. *Nature Nanotechnology*, 2(1):53–58, 2007.

[90] Lars P. Hansen, Quentin M. Ramasse, Christian Kisielowski, Michael Brorson, Erik Johnson, Henrik Topsøe, and Stig Helveg. Atomic-scale edge structures on industrial-style MoS 2 nanocatalysts. *Angewandte Chemie - International Edition*, 50(43):10153–10156, 2011.

[91] Yuanyuan Zhu, Quentin M. Ramasse, Michael Brorson, Poul G. Moses, Lars P. Hansen, Henrik Topsøe, Christian F. Kisielowski, and Stig Helveg. Location of Co and Ni promoter atoms in multi-layer MoS2 nanocrystals for hydrotreating catalysis. *Catalysis Today*, 261(October):75–81, 2016.

[92] Yutao Lu, Xiayin Yao, Jingyun Yin, Gang Peng, Ping Cui, and Xiaoxiong Xu. MoS2 nanoflowers consisting of nanosheets with a controllable interlayer distance as high-performance lithium ion battery anodes. *RSC Adv.*, 5(11):7938–7943, 2015.

[93] Takehiko. Hihara, Dong-Liang. Peng, and Kenji. Sumiyama. Effects of O2 gas on the size and structure of Cr clusters formed by plasma-gas-condensation, 2001.

[94] Amir Mohammad Ahadi, Vladimir Zaporojtchenko, Tilo Peter, Oleksandr Polonskyi, Thomas Strunskus, and Franz Faupel. Role of oxygen admixture in stabilizing TiOx nanoparticle deposition from a gas aggregation source. *Journal of Nanoparticle Research*, 15(12), 2013.

[95] Amir Mohammad Ahadi, Oleksandr Polonskyi, Ulrich Schürmann, Thomas Strunskus, and Franz Faupel. Stable production of TiOx nanoparticles with narrow size distribution by reactive pulsed dc magnetron sputtering. *Journal of Physics D: Applied Physics*, 48(3):035501, 2015.

[96] Oleksandr Polonskyi, Tilo Peter, Amir Mohammad Ahadi, Alexander Hinz, Thomas Strunskus, Vladimir Zaporojtchenko, Hynek Biederman, and Franz Faupel. Huge increase in gas phase nanoparticle generation by pulsed direct current sputtering in a reactive gas admixture. *Applied Physics Letters*, 103(3), 2013.

[97] J. A. Gonzalez, J. P. Andres, J. A. De Toro, P. Muniz, T. Munoz, O. Crisan, C. Binns, and J. M. Riveiro. Co-CoO nanoparticles prepared by reactive gas-phase aggregation. *Journal of Nanoparticle Research*, 11(8):2105–2111, 2009.

[98] Tilo Peter, Oleksandr Polonskyi, Björn Gojdka, Amir Mohammad Ahadi, Thomas Strunskus, Vladimir Zaporojtchenko, Hynek Biederman, and Franz Faupel. Influence of reactive gas admixture on transition metal cluster nucleation in a gas aggregation cluster source. *Journal of Applied Physics*, 112(11):1–7, 2012.

[99] Aleš Marek, Jan Valter, Stanislav Kadlec, and Jiří Vyskočil. Gas aggregation nanocluster source - Reactive sputter deposition of copper and titanium nanoclusters. *Surface and Coatings Technology*, 205(SUPPL. 2):573–576, 2011.

[100] Michael W Majeski, Igor L Bolotin, and Luke Hanley. Cluster Beam Deposition of Cu2-xS Nanoparticles into Organic Thin Films. *ACS Applied Materials and Interfaces*, 6:12901–12908, 2014.

[101] Yanping Chen, Kui Ding, Ling Yang, Bo Xie, Fengqi Song, Jianguo Wan, Guanghou Wang, and Min Han. Nanoscale ferromagnetic chromium oxide film from gas-phase nanocluster deposition. *Applied Physics Letters*, 92(17):2008–2010, 2008.

[102] Martin J. Cuddy, Kenton P. Arkill, Zhi Wei Wang, Hannu-Pekka Komsa, Arkady V. Krasheninnikov, and Richard E. Palmer. Fabrication and atomic structure of size-selected, layered MoS2 clusters for catalysis. *Nanoscale*, 6(21):12463–12469, 2014.

[103] Daniel Escalera-Lopez, Yubiao Niu, Jinlong Yin, Kevin Cooke, Neil V. Rees, and Richard E. Palmer. Enhancement of the Hydrogen Evolution Reaction from Ni-MoS2 Hybrid Nanoclusters. *ACS Catalysis*, 6(9):6008–6017, 2016.

[104] L. van Haandel, G. M. Bremmer, E. J M Hensen, and Th Weber. Influence of sulfiding agent and pressure on structure and performance of CoMo/Al2O3 hydrodesulfurization catalysts. *Journal of Catalysis*, 342:27–39, 2016.

[105] S Doniach and M Sunjic. Many-electron singularity in X-ray photoemission and X-ray line spectra from metals. *Journal of Physics C: Solid State Physics*, 3(2):285–291, 1970.

[106] Albert Bruix, Henrik Gøbel Füchtbauer, Anders K Tuxen, Alexander S Walton, Mie Andersen, Søren Porsgaard, Flemming Besenbacher, Bjørk Hammer, and Jeppe V Lauritsen. In Situ Detection of Active Edge Sites in Single-Layer MoS2 Catalysts. *ACS nano*, (9):9322–9330, 2015.

[107] J. H. Nielsen, L. Bech, K. Nielsen, Y. Tison, K. P. Jørgensen, J. L. Bonde, S. Horch, T. F. Jaramillo, and I. Chorkendorff. Combined spectroscopy and microscopy of supported MoS2 nanoparticles. *Surface Science*, 603(9):1182–1189, 2009.

[108] B. Guichard, M. Roy-Auberger, E. Devers, C. Legens, and P. Raybaud. Aging of Co(Ni)MoP/Al2O3 catalysts in working state. *Catalysis Today*, 130(1):97–108, 2008.

[109] K. Marchand, C. Legens, D. Guillaume, and P. Raybaud. A Rational Comparison of the Optimal Promoter Edge Decoration of HDT NiMoS vs CoMoS Catalysts. *Oil and Gas Science and Technology*, 64(6):719–730, 2009.

[110] R T Poole, P C Kemeny, J Liesegang, J G Jenkin, and R C G Leckey. High resolution photoelectron studies of d bands of some metals. *Journal of Physics F*, 3(3):L46–L48, 1973.

[111] Claudia L. Bianchi, Maria G. Cattania, and Pierangela Villa. XPS characterization of Ni and Mo oxides before and after "in situ" treatments. *Applied Surface Science*, 70-71(PART 1):211–216, 1993.

[112] C.H. Li and P.K.S. Tam. An iterative algorithm for minimum cross entropy thresholding. *Pattern Recognition Letters*, 19(8):771–776, 1998.

[113] Jakob Kibsgaard, Thomas F. Jaramillo, and Flemming Besenbacher. Building an appropriate active-site motif into a hydrogen-evolution catalyst with thiomolybdate [Mo3S13]2- clusters. *Nature Chemistry*, 6(3):248–253, 2014.

[114] Daniel Merki, Heron Vrubel, Lorenzo Rovelli, Stéphane Fierro, and Xile Hu. Fe, Co, and Ni ions promote the catalytic activity of amorphous molybdenum sulfide films for hydrogen evolution. *Chemical Science*, 3(8):2515, 2012.

[115] Y Hori, K. Kikuchi, and Shin Suzuki. Production of CO and CH4 in Electrochemical Reduction of CO2 at Metal Electrodes in Aqueous Hydrogencarbonate Solution. *Chemistry Letters*, pages 1695–1698, 1985.

[116] Y. Hori, A. Murata, and R. Takahashi. Formation of hydrocarbons in the electrochemical reduction of carbon dioxide at a copper electrode in aqueous solution. *Journal of the Chemical Society, Faraday Transactions 1: Physical Chemistry in Condensed Phases*, 85(8):2309, 1989.

[117] C. W. Li and M. W. Kanan. CO2 Reduction at Low Overpotential on Cu Electrodes Resulting from the Reduction of Thick Cu2O Films. pages 10–13, 2012.

[118] Min Liu, Yuanjie Pang, Bo Zhang, Phil De Luna, Oleksandr Voznyy, Jixian Xu, Xueli Zheng, Cao Thang Dinh, Fengjia Fan, Changhong Cao, F. Pelayo García de Arquer, Tina Saberi Safaei, Adam Mepham, Anna Klinkova, Eugenia Kumacheva, Tobin Filleter, David Sinton, Shana O. Kelley, and Edward H. Sargent. Enhanced electrocatalytic CO2 reduction via field-induced reagent concentration. *Nature*, 537(7620):382–386, 2016.

[119] Christina W Li, Jim Ciston, and Matthew W Kanan. Electroreduction of carbon monoxide to liquid fuel on oxide-derived nanocrystalline copper. *Nature*, 508(7497):504–7, 2014.

[120] Xiaofeng Feng, Kaili Jiang, Shoushan Fan, and Matthew W. Kanan. A Direct Grain-Boundary-Activity Correlation for CO Electroreduction on Cu Nanoparticles. *ACS Central Science*, 2(3):169–174, 2016.

[121] Arnau Verdaguer-Casadevall, Christina W. Li, Tobias P. Johansson, Soren B. Scott, Joseph T. McKeown, Mukul Kumar, Ifan E L Stephens, Matthew W. Kanan, and Ib Chorkendorff. Probing the Active Surface Sites for CO Reduction on Oxide-Derived Copper Electrocatalysts. *Journal of the American Chemical Society*, 137(31):9808–9811, 2015.

[122] Hemma Mistry, Ana Sofia Varela, Cecile S. Bonifacio, Ioannis Zegkinoglou, Ilya Sinev, Yong-Wook Choi, Kim Kisslinger, Eric A. Stach, Judith C. Yang, Peter Strasser, and Beatriz Roldan Cuenya. Highly selective plasma-activated copper catalysts for carbon dioxide reduction to ethylene. *Nature Communications*, 7:12123, 2016.

[123] André Eilert, Filippo Cavalca, F. Sloan Roberts, Jürg Osterwalder, Chang Liu, Marco Favaro, Ethan J. Crumlin, Hirohito Ogasawara, Daniel Friebel, Lars G.M. Pettersson, and Anders Nilsson. Subsurface Oxygen in Oxide-Derived Copper Electrocatalysts for Carbon Dioxide Reduction. *Journal of Physical Chemistry Letters*, 8(1):285–290, 2016.

[124] Karen Chan, Charlie Tsai, Heine A. Hansen, and Jens K. Nørskov. Molybdenum sulfides and selenides as possible electrocatalysts for CO 2 reduction. *ChemCatChem*, 6(7):1899–1905, 2014.

[125] Yanwei Lum, Youngkook Kwon, Peter Lobaccaro, Le Chen, Ezra Lee Clark, Alexis T. Bell, and Joel W. Ager. Trace Levels of Copper in Carbon Materials Show Significant Electrochemical CO2 Reduction Activity. *ACS Catalysis*, 6(1):202–209, 2016.

[126] Chung Shou Chen, Albertus D. Handoko, Jane Hui Wan, Liang Ma, Dan Ren, and Boon Siang Yeo. Stable and selective electrochemical reduction of carbon dioxide to ethylene on copper mesocrystals. *Catal. Sci. Technol.*, 5(1):161–168, 2015.

[127] F. Sloan Roberts, Kendra P. Kuhl, and Anders Nilsson. Electroreduction of Carbon Monoxide over a Copper Nanocube Catalyst: Surface Structure and pH Dependence on Selectivity. *ChemCatChem*, 8(6):1119–1124, 2016.

[128] Klaas Jan P Schouten, Zisheng Qin, Elena Pérez Gallent, and Marc T M Koper. Two pathways for the formation of ethylene in CO reduction on single-crystal copper electrodes. *Journal of the American Chemical Society*, 134(24):9864–9867, 2012.

[129] Chuan Shi, Heine a Hansen, Adam C Lausche, and Jens K Nørskov. Trends in electrochemical CO2 reduction activity for open and close-packed metal surfaces. *Physical chemistry chemical physics : PCCP*, 16(10):4720–7, 2014.

[130] Ruud Kortlever, Jing Shen, Klaas Jan P Schouten, Federico Calle-Vallejo, and Marc T M Koper. Catalysts and Reaction Pathways for the Electrochemical Reduction of Carbon Dioxide. *Journal of Physical Chemistry Letters*, 6(20):4073–4082, 2015.

[131] Joseph H Montoya, Chuan Shi, Karen Chan, and Jens K Nørskov. Theoretical Insights into a CO Dimerization Mechanism in CO2 Electroreduction. *The Journal of Physical Chemistry Letters*, 6(11):2032–2037, 2015.

[132] Ronald Inglehart, Roberto Foa, Christopher Peterson, and Christian Welzel. Development, Freedom, and Rising Happiness: A Global Perspective (1981-2007). *Perspectives on Psychological Science*, 3(4):264–285, 2008.

[133] Ken Wilber. *A Brief History of Everything.* Shambala Publications, Inc., 1996.

Appendix A

Personal Thoughts on Sustainable Development

The political focus on enhancing economic growth is understandable, since it is an immensely important aspect of societal progress. But it should be remembered that economic growth has no intrinsic value in itself; rather, the economy should be seen as an instrument for making people's lives better.

Inglehart et al. has conducted a very interesting study where they correlate the subjective feeling of well-being (SWB) of citizens in different countries with the gross national product (GDP) per capita of that country [132], the results of which can be seen in Figure A.1. There are two major take-home messages in the figure: Firstly, poor countries generally have lower SWB than rich countries. Secondly, after a certain amount of wealth is attained, the SWB only increases insignificantly. In this light, one could formulate three very general criteria for healthy sustainable development[1]:

1 Economic growth in developing countries is needed to bring the poorest countries up to a certain material standard of living.

2 Richer countries should focus on improving the perceived quality of life for their citizens without a narrow focus on economy.

3 Criteria 1 and 2 should be obtained in a sustainable way.

The overall goal of my Ph.D. lies within the third criterion - helping to make development possible in a sustainable way by better catalyst technology. But for the interested readers, I will provide a few personal thoughts on the broader perspectives of sustainable development, which are especially important for the richer countries, where economic growth seems to have lost its power to increase the subjective well-being of its citizens (criterion 2).

[1] I got the general idea for these three criteria from a young, Danish philosopher, but the source has since been removed from the internet.

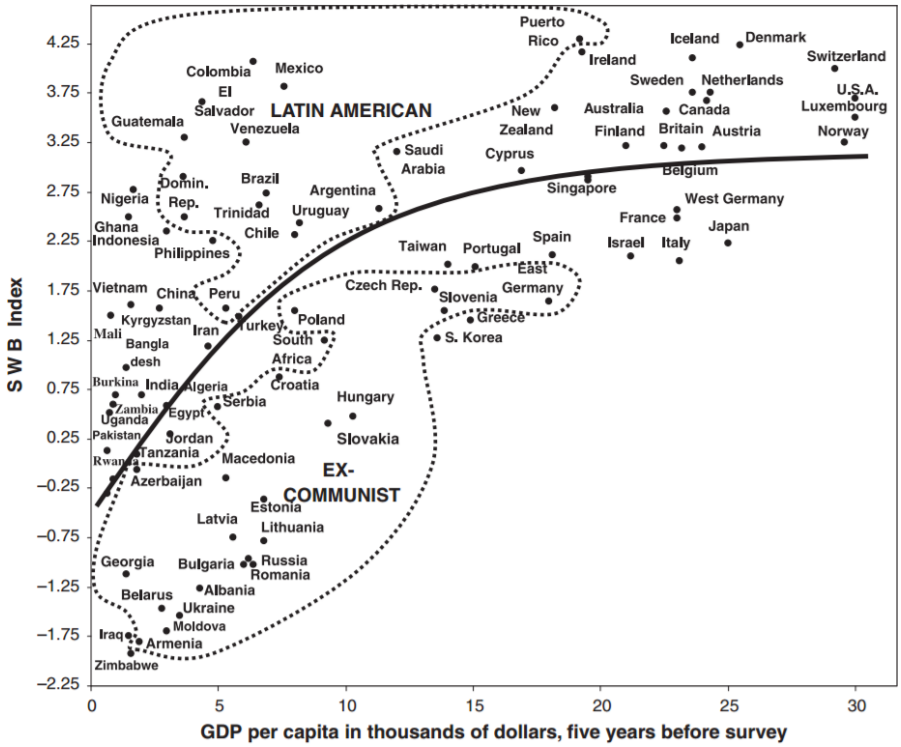

Figure A.1: The subjective well-being (SWB) plotted as a function of GDP per capita. Although richer countries are in general happier, the richest countries are not greatly affected by increases in GDP. Interestingly, economic differences cannot explain large regional variations, as evidenced by the difference between Latin America and Ex-communist countries. The GDP is taken five years before the SWB survey to ensure that the effects of changes in the economy was felt by the population. The figure is reproduced from [132].

The Sustainable Transition in a Broader Perspective

One of the striking features of Figure A.1 is the difference in SWB between Latin America and ex-communist countries. This division cannot be explained by economy alone, and a broader framework thus seem to be necessary. I personally find the so-called "4-quadrant" model which was developed by the philosopher Ken Wilber (see e.g. [133]), to be an interesting candidate for such a framework.

In Figure A.2, I present a (very generalized) overview of the aspects of human existence that are involved in the sustainable transition. The figure is divided into four quadrants. The left-hand side describe subjective concepts, whereas the right-hand side deals with objective matters. The top quadrants deal with the individual concepts/matters, whereas the lower quadrants explain the relation of those individuals to each other in a system.

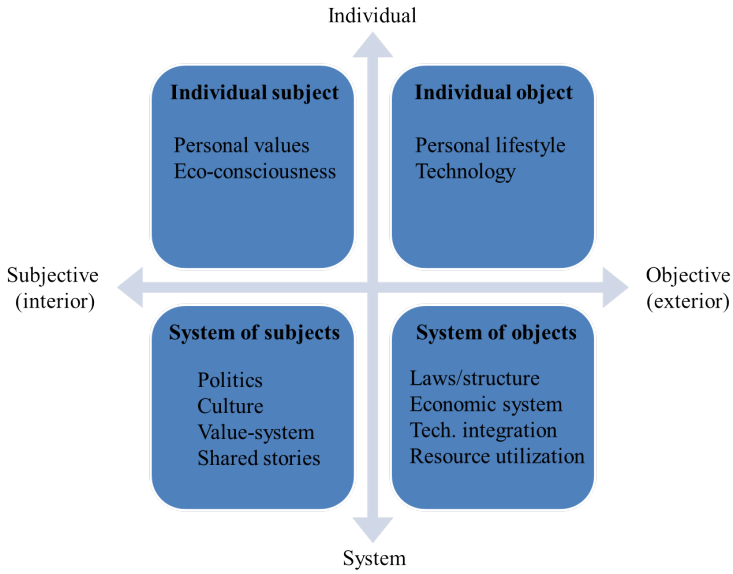

Figure A.2: Aspects of human existence that will have to be adressed in the transition to a more sustainable civilisation, grouped into four quadrants according to Wilber's four-quadrant model.

The upper left quadrant (UL) thus describes the individual subject's experience of e.g. personal meaning and values. Any individual is also born into a cultural context which is described by the lower left quadrant (LL), the "inter-subjective" component of life. Moving to the right-hand of the figure, we start with the upper left (UR) quadrant, which deals with the observable behaviour of objects. In this case the object may be a person leading a life with a certain lifestyle, or it may be the understanding or development of a certain technology. These individual objects also function in a system, described by the lower right quadrant (LR).

All of the quadrants influence each other. For instance, a certain personal belief (UL) can translate into a specific type of political agency (LL), which can influence the laws and structures of society (LR), leading to the predominance of a certain lifestyle (UR). Therefore, the sustainable transition has to take place in *all four quadrants simultaneously.* We need to develop our personal values, our shared culture and political ideologies, our individual life-styles and the technologies that we use, and our societal and economic structures. None of the quadrants can solve the problem on their own, and a narrow focus on technology (UR) or economy (LR) will not be sufficient to ensure a sustainable future.

Appendix B

Development of Synthesis Procedure for Ni-Mo-S Nanoparticles

This appendix describes the development process of the procedure used for synthesizing in-flight sulfided Ni-Mo-S nanoparticles. I hope that the details can help future researchers avoid some of the pitfalls that I encountered.

Initial Attempts

In my first attempts to produce in-flight sulfided particles, I used a pure Mo target and simply added minute amounts of H_2S to the gas flows into the aggregation zone, while keeping all other parameters similar to a normal deposition of metallic nanoparticles.

I used a 10 % H_2S diluted in 90 % H_2 and dosed it through a leak valve to a feedthrough behind the magnetron head, while monitoring the pressure in the aggregation zone indirectly through an ion gauge mounted just outside the aggregation zone, aiming a pressure of 5E-6 mbar. At this stage, it was not possible to monitor the pressure inside the aggregation zone, as no gauge was mounted there. After having adjusted the leak valve, I let in Ar at a flow of 65 SCCM just above the molybdenum target (notice that H_2S and Ar are introduced through different feedthroughs). I chose not to dose He, as this would be an unnecessary complication for initial tests.

With these conditions I was able to get deposition currents on the order of 5 pA on a glassy carbon substrate, but XPS of the deposition showed only molybdenum, and no sulfur. Also, the magnetron plasma was highly unstable, with behaviour that indicated electric arcing as described in [30].

Deposition with Pure H_2S

I suspected that the hydrogen gas in the H_2S/H_2 mixture was problematic, and therefore acquired a bottle with pure H_2S (Alpha Gaz, N25 - <1 % impurities). I reduced the target pressure to 1E-6 mbar, and once again ran with an Ar flow of 65 SCCM.

The change of H_2S gas did not remove the arcing behaviour. In order to stabilize the plasma I started to run the power-supply in a current-limited mode, so that a constant current was sustained, whereas earlier users had run the power supply on a voltage-limited setting. It was now possible to achieve deposition currents on the order or 50 pA, but XPS of a sample only showed a S/Mo ratio of 0.26, which is almost an order of magnitude less that what would be expected for MoS_2.

Mixing H_2S with Ar in Gas Flow

In order to increase the sulfur content of the nanoparticles, I moved the leak valve inlet so that the H_2S would be mixed with the Ar stream and thus introduced directly above the molybdenum target. I suspected that H_2S introduction behind the magnetron head had screened the plasma from the H_2S, and thus lowered the sulfur content in the nanoparticles. I once again run with 1E-6 mbar H_2S, but now with a slightly lower Ar flow of 40 SCCM, as this optimized the deposition current.

I now achieved very high deposition currents on the order of 400 pA, but I also noted that the pressure of H_2S during the deposition had increased significantly from 1E-6 mbar to 1E-4 mbar, by measuring the pressure without Ar after deposition. Strangely, XPS of the deposition exclusively showed sulfur and no molybdenum. Later inspection in ISS showed minute amounts of molybdenum besides the large S concentration in the surface. Out of curiosity, I brought the sample to the Center for Electron Nanoscopy (CEN) where Elisabetta Maria Fiordaliso inspected it in SEM, resulting in the image in Figure B.1.

The morphology of this sample is highly unusual for a nanoparticle deposition in several ways: Firstly, the particles have sizes in the micrometer range, secondly they have elongated "cigar"-shapes, thirdly they have a layered structure as evidenced in the higher magnification on Figure B.1 b). EDX performed on the particles indicated that they consist of sulfur, which is consistent with the XPS measurements. It thus seemed as though large quantities of sulfur had been deposited as, or grown into, these peculiar shapes.

All of the above led to a key insight: H_2S might be condensing on the chamber walls, due to the LN_2 cooling, which could explain the gradual increase in H_2S pressure. I speculate that the high H_2S pressure could lead to deposition of the pure sulfur agglomerates.

Throughout the different deposition experiments, I had repeatedly experienced the build-up of contaminants on the magnetron head, which caused it to short-circuit, and forced me to open the chamber to clean it manually. I expect that

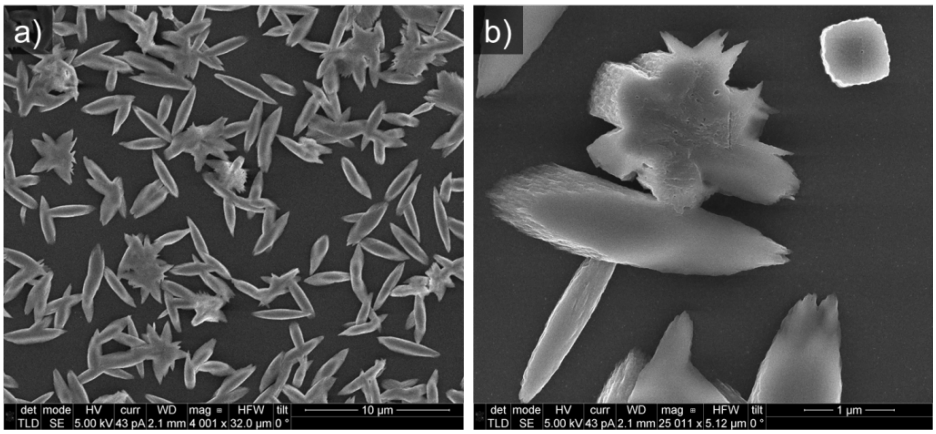

Figure B.1: Scanning electron micrograph of pure sulfur agglomerates deposited on a glassy carbon substrate. Image obtained by Elisabetta Maria Fiordaliso at the Center for Electron Nanoscopy (CEN).

these contaminations were due to H_2S condensation as well.

Removing LN_2 Cooling and Final Iterations in Synthesis Procedure

To avoid H_2S agglomeration, I now decoupled the LN_2 cooling, which resulted in much more stable depositions. The XPS spectra now indicated S/Mo rates in the range from 1-2, accompanied by chemical shifts indicating sulfidation. Thus, a working methodology for producing molybdenum sulfides had been established. However, it proved difficult to reproduce samples, as the H_2S pressure had a tendency to drop during deposition. It was not possible to regulate the leak valve during deposition, as the H_2S pressure was only a perturbation to the total pressure in the aggregation zone, and thus had to be measured before introducing argon.

In order to stabilize the H_2S pressure, I installed a mass-flow-controller to deliver a constant flow. Also, to complement the ion gauge used for the previous measurements, I installed a pirani gauge directly connected to the aggregation zone, making it possible to measure aggregation zone pressures during deposition. With these final modifications, I had established a reproducible methodology for depositing in-flight sulfided molybdenum-nickel sulfides by reactive gas aggregation.

Appendix C

Additional XPS spectra

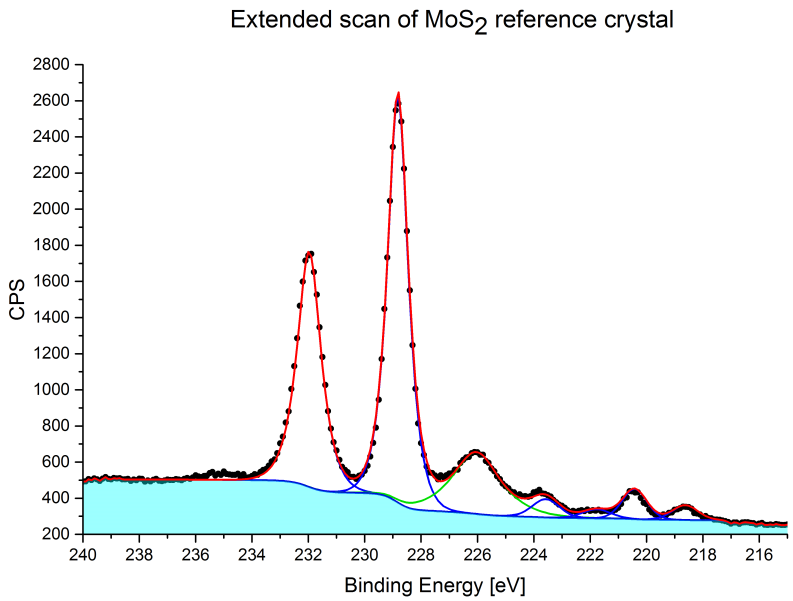

Figure C.1: XPS spectrum showing the Mo3d/S2s lines of a MoS_2 reference single crystal from SPI Supplies, where the satellites from the Mo3d peaks are included in the fit.

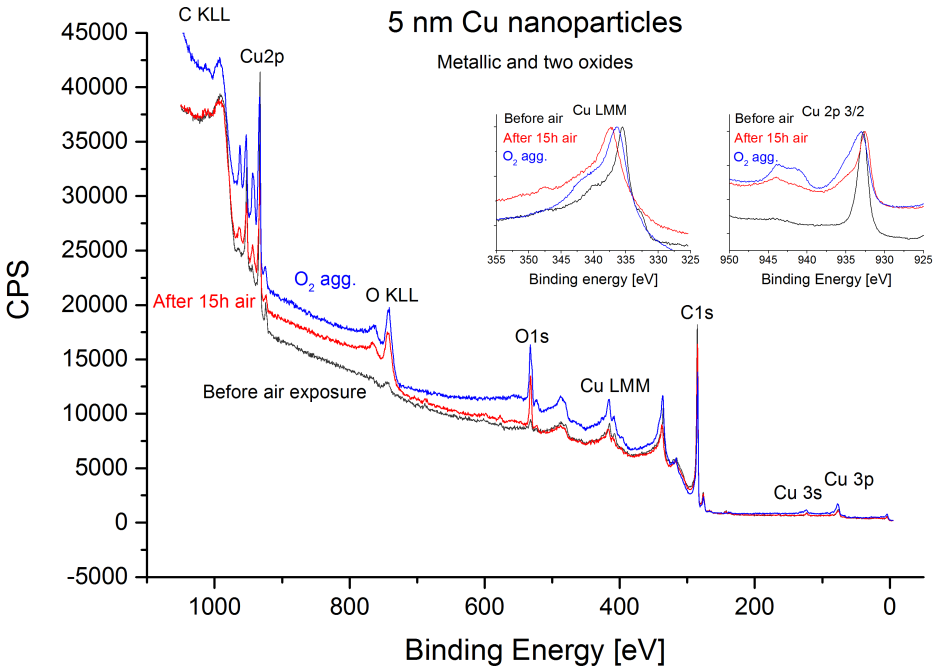

Figure C.2: XPS spectrum showing three copper nanoparticles in three different oxidation states. The black line corresponds to metallic nanoparticles, as deposited with no exposure, the red line is the same nanoparticles after 15 hours of air exposure. The blue spectrum was obtained on CuO_x nanoparticles synthesized by letting O_2 into the aggregation zone during gas aggregation. The spectral shape of the $Cu2p_{3/2}$ and LMM Auger feature suggests that the the particles are metallic before air exposure, in the Cu^+ state after air exposure, and Cu^{2+} if synthesized with O_2 in the aggregation zone (see e.g. http://xpssimplified.com/elements/copper.php). I did not pursue the in-flight oxidized Cu nanoparticle synthesis further.

Appendix D

Outlook – Work in Progress

Stage for Temperature Programmed Desorption

Together with Jakob Ejler Sørensen, who I supervised in his master project, we designed a UHV stage for doing temperature programmed desorption (TPD) in the Omicron setup. The aim was to do CO-TPDs on Cu nanoparticles, which requires cryogenic temperatures. Therefore, we chose a design where samples could be inserted in a LN_2-cooled copper block, where a filament could heat the sample, while the temperature of the sample was measured through a thermocouple. The final design can be seen in Figure D.1. Jakob is currently continuing the work on the TPD-stage in his Ph.D. project.

Cluster/Single Atom Depositions

Towards the end of my P.D, we grew interested in depositing single atoms or small clusters. Figure D.2 a) shows a mass spectrum in the very low mass-range, from single Pt atoms to Pt_{10} clusters. Notice that the sign of the current is reversed as compared to other mass-spectra in this thesis, since the clusters are positively charged. Figure D.2 b) shows a STEM image of a sample with deposited single Pt atoms.

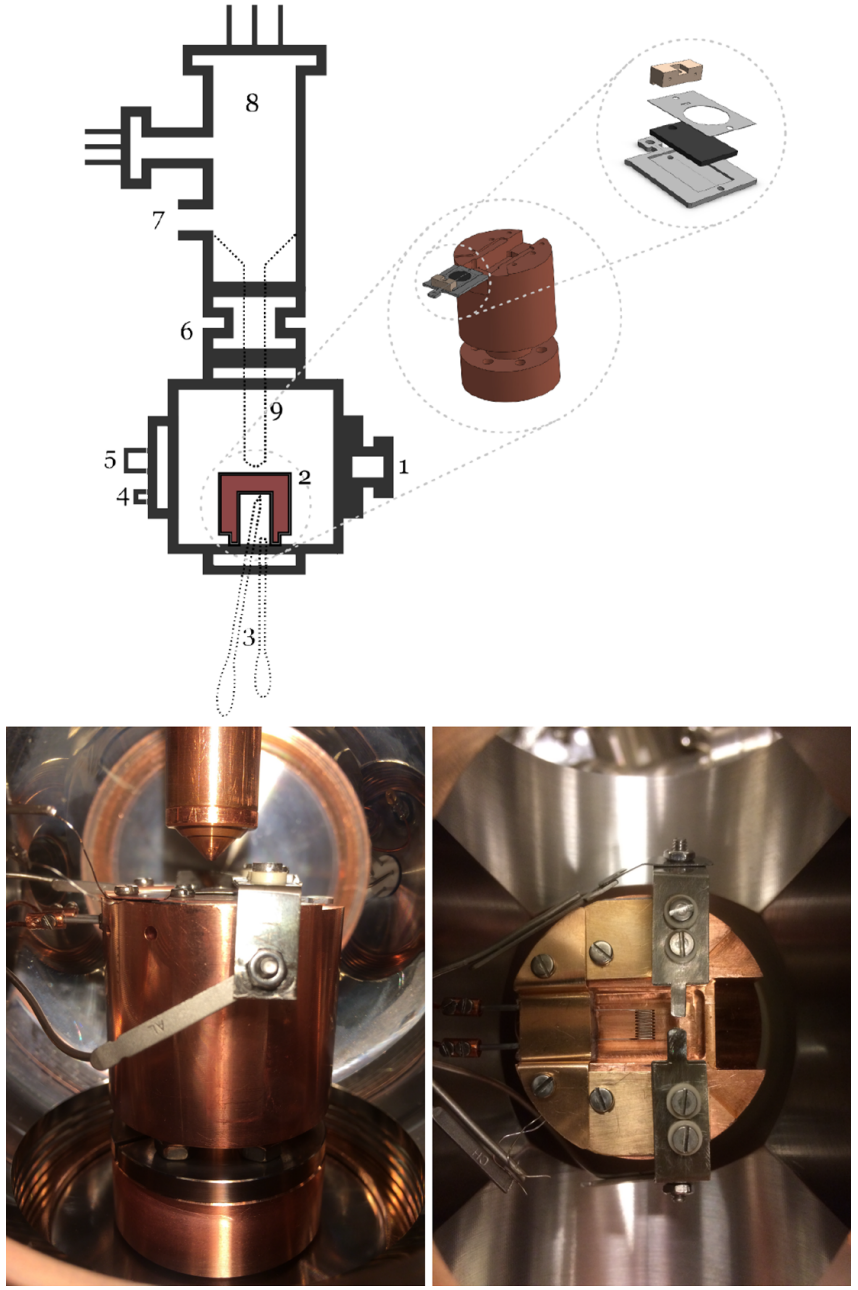

Figure D.1: Top: Sketch of the TPD chamber and stage, where the numbers indicate 1) connector flange to main chamber 2) TPD stage 3) LN_2 feedthroughs 4) Electrical feedthroughs for heating filament 5) Thermocouple feedthrougs 6) Connection to QMS 7) Differential pumping of QMS 8) The QMS 9) QMS sniffer. Bottom: Images of the actual TPD stage. Image from Jakob Ejler Sørensen's master thesis.

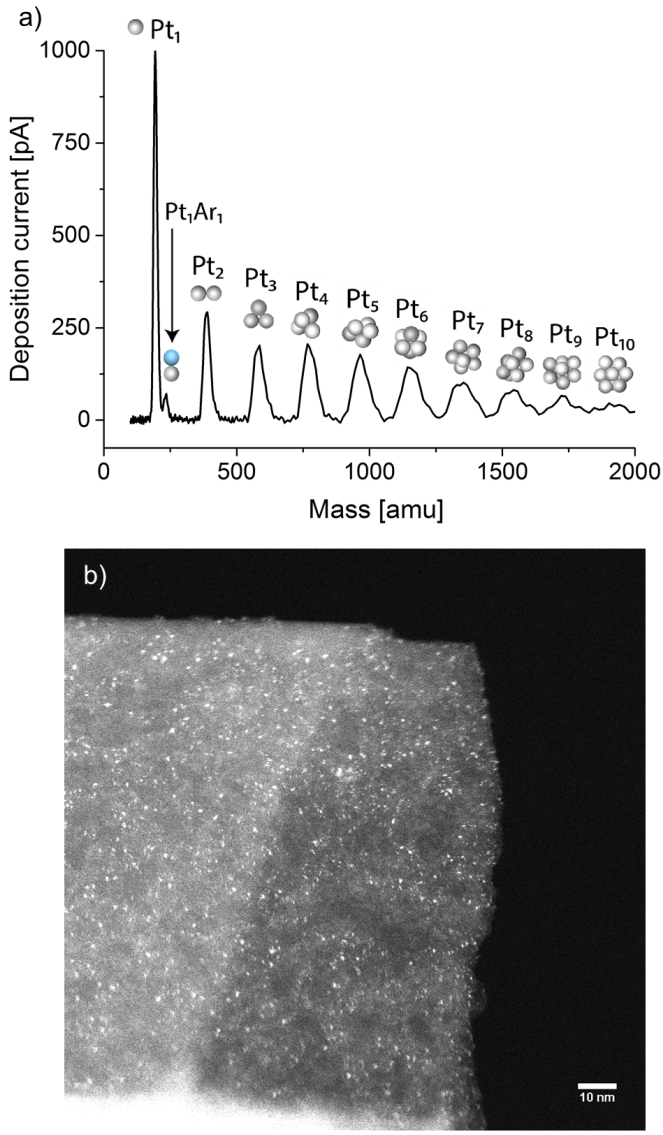

Figure D.2: **a)** Mass spectrum showing Pt clusters produced in the Nanobeam2011 nanoparticle source. **b)** STEM image of single atoms of Pt deposited on a graphene/lacey carbon/Cu TEM grid. Some sintering may have occured, since the bright dots do not appear to have the same size. Further quantification was beyond the scope of my Ph.D. The image was obtained in collaboration with Christian Elkjær at the probe-corrected FEI Titan Analytical 80-300ST TEM located at DTU's Center for Electron Nanoscopy (CEN)

Appendix E

Appended Papers

Paper I: Scalability and Feasibility of Photoelectrochemical H_2 Evolution: The Ultimate Limit of Pt Nanoparticles as an HER Catalyst
E. Kemppainen, **A. Bodin**, B. Sebok, T. Pedersen, B. Seger, B. Mei, D. Bae, P. C. K. Vesborg, J. Halme, O. Hansen, P. D. Lund, and I. Chorkendorff
Energy Environ. Sci., 2015, ***8****, 2991*

Paper II: Engineering Ni−Mo−S Nanoparticles for Ultra-Deep Hydrodesulfurization: Reactive Gas Aggregation Synthesis, Characterization and Catalytic Testing
A. Bodin, A. L. Christoffersen, C. F. Elkjær, J. Kibsgaard, S. Helveg, I. Chorkendorff
In preparation - abstract included

Paper III: Dynamic Effects of Surface Oxygen in CO Electroreduction
S. B. Scott*, D. B. Trimarco*, **A. Bodin***, A. Bagger, N. Mazzanti, J. E. Sørensen, T. Pedersen, O. Hansen, I. E. L. Stephens, P. C. K. Vesborg, J. Rossmeisl, I. Chorkendorff
In preparation
*These authors contributed equally

Paper I: Scalability and Feasibility of Photoelectrochemical H_2 Evolution: The Ultimate Limit of Pt Nanoparticles as an HER Catalyst
E. Kemppainen, **A. Bodin**, B. Sebok, T. Pedersen, B. Seger, B. Mei, D. Bae, P. C. K. Vesborg, J. Halme, O. Hansen, P. D. Lund, and I. Chorkendorff
Energy Environ. Sci., 2015, ***8****, 2991*

Energy & Environmental Science

PAPER

View Article Online
View Journal | View Issue

Cite this: *Energy Environ. Sci.*, 2015, **8**, 2991

Scalability and feasibility of photoelectrochemical H_2 evolution: the ultimate limit of Pt nanoparticle as an HER catalyst†

E. Kemppainen,[a] A. Bodin,[b] B. Sebok,[b] T. Pedersen,[c] B. Seger,[b] B. Mei,[b] D. Bae,[b] P. C. K. Vesborg,[b] J. Halme,[a] O. Hansen,[c] P. D. Lund[a] and I. Chorkendorff*[b]

Received 15th July 2015,
Accepted 25th August 2015

DOI: 10.1039/c5ee02188j

www.rsc.org/ees

The recent surge in investigating electrocatalysts for the H_2 evolution reaction is based on finding a cheap alternative to Pt. However platinum's excellent catalytic activity means very little catalyst needs to be used. The present study combines model experiments with numerical modeling to determine exactly how little catalyst is needed. Specifically we investigate ultra-low Pt loadings for use in photoelectrochemical H_2 evolution using TiO_2–Ti-pn$^+$Si photocathodes. At a current density of 10 mA cm^{-2}, we photocathodically evolve H_2 at +465, +450, +350 and +270 mV *vs.*, RHE at Pt loadings of 1000, 200, 50, and 10 ng cm^{-2} corresponding to HER overpotentials of η_{1000ng} = 32 mV, η_{200ng} = 46 mV, η_{50ng} = 142 mV, and η_{10ng} = 231 mV. To put this in perspective, if 30% of the world's current annual Pt production was used for H_2 evolution catalysis, using a loading of 100 ng cm^{-2} and a current of 10 mA cm^{-2} would produce 1 $TW_{average}$ of H_2. The photoelectrochemical data matched the modeling calculations implying that we were near the fundamental maximum in performance for our system. Furthermore modeling indicated that the overpotentials were dominated by mass transfer effects, rather than catalysis unless catalyst loadings were less than 1000 ng cm^{-2}.

Broader context

In the last decade there has been an enormous push to find a cheaper, more earth-abundant catalyst than Pt for the hydrogen evolution reaction. This push is based on the theory that Pt is un-scalable if society would completely convert to a H_2 based society. Interestingly, there have been relatively few works actually investigating if and how un-scalable using platinum as a H_2 evolution catalyst actually is. In this manuscript we take the specific case of using a photoelectrochemical water splitting device, and determine how little Pt is needed (and thus the scalability) to effectively evolve H_2 from both an experimental and a theoretical modeling standpoint. Our experimental results allow us to come very close to achieving our limit imposed by our modeling, but not surpass it. We feel this verifies the validity of our model, and thus the fundamental limits of Pt for H_2 evolution in our system. From these results we find that the Pt consumed/terawatt would be on the order of 10% of the annual worldwide Pt production (depending upon photocurrent and overpotential). Thus this work should help to quantitatively put into perspective the scalability of Pt for photoelectrochemical water splitting.

Introduction

Currently the primary energy source for electricity and transportation is from fossil fuels, and the replacement of these fuels by hydrogen is one of the ways to continue to fulfil society's energy demand, while simultaneously reducing greenhouse gas emissions.[1,2] While we have ways to convert between hydrogen and electricity (*via* fuel cells and (photo)electrolysers), there are still several challenges that need to be addressed.[2–5]

Renewable hydrogen can be produced using different approaches, *i.e.* electrolysis powered by a renewable source of energy, like wind energy or sunlight. Additionally, an integrated photoelectrocatalytic (PEC) approach, where solar energy is directly converted into hydrogen is also a possibility.[2–5] Nevertheless, industrial scalability of both technologies requires reduction of capital costs to obtain hydrogen prices on a $ per J level compatible to those of today's fossil fuel prices. It is widely considered that capital costs of either electrolysers or PEC devices can be reduced by utilizing cheap and abundantly available materials to drive the hydrogen evolution reaction (HER) or the oxygen

[a] *Department of Applied Physics, New Energy Technologies Group, Aalto University, P.O. Box 14100, FI-00076 AALTO, Finland*
[b] *Department of Physics, CINF, Technical University of Denmark, DK-2800, Kgs. Lyngby, Denmark. E-mail: ibchork@fysik.dtu.dk*
[c] *Department of Micro- and Nanotechnology, Technical University of Denmark, DK-2800, Kgs. Lyngby, Denmark*

† Electronic supplementary information (ESI) available: Simulation details. See DOI: 10.1039/c5ee02188j

evolution reaction (OER) to replace platinum group metals, which are relatively scarce and expensive.[6] In particular in the last 5–10 years fast progress has been made in the development of nonprecious metal HER catalysts to be implemented into these clean-energy technologies.[2,7–14] Nevertheless, to date platinum is still the most widely used HER catalyst due to its world-record exchange current density and low Tafel slope. Additionally, Pt is known to be highly durable in the acidic environments used in electrolysers or PEC devices.[15]

While a low Tafel slope is certainly an important requirement for HER catalysts used in electrolysers, typically operated at high current densities ($\sim$A cm^{-2}), in photoelectrocatalytic devices high Pt exchange current density appears to be a more important criterion when chosen the HER catalyst.[2] This is due to the lower current densities of 5–20 mA cm^{-2}, which PEC devices will operate at due to solar flux limitations. Furthermore, it is often neglected in the development of efficient PEC devices that catalysts (HER or OER) will absorb light reducing the light limited current density provided by the photon absorber. Consequently, the catalysts amount used to drive HER or OER in such a device is a critical issue and significant light absorption by the catalyst material must be reduced.[16]

The best nonprecious metal HER catalysts reported so far can be separated into different classes of materials such as sulphides and phosphides, which usually contain transition metal cations of Mo, Co, Fe, or Ni.[2,10–14] With an overpotential of 50 mV to produce current densities of 10 mA cm^{-2} in acidic electrolytes, FeP nanoparticles are the state-of-the-art nonprecious HER catalysts.[17] Nevertheless exchange current densities are still an order of magnitude lower than that of conventional Pt HER catalysts. In general, high loadings are required for these non-noble HER catalysts to obtain low overpotentials. Hence, cost savings are lower than would be expected and the high-catalyst loading required might prevent the use in PEC devices. Indeed it was recently shown for CoP-modified Si photocathodes that significantly higher mass loadings (10 times) are required to achieve fill factors similar to those of Pt-modified electrodes, which is in agreement with the lower HER activity of CoP.[18] These high loadings of CoP drastically reduced the photocurrent density due to parasitic light absorption decreasing the overall efficiency of the Si-based photocathode.[18] While this might not be an issue for small band gap photocathodes on the backside of a monolithic device, the efficiency will be limited in a design with a large band gap photocathode and Pt appears to be still the optimal choice for HER catalysts in these PEC devices.[16,19] Additionally the stability of these non-precious metal catalysts have yet to be proven. The state-of-the-art FeP dissolves rather fast[17] and the reported data on Ni_2P and CoP also suggest that these materials are far from being stable making it a challenge to utilize them with low coverage.[11,12] It should also be mentioned that although there is no particular reason to believe Pt should not be stable under the conditions described here, there could also be long term issues that have not been realized yet.[20] Thus even though these new classes of recently discovered HER materials are promising alternatives to the conventional Pt-group metals, a material matching the performance of Pt has not yet been reported. Taking this into account Pt appears to be still the optimal choice for HER catalysts in PEC devices and the question arises if Pt HER catalysts might be feasible on a TW level in a PEC device?

With an annual Pt production of 180 ton per year[6] the Pt loading necessary to operate a photocathode at moderate current densities (on the order of 10 mA cm^{-2}),[2,21] and low overpotentials ($<$50 mV) determines the potential for Pt to be used in a PEC device. Only recently have researchers started to probe the idea that ultra-low Pt loadings for the HER could make this catalyst scalable even on the TW level. Dasgupta *et al.*[22] used atomic layer deposition (ALD) to produce Pt nanoparticles on the surface of TiO_2-coated Si microwire arrays. However, due to the procedure and the substrate used, defining an exact limit for the required Pt loading appears to be difficult. Thus, the Pt nanoparticle loadings that were studied ranged from $\sim$280 ng cm^{-2} (per geometrical electrode area) to several micrograms per cm^2, and the Pt nanoparticle size-distribution was loading dependent. Another approach is to nanostructure or pattern the HER catalyst.[23,24] Chen *et al.*[24] investigated patterned Pt structures with different electrode filling fractions to reduce the parasitic light absorption effect of HER catalysts.[24] While the authors obtained quite impressive results from these films, the exact loading was difficult to determine due to surface roughness of the films.

In this work we investigate ultra-low loadings of Pt nanoparticles for scalable photocathodic H_2 evolution. This approach differs from the film based approach and allows us a uniform dispersion of platinum across our electrode. While we use a cluster-source sputtering approach to optimize the conditions, there are many methods to produce nanoparticles cheaper *via* solution based methods.

In this work we use well defined, size-selected Pt nanoparticles (diameter of 5 nm). The photoelectrocatalytic performance of planar TiO_2-protected n^+p-Si photocathodes in acidic solutions was investigated experimentally. Furthermore, a model combining the effects of mass transport, equilibrium hydrogen coverage and HER kinetics was used to describe the current–overpotential characteristics of these planar Si-photoelectrodes partially covered with Pt HER nanoparticles. The effect of mass transport and HER kinetics on the catalytic properties of individual Pt particles and the photoelectrode assemblies were assessed by this model and a good agreement between the experimental and theoretical data was obtained. Thus, using a combined experimental and theoretical approach the Pt HER catalyst amount needed for TW scale-up was assessed. The data provided here shows the dependence of Pt nanoparticle loading on overpotential for hydrogen evolution. For an acceptable HER overpotential of 50 mV, 54 tons of Pt metal, corresponding to a coverage of 100 ng cm^{-2} Pt (d = 5 nm) on a planar electrode, is required to achieve a TW scale-up with a PEC device operated at 10 mA cm^{-2} (12% solar-to-hydrogen efficiency). If larger overpotentials for HER are feasible, even lower Pt utilization is possible. This works shows that the use of Pt nanoparticles HER catalyst may potentially be a viable option for terawatt scale PEC applications.

It should be noted that for any PEC device, there needs to be a corresponding anodic reaction. While understanding these

anodic reactions (such as O_2 evolution) is important, this work only focuses on photocathodic H_2 evolution and its corresponding overpotential and does not analyse anodic reactions or their corresponding overpotentials. For readers interested in how overpotentials at both electrodes effect photocatalytic efficiency we refer to the excellent review by Walter *et al.*[25] and more recent works by Hu *et al.*[26] and Seitz *et al.*[27]

Experimental

Preparation of TiO_2-protected Si-based photocathodes

TiO_2 protected silicon photocathodes with n^+p junctions were produced as in our previous work.[19,28]

Preparation of Pt nanoparticle and electrochemical characterization

Mass-selected Pt nanoparticles were produced in a five-step process by (1) sputtering a Pt target with Ar^+-ions in a magnetron sputter head, (2) allowing the sputtered Pt to condense into nanoparticles in a LN_2-cooled "aggregation zone", where both He and Ar was present to facilitate faster aggregation,[29] (3) super-sonic expanding the nanoparticles from the aggregation zone into UHV through an aperture and into an electronic lens system, which focuses the negatively charged particles into a narrow beam, (4) mass-selecting the nanoparticles in a lateral time-of-flight mass-selector,[30] and (5) landing the particles on the substrate.

The particle production was conducted in a Nano-Beam 2011 nanoparticle source (Birmingham Instruments Inc.) with a base pressure in the low 10^{-10} mbar range, which is connected to another UHV system (Omicron NanoTechnology), wherein the nanoparticles are deposited. This latter chamber is equipped with characterization techniques such as XPS (SPECS XR 50 X-ray gun coupled to Omicron NanoSAM 7 channel energy analyser), ISS (Omicron ISE100 ion gun) and SEM (ZEISS UHV-Gemini Supra), and has a base pressure in the low 10^{-11} mbar range. For further details about the preparation of mass selected nanoparticles see Hernandez-Fernandez *et al.*[31]

Platinum particles having a mass of 850 000 amu were deposited on the planar TiO_2-protected Si photocathodes with calculated loadings of 10, 50, 200 and 1000 ng cm^{-2}, respectively. The deposited photocathodes were characterized in UHV with XPS using Mg Kα radiation. Furthermore, one additional sample for each loading was made, for investigation with SEM. The 10 ng cm^{-2} sample was also investigated with ISS, in order to verify that Pt was on the surface.

The mass of 850 000 amu was chosen for the time-of-flight mass-selector because it corresponds to a particle diameter of 5 nm. The size distribution of the deposited nanoparticles was determined with *ex situ* TEM imaging (Tecnai T20 G2) with samples prepared on TEM grids under the same deposition conditions as the photocathodes. (Higher resolution TEM images can be found in the ESI†.) The size of the nanoparticles on the pictures was examined using the software ImageJ. Only particles with circularity between 0.8–1 were analysed in order to avoid taking into account particles that were landed on top of each other. SEM images were taken of one sample of each loading. The images were obtained with an acceleration voltage of 7 kV, and a beam current of 400 pA with an in-lens detector, which detects almost exclusively secondary electrons in order to visualize the topography of the surface.

All Pt wires were cleaned immediately before use in photoelectrochemical testing. Cleaning consisted first of a 15 second rinse in fresh aqua regia, then thorough washing in millipore water. Finally the electrodes were flame annealed.

For the photoelectrochemical measurements, a Bio-Logic VSP potentiostat along with EC Lab software was used. The photoelectrochemical H_2 evolution experiments were performed in a three-electrode cell with an H-cell design and a glass frit between the working and counter electrode compartments to prevent any crossover. The experiments were carried out in an aqueous 1 M $HClO_4$ (Aldrich 99.99%) solution. The electrolyte was cleaned overnight using a chronoamperometric measurement with two Pt mesh electrodes used as working and counter electrodes. For PEC measurements a Pt mesh counter electrode and saturated $Hg/HgSO_4$ reference electrode (VWR International) were used. The solution was saturated with hydrogen gas 30 minutes before the start of any experiment, and for the entire duration of the experiment.

A 1000 W xenon lamp (Oriel) was used with a 635 nm cut-off filter and an AM1.5 filter to simulate the red part of the solar spectrum. The light intensity reaching the sample was calibrated to match that of the total light intensity of the red part of the solar spectrum ($\lambda > 635$ nm, 38.6 mW cm^{-2}). For all cyclic voltammograms (CV's) the electrodes were scanned at a sweep rate of 50 mV s^{-1}. The 3rd anodic sweep is shown in all graphs. The actual loading of Pt nanoparticles was verified using Inductively Coupled Plasma Mass Spectrometry (ICP-MS, iCAP-QC ICP-MS, Thermo Fisher Scientific) after dissolving the size-selected Pt nanoparticles in aqua regia solution. For all samples, the ICP-MS results closely matched that determined from the cluster source deposition.

Simulation details

All calculations were done for a model system where spherical Pt nanoparticles of 5 nm diameter were simulated. It was assumed that each Pt nanoparticle was embedded 0.25 nm into a 100 nm thick TiO_2 substrate (Fig. 1). This means that 95% of its (free sphere-) surface area was exposed to electrolyte. The conductivity of the TiO_2 substrate was assumed to be 1 S m^{-1},[32] corresponding to slightly reduced TiO_2 but it could be much lower without affecting the modelling results (Table 1). The electrode was assumed to be an array of identical unit cells, so to simplify calculations it was simulated as a single Pt particle in a 2D cylindrical unit cell, corresponding to a diffusional domain approximation with uniform particle spacing.[33,34] Periodic boundary conditions were replaced by zero-flux boundary conditions at the outer edge of the cell, whose area (*i.e.* radius, R_{cell}) corresponds to the average Pt loading (L_{Pt}) over the electrode area.

$$R_{cell} = \frac{d_{c-c}}{2} = \sqrt{\frac{4{r_{Pt}}^3 \rho_{Pt}}{3L_{Pt}}} \quad (1)$$

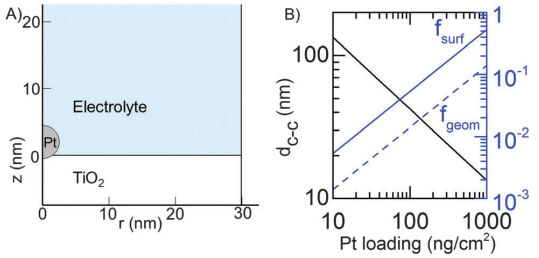

Fig. 1 (A) Detail of the model geometry near the Pt particle. Symmetry axis is at $r = 0$ and the vertical line at $r \approx 30$ nm is the outer wall of the simulation cell (Pt loading is 50 ng cm^{-2}). The TiO_2 substrate continues to $z = -100$ nm and electrolyte to $z = 100$ μm. (B) The properties of the simulated unit cell. The black line shows the average center-to-center distance of the platinum nanoparticles as a function of the loading. The solid blue line shows the ratio of Pt surface area to the geometrical electrode area (f_{surf}) and the dashed blue line the fraction of the electrode area covered with Pt (f_{geom}).

where d_{c-c} is the average center-to-center distance between nearest neighbor nanoparticles, r_{Pt} the radius of the nanoparticles (2.5 nm), ρ_{Pt} the density of Pt (21.45 g cm^{-3}) and L_{Pt} the amount of Pt per electrode area (10–1000 ng cm^{-2}). As shown in Fig. 1 a Pt loading of 10 ng cm^{-2} corresponds to an average center-to-center d_{c-c} of 134 nm, while a Pt loading of 1000 ng cm^{-2} corresponds to about a 13.4 nm distance. For comparison, simulations were performed for a TiO_2 film covered with a 2.5 nm thick uniform Pt film, later referred to as "flat Pt". The radius of the simulation cell was set to 50 nm in that case.

The current density $i_{Pt/geom}$ was calculated by integrating the local current density at the Pt surface over the exposed surface area and dividing it by either the exposed Pt area (A_{Pt}) or the area of the unit cell (A_{geom}).

The steady state was calculated with a transient simulation starting from equilibrium conditions at 0 V *vs.* RHE. The concentration profiles took at most about 10 seconds simulation time to converge to steady state, and all simulations were run for 20 s simulation time to ensure steady state. *IV*-curves were calculated using the state at the last calculated time point.

To facilitate comparisons between simulated overpotential and measured *IV*-curves of the whole devices, the effect of the silicon PV cell was simulated with the *IV*-curve of an ideal PV cell

$$i = i_{Ph} + i_{rec}\left(e^{\frac{q_e V}{nk_B T}} - 1\right) \quad (2)$$

where i_{Ph} is the photocurrent density (and in this model also the short circuit current density), i_{rec} corresponds to recombination rates in the device, V is the photovoltage, and n is the ideality factor. With PV cells made of silicon diffusion current ($n = 1$) dominates the *IV* curve near the open circuit voltage, so $n = 1$ was used to simulate the losses in the PV device.[39] Under the chosen illumination ($\lambda > 635$ nm, 38.6 mW cm^{-2}) the maximum photocurrents of the measured Si-based photocathodes were determined to be between −22 and −22.4 mA cm^{-2} and the average open circuit voltage was 0.495 V *vs.* RHE in agreement with previous reports on similar Si-based photocathodes.[28] Therefore, i_{Ph} and $V = V_{OC}$ were chosen to be −22.0 mA cm^{-2} and 0.495 V *vs.* RHE ($i_{rec} = 9.8196 \times 10^{-8}$ mA cm^{-2}), respectively. The material properties and simulation parameters used in this work are summarized in Table 1 (for further information about the simulations, *e.g.* the hydrogen evolution kinetics see ESI†).

Results and discussion

Characterization of size-selected Pt nanoparticles

TEM images of the Pt nanoparticles were taken from different areas of the Cu TEM grids they were deposited on, and the resulting size distribution along with a close-up picture of typical particles (Fig. 2A) is shown in Fig. 2. According to the determined size-distribution, the average particle size is 5.0 ± 0.3 nm.

Table 1 Material properties and simulation parameters

Symbol	Explanation	Value
T	Temperature	298.15 K
h_{el}	Electrolyte diffusion layer thickness	5 μm
h_{TiO_2}	TiO_2 layer thickness	100 nm
σ_{TiO_2}	Conductivity of TiO_2	1 S m^{-1} [32]
d_{Pt}	Pt particle diameter	5 nm
ρ_{Pt}	Pt density	21 450 kg m^{-3} [35]
σ_{Pt}	Pt conductivity	9.43×10^6 S m^{-1} [35]
$i_{0,V}$	Volmer reaction exchange current density	100 mA cm^{-2} [36]
r_H	Ratio of Heyrovsky and Volmer rates	0 [36]
r_T	Ratio of Tafel and Volmer rates	9.5
Θ^0	Equilibrium H-coverage	0.67 [37]
$c_{H^+,0}$	Bulk proton concentration	1.0 M
$c_{H_2,0}$	Bulk H_2 concentration	0.7698 mM [38]
D_{H^+}	Proton diffusion coefficient	9.3110×10^{-5} cm^2 s^{-1} [35]
$D_{ClO_4^-}$	Perchlorate ion diffusion coefficient	1.7908×10^{-5} cm^2 s^{-1} [35]
D_{H_2}	H_2 diffusion coefficient	5.1100×10^{-5} cm^2 s^{-1} [35]
μ_{H^+}	Proton mobility	3.624×10^{-3} cm^2 (V s)$^{-1}$ [35]
$\mu_{ClO_4^-}$	Perchlorate ion mobility	6.970×10^{-4} cm^2 (V s)$^{-1}$ [35]
i_{ph}	Si PV-cell photocurrent density	−22.0 mA cm^{-2}
V_{oc}	Si PV-cell open circuit voltage	0.495 V *vs.* RHE
i_{rec}	Recombination current density	9.8196×10^{-8} mA cm^{-2}

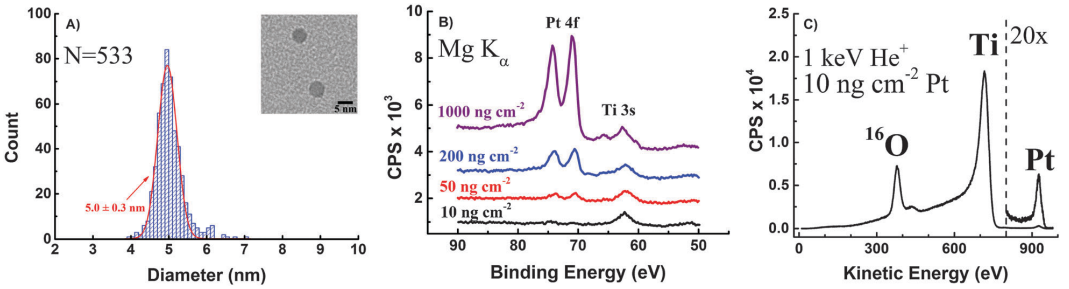

Fig. 2 Characterization of size-selected Pt nanoparticles: (A) size-distribution of the deposited Pt nanoparticles determined by bright-field TEM imaging and Gaussian distribution fitted to the data (red curve). The inset shows a close-up of typical particles. (B) XPS spectra of Pt 4f peaks for different particle loadings. (C) ISS spectra of a sample with 10 ng cm^{-2} Pt loading confirming the successful deposition of Pt particles.

Furthermore, Pt nanoparticles deposited on TiO_2-protected Si photocathodes were investigated by XPS. Wide range survey spectra only showed O, Ti, C and Pt on the surface of the samples confirming that the Si surface was fully covered by a TiO_2 film (Fig. S2 in ESI†).

Detailed spectra of the region around the Pt 4f peaks taken in case of each loading are shown in Fig. 2B.

The Pt 4f peak is decreasing with each loading and finally disappears in case of the 10 ng cm^{-2} Pt loading due to the low loading, which is below the detection limit of XPS. However, significant catalytic activity and reasonably low overpotentials were determined for the sample with 10 ng cm^{-2} Pt loading, meaning that Pt contaminations (*e.g.* during catalyst preparation or from the electrolyte) below the detection limit of XPS could significantly contribute to the activity of presumably Pt-free materials. Thus, XPS analysis is certainly not a reliable way to prove the absence of Pt in non-noble metal catalyst used in ORR or HER reaction and surface spectroscopic methods with much higher sensitivity are required to unambiguously show the absence of trace amounts of noble metals like Pt. Here, in order to have spectroscopic evidence for the successful deposition of 10 ng cm^{-2} Pt on TiO_2-protected Si photocathodes, the sample was further investigated using ISS. The peak at approx. 927 eV can clearly be assigned to Pt (Fig. 2C). The intensity of the signal suggests that even lower Pt loadings can be easily identified using ISS which makes ISS more suitable for detecting trace amounts of Pt in non-noble metal catalysts.

Finally, each of the 4 different loading Pt samples were investigated with SEM. Pt particles can be seen as bright dots on the rough TiO_2 substrate, and the differences in coverage's are clearly distinguishable (Fig. 3).

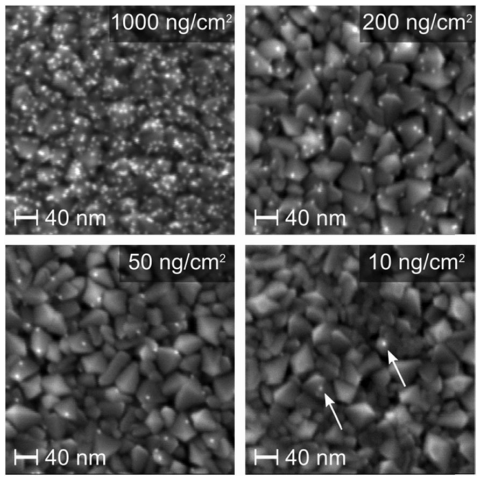

Fig. 3 SEM micrographs of four samples of different Pt nanoparticle loading. The particles in the lowest-loading image are marked by arrows.

Photoelectrochemical hydrogen evolution with size-selected Pt nanoparticles on TiO_2/np$^+$-Si photocathodes

The mass-selected Pt nanoparticle (d = 5 nm) modified TiO_2-protected Si photocathodes with Pt mass loadings of 10, 50, 200 and 1000 ng cm^{-2} (confirmed by ICP-MS) were tested in photoelectrochemical hydrogen evolution in acidic electrolyte. The respective *IV*-curves of the four different samples are shown in Fig. 4. For all samples an open-circuit photovoltage (V_{oc}) of 495 ± 4 mV and a light-limited photocurrent of ~22 mA cm^{-2} was obtained. These values are in good agreement with our previously reported TiO_2-protected Si photocathodes modified with Pt nanoparticles using a conventional drop casting procedure of a Pt-salt solution.[20,28] Furthermore, the results indicate that light blocking due to the HER catalyst is completely circumvented in these experiments.[19]

For comparison of the different Pt mass-loadings the overpotential η (defined as $V_{oc} - V_{10mA\,cm^{-2}}$) necessary to drive a current density of 10 mA cm^{-2} will be used as a figure of merit. The overpotentials required to achieve 10 mA cm^{-2} are highly dependent on the Pt nanoparticle loading. With the highest Pt loading (1000 ng cm^{-2}) η_{1000ng} = 32 mV was obtained, which is also in good agreement with similar previously reported Si-based photocathodes modified by drop casted Pt nanoparticles or compact Pt films.[20,28] With lower loadings the required overpotential increases and overpotential of η_{200ng} = 46 mV, η_{50ng} = 142 mV, and η_{10ng} = 231 mV were measured, respectively.

One issue we did find with the ultra-low loading Pt samples was that even after extensive cleaning, there were still issues

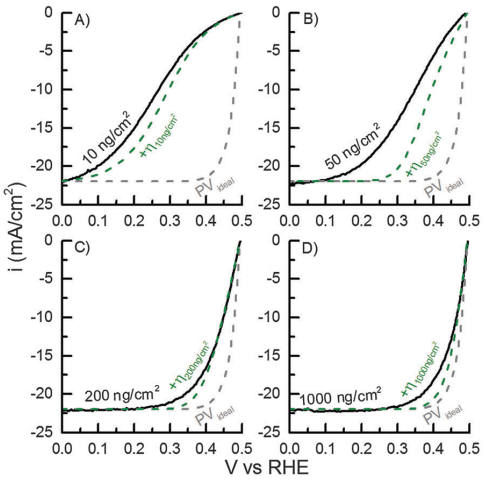

Fig. 4 Measured *IV*-curves of 10, 50, 200 and 1000 ng cm^{-2} Pt loadings on TiO_2-covered $p^+|p|n^+$-Si PV cell (black lines) and the simulated *IV*-curves for the same loadings including the calculated HER overpotentials (η) (green dashed lines). The *IV*-curve for an ideal PV cell with n = 1 (grey dashed line, eqn (2)) is shown for comparison.

with contamination during photoelectrochemical testing. This was attributed to the epoxy resin encasing the photoelectrode. As expected, the issues due to contamination worsened with decreasing loading. Nevertheless for all of the samples shown in this work, at least 5 stable scans were completed before any noticeable drops in performance were measured. However, due to these contamination issues, we could not accurately do long term testing such as chronoamperometry measurements.

Simulations

Effects of Pt loading on HER overpotential. To fully describe the experimental behaviour observed the *IV*-curves for the different Pt nanoparticle loadings were simulated using a ratio of Tafel and Volmer rates (r_T) of 9.5 and a diffusion layer thickness of 5 μm (for further explanation see text in ESI,† and Fig. S4 and S7). The comparison between the simulated *IV*-curves revealed that the simulation describes the trend for the different Pt nanoparticle loadings quite well (Fig. 4, green). For the lowest Pt nanoparticle loading (10 ng cm^{-2}, Fig. 4A) the measured *IV*-curve is described accurately at low overpotentials and low current densities. Hence, the exchange current density assumed in the simulations is close to the real exchange rate, which is supported by simulations for different exchange current densities (Fig. S7, ESI†). In case of highest Pt nanoparticle loadings (200 ng cm^{-2} and 1000 ng cm^{-2}, Fig. 4C and D) the calculations, however, slightly overestimated the HER overpotential initially at low current densities, which was most likely due to differences between true and simulated mass transport conditions (see next section and Fig. S5, ESI†). For the two low Pt nanoparticle loadings (10 ng cm^{-2} and 50 ng cm^{-2}, Fig. 4A and B), HER reaction kinetics is a major part of the total overpotential. Therefore, the effects of reaction kinetics and mass transport were thoroughly analyzed.

Independent of the Pt nanoparticle loading, the deviation of the calculated overpotential and the experimental data increases with higher current densities and the simulation clearly underestimates the experimental HER overpotential. The difference between calculated and measured *IV*-curve at current densities higher than 15 mA cm^{-2} may be related to ideal PV cell characteristics overestimating the fill factor compared to the real silicon PV device used in the experiment.

HER mass transport losses. To elaborate on the differences between measured and calculated *IV*-curves, the effect of mass transport phenomena on the simulated *IV*-curves (dashed green curves in Fig. 4) for the different Pt nanoparticle loadings was further explored. To analyze the effects due to mass transport losses we can write the overpotential as followed:

$$\eta_{\text{total}} = \eta_{\text{Kinetic}} + \eta_{\text{MT}} \quad (3)$$

where η_{total} is the total overpotential and η_{Kinetic} and η_{MT} are the losses due to kinetic and mass transfer, respectively. While losses due to mass transfer are not typically thought of as overpotentials, denoting it this way allows us to directly compare the kinetic and mass transfer losses. Although this direct summation of the two components appears convenient, it is accurate only with small current densities, because eqn (3) is an approximation based on the Taylor expansion of Butler–Volmer equation.[40] However, both total and mass transport overpotential could be determined accurately (eqn (S5b) and (S11b)) and the relative significance of mass transfer and reaction kinetics could be distinguished.

Fig. 5A shows the average current density, normalized by the geometric electrode area i_{geom} as a function of total overpotential (solid lines), and pure mass transfer overpotential for the different Pt nanoparticle loadings used in Fig. 4. The mass transport overpotential was determined almost completely by H_2 concentration, because the changes in the surface concentrations of protons and H_2 were similar (both due to HER and mass transport), but the equilibrium concentration of H_2 was small compared to the proton concentration, and therefore it dominated the Nernst potential.

The dashed lines in Fig. 5A overlap, which illustrates that mass transport losses are almost independent of Pt loading. The losses increase slightly when loading is decreased, but in all cases they correspond to approximately the same H_2 transport rate. The fact that mass transfer losses are basically independent of Pt loadings can be rationalized by realizing that the H_2 molecules have to travel a much longer distance in the axial direction (about 5 μm, see Fig. S5, ESI†) than the distance between two neighboring Pt particles (134 nm for 10 ng cm^{-2}).

Although the H_2 transport rate in simulations for Fig. 4 and 5 was unusually high, it explains the total overpotential with 1000 ng cm^{-2} better than our initial estimate that was based on typical literature values (Fig. S5, ESI†).[41,42] The cause of high mass transport rate may be associated to the potential sweep rate used in the photoelectrochemical hydrogen evolution experiments, which was partly necessitated by contamination and performance drop with low loadings (for further details see ESI†).

Fig. 5B illustrates what fraction of the total overpotential is due to mass transfer, and it is evident that with 1000 ng cm^{-2}, even with the high mass transport rate, mass transport losses

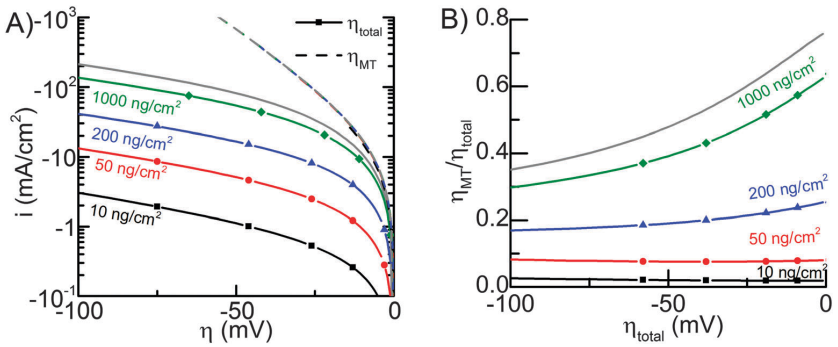

Fig. 5 (A) The simulated HER overpotentials for various loadings. Dotted lines indicate *i*–*V* curves assuming only mass transfer losses with no kinetic losses (*i.e.* perfect catalysis). Solid lines indicate *i*–*V* curves of total overpotential (*i.e.* mass transfer losses plus kinetic losses). (B) The fraction of mass transport overpotential of the total overpotential. The grey lines in both (A) and (B) correspond to a flat Pt surface.

correspond to more than half of the total overpotential up to about 20 mA cm^{-2} current density (25 mV total overpotential).

Considerations of Pt consumption for efficient PEC hydrogen evolution devices

Using the experimental and theoretical results obtained for the well-defined, mass-selected Pt nanoparticle modified photocathodes investigated in this study, the Pt consumption depending on an affordable overpotential for hydrogen evolution can be defined based on the calculated *IV*-curves. The amount of H_2 needed to be produced if society switches to a completely sustainable future is unknown, but it will most likely be in the terawatt range. The average PEC power density is calculated using:

$$P_{avg} = 0.15 \times i \times 1.23V = 0.1854V \times i \quad (4)$$

where 0.15 is the capacity factor of sunlight and *i* current density. A capacity factor of 0.15 is a conservative estimate and usually a capacity factor of 20% is suggested by NREL.[43] For 10 mA cm^{-2} this yields an average power (H_2 generation rate) of 18.54 W m^{-2}, or 1.854 mW cm^{-2}. The required area per TW is given by:

$$A_{TW} = 1\frac{TW}{P_{avg}} = \frac{542\,000\ km^2}{i[mA\ cm^{-2}]} \quad (5)$$

The required area can be calculated to be 54 200 km^2 and 27 100 km^2 for 10 mA cm^{-2} and 20 mA cm^{-2}, respectively. Finally, Pt consumption is calculated by multiplying the area per TW by the Pt loading.

Depending on the acceptable overpotential the total Pt consumption can finally be calculated (Fig. 6). While the exact numbers for irradiation, capacity factor, and efficiency can be debated, the current numbers allow an order of magnitude determination of the feasibility of using Pt in photoelectrochemical devices and although some simulation parameters might not correspond to the actual reaction kinetics, they provide a reasonably good fit to experimental results for current densities up to 20 mA cm^{-2}.

For a photocathode covered with a compact Pt film the overpotential to achieve a current density of 10 mA cm^{-2} in the simulated conditions is 9 mV, while for high Pt nanoparticle loadings of 1000 ng cm^{-2}, 12 mV overpotential is required. The portion of mass transport losses is about 6.5 mV, so higher Pt loadings will not significantly improve the photoelectrode performance (Fig. 5) and a Pt loading of 1000 ng cm^{-2} can be considered as a compact Pt film electrode with negligible kinetic losses. Therefore, in a photoelectrochemical device with minimal overpotential losses, Pt nanoparticle loadings of 1000 ng cm^{-2} are sufficient for standard illumination conditions (AM1.5) and the total Pt consumption would be 542.4 tons per TW. On the other hand, if an increase in overpotential to 50 mV, which is well within the range of a good non-noble metal HER catalyst,[10–13,17] is acceptable due to a sufficient photovoltage, the Pt consumption drops by an order of magnitude to about 100 ng cm^{-2}, corresponding to 54 tons per TW_{avg} (for Pt nanoparticles with d = 5 nm).

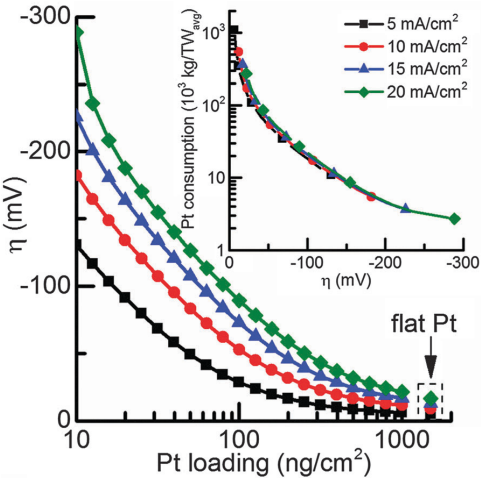

Fig. 6 Overpotential as a function of Pt loading for current densities in the range from 5–20 mA cm^{-2}. The inset the total Pt consumption to reach 1 TW_{avg} of water splitting as a function of overpotential using a capacity factor of 15%.

For comparison, the total global mining production of Pt is around 180 tons per year and the annual net consumption for jewelry and automotive catalytic converters are ~70 ton and ~65 ton respectively. In this light, the use of Pt in an efficient PEC system might be feasible even on a TW scale.[6,44,45] The total energy demand could realistically be an order of magnitude larger (10 TW) but the investment will also be distributed over many years and furthermore Pt can be recovered.

When platinum is compared to the scalability of other well-known non-noble metal HER catalysts (Table 2), such as MoS_2,[46] CoP,[12] Ni_2P,[11] and FeP[17] it appears to be one of the most scalable. In Table 2 we assumed a photoelectrolysis capacity factor of 15% for all materials and used 2010 materials production data.[6] In most cases the metal would be the limiting factor in production, however for FeP it would be the phosphorous. An overpotential of 75 mV was used because all of the optimal catalysts have data at this point. Choosing a lower overpotential would increase the amount of catalyst needed per TW for all of the materials, but it would have the least effect on Pt since it has the lowest Tafel slope. For our Pt data we used the modelled value at 50 ng cm^{-2} because at that loading we can reach the order of magnitude of current (~10 mA cm^{-2}) that will be needed in a photoelectrolysis device. It should be noted that if we used our experimental values at 50 ng cm^{-2} in Table 2, the amount needed would be slightly higher, but would still be relatively low in comparison to MoS_2, CoP, and Ni_2P.

An important thing to consider when reviewing Table 2 is to realize that the value for Pt is extremely optimized whereas materials such as MoS_2 and phosphides still have a much larger potential to be optimized by nanoscaling and better dispersion. While FeP appears very promising from Table 1, it has severe durability issues (doubling of overpotential within ~16 hours) thus limiting its current applicability. Since FeP has only recently been discovered, it is unknown whether these durability issues are fundamental or are simply a technical barrier that can be overcome.

In the present model, Pt nanoparticles with a diameter of 5 nm are assumed. It should be noted that the particle size also affects the overpotential for a given Pt loading: for larger particles less surface area per mass unit is available, so local current densities are higher and higher kinetic overpotentials are expected for the same mass loading. Correspondingly, the overpotential will decrease as the Pt nanoparticle diameter decreases and less Pt is needed to match a given overpotential for any current density. This effect is highlighted in Fig. S7 (ESI†) for Pt nanoparticles with different diameters (d = 2, 5, and 10 nm). However, this will come with a cost of stability as the surface energy will go up with decreasing diameter and the particles will be more prone to sintering and corrosion.[47] Durability is an issue that we have not analyzed with respect to platinum's practical feasibility. Whether the Pt consumption/terawatt for a PEC water splitting device will be stable/durable for 1 month, 1 year or 10 years would obviously be of critical importance.

Interestingly, this approach of reducing the catalyst loading having well-dispersed nanoparticles may not work for a photoanode. In case of photoanode protection with TiO_2 thin films we have recently shown that band bending in TiO_2 protection layers should be avoided and a pinch-off effect will occur when using nanoparticular OER catalysts.[48] Thus, even if another less scarce OER catalyst than IrO_2 applicable for water oxidation in acidic environment will be found, the well-dispersed nanoparticle approach would not work using TiO_2 protection layers. Unfortunately, except for compact IrO_2 thin films, TiO_2 protection layers, currently are the only known protection layers suitable in these conditions.[20,28,48–50] On the other hand photoanode protection might be easier in alkaline electrolyte and NiO thin films might be most promising.[51]

Table 2 Current state-of-the-art H_2 evolution catalysts and what percent of the global production (2010 values) would be needed to produce 1 TW worth of H_2 at an overpotential of 75 mV and 15% capacity

Catalyst	Ref.	i@75 mV η (mA mg^{-1})	% of Annual production/TW
MoS_2	46	0.6	2200 (of Mo)
CoP	12	6.5	670 (of Co)
Ni_2P	11	1.5	220 (of Ni)
FeP	17	48	0.13 (of P)
Pt	This work	171 600	16

Conclusions

In this work an experimental and theoretical approach was used to address the scalability of a photoelectrochemical device to the TW level using a TiO_2–Ti-pn$^+$Si photocathode as stable photon absorber and Pt as hydrogen evolution catalyst. The experimentally determined dependence of the HER overpotential with Pt nanoparticle loading was reproduced in the modelling approach. Thus, effects of mass-transport and hydrogen evolution kinetics could be investigated and the modelling results could be utilized to connect the Pt loadings and overpotentials required for hydrogen evolution. The presented data clearly shows that for an acceptable overpotential of 50 mV, which is the current state-of-the art overpotential for non-noble metal HER catalysts (FeP. 1 mg cm^{-2}), only 100 ng cm^{-2} of Pt or 54 tons per TW_{avg} are needed to scale-up a PEC device to the TW scale. Thus, this work demonstrated that 30% of the world's current annual Pt production could be utilized to achieve a 1 TW_{avg} worth of H_2 generation (assuming current densities of 10 mA cm^{-2} and a capacity factor of 15%) at overpotentials of 50 mV (Pt nanoparticles d = 5 nm).

Acknowledgements

For funding we gratefully acknowledge the Danish National Research Foundation's Center for Individual Nanoparticle Functionality (DNRF54) and Nordic Energy Research for Nordic Initiative for Solar Fuel Development (N-I-S-F-D).

Notes and references

1 N. S. Lewis and D. G. Nocera, *Proc. Natl. Acad. Sci. U. S. A.*, 2006, **103**, 15729–15735.

2 P. C. K. Vesborg, B. Seger and I. Chorkendorff, *J. Phys. Chem. Lett.*, 2015, 951–957.
3 H. B. Gray, *Nat. Chem.*, 2009, **1**, 112.
4 S. Dahl and I. Chorkendorff, *Nat. Mater.*, 2012, **11**, 100–101.
5 N. S. Lewis, *Science*, 2007, **315**, 798–801.
6 P. C. K. Vesborg and T. F. Jaramillo, *RSC Adv.*, 2012, **2**, 7933.
7 J. K. Nørskov, T. Bligaard, A. Logadottir, J. R. Kitchin, J. G. Chen, S. Pandelov and U. Stimming, *J. Electrochem. Soc.*, 2005, **152**, J23.
8 B. Hinnemann, P. G. Moses, J. Bonde, K. P. Jørgensen, J. H. Nielsen, S. Horch, I. Chorkendorff and J. K. Nørskov, *J. Am. Chem. Soc.*, 2005, **127**, 5308–5309.
9 T. F. Jaramillo, K. P. Jørgensen, J. Bonde, J. H. Nielsen, S. Horch and I. Chorkendorff, *Science*, 2007, **317**, 100–102.
10 J. R. McKone, B. F. Sadtler, C. A. Werlang, N. S. Lewis and H. B. Gray, *ACS Catal.*, 2013, **3**, 166–169.
11 E. J. Popczun, J. R. McKone, C. G. Read, A. J. Biacchi, A. M. Wiltrout, N. S. Lewis and R. E. Schaak, *J. Am. Chem. Soc.*, 2013, **135**, 9267–9270.
12 E. J. Popczun, C. G. Read, C. W. Roske, N. S. Lewis and R. E. Schaak, *Angew. Chem., Int. Ed.*, 2014, **53**, 5427–5430.
13 J. Kibsgaard and T. F. Jaramillo, *Angew. Chem., Int. Ed.*, 2014, **53**, 14433–14437.
14 Y. Hou, B. L. Abrams, P. C. K. Vesborg, M. E. Björketun, K. Herbst, L. Bech, A. M. Setti, C. D. Damsgaard, T. Pedersen, O. Hansen, J. Rossmeisl, S. Dahl, J. K. Nørskov and I. Chorkendorff, *Nat. Mater.*, 2011, **10**, 434–438.
15 S. Trasatti, *Electrochim. Acta*, 2000, **45**, 2377–2385.
16 B. Seger, I. E. Castelli, P. C. K. Vesborg, K. W. Jacobsen, O. Hansen and I. Chorkendorff, *Energy Environ. Sci.*, 2014, **7**, 2397–2413.
17 J. F. Callejas, J. M. McEnaney, C. G. Read, J. C. Crompton, A. J. Biacchi, E. J. Popczun, T. R. Gordon, N. S. Lewis and R. E. Schaak, *ACS Nano*, 2014, **8**, 11101–11107.
18 C. W. Roske, E. J. Popczun, B. Seger, C. G. Read, T. Pedersen, O. Hansen, P. C. K. Vesborg, B. S. Brunschwig, R. E. Schaak, I. Chorkendorff, H. B. Gray and N. S. Lewis, *J. Phys. Chem. Lett.*, 2015, **2**, 1679–1683.
19 D. Bae, T. Pedersen, B. J. Seger, M. Malizia, A. Kuznetsov, O. Hansen, I. Chorkendorff and P. C. K. Vesborg, *Energy Environ. Sci.*, 2015, **8**, 650–660.
20 B. Seger, D. S. Tilley, T. Pedersen, P. C. K. Vesborg, O. Hansen, M. Grätzel and I. Chorkendorff, *RSC Adv.*, 2013, **3**, 25902–25907.
21 J. R. McKone, N. S. Lewis and H. B. Gray, *Chem. Mater.*, 2014, **26**, 407–414.
22 N. P. Dasgupta, C. Liu, S. Andrews, F. B. Prinz and P. Yang, *J. Am. Chem. Soc.*, 2013, **135**, 12932–12935.
23 L. Ji, M. D. McDaniel, S. Wang, A. B. Posadas, X. Li, H. Huang, J. C. Lee, A. a. Demkov, A. J. Bard, J. G. Ekerdt and E. T. Yu, *Nat. Nanotechnol.*, 2014, **10**, 84–90.
24 Y. Chen, K. Sun, H. Audesirk, C. Xiang and N. Lewis, *Energy Environ. Sci.*, 2015, **8**, 1736–1747, DOI: 10.1039/C5EE00311C.
25 M. Walter, E. L. Warren, J. R. McKone, S. W. Boettcher, Q. Mi, E. A. Santori and N. S. Lewis, *Chem. Rev.*, 2010, **110**, 6446–6473.
26 S. Hu, C. Xiang, S. Haussener, A. D. Berger and N. S. Lewis, *Energy Environ. Sci.*, 2013, **6**, 2984–2993.
27 L. C. Seitz, Z. Chen, A. J. Forman, B. a. Pinaud, J. D. Benck and T. F. Jaramillo, *ChemSusChem*, 2014, **7**, 1372–1385.
28 B. Seger, T. Pedersen, A. B. Laursen, P. C. K. K. Vesborg, O. Hansen and I. Chorkendorff, *J. Am. Chem. Soc.*, 2013, **135**, 1057–1064.
29 H. Haberland, *J. Vac. Sci. Technol., A*, 1992, **10**, 3266.
30 B. von Issendorff and R. E. Palmer, *Rev. Sci. Instrum.*, 1999, **70**, 4497–4501.
31 P. Hernandez-Fernandez, F. Masini, D. N. McCarthy, C. E. Strebel, D. Friebel, D. Deiana, P. Malacrida, A. Nierhoff, A. Bodin, A. M. Wise, J. H. Nielsen, T. W. Hansen, A. Nilsson, I. E. L. Stephens and I. Chorkendorff, *Nat. Chem.*, 2014, **6**, 732–738.
32 U. Diebold, *Surf. Sci. Rep.*, 2003, **48**, 53–229.
33 H. Reller, E. Kirowa-Eisner and E. Gileadi, *J. Electroanal. Chem. Interfacial Electrochem.*, 1982, **138**, 65–77.
34 R. G. Compton, G. G. Wildgoose, N. V. Rees, I. Streeter and R. Baron, *Chem. Phys. Lett.*, 2008, **459**, 1–17.
35 *CRC Handbook of Chemistry and Physics*, ed. D. R. Lide, CRC Press, 95th edn, 2014.
36 J. Durst, C. Simon and H. A. Gasteiger, *J. Electrochem. Soc.*, 2015, **162**, F190–F203.
37 N. M. Markovic and P. N. J. Ross, *Surf. Sci. Rep.*, 2002, **45**, 117–229.
38 K. Aoki, H. Toda, J. Yamamoto, J. Chen and T. Nishiumi, *J. Electroanal. Chem.*, 2012, **668**, 83–89.
39 U. Stutenbaeumer and B. Mesfin, *Renewable Energy*, 1999, **18**, 501–512.
40 A. J. Bard and L. R. Faulkner, *Electrochemical Methods: Fundamentals and Applications*, WILEY-VCH Verlag, 2001.
41 K. Stephan and H. Vogt, *Electrochim. Acta*, 1979, **24**, 11–18.
42 C. A. C. Sequeira, D. M. F. Santos, B. Šljukić and L. Amaral, *Braz. J. Phys.*, 2013, **43**, 199–208.
43 http://www.nrel.gov/analysis/tech_cap_factor.html.
44 P. J. Loferski, *2012 Minerals Yearbook*, Platinum-group metals, 2013.
45 World Platinum Investment Council, *Platinum Quarterly Q1 2015*, 2015.
46 H. Wang, Z. Lu, D. Kong, J. Sun, T. M. Hymel and Y. Cui, *ACS Nano*, 2014, **8**, 4940–4947.
47 J. C. Meier, I. Katsounaros, C. Galeano, H. J. Bongard, A. A. Topalov, A. Kostka, A. Karschin, F. Schüth and K. J. J. Mayrhofer, *Energy Environ. Sci.*, 2012, **5**, 9319.
48 B. Mei, T. Pedersen, P. Malacrida, D. Bae, R. Frydendal, O. Hansen, P. C. K. Vesborg, B. Seger and I. Chorkendorff, *J. Phys. Chem. C*, 2015, **119**, 15019–15027.
49 S. Hu, M. R. Shaner, J. A. Beardslee, M. Lichterman, B. S. Brunschwig and N. S. Lewis, *Science*, 2014, **344**, 1005–1009.
50 B. Mei, B. Seger, T. Pedersen, M. Malizia, O. Hansen, I. Chorkendorff and P. C. K. Vesborg, *J. Phys. Chem. Lett.*, 2014, **5**, 1948–1952.
51 B. Mei, A. A. Permyakova, R. Frydendal, D. Bae, T. Pedersen, P. Malacrida, O. Hansen, I. E. L. Stephens, P. C. K. Vesborg, B. Seger and I. Chorkendorff, *J. Phys. Chem. Lett.*, 2014, **5**, 3456–3461.

Paper II: Engineering Ni–Mo–S Nanoparticles for Ultra-Deep Hydrodesulfurization: Reactive Gas Aggregation Synthesis, Characterization and Catalytic Testing
A. Bodin, A. L. Christoffersen, C. F. Elkjær, J. Kibsgaard, S. Helveg, I. Chorkendorff
In preparation - abstract included

Engineering Ni-Mo-S Nanoparticles for Ultra-Deep Hydrodesulfurization: Reactive Gas Aggregation Synthesis, Characterization and Catalytic Testing

Anders Bodin[1], Ann-Louise N. Christoffersen[1], Christian F. Elkjær[2], Jakob Kibsgaard[1], Stig Helveg[2], and Ib Chorkendorff [*1]

[1]Department of Physics, Technical University of Denmark, Fysikvej, Building 312, DK-2800 Kgs. Lyngby, Denmark
[2]Haldor Topsøe A/S, Nymøllevej 55, DK-2800 Kgs. Lyngby, Denmark

July 23, 2017

Abstract

With the aim of engineering highly active nanoparticle catalysts for ultra-deep hydrodesulfurization (HDS), we present the synthesis of well-defined model systems of mass-selected Ni-Mo-S nanoparticles by aggregation of sputtered metal from a $Mo_{75}Ni_{25}$ target in a reactive atmosphere of Ar and H_2S. The nanoparticles are undersulfided with a stoichiometry of $Mo_{0.8}Ni_{0.2}S_{1.1}$, and exhibit high-surface area morphologies with many under-coordinated sites, which is desired for desulfurization of molecules where the location of the sulfur atoms makes the HDS sterically hindered. Before deposition on a substrate, the nanoparticles are filtered by mass in a quadrupole mass filter, and it is shown that varying the deposition mass can significantly alter the nanoparticle structures. Using a micro-reactor system, we assess the catalytic activity of the Ni-Mo-S nanoparticles for HDS of dibenzothiophene and show that nanoparticles produced by reactive gas-phase aggregation are more than twice as active as nanoparticles produced by post-sulfiding metallic Ni-Mo nanoparticles.

[*]Corresponding author. Email: ibchork@fysik.dtu.dk.

Paper III: Dynamic Effects of Surface Oxygen in CO Electroreduction
S. B. Scott*, D. B. Trimarco*, **A. Bodin***, A. Bagger, N. Mazzanti, J. E. Sørensen, T. Pedersen, O. Hansen, I. E. L. Stephens, P. C. K. Vesborg, J. Rossmeisl, I. Chorkendorff
In preparation
*These authors contributed equally

Dynamic effects of surface oxygen in CO electroreduction

Soren B. Scott [*1,2], **Daniel B. Trimarco** [*1], **Anders Bodin** [*1], Alexander Bagger[2], Nicola Mazzanti[1], Jakob E. Sørensen[1], Thomas Pedersen[3], Ole Hansen[3], Ifan E. L. Stephens[1], Peter C. K. Vesborg[1,3], Jan Rossmeisl[2], and Ib Chorkendorff [†1,3]

[1]Department of Physics, Technical University of Denmark, Fysikvej, Building 312, DK-2800 Kgs. Lyngby, Denmark

[2]Department of Chemistry, University of Copenhagen, Universitetsparken 5, DK-2100 København Ø, Denmark

[3]Department of Micro- and Nanotechnology, Technical University of Denmark, Ørsteds Plads, Building 344, DK-2800 Kgs. Lyngby, Denmark

July 17, 2017

Sustainable fuel and chemical production by electroreduction of carbon monoxide with use of renewable electricity will likely contribute to reducing the net emissions of anthropogenic greenhouse gasses[1]. While significant progress has been made in catalyzing the two-electron reduction of carbon dioxide to carbon monoxide (CO)[2;3] or formic acid[3;4], at present the further electrochemical reduction of carbon monoxide to hydrocarbons suffers from poor energetic efficiency and selectivity on known catalysts[5;6].

Recently, it has been shown that copper surfaces effectively catalyze CO reduction to multi-carbon products when prepared from an oxidized precursor[7;8;9]. However, the reason for the increased activity is still debated[10;11;12;13], and elucidation of the reaction mechanism is often hindered by changes in the electrode surface under reaction conditions[14;12;13].

In this study we use mass-selected copper nanoparticles as a model catalyst for elucidating the effect of surface oxygen on the CO electroreduction reaction, demonstrating a highly active transient electrocatalytic pathway for methane production. Using a newly developed electrochemical mass spectrometry (EC-MS) setup with unprecedented sensitivity, we are able to observe the electrocatalytic activity of an oxidized surface before it is reduced during electrolysis. We find that, in contrast to reduced oxide-derived copper surfaces, adsorbed oxygen on copper activates an electrocatalytic pathway towards the single-carbon products without affecting two-carbon product formation.

Based on density functional theory (DFT) calculations, we propose that the dynamic methane production can be attributed to surface oxygen stabilizing the $*$CHO reaction intermediate on under-coordinated sites with respect to adsorbed CO.

In addition to providing mechanistic insight, this result suggests a new design paradigm for improving activity and tuning selectivity of electrocatalysts by stabilizing or regenerating metastable active sites.

Our experiments were conducted in the EC-MS setup sketched in Figure 1a, where the sample is incorporated in a polychlorotrifluoroethylene (PCTFE) EC-MS cell and separated from the mass spectrometer by means of a microfabricated membrane chip (Figure 1a, left inset), allowing a controlled transfer of reaction products from the electrolyte to the vacuum. The distance between the sample and the membrane is defined by a 100 μm Teflon spacer forming a thin layer of electrolyte (0.5 M

[*]These authors contributed equally to this work.

[†]Corresponding author. Email: ibchork@fysik.dtu.dk.

potassium carbonate, pH=12). During operation, the electrolyte is kept stagnant and is continuously saturated by reactant gas from the microchip membrane. The working volume can be flushed or purged with fresh electrolyte or gas respectively (see SI for more details on the EC-MS system).

The samples were prepared by depositing mass-selected copper nanoparticles with a diameter of 4.8 ± 0.2 nm onto a 5 mm glassy carbon disc with 5% projected surface coverage, corresponding to a total mass loading of 24 ng (Figure 1a, right inset). Operating at these low loadings minimizes particle-particle interaction and mass transport phenomena.

Our experiments were based on constant-potential electrolysis (chronoamperometry) as shown in

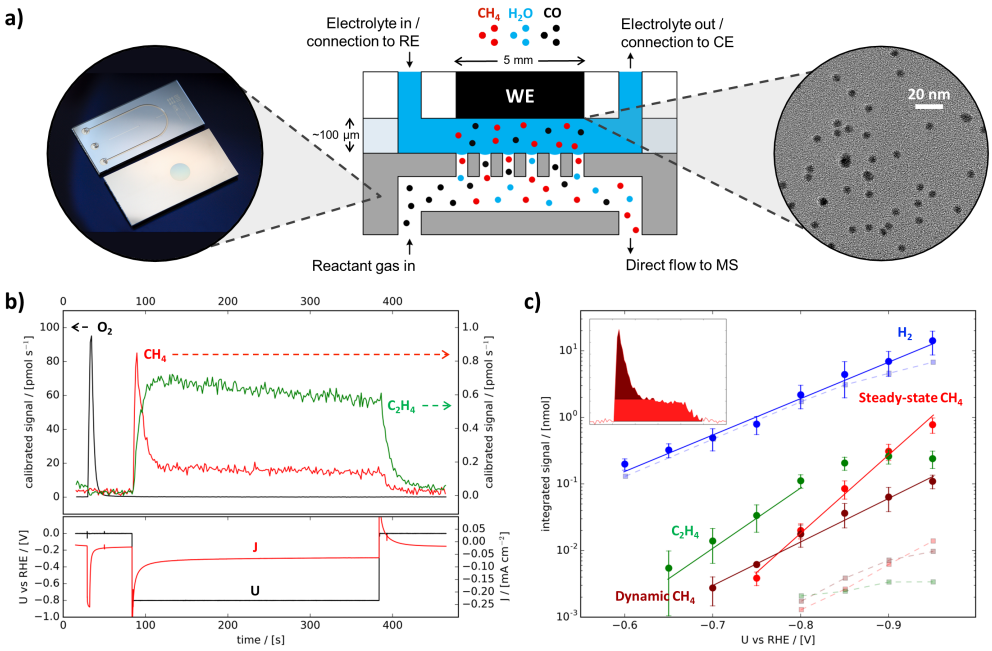

Figure 1: Experimental setup and demonstration of the transient methane production phenomenon. **a**, Schematic of the experimental setup. Left inset: Membrane chip used to interface the electrochemical environment with the vacuum of the mass spectrometer (not drawn to scale). Right inset: TEM image of Cu nanoparticles as deposited onto a glassy carbon substrate as the working electrode (WE). The WE and the membrane chip are separated by 100 μm stagnant thin film of electrolyte (the working volume). **b**, EC-MS plot of a typical constant-potential electrolysis experiment showing the calibrated MS signals for oxygen (O_2, black) methane (CH_4, red), and ethylene (C_2H_4, green) during a five minute constant-potential step at a working potential of -0.80 V vs RHE preceded by a five second flush of aerated electrolyte (exchanging working volume electrolyte more than 10 times) while at a resting potential of 0 V vs RHE. The potential (black) and electrical current density (red) are shown below on the same time axis. **c**, Integrated MS signals during one minute constant-potential steps plotted as a function of working potential as a Tafel plot. The aerated electrolyte was flushed for five seconds prior to each step, and the resting potential between steps was 0 V vs RHE. Datapoints and error bars represent the mean and standard deviation, respectively, of measurements on four separate samples. The methane signal is divided into dynamic (dark red) and steady-state (light red) contributions as indicated in the inset. H_2, O_2, CH_4, and C_2H_4 were measured at m/z = 2, 32, 15, and 26, respectively. For details on quantification, see SI.

Figure 1b, with the top panel of showing the calibrated MS signals for oxygen (O_2), methane (CH_4), and ethylene (C_2H_4), respectively (quantified as described in SI), and the bottom panel showing the electrical potential and current. We refer to this type of plot as an EC-MS plot.

To investigate the influence of oxygen on CO electroreduction activity, we expose the sample to dioxygen (O_2) by flushing the working volume with aerated electrolyte for five seconds (exchanging the electrolyte more than 10 times) while holding the sample at a *resting potential* 0 V vs RHE ($t = 40\,s$). The cathodic current during the flush is attributed to oxygen reduction. A *working potential* of -0.8 V vs RHE is then applied at $t = 85\,s$ for five minutes.

At the onset of the working potential step we observe a surprising phenomenon: a high initial production of CH_4 followed by a decline to steady state. Interestingly, this is only observed for CH_4, while the H_2 and C_2H_4 production rates remain steady during the five minutes of electrolysis, indicating that the phenomenon only effects the single-carbon (C1) electrocatalytic pathway.

In order to characterize this transient phenomenon, we separate the integrated CH_4 signal into two parts as indicated in the inset to Figure 1c: (1) the dynamic initial burst of CH_4 activity, and (2) CH_4 produced at the subsequent steady-state level. The integrated MS signals of dynamic CH_4, steady-state CH_4, C_2H_4, and H_2, respectively, from one-minute constant-potential steps are shown in Figure 1c as a function of working potential. Prior to each working potential step, the electrode was exposed to a five second flush of aerated electrolyte at a constant resting potential of 0 V vs RHE, as in the experiment shown in Figure 1b. Error bars represent mean and standard deviation between measurements on four separate samples. Control experiments on blank substrates show minute levels of hydrocarbon production (see SI for more detail), which we attribute to trace impurities[15], but similar levels of hydrogen production, which also indicates that the majority of HER activity is due to the glassy carbon substrate.

When quantified in this way, it is clear that steady-state CH_4 and dynamic CH_4 have distinct potential dependencies. The Tafel slope for steady-state CH_4 is 91 mV/decade, while for dynamic CH_4 it is 151 mV/decade. Ethylene has a Tafel slope of 122 mV/decade from -0.65 V to -0.80 V vs RHE and then tapers off. These Tafel slopes, and the deviation towards lower C_2H_4 activity at higher overpotentials, are in good agreement with previous reports on CO_2 electroreduction on polycrystalline copper[16;17].

To verify that we cannot activate the dynamic CH_4 production without O_2 in the electrolyte, Ar (Figure 2a) or O_2 (Figure 2b) was dosed via the reactant gas through the membrane of the chip while holding the sample at 0 V vs RHE prior to a two minute constant-potential step at -0.90 V vs RHE. Dynamic methane production is activated when O_2 is dosed but not in the Ar control experiment. Production of steady-state CH_4, C_2H_4, and H_2 all remain unaffected.

Previous EC-MS studies of CO electroreduction on Cu utilizing potential scans (cyclic voltammetry) have not observed similar dynamic phenomena, even where the sample has seen an oxidizing environment prior to experiments[8;18]. Likewise, potential scans on our EC-MS system do not show any sign of dynamic CH_4, as seen in Figure 2c, which shows an EC-MS plot of a potential scan at 5 mV/s. This is likely due to the sample getting reduced on the cathodic scan before any hydrocarbons are produced.

To probe the conditions necessary to activate the catalyst for dynamic CH_4 production, we varied the resting potential at which O_2 was introduced, as shown in Figure 2d. Here, the integrated MS signals during one-minute constant-potential steps at -0.85 V vs RHE are plotted against the preceding resting potential, during which O_2 was introduced by a five-second flush of aerated electrolyte. This experiment demonstrates that dynamic CH_4 is only activated when the potential during O_2 exposure is anodic of -0.20 V vs RHE. The dynamic CH_4 production then increases as function of resting potential until it reaches a plateau around +0.20 V vs RHE, suggesting that the relevant surface sites have become saturated. A similar saturation can likewise be obtained by varying the duration of O_2 exposure without changing the resting potential (see SI for more details).

Interestingly, when O_2 was introduced at potentials anodic of 0 V vs RHE, the steady-state activity was also increased, indicating that higher degrees of oxidation influence only the steady-state activity of CH_4 and C_2H_4. Without O_2 in the electrolyte a similar increase in steady-state CO electroreduction activity can be obtained at potentials anodic of +0.5 V vs RHE, but without activating the dynamic

CH_4 production (see SI for more details). This steady-state increase in CO electroreduction activity is consistent with observations on oxide-derived Cu electrodes.[7;9;19]

The observation that dynamic CH_4 production is activated by O_2 exposure up to a saturation point, but not activated by electrochemical oxidation, suggests that the increased activity is due to metastable oxidation of specific active sites on the Cu surface. The surface sites relevant for this study are illustrated by Figure 3a which shows a Wulff construction of a Cu NP approximately 5 nm in diameter. Surface atoms are color-coded according to their coordination number (CN).

Prior DFT studies have investigated the rate- and potential- limiting elementary steps in CO_2 and CO electroreduction on various reduced copper surface sites.[20] On terraced sites (CN = 8 or 9), the binding energy of $*CO$ is very small ($|E(*CO)| < 0.1$ eV), and CO adsorption is rate-limiting. Thus we do not expect the flat surfaces to contribute significantly to catalyzing the reaction. On undercoordinated sites, the first proton-electron transfer to $*CO$, forming $*CHO$, is potential-limiting for CO reduction to methane. The limiting overpotential is larger for kinks (CN = 6) than for steps (CN = 7), as the higher reactivity of kink sites lowers the free energy of $*CO$ (double-bonded to the surface) by a greater amount than that of $*CHO$ (single-bonded). Our calculations, shown as free

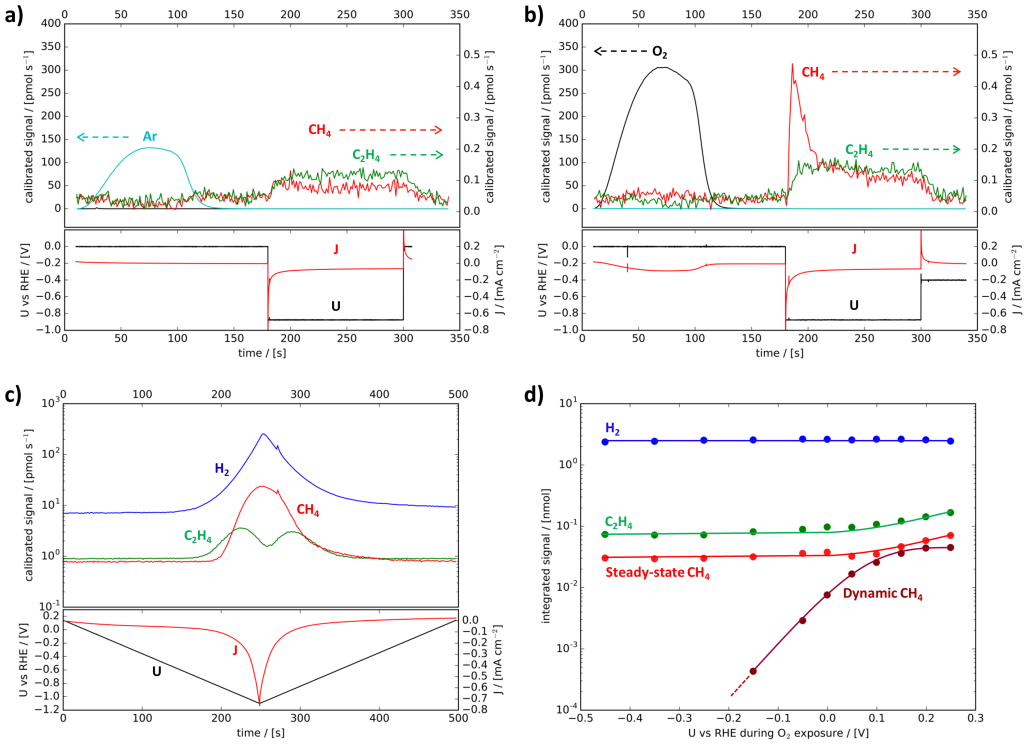

Figure 2: Influence of oxygen on dynamic methane production. a-b, The effect of oxygen demonstrated by two constant-potential electrolysis experiments at a working potential of -0.90 V vs RHE. Gaseous Ar (a) or O_2 (b) was dosed through the microchip membrane while holding the resting potential at 0 V vs RHE. The experiments are plotted as EC-MS plots with the top panel showing the mass spectrometer signals for argon (Ar, cyan), oxygen (O_2, black), methane (CH_4, red) and ethylene (C_2H_4, green) and the bottom panel showing the electrical potential (black) and geometric current density (red). **c**, Potential scan as an EC-MS plot. **d**, The integrated mass spectrometry signal of steady-state methane (CH_4, red), dynamic methane (CH_4, dark red) and steady state ethylene (C_2H_4, green) during a one minute constant-potential steps at -0.85 V vs RHE as function of the resting potential during oxygen exposure immediately preceding the constant-potential step.

energy diagrams for the first steps of CO reduction at step and kink sites in the blue traces ('without oxygen') of Figures 3c and 3d, respectively, reproduce this result. An electrical potential of -0.8 V vs RHE, corresponding to the experimental condition in Figure 1, has been implemented for these calculations as an adjustment to the reference state of hydrogen, i.e. by the computational hydrogen electrode (CHE).

Our calculations predict that ∗CO at step and kink sites is destabilized by adjacent surface-adsorbed atomic oxygen (surface oxygen, ∗O). While ∗CHO on step sites is destabilized by a similar amount, leaving the limiting potential unchanged, ∗CHO on kink sites is stabilized with respect to ∗CO by surface oxygen. This effect was observed as a general trend independent of the exact adsorption site used for ∗O. These results are shown as free energy diagrams in the red traces ('with oxygen') of Figures 3c and 3d, respectively, where the exact choice of ∗O site, indicated in the insets, is based on stability with respect to ∗OH. In summary, we expect that the effect of surface oxygen is to increase the rate of CO electroreduction to CH_4 at sites which normally bind CO too strongly.

We attribute the transient nature of the pathway to the fact that the surface oxygen is only

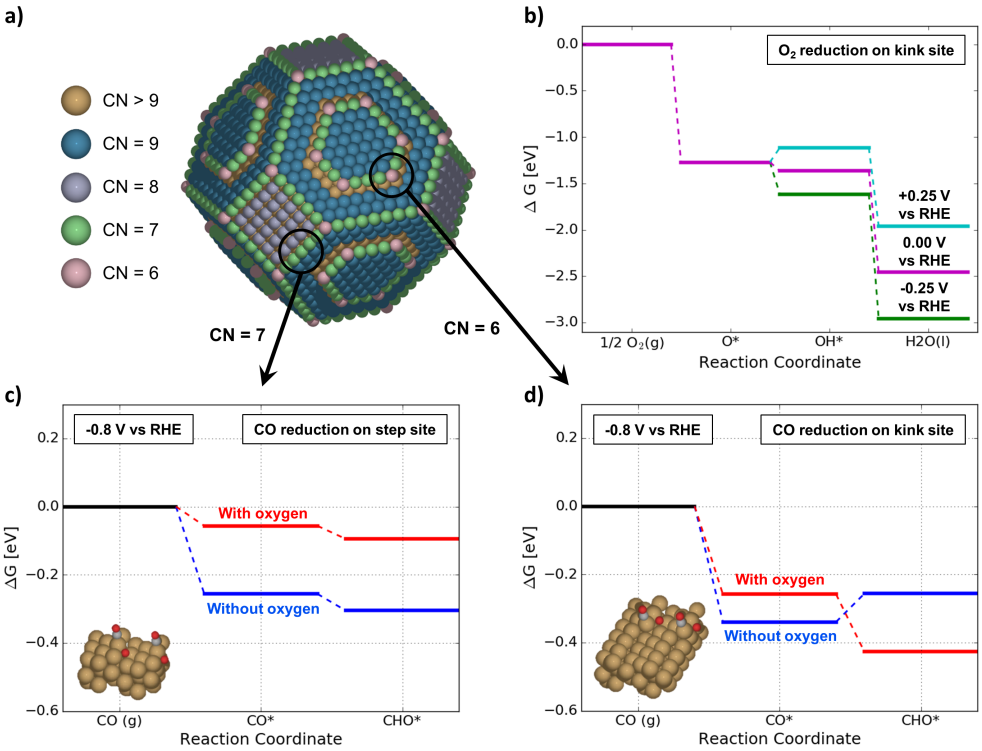

Figure 3: Atomic scale modeling of the influence of oxygen on the catalytic pathway towards methane. **a**, Wulff construction of a Cu particle approximately 5 nm in diameter, illustrating the coordination numbers of the surface atoms. **b**, Free energy diagram for the oxygen reduction reaction on the kink site at three different potentials. At +0.25 V vs. RHE the oxygen is stable, whereas more negative potentials cause a further reduction to *OH. Kinetic barriers between reaction intermediates are not included, and thus the adsorbed oxygen could be metastable at e.g. 0 V vs. RHE, even though the reaction to *OH is slightly downhill in energy. **c-d**, Free energy diagrams calculated with density functional theory for the potential dependent steps for CO electroreduction to CH_4 for **b** the step and **c** the kink site, without (blue) and with (red) an adsorbed oxygen atom at the most stable nearby site. In each case, the unit cell used for the calculation with the adsorbed oxygen is shown as an inset. Both diagrams are shown with an applied potential of -0.8 V vs RHE, similar to the experiment shown in Figure 1b.

short-lived at CO-electroreduction potentials before being reduced to water. At resting potentials, however, the oxygen can be stable as shown in figure 3b, which displays a free energy diagram of the oxygen reduction reaction on the kink site at three different resting potentials. At +0.25 V vs. RHE the oxygen is stable, whereas more negative potentials cause a further reduction to *OH. It should, however, be noted that kinetic barriers between reaction intermediates are not included in the calculations. If there is such a kinetic barrier for ∗O reduction to ∗HO at e.g. 0 V vs. RHE, then ∗O could be a metastable state at the O_2 dosing potential, and be present transiently even at CO reduction potentials. The duration of dynamic methane activity would then correspond to the lifetime of this metastable active site. Fitting of the experimentally measured CH_4 signal with a model of CH_4 diffusion and evaporation in the EC-MS system (SI) indicates that the lifetime of the active site is on the order of 1 second at -0.85 V vs RHE. During this lifetime, an active site turns over between 2 and 20 CH_4 molecules, where the uncertainty lies primarily in estimating the number of active sites (SI).

The decoupled dynamic behavior of CH_4 and C_2H_4 production is consistent with the understanding that C1 and C2 pathways in CO reduction have distinct rate-limiting steps[5;21]. However, our results stand in contrast to earlier observations of oxidized Cu activating a C2 pathway, leading to increased C_2H_4 formation[9;12]. The difference is that our time-resolved product detection and constant-potential experiment methods enable us to isolate the effect of surface oxygen, which is reduced quickly and affects only the C1 CO electroreduction pathway. Also note that our results are obtained on nanoparticles which have a high concentration of undercoordinated kink sites as compared to polycrystalline surfaces.

While EC-MS has successfully been used to determine reaction selectivity in lithium batteries[22], investigating the catalytic mechanism for oxygen evolution reaction[23], and study single crystals for CO_2 electroreduction[24], this is, to the best of our knowledge, the first time EC-MS has been used to study an intrinsically transient phenomenon. The newly developed EC-MS system used in our study can potentially open new research fields, such as studying the OER activity of metallic transition metals or the intrinsic activity of catalysts that become poisoned by intermediates. On the industrial level, mastering such transient phenomena could make it possible to steer electrocatalytic processes to produce products beyond the reach of steady electrolysis.

Methods summary

Electrochemical mass spectrometry: Our EC-MS setup uses a micro-fabricated membrane chip (right inset of Figure 1a) to make a liquid-vacuum junction between electrolyte and mass spectrometer, allowing volatile electrochemical products to be detected while simultaneously dosing reactant gas through the membrane[25]. A glassy carbon disc (Ø 5 mm) was mounted as working electrode (WE) in an electrochemical cell which enables electrolyte flow and connections to external counter and reference electrodes, thus establishing a 3-electrode setup. The electrochemical cell was mounted on top of the membrane chip with a 100 μm Teflon spacer defining the distance between WE and membrane chip. All experiments were carried out in a 0.5 M potassium carbonate buffer with pH=12. See SI for further details.

Sample synthesis and characterization: Mass-selected copper nanoparticles with a diameter of $d = 4.8 \pm 0.2$ nm were used as a model catalyst. The nanoparticles were synthesized in an ultra-high vacuum nanoparticle source (Nanobeam 2011, Birmingham Instruments Inc.) by magnetron sputtering of a copper target and gas-phase nanoparticle aggregation in 0.4 mbar of He and Ar, followed by super-sonic expansion through an aperture into a differentially pumped UHV region where the particles do not grow further. Subsequently, particles with $m = 350,000$ amu were selected in a lateral time-of-flight mass filter with mass resolution of m/Δm=20[26]. The particles were deposited onto sputter-cleaned glassy carbon discs with 5 % projected surface coverage, corresponding to a total mass loading of 24 ng of Cu on each sample. Cleanliness of the samples was ensured by X-ray photoelectron spectroscopy (SPECS XR 50 X-ray gun coupled to Omicron NanoSAM 7 channel energy analyzer) and ion scattering spectroscopy (Omicron ISE100 ion gun) before and after deposition of nanoparticles; the spectroscopies were performed in a UHV system coupled to the nanoparticle source (Scienta Omicron), thus avoiding air exposure before the sample was taken out for EC-MS measurements. The nanoparticle size-distribution was found from TEM images acquired in a FEI Tecnai T20 G2 transmission electron microscope, analyzed in the software ImageJ. A small fraction of particles are larger than $d = 4.8 \pm 0.2$ nm, due to particles landing on top of each other, or particles with double mass which cannot be discriminated from the desired mass in the mass filter[27]. Spectroscopy and microscopy is presented in supplementary information.

Substrate cleaning procedure: All glassy carbon substrates were cleaning using the following procedure: 1) Rinsing in ultrapure water 2) Cleaning in 65% suprapure nitric acid for one hour, then rinsing in ultrapure water 3) Polishing with 1/4 μm diamond paste 4) Sonicating two times for 10 minutes, first in ethanol and then in ultrapure water 5) Repeating the acid treatment (step 2) and 6) Sonicating two times in ultrapure water for 10 minutes. After cleaning, 3d and 5d metal impurities were below the detection limit of XPS, but the ISS measurements still showed traced amounts, as it is an extremely sensitive technique (see supplementary information).

Glassware and EC cell cleaning procedure: Before each experiment, all components of the setup that were exposed to electrolyte during experiments were cleaned by leaving them overnight in 3:1 solution of 98% sulfuric acid and 30% hydrogen peroxide (Piranha solution). This effectively removed organic impurities and non-precious metals. All components were then thoroughly rinsed five times with water to remove the solvent and any residual contamination.
Electrolyte preparation: All experiments were performed in a 0.5 M potassium carbonate buffer titrated to pH 12 with KOH. The electrolyte was prepared by saturating 200 ml of 1.0 M KOH with CO_2, to a pH of 7.8. This was then tritrated to pH 12 using 213.5 ml 1.0 M KOH.
Density functional theory: The two DFT models were created in ASE[28]. A 211 stepped slab with a (3,3,3) unit cell and a kink model by removing atoms from a larger 211 slab with unit cell size (3,6,3). In both structures the two lower atomic layers where kept fixed. For the electronic structure calculations the projector-augmented wave method was used together with the revised Perdew-Burke-Ernzerhof (RPBE)[29] functional in the GPAW software[30;31]. For all calculations a 0.17 grid spacing were applied, the forces were relaxed down below 0.05 eV/Å and a (4 x 4 x 1) and (4 x 2 x 1) k-point sampling were used for the step and kink structure, respectively. The hydrogen electrode was employed[32] to calculate the free energy diagrams. For zero point, entropy and heat capacity we apply values from reference[33] and as intermediate water corrections we use 0.25 eV for R-OH intermediates and 0.1 eV for R=O intermediate similar to the results of A. Petersson[34].

Acknowledgments: Supported by the Villum Foundation V-SUSTAIN grant 9455 to the Villum Center for the Science of Sustainable Fuels and Chemicals.

Author Contributions: S. B. Scott, D. B. Trimarco, A. Bodin, N. Mazzanti, and J. E. Sørensen performed the experiments with supervision from O. Hansen, I. L. Stephens, P. C. K. Vesborg, and I. Chorkendorff; A. Bagger did the DFT modelling with supervision from J. Rossmeisl; S. B. Scott performed analysis and modelling of experimental data; D. B. Trimarco, P. C. K. Vesborg, S. B. Scott, and T. Pedersen developed the EC-MS technique with supervision from O. Hansen and I. Chorkendorff; S. B. Scott, D. B. Trimarco, and A. Bodin wrote the paper with contributions from A. Bagger and discussion with all authors.

References

[1] Steven Chu, Yi Cui, and Nian Liu. The path towards sustainable energy. *Nature Materials*, 16(1):16–22, 2016.

[2] Christina W. Li and Matthew W. Kanan. CO2 reduction at low overpotential on Cu electrodes resulting from the reduction of thick Cu2O films. *Journal of the American Chemical Society*, 134(17):7231–7234, 2012.

[3] Min Liu, Yuanjie Pang, Bo Zhang, Phil De Luna, Oleksandr Voznyy, Jixian Xu, Xueli Zheng, Cao Thang Dinh, Fengjia Fan, Changhong Cao, F. Pelayo García de Arquer, Tina Saberi Safaei, Adam Mepham, Anna Klinkova, Eugenia Kumacheva, Tobin Filleter, David Sinton, Shana O. Kelley, and Edward H. Sargent. Enhanced electrocatalytic CO2 reduction via field-induced reagent concentration. *Nature*, 537(7620):382–386, 2016.

[4] S Gao, Y Lin, X Jiao, Y Sun, Q Luo, W Zhang, D Li, J Yang, and Y Xie. Partially oxidized atomic cobalt layers for carbon dioxide electroreduction to liquid fuel. *Nature*, 529(7584):68–71, 2016.

[5] Ruud Kortlever, Jing Shen, Klaas Jan P Schouten, Federico Calle-Vallejo, and Marc T M Koper. Catalysts and Reaction Pathways for the Electrochemical Reduction of Carbon Dioxide. *The Journal of Physical Chemistry Letters*, 6(20):4073–4082, 2015.

[6] Zarko P. Jovanov, Heine A. Hansen, Ana Sofia Varela, Paolo Malacrida, Andrew A. Peterson, Jens K. Nørskov, Ifan E L Stephens, and Ib Chorkendorff. Opportunities and challenges in the electrocatalysis of CO2 and CO reduction using bifunctional surfaces: A theoretical and experimental study of Au-Cd alloys. *Journal of Catalysis*, 343(April):215–231, 2016.

[7] Christina W Li, Jim Ciston, and Matthew W Kanan. Electroreduction of carbon monoxide to liquid fuel on oxide-derived nanocrystalline copper. *Nature*, 508(7497):504–507, 2014.

[8] F. Sloan Roberts, Kendra P. Kuhl, and Anders Nilsson. High selectivity for ethylene from carbon dioxide reduction over copper nanocube electrocatalysts. *Angewandte Chemie - International Edition*, 54(17):5179–5182, 2015.

[9] Chung Shou Chen, Albertus D. Handoko, Jane Hui Wan, Liang Ma, Dan Ren, and Boon Siang Yeo. Stable and selective electrochemical reduction of carbon dioxide to ethylene on copper mesocrystals. *Catal. Sci. Technol.*, 5(1):161–168, 2015.

[10] Arnau Verdaguer-Casadevall, Christina W. Li, Tobias P. Johansson, Soren B. Scott, Joseph T. Mckeown, Mukul Kumar, Ifan E L Stephens, Matthew W. Kanan, Ib Chorkendor, and Ib Chorkendorff. Probing the active surface sites for CO reduction on oxide-derived copper electrocatalysts. *Journal of the American Chemical Society*, 137(31):9808–9811, 2015.

[11] Ana Sofia Varela, Matthias Kroschel, Tobias Reier, and Peter Strasser. Controlling the selectivity of CO2 electroreduction on copper: The effect of the electrolyte concentration and the importance of the local pH. *Catalysis Today*, 260:8–13, 2016.

[12] Hemma Mistry, Ana Sofia Varela, Cecile S. Bonifacio, Ioannis Zegkinoglou, Ilya Sinev, Yong-wook Choi, Kim Kisslinger, Eric A. Stach, Judith C. Yang, Peter Strasser, and Beatriz Roldan Cuenya. Highly selective plasma-activated copper catalysts for carbon dioxide reduction to ethylene. *Nature Communications*, 7:1–8, 2016.

[13] Andre André Eilert, Filippo Cavalca, F Sloan Roberts, Ju Jürg Osterwalder, Chang Liu, Ethan J Crumlin, Hirohito Ogasawara, Daniel Friebel, Lars G M Pettersson, Marco Favaro, Ethan J Crumlin, Hirohito Ogasawara, Daniel Friebel, Lars G M Pettersson, and Anders Nilsson. Subsurface Oxygen in Oxide-Derived Copper Electrocatalysts for Carbon Dioxide Reduction. *Journal of Physical Chemistry Letters*, (8):285–290, 2017.

[14] Dahee Kim, Seunghwa Lee, Joey D. Ocon, Beomgyun Jeong, Jaeyoung Kwang Lee, Kwang Lee, and Jaeyoung Kwang Lee. Insights into autonomously formed oxygen-evacuated Cu2O electrode for the selective production of C2H4 from CO2. *Phys. Chem. Chem. Phys.*, 17(2):1–9, 2015.

[15] Yanwei Lum, Youngkook Kwon, Peter Lobaccaro, Le Chen, Ezra Lee Clark, Alexis T. Bell, and Joel W. Ager. Trace Levels of Copper in Carbon Materials Show Significant Electrochemical CO2 Reduction Activity. *ACS Catalysis*, 6(1):202–209, 2016.

[16] Yoshio Hori, Akira Murata, and Ryutaro Takahashi. Formation of hydrocarbons in the electrochemical reduction of carbon dioxide at a copper electrode in aqueous solution. *Journal of the Chemical Society, Faraday Transactions 1: Physical Chemistry in Condensed Phases*, 85(8):2309, 1989.

[17] Kendra P. Kuhl, Etosha R. Cave, David N. Abram, and Thomas F. Jaramillo. New insights into the electrochemical reduction of carbon dioxide on metallic copper surfaces. *Energy & Environmental Science*, 5(2012):7050–7059, 2012.

[18] Klaas Jan P Schouten, Zisheng Qin, Elena Pérez Gallent, and Marc T M Koper. Two pathways for the formation of ethylene in CO reduction on single-crystal copper electrodes. *Journal of the American Chemical Society*, 134(24):9864–9867, 2012.

[19] F. Sloan Roberts, Kendra P. Kuhl, and Anders Nilsson. Electroreduction of Carbon Monoxide Over a Copper Nanocube Catalyst: Surface Structure and pH Dependence on Selectivity. *ChemCatChem*, pages 1119–1124, 2016.

[20] Chuan Shi, Heine a Hansen, Adam C Lausche, and Jens K Nørskov. Trends in electrochemical CO2 reduction activity for open and close-packed metal surfaces. *Physical Chemistry Chemical Physics*, 16(10):4720–4727, 2014.

[21] Joseph H Montoya, Chuan Shi, Karen Chan, and Jens K Nørskov. Theoretical insights into a co dimerization mechanism in CO_2 electroreduction. *The Journal of Physical Chemistry Letters*, pages 2032–2037, 2015.

[22] Bryan D. McCloskey, Rouven Scheffler, Angela Speidel, Girish Girishkumar, and Alan C. Luntz. On the mechanism of nonaqueous li–o2 electrochemistry on c and its kinetic overpotentials: Some implications for li–air batteries. *The Journal of Physical Chemistry C*, 116(45):23897–23905, 2012.

[23] Alexis Grimaud, Oscar Diaz-morales, Binghong Han, Wesley T Hong, Yueh-lin Lee, Livia Giordano, Kelsey A Stoerzinger, Marc T M Koper, and Yang Shao-Horn. Activating lattice oxygen redox reactions in metal oxides to catalyse oxygen evolution. *Nat. Chem.*, 9(5):457–465, 2017.

[24] Klaas Jan P Schouten, Elena Perez Gallent, and Marc T M Koper. The influence of pH on the reduction of CO and CO2 to hydrocarbons on copper electrodes. *Journal of Electroanalytical Chemistry*, 716:53–57, 2013.

[25] Daniel B. Trimarco, Thomas Pedersen, Ole Hansen, Ib Chorkendorff, and Peter C K Vesborg. Fast and sensitive method for detecting volatile species in liquids. *Review of Scientific Instruments*, 86(7), 2015.

[26] B von Issendorff and R E Palmer. A new high transmission infinite range mass selector for cluster and nanoparticle beams. *Rev. Sci. Instrum.*, 70(4497-4501), 1999.

[27] Hernandez-Fernandez P Deiana D Strebel C E McCarthy D N Bodin A Malacrida Paolo Stephens Ifan Chorkendorff I Masini F. Exploring the phase space of time of flight mass selected PtxY nanoparticles. *Phys. Chem. Chem. Phys*, 16(48)(26506-26513), 2014.

[28] Sune R. Bahn and Karsten W. Jacobsen. An object-oriented scripting interface to a legacy electronic structure code. *Computing in Science and Engineering*, 4(3):56–66, 2002.

[29] B. Hammer, L. Hansen, and J. Nørskov. Improved adsorption energetics within density-functional theory using revised Perdew-Burke-Ernzerhof functionals. *Physical Review B*, 59(11):7413–7421, 1999.

[30] J. J. Mortensen, L. B. Hansen, and K. W. Jacobsen. Real-space grid implementation of the projector augmented wave method. *Physical Review B - Condensed Matter and Materials Physics*, 71(3):1–11, 2005.

[31] J Enkovaara, C Rostgaard, J J Mortensen, J Chen, M Dułak, L Ferrighi, J Gavnholt, C Glinsvad, V Haikola, H a Hansen, H H Kristoffersen, M Kuisma, a H Larsen, L Lehtovaara, M Ljungberg, O Lopez-Acevedo, P G Moses, J Ojanen, T Olsen, V Petzold, N a Romero, J Stausholm-Møller, M Strange, G a Tritsaris, M Vanin, M Walter, B Hammer, H Häkkinen, G K H Madsen, R M Nieminen, J K Nørskov, M Puska, T T Rantala, J Schiøtz, K S Thygesen, and K W Jacobsen. Electronic structure calculations with GPAW: a real-space implementation of the projector augmented-wave method. *Journal of physics. Condensed matter : an Institute of Physics journal*, 22(25):253202, 2010.

[32] J K Nørskov, J Rossmeisl, A Logadottir, L Lindqvist, J R Kitchin, T Bligaard, and H Jónsson. Origin of the overpotential for oxygen reduction at a fuel-cell cathode. *Journal of Physical Chemistry B*, 108(46):17886–17892, 2004.

[33] Karen Chan, Charlie Tsai, Heine A. Hansen, and Jens K. Nørskov. Molybdenum sulfides and selenides as possible electrocatalysts for CO 2 reduction. *ChemCatChem*, 6(7):1899–1905, 2014.

[34] Andrew A. Peterson, Frank Abild-Pedersen, Felix Studt, Jan Rossmeisl, and Jens K. Nørskov. How copper catalyzes the electroreduction of carbon dioxide into hydrocarbon fuels. *Energy & Environmental Science*, 3(9):1311, 2010.